Tissue Harmonic Synthetic Aperture Imaging

Rasmussen, Joachim

Publication date:
2013

Document Version
Publisher's PDF, also known as Version of record

Tissue Harmonic Synthetic Aperture Imaging

Joachim Hee Rasmussen

November 28, 2013

Technical University of Denmark
Department of Electrical Engineering
DK-2800 Kgs. Lyngby
Denmark

Submitted in partial fulfillment of the requirements for the degree of Doctor of Philosophy at Technical University of Denmark.

DEDICATION

To Harry,

a continuous acoustic source of song, laughter, and wisdom.

PREFACE

This Ph.D. dissertation has been submitted to the Technical University of Denmark in partial fulfillment of the requirements for the degree of Doctor of Philosophy.
The work has been supervised by Professor Dr. Techn. Jørgen Arendt Jensen.

The work presented in this dissertation is a recapitulation of the research work carried out from July 1st, 2010 to November 30th, 2013 at the Center for Fast Ultrasound Imaging, Department of Electrical Engineering, Technical University of Denmark. It includes two journal papers and four conference papers.

During my time at the Center for Fast Ultrasound Imaging, my knowledge of medical imaging and in particular, ultrasound imaging has been taken to a whole new level. I have had the privilege of working in one of the pioneering research groups with some of the most advanced ultrasound equipment the world has ever seen. The project has taken me to conferences all over the world from Aalborg, Denmark, to Dresden in Germany, and to both coasts of the United States. I have enjoyed these travels where I got the opportunity to spend leisure time with my delightful colleges and to expand my knowledge of the field outside our research group. Yet another privilege of this project was the opportunity to teach master students in biomedical product development for three semesters. The interaction with joyful and young students could lift my spirits on any dreary autumn day.

Joachim Hee Rasmussen
Kgs. Lyngby, November 2013

ACKNOWLEDGEMENTS

First of all, I would like to thank my supervisor, Professor Jørgen Arendt Jensen from the Technical University of Denmark, for giving me the opportunity and chance to work with advance ultrasound imaging techniques and for teaching me the scientific disciplines expected at Ph.D. level. He has exhibited great enthusiasm in driving my results forward and got me to accomplish further than I thought possible.

I would also like to thank Ph.D Martin Hemmsen from the Technical University of Denmark, who provided great help for beamforming techniques during the project.

I would like to thankfully mention my current and former colleagues for numerous discussions, inputs, talks, and good times, amongst others Michael Johannes Pihl, Morten Fischer Rasmussen, Jacob Bjerring Olesen, Jens Munk Hansen, Carlos Armando Villagomez Hoyos, David Bradley, Yigang Du, Ye Li, An Pham, Matthias Bo Stuart, Borislav Tomov, Peter Møller Hansen, Andreas Hjelm Brandt, and Signe Sloth Madsen. Futhermore, Henrik Laursen, Nina Kjærgaard, and Elna Sørensen for their always kind help.

A very special thanks goes to my friends Niels, Christian, Peter, Kasper, Jesper, Kasper, and Anders without whom I would have finished my studies much sooner.

Last but definitely not least I would like to thank my wonderful wife Marie-Louise for the enormous support and understanding during the project. You are always there for me. I owe much of this dissertation to you - I could not have succeeded without you.

Thanks to you all

ABSTRACT

The main purpose of this PhD project is to develop an ultrasonic method for tissue harmonic synthetic aperture imaging. The motivation is to advance the field of synthetic aperture imaging in ultrasound, which has shown great potentials in the clinic. Suggestions for synthetic aperture tissue harmonic techniques have been made, but none of these methods have so far been applicable for *in-vivo* imaging. The basis of this project is a synthetic aperture technique known as synthetic aperture sequential beamforming (SASB). The technique utilizes a two step beamforming approach to drastically reduce system complexity compared to conventional synthetic aperture techniques. In this project, SASB is sought combined with a pulse inversion technique for 2nd harmonic tissue harmonic imaging. The advantages in tissue harmonic imaging (THI) are expected to further improve the image quality of SASB. The first part of the scientific contribution investigates an implementation of pulse inversion for THI on the experimental ultrasound system SARUS. The technique is initially implemented for linear array transducers and then expanded for convex array transducers. The technique is evaluated based on spatial resolution. The concept of harmonic energy leakage is investigated and minimized using harmonic matched filters. The second part of the study demonstrates that a combination of SASB with THI is feasible for a linear array transducer on SARUS. The method is expanded for convex array transducer and implemented on a commercial ultrasound system. An optimization study of the scan settings for SASB with THI is performed. In the final part, a clinical investigation of the clinical relevance of SASB with THI is performed. The clinical relevance is determined by the image quality, sensitivity and specificity of the technique. Clinical scans were conducted in collaboration with medical professionals at Copenhagen University. In a series of double blinded trials, image quality and recognition of pathology using SASB with THI was compared with conventional THI. The results of the clinical trial documented, that SASB with THI provided as good image quality and specificity as conventional THI and provided 6% better sensitivity compared with conventional THI.

NOMENCLATURE

α	Opening angle
α_0	Attenuation parameter
A	Amplitude
β	Non-linearity parameter
$\mathbf{B}$	Bulk modulus
c	Speed of sound
c_p	Phase speed
Δ	Width of active aperture
d	Distance
f	Frequency
f_0	Fundamental frequency
Γ	Attenuation function
γ	Attenuation parameter
h	Sample in second stage image line
J_n	Bessel function of n^{th} order
λ	Wave length
l	Sample in first stage image line
∇	Divergence
N	Noise power
n	Harmonic number
ω	Angular frequency
Φ	Image point angle
P	Pressure
ρ	Density
$\vec{r}_e$	Transmit origin
$\vec{r}_{fp}$	Receive focal point

$\vec{r}_{ip}$	Image point
$\vec{r}_r$	Receive element
$\vec{r}_\theta$	Scanline reference point
$\vec{r}_{tfp}$	Transmit focal point
$\vec{r}_{VS}$	Virtual source position
S	Signal power
θ	Propagation direction
t	Time
t_{dk}	Time delay
$\vec{u}$	Particle velocity
$\mathcal{W}$	Apodization function
x	Propagation distance
z	Transmit focal distance

ABBREVIATIONS

biPBF	Bipolar pixel based focusing
DRF	Dynamic receive focusing
DRFTHI	Dynamic receive focusing tissue harmonic imaging
F#	F-number
FWHM	Full width at half maximum
FWOTM	Full with at one tenth maximum
IQ	In-phase and quadrature
PI	Pulse inversion
PM	Power modulation
PSF	Point spread function
RF	Radio frequency
SAI	Synthetic aperture imaging
SARUS	Synthetic aperture real-time ultrasound system
SASB	Synthetic aperture sequential beamforming
SASBTHI	Synthetic aperture sequential beamforming tissue harmonic imaging
SNR	Signal to noise ratio
THI	Tissue harmonic imaging
THSAI	Tissue harmonic synhtetic aperture imaging
TOF	Time of flight
URI	Ultrasound research interface
VAS	Visual analog scale
VS-scaling	Virtual source scaling

CONTENTS

CHAPTER

ONE

INTRODUCTION

The overall purpose of this study has been to develop a technique for tissue harmonic synthetic aperture imaging and investigate its potentials in theory and experiments. In all imaging techniques, the mission is to obtain as high resolution as possible without the trade of e.g. frame rate, penetration depth, and extensive hardware requirements. Generally, the default imaging imaging technique on many ultrasound systems has remained unchanged since the introduction of B-mode imaging. Tissue harmonic imaging was discovered almost by accident about 15 years ago, but has steadily been accepted as an improvement in image quality in B-mode imaging, where it has now taken the place as the default imaging technique on many modern day scanners. Along with the improvements in digital hardware and processing power on modern day scanners, advanced beamforming techniques such as synthetic aperture imaging are becoming popular. Just recently, Philips (Philips Healthcare, Best, Netherlands) released the EPIQ ultrasound system, which is a new ultrasound platform based entirely on synthetic aperture imaging. The increased interest in synthetic aperture imaging, makes it tempting to implement a tissue harmonic synthetic aperture technique, however the solutions that have been suggested so far are only valid for single element transducers [44, 61] or struggle with extensive beamforming, massive data processing, and low frame rates [4, 6].

Synthetic aperture sequential beamforming is a synthetic aperture technique, that has been introduced as a mean to reduce the computational requirements by the use of a two stage beamforming process [39, 41]. The technique utilizes a multi-element transmit array to generate a virtual source which is used as reference in the beamforming process. The acoustic field transmitted by the multi-element transmit array is suspected to be intense enough for the generation of harmonics required for tissue harmonic imaging. A synthetic aperture sequential beamforming tissue harmonic imaging (SASBTHI) is suggested as a synthetic aperture technique for producing *in-vivo* high resolution tissue harmonic images with minimal beamforming requirements.

A major part of this research project has been concerned with implementation and optimization of ultrasound imaging using SASBTHI on the commercially available ultrasound platform ProFocus UltraView from BK Medical (BK Medical ApS, Herlev, Denmark). The scope of the study was to investigate the technical performance of the technique and to prove its clinical relevance based on general image quality and representation of pathology.

Chapter 2 presents the theoretical background for tissue harmonic imaging. It initially describes the theory of the acoustic wave equation starting with the linear approximation to the wave equation. The non-linear propagation of acoustic waves are explained and examples of approximations to the non-linear wave equation are given. The theoretical improvements in penetration and resolution in harmonic ultrasound imaging are explained and different techniques for performing tissue harmonic imaging are discussed.

Chapter 3 presents the theory of the beamforming in fixed focus, dynamic receive focus, synthetic aperture, and synthetic aperture sequential beamforming.

Chapter 4 - describes the requirements for combining tissue harmonic imaging with a synthetic aperture beamforming technique. Examples from previous studies are given and for each technique the advantages and disadvantages are discussed. Finally, the synthetic aperture tissue harmonic technique that is used in this project is described.

Chapter 5 - presents the experimental studies that were performed during the project. The studies are divided into two categories:

- implementation and optimization of tissue harmonic imaging
- implementation and optimization of synthetic aperture sequential beamforming tissue harmonic imaging

In the first study, the experimental ultrasound system SARUS is used for an implementation of the pulse inversion technique for tissue harmonic imaging. The systems capability to perform pulse inversion is studied using a linear array transducer. In this study, 2nd harmonic imaging is performed and evaluated. The pulse inversion is further investigated for 3rd harmonic imaging using a convex array transducer on SARUS. Comparisons of fundamental, 2nd harmonic, and 3rd harmonic imaging is performed. The outcome of these studies is documented in Paper I and II.

In the second study, SASBTHI is implemented for a linear array transducer on SARUS and for a convex

array transducer on the commercially available ultrasound system UltraView. For the implementation on SARUS, the resolution of the technique is studied in an experiment where the position of the virtual source is changed. The results from this measurement are compared to the resolution of THI using dynamic receive focus on SARUS. The results are presented in Paper V.

For the implementation the UltraView system, an extensive study of resolution is conducted, where the effects of virtual source position, F#, and line density on the resolution are investigated. A gray scale compensation technique for improving image quality in SASBTHI is developed and discussed. Finally, SASBTHI is compared in a series of measurements of SNR and resolution to DRFTHI and on visual comparisons of *in-vivo* images. The technical results of this study are presented in Paper VI.

Chapter 6 presents the clinical evaluation of SASBTHI. The study was conducted in collaboration with Martin Christian Hemmsen (Post Doc. at Technical University of Denmark), Peter Møller Hansen (Ph.D student at University of Copenhagen), Andreas Hjelm Brandt (Ph.D student at University of Copenhagen), Signe Sloth Madsen (M.D. student University of Copenhagen), and health care professionals at Copenhagen University Hospital, Rigshospitalet, Department of Radiology. The purpose of the study was to demonstrate, that SASBTHI is at least as good as conventional imaging in terms of resolution, contrast, unwanted artifacts, and penetration and also, that SASBTHI is as good as conventional imaging in representing pathology in images. SASBTHI was initially evaluated in a pre-clinical investigation as a part of a Master's project conducted at University of Copenhagen and was presented in Paper III and IV. Subsequently a more thorough clinical investigation has been initiated in collaboration with the University of Copenhagen. As the investigations are still undergoing, the results have not yet been presented in any publications.

Contributions

The contributions to the field of ultrasound imaging developed during my PhD project period include one submitted journal article, one early draft journal article, four published conference papers, one published co-authored journal article, and one co-authored published conference paper.

Journal Papers

- J. H. Rasmussen, Y. Du, M. C. Hemmsen, and J. A. Jensen, "*Tissue Harmonic Synthetic Aperture Ultrasound Imaging*", submitted to Journal of the Acoustic Society of America, March 2013
- J. H. Rasmussen, M. C. Hemmsen, A. H. Brandt, P. M. Hansen, M. B. Nielsen, and J. A. Jensen,

Tissue Harmonic Synthetic Aperture Imaging Optimized for Duplex In-Vivo Imaging, draft for *IEEE Transactions on Ultrasonics, Ferroelectrics and Frequency Control*

Conference Papers and Abstracts

- J. Rasmussen, Y. Du, and J. A. Jensen, *Non-linear Imaging Using an Experimental Synthetic Aperture Real Time Ultrasound Scanner*, presented at *Nordic-Baltic Conference on Biomedical Engineering and Physics*, 2011, Aalborg, Denmark
- J. H. Rasmussen, Y. Du, and J. A. Jensen, *Third Harmonic Imaging using Pulse Inversion*, presented at *IEEE International Ultrasonics Symposium*, 2011, Orlando, Florida, United States
- J. H. Rasmussen, M. C. Hemmsen, S. S. Madsen, P. M. Hansen, M. B. Nielsen, and J. A. Jensen, *Implementation of Tissue Harmonic Synthetic Aperture Imaging on a Commercial Ultrasound System*, presented at *IEEE International Ultrasonics Symposium*, 2012, Dresden, Germany
- J. H. Rasmussen, M. C. Hemmsen, S. S. Madsen, P. M. Hansen, M. B. Nielsen, and J. A. Jensen, *Preliminary Study of Synthetic Aperture Tissue Harmonic Imaging on In-vivo Data*, presented at *SPIE Medical Imaging*, 2013, Orlando, Florida, United States

Co-authored Papers and Abstracts

- J. A. Jensen, H. Holten-Lund, R. T. Nilsson, M. Hansen, U. D. Larsen, R. P. Domsten, B. G. Tomov, M. B. Stuart, S. I. Nikolov, M. J. Pihl, Y. Du, J. H. Rasmussen, and M. F. Rasmussen, *SARUS: A synthetic aperture real-time ultrasound system*, IEEE Transactions on Ultrasonics, Ferroelectrics, and Frequency Control, Volume 60, Issue 9, pp. 1838-1852, 2013
- Y. Du, J. Rasmussen, H. Jensen, and J. A. Jensen, *Second Harmonic Imaging using Synthetic Aperture Sequential Beamforming*, presented at *IEEE International Ultrasonics Symposium*, 2011, Orlando, Florida, United States

CHAPTER

TWO

NON-LINEAR ACOUSTICS AND HARMONIC IMAGING

In this chapter, the theoretical derivation of the wave equation is described. Both the linear and non-linear approximations of the wave equation are presented. The theory on the wave equation and non-linearity used in Sections 2.1-2.4 is based mainly on the books by Beyer [7] and Pierce [49] and on a short course given by Humphrey [33]. The improvements in resolution and attenuation by harmonic imaging is described and a historical perspective on tissue harmonic imaging is given. Finally, the advantages of tissue harmonic imaging compared with fundamental imaging are discussed, and examples of tissue harmonic techniques are presented.

2.1 The Nature of Acoustic Waves

When an ultrasound transducer emits an acoustic waveform, the piezoelectric-electric elements in the transducer translate the electrical acoustic signals into a series of acoustic pressure waveforms. These pressure waveforms propagate from the transducer surface and interact with the different tissues. How these acoustic pressure waveforms propagate and affect the local tissue pressure and density can be described by the wave equation. In Fig. 2.1 a transducer is shown emitting a plane pressure wave. In Fig. 2.1a a local particle is shown as a black dot within a region of the medium outlined by the dashed cube. As the waveform propagates, it affects the local particle, which experiences a local displacement corresponding to a particle velocity, a change in local pressure, and a change in local density as seen in Fig. 2.1b. The wave equation can describe these changes.

The wave equation consists of three basic parameters:

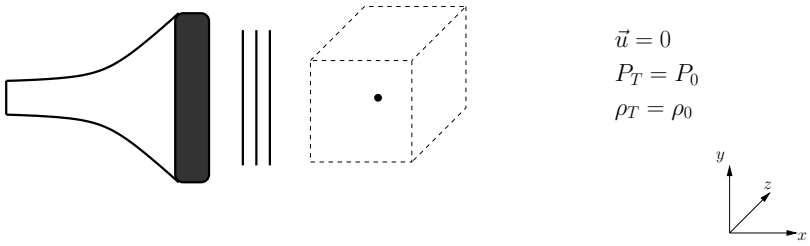

(a) Local particle in medium in its unperturbed state.

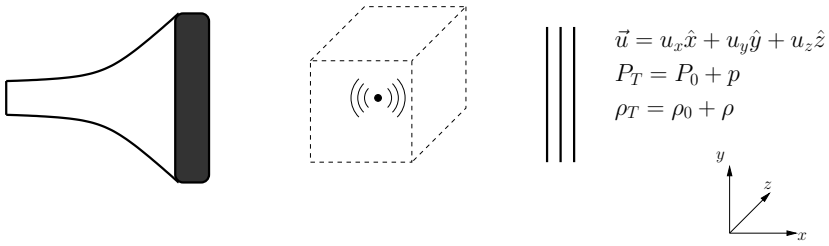

(b) Local particle in medium affected by the acoustic waveform.

Figure 2.1: Schematic illustration of a transducer emitting a plane wave. A local particle in an area of the medium (shown by the black dot inside a box) rests in its unperturbed state in 2.1a, where the local unperturbed pressure is P_0 and the unperturbed density is ρ_0. When an acoustic waveform interacts as in 2.1b, the particle is given a local movement described by a local velocity, $\vec{u}$, a local change in pressure, p, and a local change in density, ρ.

- Particle velocity, $\vec{u}$
  This is the local velocity of a particle in the medium affected by the acoustic wave (not to be confused with the speed of sound, c).

- Total pressure, P_T
  The sum of the unperturbed pressure, P_0, in the medium and changes in the pressure, p, exerted by the acoustic pressure waveform.

- Total density, ρ_T
  The sum of the unperturbed density, ρ_0, in the medium and changes in the density, ρ, caused by the waveform.

When no acoustic wave is present, the medium rests in its unperturbed state. That is,

$$\vec{u} = 0 \tag{2.1a}$$

$$\rho_T = \rho_0 \tag{2.1b}$$

$$P_T = P_0 \tag{2.1c}$$

When an acoustic wave is present, the medium is affected by the acoustic components ρ and p and the particle experiences a displacement translated into a local velocity.

$$\vec{u} = u_x\hat{x} + u_y\hat{y} + u_z\hat{z} \tag{2.2a}$$

$$\rho_T = \rho_0 + \rho \tag{2.2b}$$

$$P_T = P_0 + p \tag{2.2c}$$

where $\hat{x}$, $\hat{y}$, and $\hat{z}$ are unit vectors in the Cartesian coordinate system.

The acoustic wave equation is obtained by combining three governing equations:

- The equation of continuity,

$$\frac{\partial \rho}{\partial t} = -\nabla \cdot (\rho_T \vec{u}) \tag{2.3}$$

- The equation of force,

$$-\nabla P_T = \rho_T \left[(\vec{u} \cdot \nabla) + \frac{\partial}{\partial t} \right] \vec{u} \tag{2.4}$$

- The equation of state (density vs. pressure),

$$P_T = P_0 + \left(\frac{\partial P_T}{\partial \rho_T}\right)_0 (\rho_T - \rho_0) + \left(\frac{\partial^2 P_T}{\partial \rho_T^2}\right)_0 (\rho_T - \rho_0)^2 + \cdots \tag{2.5}$$

where ∇ is the divergence and t is time.

The first equation describes conservation of mass, which states, that any changes in mass influx in an area of the medium must result in a change of mass within that same area. The second equation describes conservation of momentum, where the force due to the pressure gradient results in an change in momentum. Finally, the third equation describes the relationship between pressure and density in the medium.

2.2 The Assumption of Linear Acoustic Wave Propagation

In order to combine the three equations in (2.3), (2.4), and (2.5), a natural simplification is to linearize the three terms. In this process, any terms which are of second order or higher in the acoustic variables ρ and p are neglected. The result is a linear acoustic wave equation.

Consider that acoustic parameters are made up of successively higher order terms, which decrease in magnitude:

$$\rho_T = \rho_0 + \rho_1 + \rho_2 + \cdots \tag{2.6a}$$

$$\vec{u} = \vec{u}_1 + \vec{u}_2 + \cdots \tag{2.6b}$$

$$P_T = P_0 + p_1 + p_2 + \cdots \tag{2.6c}$$

Then, for instance, the product of ρ_T and $\vec{u}$ will be:

$$\rho_T \vec{u} = \underbrace{\rho_0 \vec{u}_1}_{\text{1st order}} + \underbrace{\rho_0 \vec{u}_2 + \rho_1 \vec{u}_1}_{\text{2nd order}} + \cdots \tag{2.7}$$

By keeping only the 1st order terms for all acoustic variables, the three basic equations (2.3), (2.4), and

(2.5), reduce to:

$$\frac{\partial \rho_T}{\partial t} = -\nabla \cdot (\rho_T \vec{u}) \Rightarrow \frac{\partial \rho}{\partial t} = -\rho_0 \nabla \cdot (\vec{u}) \tag{2.8a}$$

$$-\nabla P_T = \rho_T \left[(\vec{u} \cdot \nabla) + \frac{\partial}{\partial t} \right] \vec{u} \Rightarrow -\nabla P = \rho_0 \frac{\partial \vec{u}}{\partial t} \tag{2.8b}$$

$$P_T = P_0 + \left(\frac{\partial P_T}{\partial \rho_T} \right)_0 (\rho_T - \rho_0) + \left(\frac{\partial^2 P_T}{\partial \rho_T^2} \right)_0 (\rho_T - \rho_0)^2 + \cdots \Rightarrow p = \left(\frac{\partial P_T}{\partial \rho_T} \right) \rho = \frac{\mathbf{B}}{\rho_0} \rho \tag{2.8c}$$

where $\mathbf{B}$ is the bulk modulus of the medium.

Under the circumstances, that the changes in particle speed, medium density, and medium pressure are much less than the initial values ($|u| << c$, $|\rho| << \rho_0$, and $|p| << \rho_0 c^2$), the three equations in (2.8) can be combined into the linear wave equation:

$$\nabla^2 p - \frac{1}{c_0^2} \frac{\partial^2 p}{\partial t^2} = 0, \tag{2.9}$$

where $c_0 = \sqrt{\frac{\mathbf{B}}{\rho_0}}$ is the speed of sound and $\nabla^2 = \frac{\partial^2}{\partial x^2} + \frac{\partial^2}{\partial y^2} + \frac{\partial^2}{\partial z^2}$.

2.3 The Non-Linear Acoustic Wave Approximation

The linear wave equation depends on two main assumptions:

1. That the particle velocity u of the wave is infinitesimal compared to the speed of sound c
2. That the pressure-density relationship of the medium is linear.

If the acoustic pressure, however is sufficiently great, these assumption no longer hold up, and non-linear effects need to be included to account for the non-linear relationship between pressure and density.

The Taylor expansion of the equation of state in (2.5) is in itself an approximation to the true P_T. In the linear approximation of the equation of state in (2.8), only the first order term was considered. By including several higher order terms, a more accurate approximation to the true non-linear wave can be obtained. Including an infinite string of successively higher order terms into one equation however, not only increases the demands on the formulation of the equation, but also increases the effort it takes to compute the results to a degree beyond reason. Several suggestions to a non-linear wave equation, that vary in complexity, exist nonetheless. Examples of these wave equations are the one-dimensional diffusion model (Burgers) [27], the three-dimensional parabolic model (Khokhlov-Zablotskaya-Kuznetsov) [43], and the full wave model (Westervelt) [59], which are all approximations

to the second order of the wave equation.

The Westervelt non-linear wave equation describes the propagation of a non-linear, quasi-planar sound wave and is an approximation of the second order wave equation. It assumes that the medium in which the acoustic wave propagates is homogeneous and that the unperturbed density and pressure is uniform. While this is only an approximation to the actual full non-linear wave equation, it serves to take non-linearity into account.

$$\underbrace{\nabla^2 p - \frac{1}{c_0^2}\frac{\partial^2 p}{\partial t^2}}_{\text{linear wave eq.}} + \underbrace{\frac{\delta}{c_0^4}\frac{\partial^3 p}{\partial t^3}}_{\text{absorption}} = \underbrace{-\frac{\beta}{\rho_0 c_0^4}\frac{\partial^2 p^2}{\partial t^2}}_{\text{non-linearity}} \tag{2.10}$$

The Westervelt equation can be broken down into three parts. The first two terms of the equation represent diffraction and linear propagation and are in fact the linear wave equation in (2.9). The next term accounts for thermoviscous losses or absorption in the medium, while the last term describes the degree of non-linearity of the propagating acoustic wave based on the non-linearity parameter, β. The non-linearity parameter can be found by rewriting the equation of state in (2.5).

$$P_T = P_0 + \left(\frac{\partial P_T}{\partial \rho_T}\right)_0 (\rho_T - \rho_0) + \left(\frac{\partial^2 P_T}{\partial \rho_T^2}\right)_0 (\rho_T - \rho_0)^2 + \cdots \Rightarrow \tag{2.11a}$$

$$P_T = P_0 + \frac{A}{\rho_0}(\rho_T - \rho_0) + \frac{B}{2\rho_0^2}(\rho_T - \rho_0)^2 + \cdots \tag{2.11b}$$

where

$$\frac{A}{\rho_0} = \left(\frac{\partial P_T}{\partial \rho_T}\right)_0 = \frac{\mathbf{B}}{\rho_0} \tag{2.12a}$$

$$B = \left[\rho_0^2 \left(\frac{\partial^2 p}{\partial \rho^2}\right)_{\rho=\rho_0}\right] \tag{2.12b}$$

and the non-linearity parameter is:

$$\beta = 1 + \frac{B}{2A} \tag{2.13}$$

2.4 Non-Linearity

The non-linearity parameter β describes how much the wavefronts of a propagating acoustic waveform are distorted. Different media and tissues exert different degrees of non-linearity on the propagating acoustic wave, causing β to vary for different tissues. Table 2.1 shows the different β values for different tissues.

Table 2.1: Degree of non-linearity for various tissues [22, 23].

Medium	β
water	3.5
blood	4
liver	4.9
soft non-fatty tissue	4.15-5
soft fatty tissue	5.8-6.65

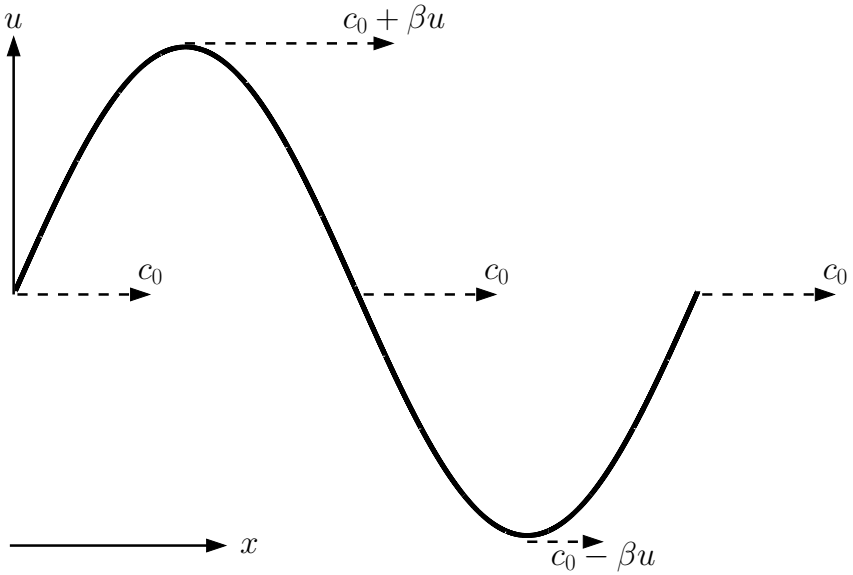

Figure 2.2: Schematic illustration of the changes in waveform speed produced by the alternations in acoustic pressure. A waveform with local particle velocity u propagates along the axis x. The mean propagation velocity of the waveform will be c_0. The density of the medium will be affected by the changes in acoustic pressure and so will the phase speed, c_p. At the relatively high pressure peaks in the waveform the phase speed of the waveform will be $c_p = c_0 + \beta u$. At the relatively low pressure trough the phase speed will be $c_p = c_0 - \beta u$.

The non-linearity parameter specifically describes the amount of change in local wavefront speed caused by the non-linearity of the medium. In the waveform, the local acoustic amplitude varies and so does the acoustic pressure exerted on the medium. This causes alternations in the density of the medium and thereby changes the speed of sound in the medium. Recall from (2.9), that $c = \sqrt{\frac{\mathbf{B}}{\rho_0}}$, where ρ_0 is the mean density of the medium and $\mathbf{B}$ is the bulk modulus of the medium. Here, the linear relationships between ρ_0 and c and between p and ρ were based on approximations to the first order of the acoustic variables in (2.6). Expanding the approximation to include the second order terms as well, results in a second order, non-linear relationship between pressure and density and between density and propagation

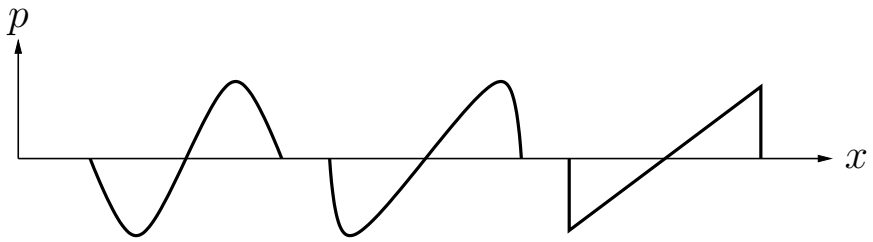

Figure 2.3: Schematic illustration of the changes in waveform shape as the waveform propagates. A waveform with local acoustic pressure p propagates along the axis x. As the propagation distance increases, more harmonics are generated, and the shape of the waveform changes from a sine-shape to a sawtooth-shape.

speed. The phase speed, c_p, of the propagating waveform may then be written as [7, 23]:

$$c_p = c_0 \left(1 + \frac{B}{2A}\frac{u}{c_0}\right)^{2A/B+1}. \tag{2.14}$$

This means that the changes in density caused by the variations in acoustic pressure from the waveform, forces the speed of the propagating waveform to change as well. For small amplitude acoustic plane waves, the phase speed in the waveform can be approximated as [23, 49]:

$$c_p = c_0 + \beta u, \text{ at the relatively high pressure peaks in the waveform} \tag{2.15a}$$

$$c_p = c_0 - \beta u, \text{ at the relatively low pressure valleys in the waveform} \tag{2.15b}$$

where c_0 is the speed of sound in the medium at rest (see Fig. 2.2).

The differences in phase speed causes the peaks of the waveform to travel faster than the valleys of the waveform. In this way distortion is introduced and the initial sinusoidal waveform is gradually changed into a sawtooth-shaped waveform as the propagation distance x increases (see Fig. 2.3). What happens in terms of the frequency content of the waveform is, that harmonic frequencies are generated and added to the spectrum of the waveform. The harmonics are generated at integer multiples of the originally transmitted fundamental frequency, f_0. That is, harmonics are generated at $n \cdot f_0$, $n = 1, 2, 3, \cdots$ (see Fig. 2.4a). As the waveform continues to propagate, the distortion of the waveform increases and the amplitude of the harmonics increase as well. The amplitude of the harmonics of the pressure waveform is given as:

$$p_n(\sigma) = \frac{2 \cdot P_0}{n \cdot \sigma} J_n(n\sigma) \tag{2.16}$$

where n is the harmonic number, J_n is the n^{th} order Bessel function, and σ is defined as

$$\sigma = \frac{x}{\overline{x}} \tag{2.17}$$

where x is the propagation distance of the waveform and

$$\overline{x} = \frac{\rho_0 c_0^3}{\beta \omega P_0} \tag{2.18}$$

where ω is the angular frequency of the transmitted plane wave. For small values of σ ($\sigma < 1$), the amplitude of the fundamental ($n = 1$) decreases as

$$p_1(\sigma) \approx P_0 \left(1 - \frac{\sigma^2}{8}\right) \tag{2.19}$$

and the 2nd harmonic ($n = 2$) increases as

$$p_2(\sigma) \approx P_0 \frac{\sigma}{2} \tag{2.20}$$

This shows, that for non-attenuating homogeneous media, the total amount of energy in the waveform remains unchanged as the wave propagates, but energy in the waveform is transferred from the fundamental frequency component into the harmonics.

2.5 Attenuation and Resolution in Harmonic Imaging

In ultrasound imaging, achieving a high penetration depth with high spatial resolution is often desirable. The axial resolution is dependent on the length of the transmitted pulse response, where a shorter pulse will lead to higher axial resolution. The lateral resolution is dependent on the center frequency (f_0) of the transmitted waveform and on the F#. Specifically, the lateral -6 dB resolution known as the full width half maximum (FWHM), is estimated as:

$$FWHM \approx 1.2 \cdot \lambda \cdot \frac{z}{\Delta} \tag{2.21}$$

where λ is the wavelength of the transmitted waveform, z is the transmit focal distance, Δ is the width of the transmit aperture, and $F\# = \frac{z}{\Delta}$ [55]. Here it is seen, that a higher f_0 results in lower FWHM value and therefore, a higher lateral resolution. In terms of achieving the highest spatial resolution, it would seem beneficial to transmit a relatively short waveform pulse, with a high f_0. In reality, however, high frequency waveforms are more prone to losses in signal strength as the waveform travels through a medium. This phenomenon is known as attenuation.

As a waveform penetrates tissues, energy in the waveform is continuously absorbed and turned into heating of the tissues. The waveform also experiences scattering from interaction with the different tissues. The two effects, absorption and scattering (which includes both refraction and reflection) are collectively known as attenuation. As a plane wave with initial amplitude A_0 propagates along the distance x, the

time and distance dependent attenuated amplitude A of the waveform can be found as [23, 29]:

$$A(x,t) = A_0 e^{-\Gamma x} e^{i\omega(t-x/c)} \tag{2.22}$$

where ω is the angular frequency and c is the speed of sound. The attenuation function $\Gamma(\omega)$ is defined as

$$\Gamma(\omega) = \alpha_0 |\omega|^{\gamma}, \gamma \in [0,2] \tag{2.23}$$

where α_0 and γ are tissue specific attenuation parameters [29].

As seen from (2.22), the amplitude of the acoustic pressure decreases as the waveform propagates and is inversely proportional to the angular frequency of transmitted waveform. This means that a waveform with a low center frequency will be able to penetrate deeper into tissues before the noise floor is met compared with a waveform with higher center frequency. This indicates, that utilizing a low f_0 would be the most beneficial, if the goal is only to get maximum possible penetration depth. Since neither resolution nor penetration depth can stand on its own in medical ultrasound, a compromise between the two must be met in terms of which center frequency to apply. This is where tissue harmonic imaging proves its usefulness.

2.6 Tissue Harmonic Imaging

In traditional ultrasound B-mode imaging, an image is acquired by transmitting a waveform with a specific center frequency, f_0, and imaging the response at that same center frequency. In the early 90's, contrast harmonic imaging was introduced as a mean to visualize blood perfusion and to increase the dynamic resolution of tissues [55]. The concept of this technique involved using contrast solutions, sometimes with a non-linearity of $\beta_{contrast} \geq 1000$ [60], injected into the blood stream of the patient. It was conceived, that when an ultrasound waveform was traveling through tissues injected with harmonic contrast agents, the waveform would cause micro bubbles in the contrast solution to vibrate at a harmonic frequency. This vibration would be of such a magnitude, that imaging could be performed, not at the fundamental frequency f_0, but at given harmonic frequency, typically at the 2nd harmonic $(2 \cdot f_0)$ [17, 18]. It was assumed, that the harmonic frequencies that were received, were purely a result of the vibration of the micro bubbles and that contributions to the harmonics from the propagation through the non-linear tissues were infinitesimal (remember, that $\beta_{tissue} << \beta_{contrast}$). It was generally thought, that even though an image was produced by harmonic imaging just prior to injection of the contras agent, the image was a result of some sort of harmonic leakage and could not be a result of non-linear propagation. It was suggested, that the leakage could arise from either poor separation of the harmonics in the spectrum of the received waveform, so that part of the spectrum of the f_0 was being visualized at $2 \cdot f_0$,

or that the transducers were imperfect and would simply emit also at $2 \cdot f_0$ [1, 22]. And so, harmonic imaging in itself was only intended to function on ultrasound systems with the addition of contrast agents.

As early as 1980, however, it was suggested by Muir and Carstensen [45], that propagation of waveform through tissues alone could generate harmonic contributions. This was soon backed up by the first experiments with single element transducers emitting in water by Carstensen et al. [10], also in 1980. The first demonstrations that showed that harmonics could be generated in tissues, were presented by Starritt et al. [53, 54] in 1985 and 1986, where diagnostic ultrasound was applied to ox liver and to human calf muscle. The first definitions of imaging based on tissue harmonic generation appeared in 1997. Here, Christopher [13] showed by non-linear simulations, that not only was the magnitude of the harmonics generated in water sufficient to produce a tissue harmonic image, but also that improvements in the lateral resolution could be obtained using harmonics. The results were confirmed by Ward et al. [58] in 1997, who showed good agreement between simulations and measurements in water using a circular piston transducer. It was shown in the same study, that the reflected beam width would decrease by $w_n/w_1 = 1/n^{0.78}$, where n is the harmonic number, thereby improving the lateral resolution. It was also shown, that the side lobe levels would quickly fall off as the harmonic number, n increased. The results were further substantiated by Averkiou et al. [2], also in 1997. Averkiou et al. showed, again by simulations and measurements, that harmonics could be generated in water as well as in muscle tissue from a cow. In this study it was also shown, that the received harmonics were not a result of harmonic leakage by faulty transmission of the $2 \cdot f_0$. This lead to a distinction between contrast harmonic imaging, where harmonics produced by vibration of micro spheres in contrast agents were used for imaging, and tissue harmonic imaging (THI), where only harmonics caused by the non-linear property of tissue itself were used.

After the introduction of THI, studies of clinical applications and advantages were soon performed [19, 20, 50, 56]. It was found that, THI provided an improvement in reduced clutter and better delineation of tissues, especially when studying patients with large body mass or when scanning at deeper depths [22]. THI is now a common and widespread technique, that has been implemented on basically all modern scanners. It has been so well founded in ultrasound imaging, that THI today often is the default scanning technique in many clinical investigations. In all sections that follow in this text, the term harmonic imaging will be used for THI only, since this type of harmonic imaging is the focus of the thesis.

2.7 Tissue Harmonic Imaging Advantages

Besides the advantages of increased penetration depth and resolution, THI benefits from several other advantages, which include:

- Reduced clutter due to narrower beam profile [22, 32]. This reduces the amount of echoes from unwanted tissues in the image. In investigations of e.g. the heart, where the air-filled regions of the lungs are sought avoided, THI will be able to image closer to those regions compared to regular imaging.
- Increased border delineation [1, 22]. The narrower main lobe in THI increases resolution, and thereby increases the border delineation.
- Reduced clutter due to lower side-lobes levels [3, 14, 58]. The lower levels of side lobes reduces the amount of echoes from unwanted tissues.
- Reduced phase aberration [1, 22]. When the acoustic wave travels across tissues with different speed of sound, phase errors are introduced. These are seen to a higher extend for higher frequency waveforms. In THI, a relatively low center frequency waveform is transmitted. This waveform will not be affected as much by reverberation as transmission at e.g $2 \cdot f_0$. Since the higher harmonics are generated only after a certain propagation depth, the amount of phase aberration will be less in the harmonic waveform than in the waveform transmitted at $2 \cdot f_0$.
- Reduced reverberation artifacts [8]. Since most of the reverberation artifacts take place in the near field, THI can reduce the amount of reverberation because the harmonic energy is low here.

2.8 Tissue Harmonic Imaging Techniques

It has been noted [1], that THI may suffer from reduced axial resolution and harmonic overlap if not performed carefully. The best axial resolution is obtained by transmitting a very short waveform. This will cause the bandwidth of the fundamental to be very large and so most of the transducer's bandwidth will be used to transmit and receive the fundamental. The way to reduce the bandwidth of the fundamental is to increase the pulse length which would also reduce the degree of overlap between the harmonics and the fundamental. However, applying a longer pulse will inherently reduce the axial resolution of the technique. In the following section, examples of THI techniques that aim to overcome this problem are described.

2.8.1 Harmonic Bandpass Filters

The most simple way to extract a given harmonic from the received spectrum is to apply a high pass or band pass filter [2, 13, 58]. The difficulties using this technique is to find a weighting between applying a narrow band filter and risking a reduced axial resolution, or applying a wider band filter and risk leakage of energy from other harmonics due to overlap. While this technique was widely used in the first studies

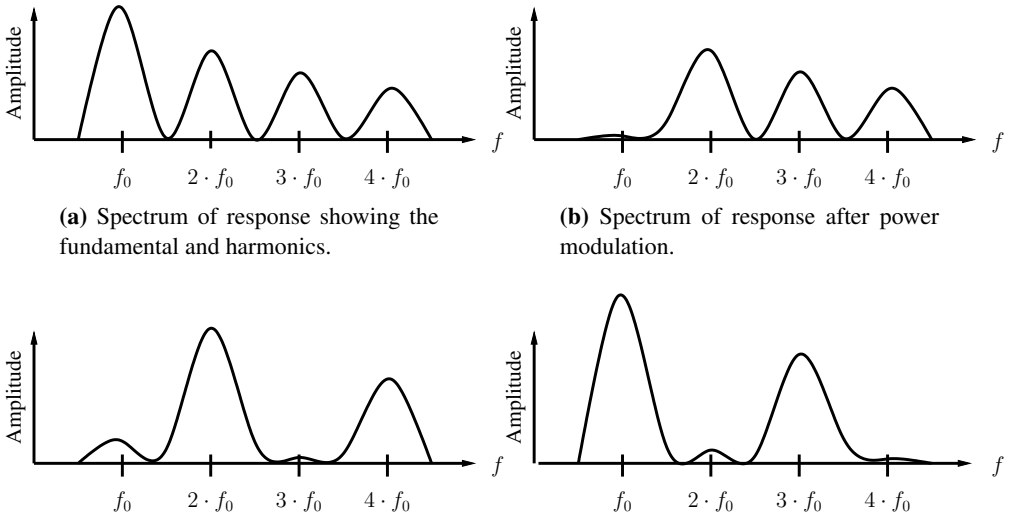

(a) Spectrum of response showing the fundamental and harmonics.

(b) Spectrum of response after power modulation.

(c) Spectrum of response after pulse summation in PI.

(d) Spectrum of response after pulse subtraction in PI.

Figure 2.4: Schematic illustration of the spectra of responses prior to and after harmonic separation by power modulation, pulse summation in PI, and pulse subtraction in PI. In power modulation in 2.4b, the fundamental is attenuated in the response. In pulse summation in 2.4c, the odd order harmonics are attenuated, while the even order harmonics gain a +6 dB increase in amplitude. In pulse subtraction in 2.4d, the fundamental and the odd order harmonics gain +6 dB in amplitude, while the even order harmonics are attenuated.

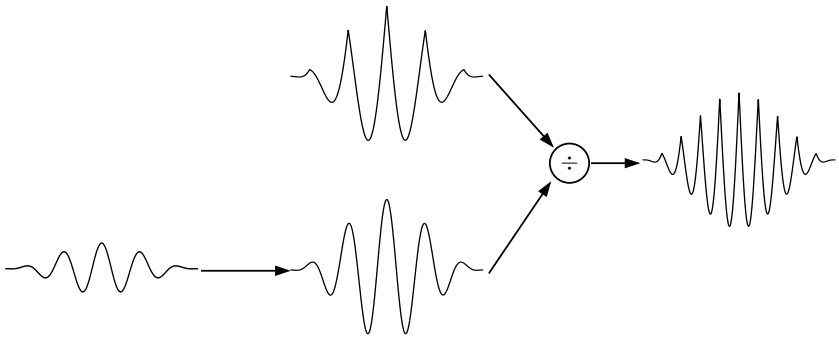

Figure 2.5: Schematic illustration of the power modulation technique. A high amplitude waveform is transmitted and its non-linear response is received (top). A second low-amplitude waveform is transmitted next and its linear response is received (bottom). The linear response is amplified to match the non-linear response in magnitude. Next, the amplified linear response is subtracted from the non-linear response resulting in a new response containing only the harmonics of the non-linear waveform.

of THI, it has now been replaced by more advanced techniques that try to remove unwanted frequencies from the received responses.

2.8.2 Power Modulation

In the power modulation (PM) scheme [9], the concept is remove the fundamental from the spectrum of the response, leaving only the harmonics. The technique is based on the property, that the generation of harmonics is dependent on the amplitude of the transmitted waveform. While a waveform transmitted at high amplitude will generate strong harmonics, the same waveform may produce no harmonics if the amplitude in transmission is sufficiently low. By transmitting identical waveforms but with either high or low transmit amplitude for the same image line, a set of paired responses differing in amplitude can be received as illustrated in Fig. 2.5. In each pair, one response (with low amplitude) will contain only the fundamental frequency f_0, while the other response (with high amplitude) will contain the fundamental and all harmonics $n \cdot f_0$, $n = 1, 2, 3, \cdots$. The linear response will differ from the non-linear response not only in the frequency content, but also in amplitude. By amplification of the linear response, the two responses can be equalized in magnitude. Next, the two responses can be subtracted from each other, thereby causing the fundamental frequency in the resulting subtracted response to diminish. The resulting subtracted response contains therefore now only the harmonics $n \cdot f_0$, $n = 2, 3, \cdots$ (see Fig. 2.4b). These can in turn be isolated using either band pass filters or using a transducer, which has limited bandwidth to only receive up to frequencies of the 2nd harmonic.

2.8.3 Pulse Inversion

In pulse inversion (PI) [11, 52, 57], the concept is to remove either all odd number harmonics ($[2 \cdot n - 1] \cdot f_0$, $n = 1, 2, 3, \cdots$) or even number harmonics ($2 \cdot n \cdot f_0$, $n = 1, 2, 3, \cdots$) from the responses. Here, two identical, but phase shifted pulses (0° phase shifted and 180° phase shifted pulse), are transmitted in turn for the same image line. Due to the phase shift, the variations in local acoustic pressure and thereby also in the local speed of sound, are no longer the same in the two waveforms. As a result, the two waveforms will be distorted differently. This is true if the assumptions are met, that there has been no motion in the medium in the time it took to transmit and receive the two waveforms and that the ultrasound transmit system is completely linear and capable of performing a perfect 180° phase shift. Differences in the responses will thereby purely be a result of how the two waveforms were distorted by the medium (see Fig. 2.6). For the received pair of responses, a 180° phase shift between the two waveforms can be detected at the fundamental. However, for the 2nd and 3rd harmonic frequencies, a corresponding 360° and 540° phase shift can be detected in the pair of waveforms respectively [1, 34], as seen in Fig. 2.7. If the two responses are summed, all signals that are perfectly in phase will double in signal strength, while all signals that have opposite phases will cancel out. To suppress the odd order harmonics then, each pair (regular and phase shifted) of the received responses are summed. The harmonic frequencies that are in phase (all even harmonics) will double in amplitude, while out of phase harmonic frequencies (all odd harmonics) will cancel out as seen in Fig. 2.4c. In Fig. 2.4d the opposite is shown, where all even harmonics are removed by pulse subtraction.

The advantage of PI is that a given harmonic may be enhanced by up to +6 dB because twice the signal energy is used for imaging. Also, due to attenuation of the neighboring harmonics, separation by band pass filtering is much easier, because a filter with greater band width may be applied without risking contributions from harmonic neighbors.

Comparing the three techniques, it is seen that all three have their advantages. In band pass filtering, only one response per emission line is needed in contrast to both PM and PI. In PM, the system itself needs not to be able to perform a perfect 180° phase shift and so, a simpler transmission stage can be applied. In PI, a +6 dB gain in a given harmonic can be obtained and the neighboring harmonics can be removed from the response, making separation by band pass filters much easier.

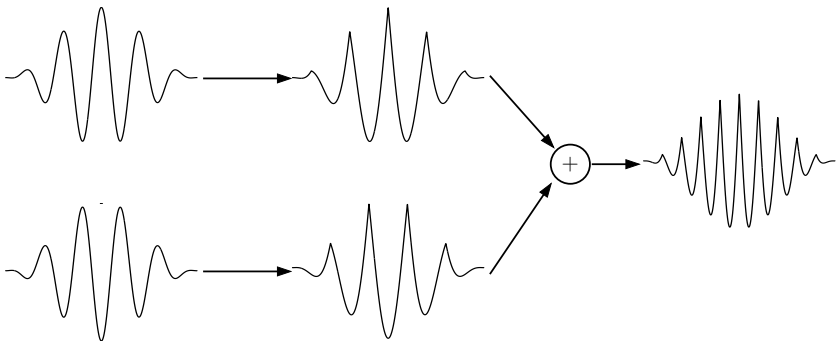

Figure 2.6: Schematic illustration of the PI technique. Two waveforms are transmitted in turn. The waveforms are inverted copies of each other, that is, a 180° phase shift has been introduced to one of the waveforms. The non-linear response for both of the transmitted waveforms are received. Since distortion is dependent on the local pressure in the wavefront, the two responses will not be exact inverted copies of each other. By summing the pulses, all signals that are of opposite phase, will cancel out, while signals that are perfectly in phase will double in amplitude. This means that all $2 \cdot n \cdot f_0$ harmonics will be enhanced by pulse summation, while all $(2 \cdot n - 1) \cdot f_0$ harmonics are suppressed for $n = 1, 2, 3, \cdots$.

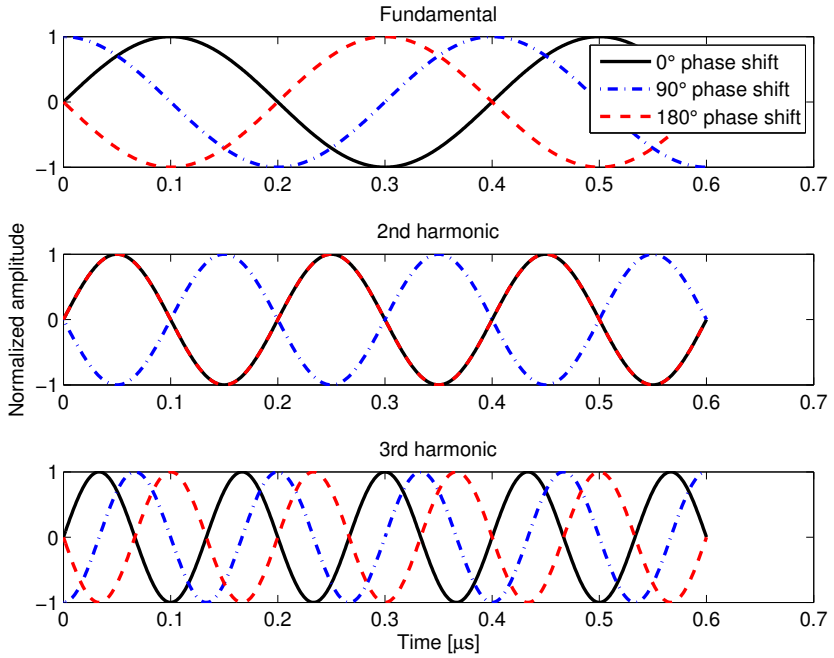

Figure 2.7: Simulation of the effect of PI on phase shift for fundamental, 2nd harmonic, and 3rd harmonic waveforms. A 0°, 90°, and 180° phase shift for the fundamental frequency is shown for each frequency band. In the waveforms, a 180° phase shift in the fundamental frequency band (red dashed curve) corresponds to a 360° shift in the 2nd harmonic frequency band and to a 540° shift in the 3rd harmonic frequency band.

CHAPTER

THREE

BEAMFORMING TECHNIQUES IN ULTRASOUND IMAGING

In this chapter three beamforming techniques, which differ in complexity will be described. Fixed transmit and receive focusing is a low complexity beamforming process, where a single fixed focal point is used in both transmit and receive. This technique creates an image that has optimal resolution at the focal point, but has poor resolution at other regions in the image. Dynamic receive beamforming is a widely used technique to obtain focused images in receive and can maintain an almost uniform resolution throughout the entire image. It is commonly used in ultrasound imaging and has become the default beamforming technique in most modern ultrasound systems. In synthetic aperture imaging, the goal is to achieve an image that is fully focused in both transmit and receive. This technique has many potentials in terms of both achieving optimal resolution and a depth independent resolution, however, complex focusing and vast computational load are inherent to the technique. A synthetic aperture technique know as synthetic aperture sequential beamforming is described, which can reduce the complexity of the beamforming process while keeping a high and depth independent resolution.

3.1 Fixed Focus Beamforming

In fixed transmit and receive focusing, a single focal point is utilized in both transmit and receive. In transmit, the excitation waveforms are properly delayed in order to focus the energy field at a desired spatial position. The responses that are received are also delayed in the beamforming process in order to ensure that samples in the responses correspond to the correct imaging depth. For fixed focus beamforming, the time delay is calculated from the round trip time of flight (TOF), which is the total time it takes an excitation waveform to propagate from the transmit origin, $\vec{r}_e$ to the receive focal point, $\vec{r}_{fp}$ through the transmit focal point, $\vec{r}_{tfp}$ and back to a receiving element on the transducer, $\vec{r}_r$, again through the

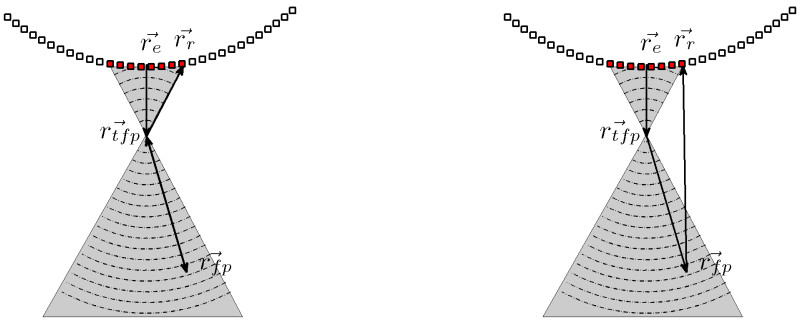

(a) Fixed transmit and receive focus.

(b) Dynamic receive focus.

Figure 3.1: Concept illustrations of the time of flight used in beamforming of fixed transmit and receive (3.1a) and dynamic receive focus(3.1b).

transmit focal point, $\vec{r}_{tfp}$. The time delay in fixed focus beamforming can then be calculated as

$$t_d\left(\vec{r}_r\right) = \frac{1}{c}\left(\|\vec{r}_{tfp} - \vec{r}_e\| \pm 2\|\vec{r}_{fp} - \vec{r}_{tfp}\| + \|\vec{r}_r - \vec{r}_{tfp}\|\right) \tag{3.1}$$

where the term $\|\|$ is the Euclidean norm and $\pm$ indicates whether the receive focal point, $\vec{r}_{fp}$ is above or below the transmit focal point, $\vec{r}_{tfp}$. Also, here it is assumed, that the speed of sound, c is known. Fig. 3.1a shows a schematic illustration of the TOF calculations for fixed focus beamforming.

In fixed focus beamforming, the image is optimally focused in both transmit and receive at the position of the focal point. However, this is only valid at the focal point, and the resolution quickly deteriorates as the distance from the focal point increases.

3.2 Dynamic Receive Beamforming

One way to improve the focusing and the resolution in ultrasound imaging is to use dynamic receive focusing (DRF). Here, a fixed focus and aperture is used in transmit, while numerous focal points and an expanding aperture is applied in receive. For every focal point in receive, a new set of time delays is calculated for every response from the individual receiving elements in the aperture. The advantages with DRF are that the image can be fully focused in receive and that an almost uniform resolution can be kept throughout the entire scan depth. These advantages have lead to DRF being the default focusing technique on basically all modern ultrasound systems.

In DRF beamforming, a time delay is calculated for the response for each of the receiving element in the aperture based on the TOF from the transmit origin on the transducer, $\vec{r}_e$ to the receive focal point, $\vec{r}_{fp}$ through the transmit focal point, $\vec{r}_{tfp}$ and back to a receiving element on the transducer, $\vec{r}_r$. The time delay can then be calculated as

$$t_d\left(\vec{r}_r\right) = \frac{1}{c}\left(\|\vec{r}_{tfp} - \vec{r}_e\| \pm \|\vec{r}_{fp} - \vec{r}_{tfp}\| + \|\vec{r}_r - \vec{r}_{fp}\|\right). \tag{3.2}$$

A schematic illustration of the TOF for DRF beamforming is shown in Fig. 3.1b.

3.3 Synthetic Aperture Imaging

Synthetic aperture imaging (SAI) was first conceived as a radar imaging technique [15, 16, 51], but has found to be useful in ultrasound imaging as well. The most basic SAI technique in ultrasound imaging is the synthetic transmit aperture imaging technique [12, 38], where an active aperture of just one element is used in transmit and the back scattered signal is received by a multiple-element aperture. The received RF-signals are stored for all channels and delay-and-sum beamforming is applied to construct a low resolution B-mode image. By moving the transmit source over the entire range of elements in the transducer, a larger aperture is synthesized and a collection of low resolution images is obtained. By coherently adding the low resolution images, a single high resolution image, that is dynamically focused in both transmit and receive is obtained. Naturally, because only one element is used in transmit, the signal-to-noise ratio (SNR) is very poor using this technique.

Several SAI techniques have been suggested to improve SNR, including the use of multi-element transmit and receive aperture, as suggested by Karaman et al. [38]. Here, a group of elements are used in transmit to increase the SNR. By focusing multiple elements in a single point in transmit, a virtual source is created as first described by Passmann and Ermert [48] and further investigated by Frazier and O'Brien [24], Nikolov and Jensen [46, 47], Gammelmark and Jensen [25], and Bae and Jeong [5].

Inherent to the SAI techniques is that they are computationally heavy and complex beamforming processes, because a full low resolution image has to be beamformed for every line in the final high resolution image. A few years ago, Kortbek et al. [40] suggested Synthetic Aperture Sequential Beamforming (SASB) as a SAI technique to reduce beamforming and system requirements in multi-element transmit synthetic aperture imaging, while maintaining high and depth independent resolution superior to conventional DRF imaging. SASB was introduced and described for linear array transducers by Kortbek et al. [40, 41] and further investigated by Hemmsen et al. [30] for convex array transducers.

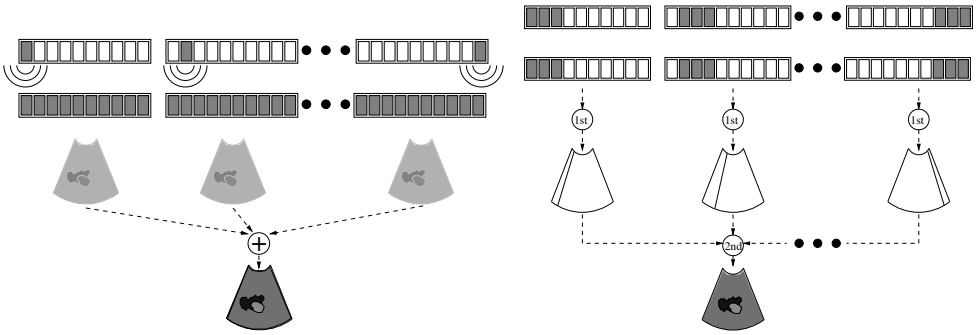

(a) Schematic illustration of SAI. **(b)** Schematic illustration of SASB.

Figure 3.2: Concept illustrations of SAI and SASB. In SAI, a single element is used in transmit, while all elements are used in receive. Low resolution images are generated and summed. In SASB, a fixed group of elements are used in transmit and receive and a fixed focus image is generated using the first stage beamformer. The first stage image lines are then used as input for the second stage beamformer, using the focus point as a virtual source.

3.4 Synthetic Aperture Sequential Beamforming

Synthetic aperture sequential beamforming (SASB) is a SAI technique for producing focused images in both transmit and receive for any type of transducer. Traditionally, SAI utilizes only one active transducer element in transmit, while all elements are used in receive (see Fig. 3.2a). In SASB, a multi-element transmit sub-aperture is utilized instead of single element transmission. The focusing in SASB is done in a two-stage procedure (see Fig. 3.2b). The first step is to create a set of image lines that are obtained using a fixed focus in both transmit and receive as in fixed focus beamforming in Section 3.1. The pressure wave that is produced in fixed focus transmit, is a result of several wave contributions emitted from the elements in the sub-aperture. At the focal point, these wave contributions will coincide into a virtual source, creating a spherical wave that emanates from this point within a limited angular region. The next step in the beamforming process is to use the first stage image lines as input in a second stage beamformer using the first stage focus point as the virtual source. The basis of SASB and other multi-element transmit aperture techniques is to calculate the focusing delays from the virtual source rather than from a single element on the transducer.

The following theory section on second stage SASB is based on the papers by Kortbek et al. [40, 41] who describes SASB theory for a linear array transducer and by Hemmsen et al. [30] who describes SASB theory for a convex array transducer. The figures for second stage SASB are shown for a convex array transducer setup, but the theory applies to linear array transducers as well.

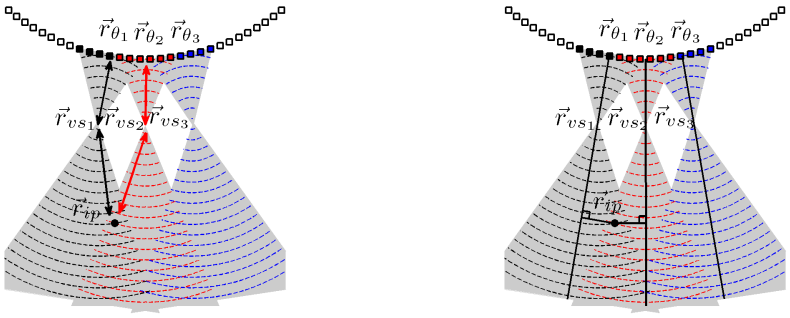

(a) Second stage SASB. Figure taken from [30].

(b) Apodization for second stage SASB. Figure taken from [30].

Figure 3.3: Concept illustrations of the time of flight used in second stage SASB beamforming (3.3a) and of the calculations of the image point angle (3.3b). In 3.3a the first stage focal point is used as a virtual source for second stage beamforming. The time of flight is calculated as the distance from the scan line reference position, $\vec{r}_{\theta_k}$ to the image point, $\vec{r}_{ip}$ through the virtual source, $\vec{r}_{VS}$ and back via the same path. In (3.3b) the image point angle, Φ between the scanline direction and the line from the image point, $\vec{r}_{ip}$ and the virtual source, $\vec{r}_{VS}$. If Φ is less than half the opening angle, α the scanline contains information on that image point and should be included in the second stage beamforming.

The focal point in first stage SASB is considered as a virtual source in second stage SASB. At the virtual source, a spherical wave emanates within a limited angular region defined by the opening angle α.

$$\alpha = 2\text{arctan}\frac{1}{2F\#} \tag{3.3}$$

Each point in the fixed focused image line contains information from an imaging point within the opening angle. Since the opening angles for several emissions may overlap to some degree, an imaging point could be represented in one or more focused first stage image lines. In Fig. 3.3a a set of focused scan lines with reference r_{θ_n} and virtual sources at r_{vs_n} are shown. The image point r_{ip} shown in the figure is represented in two first stage emissions. The overlapping contributions from the first stage image lines can be used to improve resolution.

The second stage beamformer in SASB uses the image information, that is stored in the first stage image lines for an imaging point at a given spatial position to create a new set of high resolution second stage image lines. A single sample, h in a second stage image line representing an image point at position $\vec{r}_{ip}$, can be expressed as

$$h\left(\vec{r}_{ip}\right) = \sum_{k=1}^{K(\vec{r}_{ip})} \mathcal{W}\left(k, \vec{r}_{ip}\right) \cdot l_k\left(t_{d_k}\left(\vec{r}_{ip}\right)\right) \tag{3.4}$$

where $l_k\left(t_{d_k}\left(\vec{r}_{ip}\right)\right)$ is a sample at time t_{d_k} in the first stage image line with propagation direction θ_k. The

variable $\mathcal{W}$ is apodization function with $K\left(\vec{r}_{ip}\right)$ values, which sets the weighting of the contributions of each of the first stage image lines to the second stage image line.

For second stage SASB, the time delay, t_{d_k} for a scan line is determined based on the round trip TOF, from the scan line reference position, $\vec{r}_{\theta_k}$ to the image point, $\vec{r}_{ip}$ through the virtual source, $\vec{r}_{VS}$ and back via the same path. The TOF for second stage SASB is illustrated in Fig. 3.3a. The time delay in second stage SASB can then be formulated as

$$t_{d_k}\left(\vec{r}_{ip}\right) = \frac{2}{c}\left(\|\vec{r}_{VS} - \vec{r}_{\theta_k}\| \pm 2\|\vec{r}_{ip} - \vec{r}_{VS}\|\right). \tag{3.5}$$

Since, the amount of contributing image lines in second stage SASB increases with distance from the virtual source, the value K in 3.4, is a function of position of the imaging point $\vec{r}_{ip}$. The synthesized aperture increases with range, resulting in a more range independent lateral resolution. In order to decide whether a specific first stage image line contains information on a given image point and will contribute to the second stage image, the angle, Φ between the image point, $\vec{r}_{ip}$ and the position of the virtual source, $\vec{r}_{VS}$ relative to the direction of the scan line at $\vec{r}_{\theta}$ should be determined. Φ can be found as

$$\Phi = \arccos\left(\frac{\pm\left(\vec{r}_{ip} - \vec{r}_{VS_k}\right)}{\|\vec{r}_{ip} - \vec{r}_{VS_k}\|} \cdot \frac{\vec{r}_{VS_k} - \vec{r}_{\theta_k}}{\|\vec{r}_{VS_k} - \vec{r}_{\theta_k}\|}\right) \tag{3.6}$$

The $\cdot$ in 3.6 is the dot product and $\pm$ refers to whether the image point source is positioned above or below the virtual source. A schematic illustration of the calculation of Φ is shown in Fig. 3.3b

If Φ for a given first stage image line is less than half the opening angle $\left(\Phi \leq \frac{\alpha}{2}\right)$, then this particular first stage image line contains information about the image point and should be included in the second stage beamforming. This can be stated as

$$f\left(\vec{r}_{ip}, \vec{r}_{\theta_k}, \vec{r}_{VS_k}\right) = \begin{cases} 0 & \text{if } \Phi \text{ is} > \frac{\alpha}{2} \\ 1 & \text{if } \Phi \text{ is} \leq \frac{\alpha}{2} \end{cases} \tag{3.7}$$

The total number of virtual sources that contribute to certain image point can be determined as

$$K\left(\vec{r}_{ip}\right) = \sum_{k=1}^{M} f\left(\vec{r}_{ip}, \vec{r}_{\theta_k}, \vec{r}_{VS_k}\right) \tag{3.8}$$

where M is the total number of virtual sources in the scan sequence.

The variable $\mathcal{W}$ in 3.4 is an apodization function which determines the weighting of each of the contributions from the first stage image lines to the second stage image line. The apodization can basically be any type of weighting function. For the case where the apodization is a Hamming function, the weight

for the scan line, l_{θ_k} contributing to the image point, $\vec{r}_{ip}$ can be calculated as

$$\mathcal{W}\left(k, \vec{r}_{ip}\right) = \begin{cases} 0.54 - 0.46\cos\left(2n\pi\right) & \text{if } |n| \text{ is} \leq 1 \\ 0 & \text{else} \end{cases} \tag{3.9}$$

Here n is determined as

$$n = \frac{d\left(l_{\theta_k}, \vec{r}_{ip}\right)}{\Delta} + 0.5 \tag{3.10}$$

and is given as the ratio between the shortest distance, $d\left(l_{\theta_k}, \vec{r}_{ip}\right)$ from the image point, $\vec{r}_{ip}$ to the scan line, l_{θ_k} and the width of the active aperture, Δ. The distance, $d\left(l_{\theta_k}, \vec{r}_{ip}\right)$ can be expressed as

$$d\left(l_{\theta_k}, \vec{r}_{ip}\right) = \frac{|\det\left(\left[\left(\vec{r}_{\theta_k} - \vec{r}_{VS_k}\right), \left[\vec{r}_{VS_k} - \vec{r}_{ip}\right]\right)|}{\|\vec{r}_{\theta_k} - \vec{r}_{VS_k}\|} \tag{3.11}$$

where $\vec{r}_{\theta_k}$ is the reference point of the scan line, $\vec{r}_{VS}$ is the position of the virtual source, and $\vec{r}_{ip}$ is the position of the image point. The aperture width, Δ, can be determined from the chosen $F\#$ from

$$\Delta = \frac{\sqrt{\|\vec{r}_{VS} - \vec{r}_{ip}\|^2 - d\left(l_k, \vec{r}_{ip}\right)^2}}{F\#} \tag{3.12}$$

The beamforming process in SASB is basically a combination of fixed focus beamforming and dynamic receive beamforming, which are used in the first and second stages in SASB respectively. In traditional synthetic aperture imaging, a severe drawback is the extensive beamforming and computational load that is required to produce high resolution images. In SASB, a major reduction in complexity is achieved in the first stage beamforming process, where only one set of delay values needs to be calculated. The second stage beamformer in SASB, has the complexity of a traditional DRF beamformer.

CHAPTER

FOUR

TISSUE HARMONIC SYNTHETIC APERTURE IMAGING

By combining THI with a SAI technique (THSAI), the final image could potentially be improved by both techniques. The improvements could be increased spatial resolution, reduced reverberation artifacts, reduced side lobe levels, and a narrower beam profile from THI along with a range independent fully focused image in both transmit and receive from SAI. The task in combining the two techniques is to use a SAI technique to create a field in transmit that is intense and focused enough to ensure good development of harmonic frequencies. This can be achieved for single element transducers and for single element transmit arrays by increasing the transmit amplitude to a degree where harmonics are generated. The use of several electronically focused elements in the aperture also causes the emitted ultrasound energy field to increase in intensity. In this way, harmonics can be generated without excessive heating of the individual transducer elements due to high transmit amplitudes. In the following section, a brief description of previously published THSAI techniques by other research groups will be given. This will be followed by a description of how SASB is suggested to be combined with THI.

4.1 Developments in THSAI Techniques

A combination of THI and SAI was first suggested by Li et al. in 2004 [44] for a single element transducer for use in high frequency ultrasound imaging. Here, the 50 MHz 2nd harmonic response was imaged using a single element transducer. SAI was obtained by manually moving the transducer over the region of interest, thereby synthesizing a larger aperture. A similar setup for a single element transducer was recently suggested by Yun et al. in 2013 [61] for contact acoustic imaging to investigate cracks in aluminum blocks. Here two single element transducer displaced at an angle were used with one

transducer transmitting a 2.5 MHz waveform and the other transducer receiving the 5 MHz 2nd harmonic response. Both transducers could manually be moved to synthesize a larger aperture.

The first study to suggest a combination of THI and SAI for ultrasound imaging of the human body was suggested by Bae et al. in 2008 [4]. They suggested a SAI technique known as bipolar Pixel Based Focusing (biPBF) [5] in combination with THI by band pass filtering for a multi element linear transducer array. In biPBF, radio frequency (RF) data for all receiving channels for every single scan line is stored. By combining responses from different scanlines, a larger synthetic transmit aperture can be achieved, while DRF beamforming is applied in receive. This techniques requires vast amount of data storage, since all responses from all scanline positions need to be stored for every frame and a time delay needs to be calculated for all the stored responses to create the synthetic transmit aperture. The study by Bae et al. showed, that THI in combination with biPBF could produce images with increased spatial resolution and signal to noise ratio (SNR) compared to THI in combination with DRF (DRFTHI). The images that were shown were of a wire phantom and an *in-vivo* scan that were beamformed off-line on an external personal computer. No quantitative data was produced in this study, however, and so the evaluation of resolution and SNR were based solely on visual inspection of B-mode images. Furthermore, due to the vast amount of memory needed to store the images, only a single frame was acquired for beamforming. The limits in data storage and data processing restrict the use of this technique in a clinical setting for *in-vivo* measurements.

Recently in 2012, Bae et al. [6] presented a simulation study of a new tissue harmonic synthetic aperture imaging technique, again based on the biPBF technique in combination with THI. Here, multiple virtual sources distributed throughout the image at various depths ware applied to the technique. The purpose of distributing virtual sources at different depths, was to increase the SNR and to generate a more depth independent resolution. By having multiple virtual sources for every scanline position, Bae et al. showed by visual inspection of simulated images, that the resolution of the images were more depth invariant compared to only having one virtual source per scanline position. The results on resolution were again not quantified in this study and the task of having to store and beamform vast amount of RF data was not solved.

4.2 Tissue Harmonic Synthetic Aperture Sequential Beamforming

In order to achieve a working THSAI technique using SASB, the type of THI must be selected (band pass, power modulation, or PI) and the scan sequence for SASB must selected as to ensure generation of

harmonic RF data. In this section, arguments for a SASB technique in combination with PI THI are given.

On most modern day ultrasound systems, DRFTHI is the default imaging technique. In many cases, the THI are produced by the use of PI. The advantages in PI are as previously described, that the neighboring harmonics in the response are attenuated, making isolation of a single harmonic easier for imaging. Furthermore, because two waveforms are summed to generate a single 2nd harmonic response, the amplitude of the response doubles, creating a possible +6 dB gain of the 2nd harmonic. The disadvantage in PI is that frame rate drops by a factor of two, because two emission are needed for every scanline position. However, because it is relatively easy to implement a 180° phase shift in a scan sequence, PI is suggested as the optimal THI technique to implement with SASB.

In SASB, several electronically focused elements are used in transmit to generate a virtual source. The acoustic field that is generated by SASB in transmit could potentially be sufficient to generate harmonics useful for THI. In the following chapter, implementations of synthetic aperture sequential beamforming tissue harmonic imaging (SASBTHI) on linear and convex array transducer are tested out on both commercially available and experimental ultrasound systems. The scan settings are optimized based on studies of a series of phantom scans set to investigate resolution, SNR, cystic resolution, level of side lobes, and point spread functions. The performance of the technique is compared against DRFTHI, because this technique is the default imaging technique on most modern day scanners.

CHAPTER

FIVE

TECHNICAL SETUP AND SYSTEM IMPLEMENTATION

This chapter describes and presents some of the experimental work that has been conducted under the project. First, the equipment that was used in many of the experiments is described. Next, setup and implementation of THI for both linear array and convex array transducers is shown. The PI technique is shown for 2nd harmonic imaging with a linear array transducer and for 2nd and 3rd harmonic imaging with a convex array transducer on an experimental ultrasound system. The setup and implementation of SASBTHI on the linear array transducer is described next for use on the experimental ultrasound system. The position of the virtual source is studied in measurements of the lateral and axial resolution of point scatterers and the point spread functions are studied and compared to conventional imaging. Finally, an implementation and optimization study of SASBTHI for the convex array transducer on a commercially available ultrasound system is presented. An extensive study of virtual source position, F#, line density, and SNR is shown along with a method to equalize the gray scale throughout the entire image depth. The optimized technique is compared with DRFTHI on both phantom scans and *in-vivo* scans.

5.1 Equipment

In this section, the different ultrasound platforms and transducers that are used in this project are described. The ultrasound systems are divided into experimental equipment and commercially available equipment, while the transducers are divided into linear array and convex array transducers.

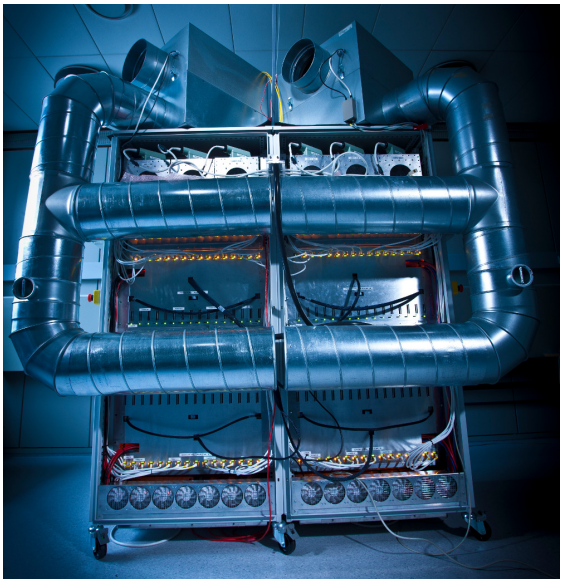

Figure 5.1: Front view of the 1024 channel experimental ultrasound system SARUS. Photo provided by Center for Fast Ultrasound Imaging, DTU - taken by J.Rosenfeld

5.1.1 Experimental Ultrasound System

The Synthetic Aperture Real-time Ultrasound System (SARUS) [35, 36, 37] is currently the most advanced ultrasound system in the world. It offers the possibility to perform basically any type of scan including highly complicated scans such as full 3-dimensional imaging, 3-dimensional blood flow imaging, and 3-dimensional synthetic aperture imaging. It features access to RF channel data, using up to 1028 channels in scan sequences, that are entirely programmable by the user. The system is unique in that no other ultrasound system offers the same amount of programmable channels and can perform the same amount of calculations at the same rate.

The advantage using SARUS is, that all relevant scan settings in the scan sequence are available to the user and are free to define. These include - and are not restricted to, transmit amplitude, transmit center frequency, pulse length, pulse shape, PI, aperture size, aperture apodization, focal points, etc. RF-data can be received and extracted to a tabletop PC for off-line beamforming using in house developed beamformers [26, 28, 42]. Unfortunately, because this is a newly developed experimental ultrasound system, it has not yet been cleared for clinical imaging. Consequently, it cannot be used for acquisition of *in-vivo* images on volunteers or patients. SARUS was therefore used in this project primarily for scans on various kind of phantoms using THI and SASBTHI. A front view of SARUS is shown in Fig. 5.1.

5.1.2 Ultrasound Research Interface

Another way to access image data from a scan is by using a commercial ultrasound system fitted with an ultrasound research interface (URI). The URI allows the user to control many of the manufacturer defined scan settings such as focal points, F#'s, line density , number of emissions, etc. in a predefined usecase. The URI also allows the user to access and extract image data at different points in the beamforming process. In this project, a commercially available BK 2202 Pro Focus UltraView scanner from BK Medical (BK Medical ApS, Herlev, Denmark) is fitted with a UA 2227 URI from BK Medical. Image IQ line data is extracted via a X64-CL Express camera link produced by Teledyne DALSA (Dalsa, Waterloo, Ontario, Canada) to a desktop PC (Esprimo 5635, Fujitsu-Siemens, Tokyo, Japan) running MATLAB (The MathWorks Inc., Natick, Massachusetts, United States). Fig. 5.2 shows the UltraView system working in URI mode during clinical scan.

The usecase specifies the general scanner settings such as speed of sound, maximum scan depth, and transducer parameters as well as the specific scan sequence settings (e.g. focus points, F#'s, center frequency, etc.). A flow chart of a usecase and scan sequence for a DRFTHI and SASBTHI duplex scan is shown in Fig. 5.3. For both scans in the example, THI is performed using PI and matched filtering to achieve 2nd harmonic IQ-data. The first two emissions in the full emission sequence are the PI emissions for scan line number one for SASBTHI. The next two emissions are for scan line number two for SASBTHI and so on, until the first full set of emissions for one frame has been performed for SASBTHI. Next, the emissions belonging to DRFTHI are conducted in the same manner. The emission sequence is set this way to minimize tissue movement between the individual image lines, which could otherwise introduce errors in the beamforming stage. Summing and matched filtering of the received paired responses is then conducted by the scanner, giving the 2nd harmonic responses. Next, beamforming using either dynamic receive focusing for DRFTHI or fixed focusing for first stage SASBTHI is performed using the beamformer implemented on the scanner. Beamformed 2nd harmonic IQ image line data is then exported via the data acquisition card on to the external PC for IQ-to-RF data conversion and second stage beamforming for SASB using an in-house developed beamformer [28], which is run in MATLAB.

The primary advantage using an URI on a commercially available ultrasound scanner is, that the system is approved for use in a clinical environment for *in-vivo* investigations. Also, many of the transducer specific settings in the usecases have already been optimized by the manufacturer, and so, no further optimization is often needed. The URI on this particular UltraView system does have some disadvantages and limitations, though. Firstly, only IQ image line data is accessible and not RF data. This limits the possibilities in signal processing because single channel data is not available. Secondly, the transmit stage on the UltraView system is limited to using only boxcar apodization. This increases the level of side lobes in transmit, compared to e.g. gauss transmit apodization. Also, many of the settings in the

Figure 5.2: The BK 2202 Pro Focus UltraView ultrasound system working in the URI mode during a clinical scan.

usecase are defined by changing variables with names and values that are not always clear nor logical. However, because the system is cleared for *in-vivo* imaging, the system can be used to inspect the clinical relevance of the implemented technique. This is makes the URI on the UltraView a valuable tool in the clinical studies that are currently performed at the Center for Fast Ultrasound Imaging at the Technical University of Denmark.

The UltraView can be fitted with a variety of commercially available transducers. In this project, a linear array transducer and two convex array transducers were applied. The transducers and their setting are described in the following section.

5.1.3 Transducers

For the experiments in this project, both linear array and convex array transducers were applied. For linear array transducers, the setup of scan lines and focal points is straight forward because of the linear geometry of the transducer. Fon convex array transducers, setup is a bit more cumbersome because scanlines and focal points fan out due to the curvature of the transducer surface. However, the convex array transducers are much more often applied in clinical scans of the abdominal region, where THI is the default scan technique. The focus of this project has therefore been, to implement and prove concepts for THI and SASBTHI for linear array transducers first, and then expand and optimize the techniques

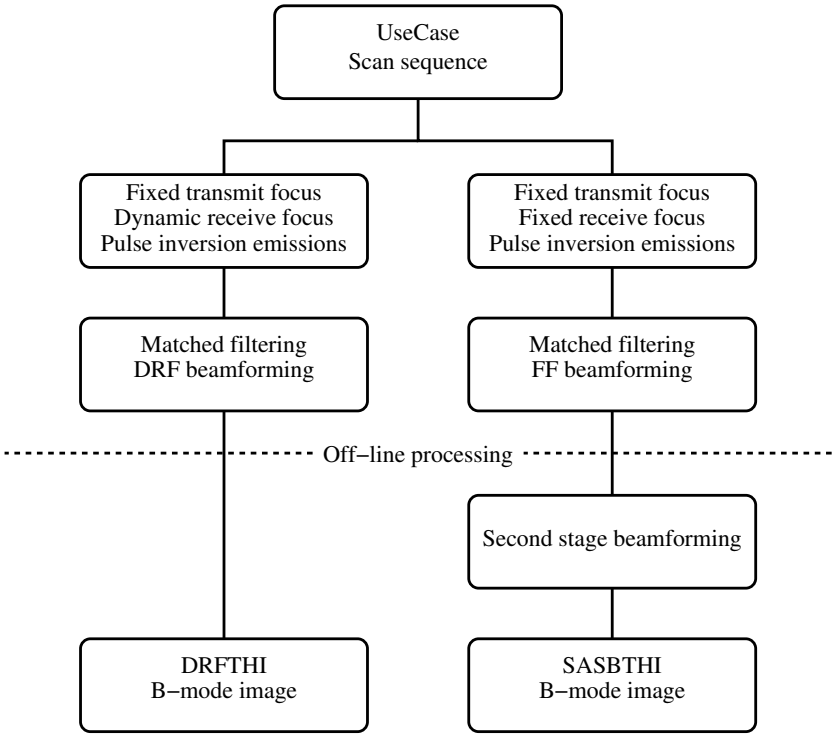

Figure 5.3: Scan sequence on the BK 2200 Pro Focus UltraView scanner. The usecase defines a scan sequence that performs two scans simultaneously in parallel. The scan for SASBTHI utilizes a fixed focus in transmit and receive, while the scan for DRFTHI utilizes dynamic receive focusing.

Table 5.1: Transducer parameters for the BK 8820e convex array transducer.

Transducer Parameters	Value
Pitch	0.33 mm
Elevation focus	65 mm
Number of elements	192
Radius of curvature	60 mm
Field of view	60.5 deg
Center frequency	3.5 MHz
Operating frequency	2-6 MHz

Table 5.2: Transducer parameters for the BK 8804 linear array transducer.

Transducer Parameters	Value
Pitch	0.208 mm
Elevation focus	20 mm
Number of elements	192
Radius of curvature	linear
Center frequency	7 MHz
Operating frequency	5-10 MHz

for convex arrays. The linear array transducer that is used in this project is the BK 8804 from BK Medical. The convex array transducers that are used are the BK 8820e from BK Medical and the STI 8820e by Sound Technology (Analogic Ultrasound Group, Pennsylvania, United States). The latter is an experimental transducer based on the BK 8820e transducer platform. The transducer parameters for the STI 8820e are the same as for the BK 8820e in Table 5.1. In the following, the two convex array transducers are collectively named the BK 8820e transducer. The transducer parameters for the BK 8804 transducer are shown in Table 5.2

5.2 THI on Linear Array Transducers

The scope of these measurements was to investigate, whether the newly developed SARUS was capable of PI for THI. The BK 8804 linear array transducer was connected to SARUS and a scan sequence for PI DRF imaging was set up. A wire phantom was scanned and used to study pulse-echo responses, B-mode images, point spread functions, and finally, the lateral resolution of the wires was measured and compared for DRF and DRFTHI.

5.2.1 Scan Parameters

An implementation of DRFTHI was conducted on SARUS using the BK 8804 linear array transducer. A total of 129 dual emissions using PI were obtained to derive the harmonic image. The total collection of received data could potentially be used for two DRF B-mode images (one for the regular pulse; one also for the inverted pulse) and one DRFTHI B-mode image (from the summed pulse). Image data was beamformed using the BFT3 toolbox [28]. The scan parameters for SARUS are seen in Table 5.3.

Table 5.3: Scan parameters for DRFTHI for BK 8804 linear array transducer on SARUS.

Scanner Parameters	DRFTHI
Speed of sound	1492 m/s
Transmit center frequency	5 MHz
Waveform cycles	2
Sampling frequency	70 MHz
No. scanlines	129
No. active elements	64
Focus Tx (mm)	40
Focus Rx (mm)	Dynamic
F# Tx	3
F# Rx	0.8
Apodization Tx	Hamming
Apodization Rx	Hamming

5.2.2 Harmonic Waveforms

A pair of received pulse-echo responses from SARUS using PI are visualized in Fig. 5.4a. Here it is seen, that SARUS is capable of performing the 180° phase shift needed in PI. The two waveforms intersect almost exactly at zero amplitude line for the whole duration of the pulses. The shape of the responses show pointed peaks and round valleys indicating that the waveforms contain harmonic frequencies. In Fig. 5.4b, the summed response is shown. This response is smaller in amplitude, because, the high amplitude fundamental has been attenuated by the pulse summation. The spectra of the original received response and the summed response are shown in Fig. 5.5. In the spectrum of the original response, the peak of the 2nd harmonic is about 11 dB lower than the peak of the fundamental. After pulse summation, the fundamental is attenuated by approximately 17 dB, while the 2nd harmonic is enhanced by approximately 4 dB. In the figure, is also shown the transfer function of the BK 8804 linear transducer. Since the transducer of the system has a limited bandwidth, the transmitted center frequency must be chosen such that it allows for the detection of the 2nd harmonic in the received signal. From the bandwidth plot of the transducer in Fig. 5.5, a 5 MHz center frequency for the excitation pulse with a 10 MHz 2nd harmonic component was chosen. Both frequencies were well within the bandwidth of the BK 8804 transducer.

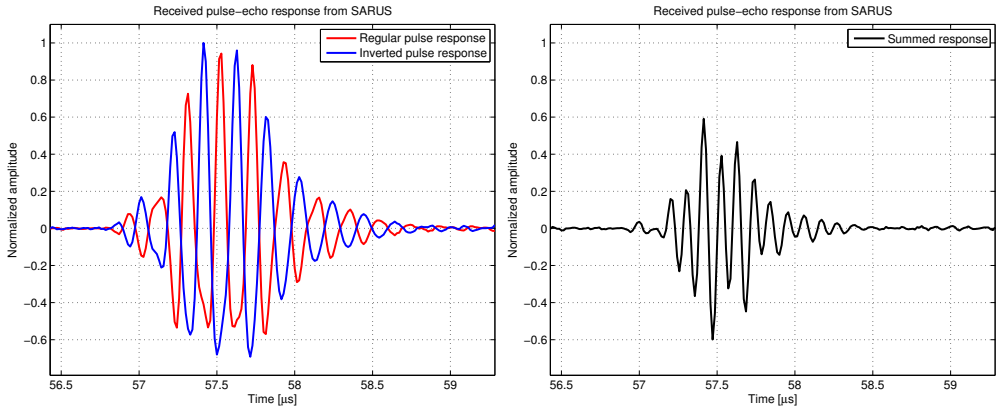

(a) Received responses **(b)** Summed response

Figure 5.4: Responses received using SARUS and the BK 8804 linear array transducer. In 5.4a, two received pulse-echo responses are shown. PI has been performed in transmit to achieve the 180° phase shift. In 5.4b, the resulting response after pulse summation is shown. The summed response in 5.4b has been normalized to the received responses in 5.4a.

5.2.3 B-mode Images

A wire phantom containing 6 equidistant wires suspended in water was scanned using PI DRF on SARUS. Two B-mode images (a DRF B-mode and a DRFTHI B-mode) were created from the collection of data from SARUS and are shown in Fig. 5.6. Only slight differences are seen in the two images, however, the application of THI to DRF imaging results in what seems to be a more narrow and tighter main lobe and a lower level of side lobes compared with DRF imaging. The shape of the main lobe and side lobes should be investigated closer by other means than just the B-mode images.

5.2.4 Point Spread Functions

In order to asses the shape and levels of the main lobe and side lobes, the point spread functions (PSF) of the two techniques are visualized in Fig. 5.7. The PSF's are visualized as contour plots with levels of 6 dB between the contour lines. In the figure, it is clearly seen that the distribution of contour lines are much more concentrated for DRFTHI in Fig. 5.7b than for DRF in Fig. 5.7a. It is also seen, that there are no side lobes in the two PSF's. The tighter main lobe of DRFTHI shows, that DRFTHI is capable of

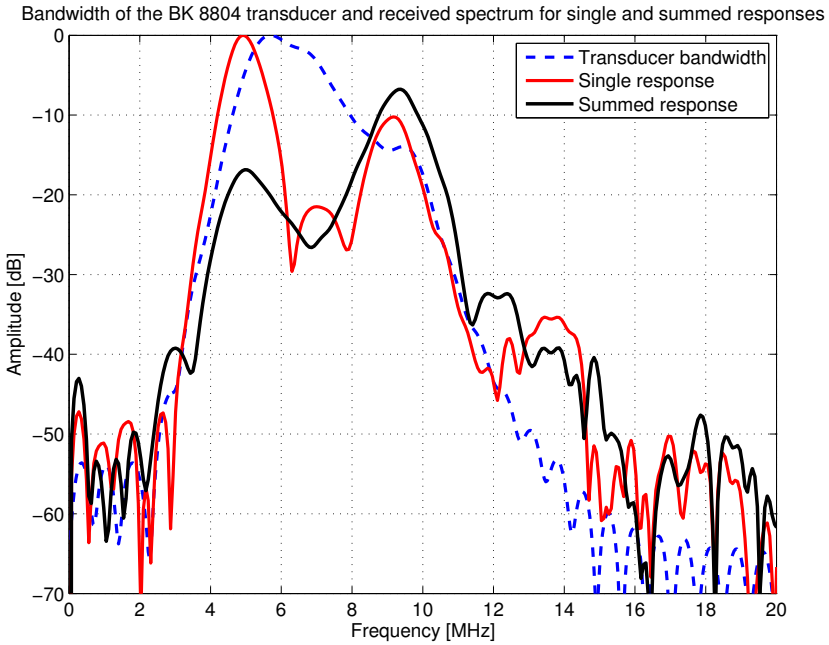

Figure 5.5: The spectra of the received responses and the resulting response after pulse summation using SARUS and the BK 8804 linear array transducer. The fundamental is found at 5 MHz, while the 2nd harmonic is found at 10 MHz. The transfer function of the transducer is also shown.

producing a higher resolution compared to DRF on SARUS.

5.2.5 Resolution

One way to quantify the resolution of a given technique is to measure the width of the main lobe of the PSF. The width is measured where the energy has dropped to half of the local maximum in the main lobe, which is equivalent to a drop in 6 dB signal strength. This measure is also known as the FWHM as described in Section 2.5. By also measuring the width where the energy has dropped to one tenth of the local maximum, the levels of side lobes can be estimated. This measure is also known as the -20 dB resolution or the full width at one tenth maximum (FWOTM).

The lateral FWHM and the lateral FWOTM was measured for the DRF and DRFTHI images from SARUS on all wires in the B-mode image and are plotted in Fig. 5.8. Here, it is seen, that DRFTHI produces almost the same lateral FWHM as DRF on SARUS. For the lateral FWOTM, the improvement in resolution is more pronounced for DRFTHI. Specifically, for the wire at 47 mm depth, which is close to the transmit focal point, the FWHM for SASBTHI is 0.70 mm and 0.99 mm for the FWOTM. In comparison, the lateral FWHM and FWOTM for DRF are 0.66 mm and 1.20 mm respectively.

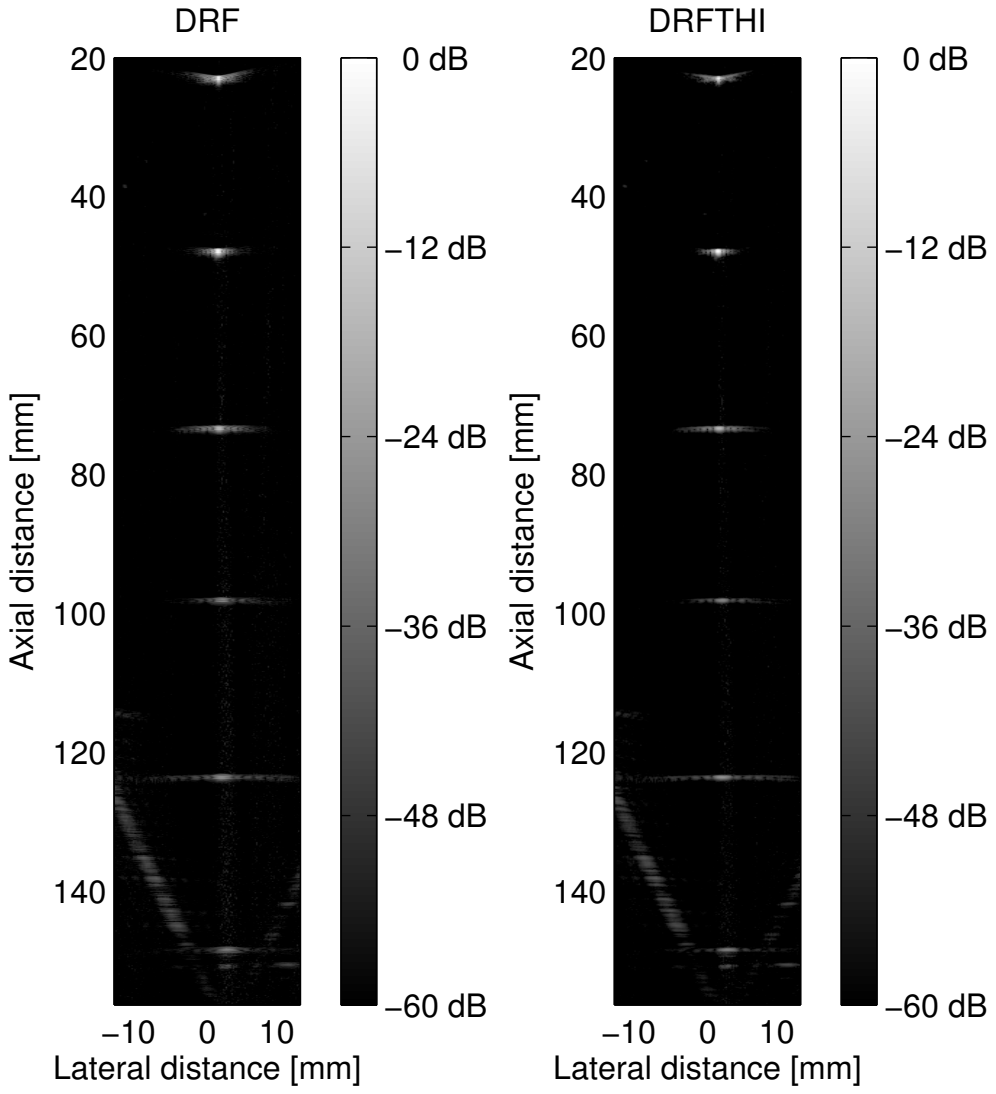

(a) DRF **(b)** DRFTHI

Figure 5.6: B-mode images of wire phantom. B-mode images by DRFTHI using SARUS and the BK 8804 linear array transducer.

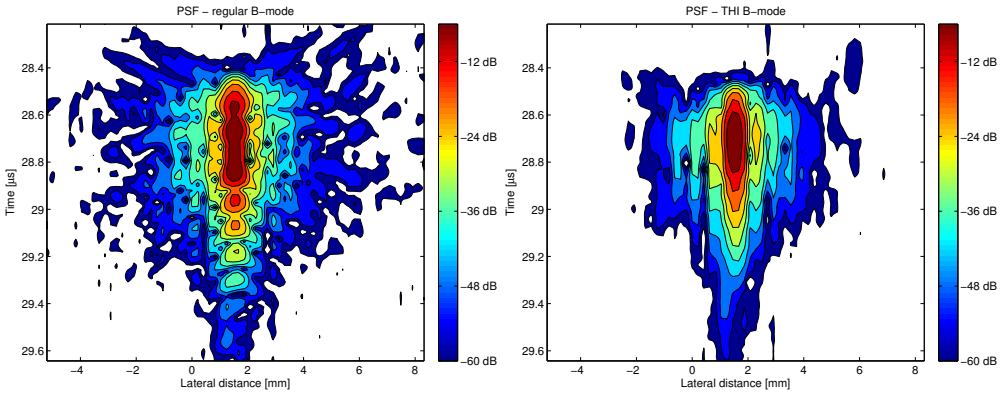

(a) DRF **(b)** DRFTHI

Figure 5.7: Contour plots of the point spread functions for regular DRF B-mode imaging (5.7a) and THI DRF B-mode (5.7b) acquired using SARUS and BK 8804. The distance between the contour lines is 6 dB.

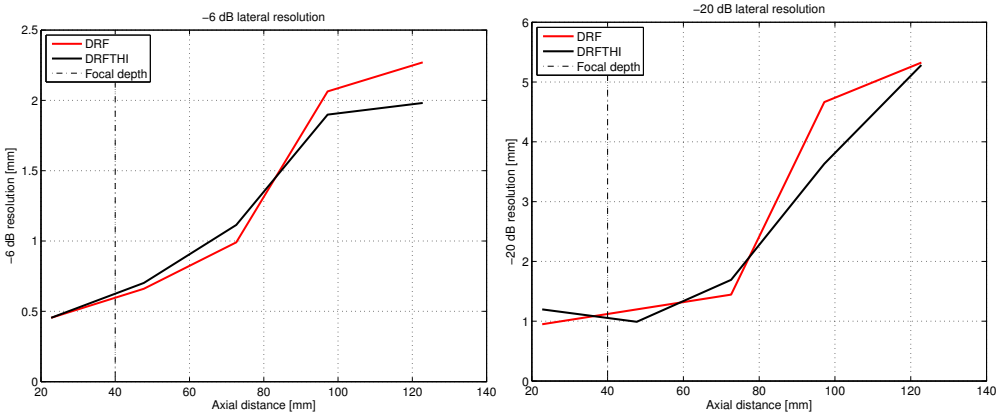

(a) lateral FWHM **(b)** lateral FWOTM

Figure 5.8: The lateral FWHM (5.8a) and FWOTM (5.8b) measured on a wire phantom using SARUS and the BK 8804 linear array transducer.

5.2.6 Section Conclusion

A PI technique was implemented on SARUS for DRFTHI. The pulse responses obtained from the scan on the wire phantom showed, that the zero crossings of each of the inverted pulse-responses were coinciding, showing that SARUS is capable of producing the 180° phase shift required for PI. B-mode images and PSF's were visualized for both techniques. The measurements of the lateral FWHM showed only minor improvements for DRFTHI. This is suspected to be because the 2nd harmonic in the spectrum was only enhanced with PI, but was not isolated using any filter. Substantial energy from the fundamental could therefore have leaked into the 2nd harmonic. This would make the main lobe of the 2nd harmonic PSF wider, which could explain the poor improvements in the lateral resolution. In the following section, the PI technique is exploited to perform both 2nd and 3rd harmonic imaging for DRFTHI and matched filters are used to reduce the leakage of energy.

5.3 THI on Convex Array Transducers

The scope of these measurements was to expand the PI technique on SARUS to produce both 2nd and 3rd THI on the BK 8820e convex array transducer. The PI technique was further expanded by the application of matched filters to isolate the harmonics for imaging and to reduce harmonic energy leakage. A wire phantom was scanned and used to study pulse-echo responses, B-mode images, PSF's, and finally, the lateral resolution of the wires was measured and compared for DRF and DRFTHI.

5.3.1 Scan Parameters

An implementation of DRFTHI was conducted on SARUS using the BK 8820e convex array transducer. The center frequency of the 8820e convex array transducer of 3.5 MHz also used as the center frequency of the transmitted waveform. The expected center frequencies for the 2nd and 3rd harmonics were therefore 7 MHz and 10.5 MHz respectively. A relatively long transmit waveform of 4 waveform cycles was applied. This was to reduce the bandwidth of each of the harmonics, so that isolation of the harmonics by matched filters was made more effective, by reducing the amount of energy leakage from neighboring harmonics. An active transmit and receive aperture of 64 elements were apodized with a Hamming function. A total of 129 dual emissions using PI were obtained to derive the harmonic images. The total collection of received data could potentially be used for two DRF B-mode images (one for the regular pulse; one also for the inverted pulse), one 2nd harmonic DRFTHI B-mode image (from the summed pulse), and one 3rd harmonic DRFTHI B-mode image (from the subtracted pulse). Image data were beamformed using the BFT3 toolbox [28]. The scan parameters for SARUS is seen in Table 5.4.

Table 5.4: Scan parameters for DRFTHI for BK 8820e convex array transducer on SARUS.

Scanner Parameters	DRFTHI
Speed of sound	1492 m/s
Transmit center frequency	3.5 MHz
Waveform cycles	4
Sampling frequency	70 MHz
No. scanlines	32
No. active elements	64
Focus Tx (mm)	40
Focus Rx (mm)	Dynamic
F# Tx	3
F# Rx	0.8
Apodization Tx	Hamming
Apodization Rx	Hamming

5.3.2 Harmonic Waveforms

A pair of received pulse-echo responses from SARUS using PI are visualized in Fig. 5.9a. The two waveforms intersect almost exactly at the zero amplitude line for the whole duration of the pulses. In Fig. 5.9c, the summed response is shown. This response is smaller in amplitude, because, the high amplitude fundamental has been attenuated by the pulse summation. The subtracted response is shown in Fig. 5.9e. Here, the maximum amplitude is twice of the original responses.

The spectra of the original received response, the summed response, and the subtracted response are shown in Fig. 5.9b, 5.9d, and 5.9f respectively. In the spectrum of the original response, the 2nd and 3rd harmonics are about 22 dB and 37 dB lower than the fundamental, respectively. After pulse summation, the fundamental and 3rd harmonic are attenuated by approximately 20 dB and 13 dB, while the 2nd harmonic is enhanced by 6 dB, which is equivalent to a double in signal amplitude. In the spectrum of the subtracted response, the fundamental and 3rd harmonic are enhanced by 6 dB in both cases, while the 2nd harmonic is attenuated by at least 20 dB. The spectra clearly show how efficient the PI technique can be in enhancing and attenuating specific harmonics. In the figures of the fundamental, 2nd harmonic, and 3rd harmonic spectra, the transfer function of the applied matched filters are shown along with the responses after matched filtering. It is seen, how the harmonics are completely removed by the filter in Fig. 5.9b, leaving only the fundamental. A similar result is seen in Fig. 5.9d, where only the 2nd harmonic is left. In Fig. 5.9f, the 2nd harmonic is completely removed from the spectrum, while the fundamental is attenuated by approximately 50 dB down to a level of -45 dB by the matched filter.

5.3.3 B-mode images

Four B-mode images were compiled from the collection of received data. Two images were made from the original received response - one with matched filtering (using only the fundamental) and one without matched filtering (using the fundamental and the harmonics in the response). Two additional images were made using pulse summation and pulse subtraction with matched filtering in both cases for 2nd and 3rd harmonic imaging, respectively. The images are shown in Fig. 5.10.

In all four images, side lobes can be detected throughout the images. Of the four images, the 3rd harmonic B-mode image presents the lowest levels of side lobes, however, the dynamic range in the image is also the lowest of the four. It is noticed, that there is a remarkably improvement in the width of the main lobe going from fundamental imaging to 2nd harmonic imaging.

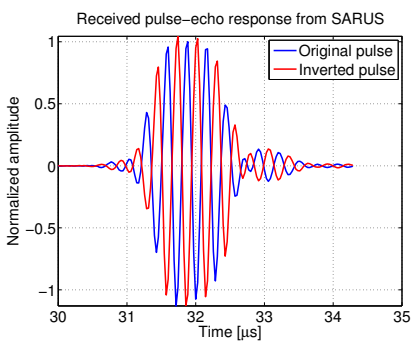

(a) Received responses

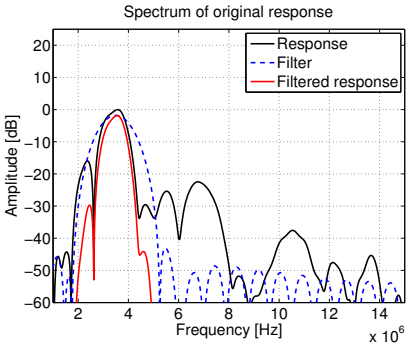

(b) Spectrum of received responses

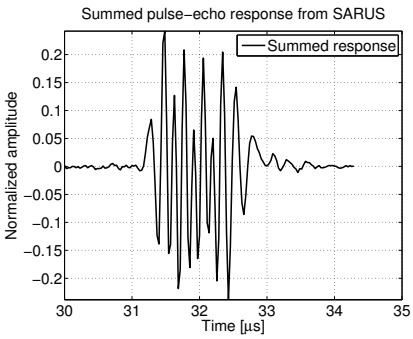

(c) Summed response

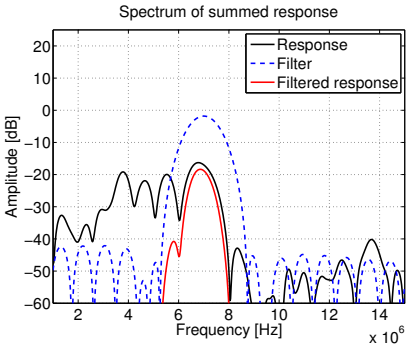

(d) Spectrum of summed response

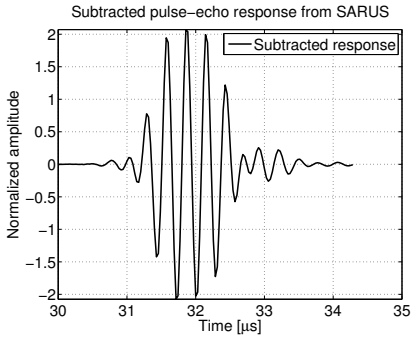

(e) Subtracted response

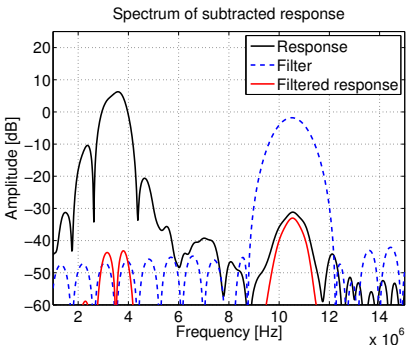

(f) Spectrum of subtracted responses

Figure 5.9: Responses and spectra received using SARUS and the BK 8820e convex array transducer. In 5.9a, two received pulse-echo responses are shown. PI has been performed in transmit to achieve the 180° phase shift. The spectrum of the received responses and the applied matched filter are shown in 5.9b. In 5.9c, the resulting response after pulse summation is shown and the spectrum and matched filter are shown in 5.9d. The resulting response after pulse subtraction is shown in 5.9e and the spectrum and filter are shown in 5.9f. The summed response in 5.9c has been normalized to the received responses in 5.9a.

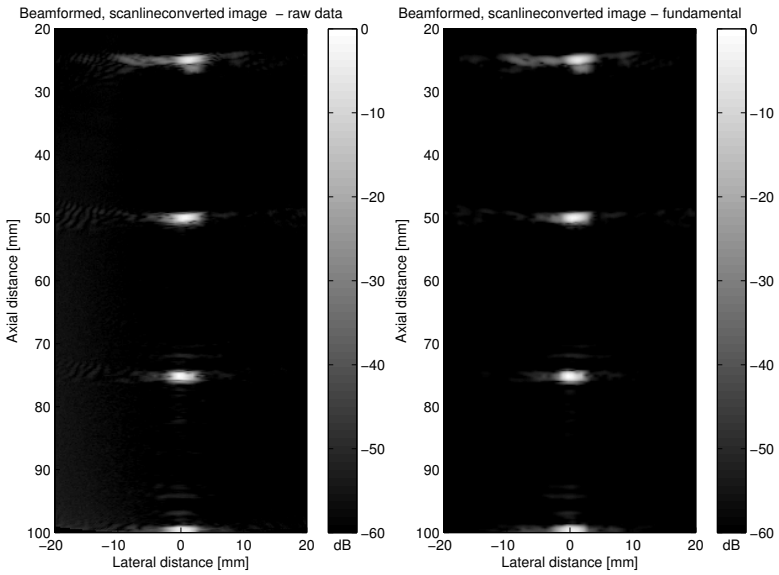

(a) Full response **(b)** Fundamental

(c) 2nd harmonic **(d)** 3rd harmonic

Figure 5.10: B-mode images of wire phantom using the BK 8820e convex array transducer. Fig. 5.10a shows the B-mode from the full response. Fig. 5.10b, 5.10c, and 5.10d show the B-mode images of the fundamental, 2nd harmonic, and 3rd harmonic respectively.

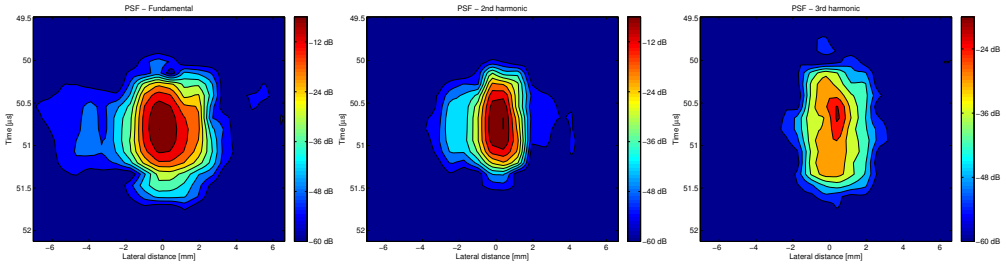

(a) Fundamental **(b)** 2nd harmonic **(c)** 3rd harmonic

Figure 5.11: Contour plots of the point spread functions for fundamental, 2nd harmonic, and 3rd harmonic DRFTHI using the BK 8804 linear array transducer and SARUS. The level between the contour lines is 6 dB.

5.3.4 Point Spread Functions

The width of the main and side lobes are studied more closely by inspecting the PSF's of fundamental, 2nd harmonic, and 3rd harmonic imaging in Fig. 5.11. Here, it is clearly seen that harmonic imaging reduces the width of the main lobe compared to fundamental imaging. Of the three techniques, it is seen, that 3rd harmonic imaging produces the tightest PSF, however, due to low signal strength, the maximum contour line in the figure is -18 dB. For fundamental and 2nd harmonic, the maximum contour line is -6 dB. This presents a significant reduction in the dynamic range of 3rd harmonic imaging in this setup. The axial resolution remains unchanged for the three techniques, since the same excitation waveform was used to create the three images.

5.3.5 Resolution

The lateral FWHM and FWOTM was measured for first 3 of the visible wires in the B-mode images and are plotted in Fig. 5.12. In the figure, it is seen, that the lateral FWHM is improved by the application of higher harmonics in imaging. The further application of harmonic matched filters after pulse summation has clearly reduced the amount of harmonic energy leakage, that was present in the previous study with the BK 8804 transducer in Section 5.2. The mean FWHM and FWOTM and the standard deviation for fundamental, 2nd harmonic, and 3rd harmonic imaging are shown in Table 5.5.

The figures and the table show, that while 3rd harmonic imaging produces the lowest FWHM value, it is 2nd harmonic imaging that produces the lowest FWOTM value. This is a bit surprising, since, the lateral resolution should be improved for all levels by the increase in harmonic imaging number. A reason for

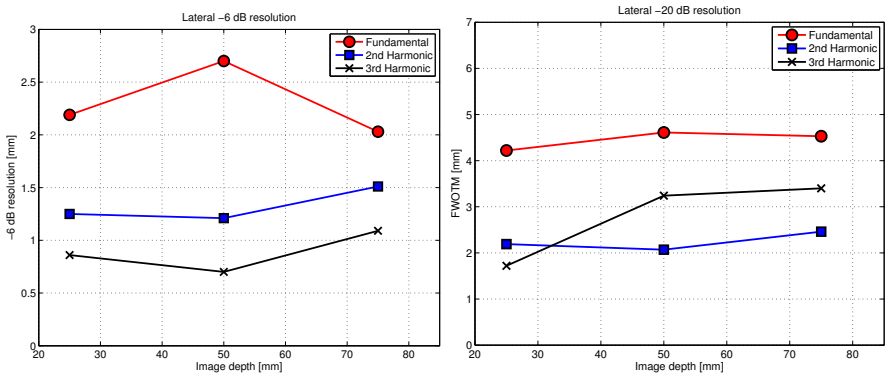

(a) Lateral FWHM **(b)** Lateral FWOTM

Figure 5.12: Lateral resolution for wires using fundamental, 2nd harmonic, and 3rd harmonic DRFTHI with the BK 8804 linear array transducer and SARUS.

Table 5.5: Mean lateral resolution and standard deviation for fundamental, 2nd harmonic, and 3rd harmonic imaging.

Scan technique	Mean lateral FWHM $\pm$ 1 std [mm]	Mean lateral FWOTM $\pm$ 1 std [mm]
Fundamental	2.31 ± 0.35	4.45 ± 0.21
2nd harmonic	1.32 ± 0.16	2.24 ± 0.20
3rd harmonic	0.98 ± 0.20	2.79 ± 0.93

this, could be that energy from the fundamental has leaked into the 3rd harmonic. In the spectrum of the 3rd harmonic in Fig. 5.9f, it is seen, that the fundamental was attenuated by approximately 50 dB down to a level of -45 dB. However, because, the maximum peak of the 3rd harmonic was no more than approximately -32 dB, there is only a difference of approximately 13 dB in the peaks of the two. The amount of leakage from the fundamental could be significantly large to affect the lateral resolution. A plot of the profile of the lateral resolution is shown in Fig. 5.13. Here, it is clearly seen, that the profile of the 2nd harmonic is relatively slimmer compared to the 3rd harmonic profile as a result of the difference in harmonic leakage.

5.3.6 Section Conclusion

A PI technique was implemented on SARUS for fundamental, 2nd harmonic, and 3rd harmonic imaging using the BK 8820e convex array transducer. The PI technique was expanded by the application of matched filters to isolate the harmonics for imaging. Harmonic leakage was completely removed from the fundamental and 2nd harmonic images, while leakage of the fundamental into the 3rd harmonic was seen. This affected the shape of the lateral resolution profile of the 3rd harmonic, making it wider than

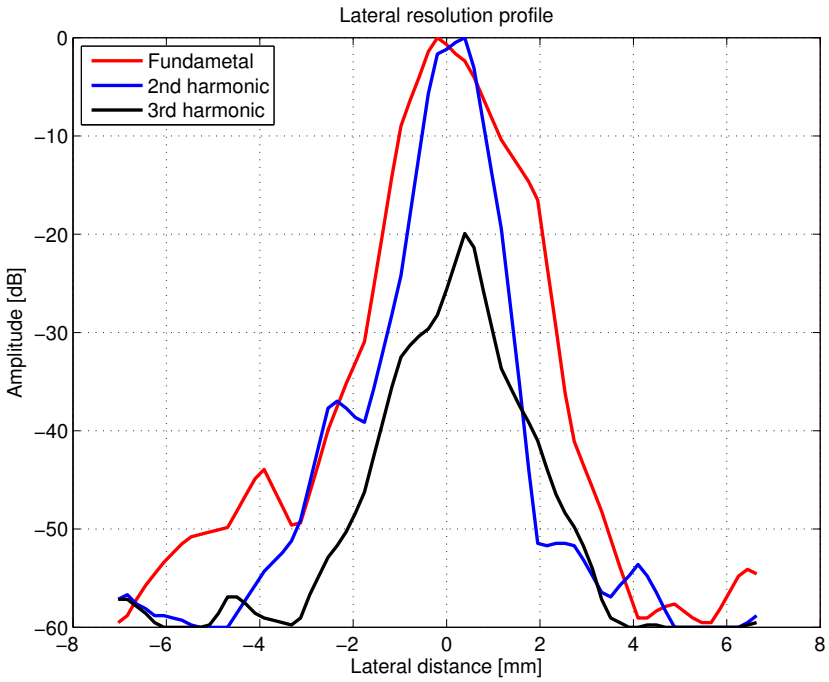

Figure 5.13: Lateral resolution profiles for fundamental, 2nd harmonic, and 3rd harmonic imaging.

the profile of 2nd harmonic at the relative -20 dB level. However, the FWHM was clearly improved by the application of higher harmonics.

5.4 SASBTHI on Linear Array Transducers

The scope of these experiments were to investigate a novel implementation of SASBTHI on SARUS using the BK 8804 linear array transducer. The data used in this section was acquired in 2011 in by Du and presented the first time in the paper by Du et al. [21]. Further research has since been conducted on the data, and the following sections shows the work that has been done during this project.

5.4.1 Scan Parameters

Scan sequences for SASBTHI and DRFTHI for a linear array transducer was implemented on SARUS. A two cycle 5 MHz transmit waveform was used with a 64 element fixed Hanning apodized sub-aperture in transmit for both SASBTHI and DRFTHI. In both cases, THI was performed using PI. For SASBTHI, receive apodization was a Hanning on a 64 element fixed sub-aperture with focal points for first stage beamforming at 10 mm, 25 mm, and 50 mm in three experiments. For the DRFTHI measurements, transmit foci at 10 mm, 20 mm, and 50 mm were used, while dynamic receive focus and an expanding aperture was used (see Table 5.6).

Table 5.6: Scan parameters for SASBTHI and DRFTHI for BK 8804 linear array transducer on SARUS.

Scanner Parameters	SASBTHI	DRFTHI
Transmit center frequency	5.0 MHz	5.0 MHz
Waveform cycles	2	2
Sampling frequency	70 MHz	70 MHz
No. scanlines	128	128
No. emissions per scanline	2	2
No. active elements	64	64
Focus Tx (mm)	[10, 25, 50]	[10, 25, 50]
Focus Rx (mm)	[10, 25, 50]	Dynamic
F# Tx/Rx	3	3
Apodization Tx/Rx	Hanning	Hanning

A water-filled wire phantom was scanned using SASBTHI and DRFTHI. RF-data was recorded using SARUS and stored. The collection of RF-data from one experiment contained RF-data pairs for every scanline position (regular response and phase shifted response). These data could be used to compile both a tissue harmonic image (using pulse summation on the correlated RF-data pairs) and a linear image (using only one of the responses from each RF-data pair). For the linear images (DRF and SASB), the fundamental frequency was isolated using matched filters (5 MHz center frequency). For the tissue harmonic images (DRFTHI and SASBTHI), the 2nd harmonic frequency was isolated using pulse summation and matched filters with 10 MHz center frequency. Beamforming of RF-data was

performed using a beamformation toolbox [26, 42] in MATLAB. For the SASB RF-data, first stage SASB beamforming was conducted using the fixed focus in transmit and receive. Next, the second stage SASB beamforming was conducted using the first stage image lines as input data with the focal point as a virtual source. For the DRF RF-data, dynamic beamforming was applied in receive.

5.4.2 B-mode Images

B-mode images were produced using three transmit focal points, for both linear imaging and tissue harmonic imaging, using SASB and DRF focusing, giving a total of 12 B-mode images (3x2x2). Examples of B-mode images for DRF, SASB, DRFTHI, and SASBTHI using a transmit focus at 25 mm are shown in Fig. 5.14. In the B-mode images it is seen that switching from fundamental imaging to THI, improves the resolution of the wires as predicted by earlier studies of THI. It is also seen, that when switching from DRF in Fig. 5.14a to SASB in Fig. 5.14b, the resolution is slightly improved, but some degree of higher side lobe level is detectable in the SASB image. In Fig. 5.14c and Fig. 5.14d the DRFTHI and SASBTHI images are shown respectively. The main lobe seems somewhat tighter in the SASBTHI image compared to DRFTHI. The level of side lobes seem to be the same in the two images.

5.4.3 Point Spread Functions

The PSF of each technique was measured and shown for a single wire depth when the focal point of 25 mm was used. The PSF's are shown in Fig. 5.15. Here, it is seen that SASB in general produces tighter main lobes compared with DRF. In Fig. 5.15a the level of side lobes for DRF is close to the same as for SASB in Fig. 5.15b. The application of THI to both techniques reduces the width of the main lobe for both techniques. The PSF's reveal that SASBTHI produces the tightest main lobe and lowest level of side lobes of all four techniques.

5.4.4 Lateral Resolution

In each case of transmit focal position, the lateral FWHM and the lateral FWOTM was measured for all visible wires in the B-mode images for all four techniques. The measured values are shown in Fig. 5.16. As can be seen from the figure, SASBTHI produces a lower FWHM value for all wire depths when the focal point is at 10 mm and 25 mm. For the case where the focal point is at 50 mm, SASBTHI produces lower FWHM value for the wires that are deeper than 50 mm. It is also seen from the figure,

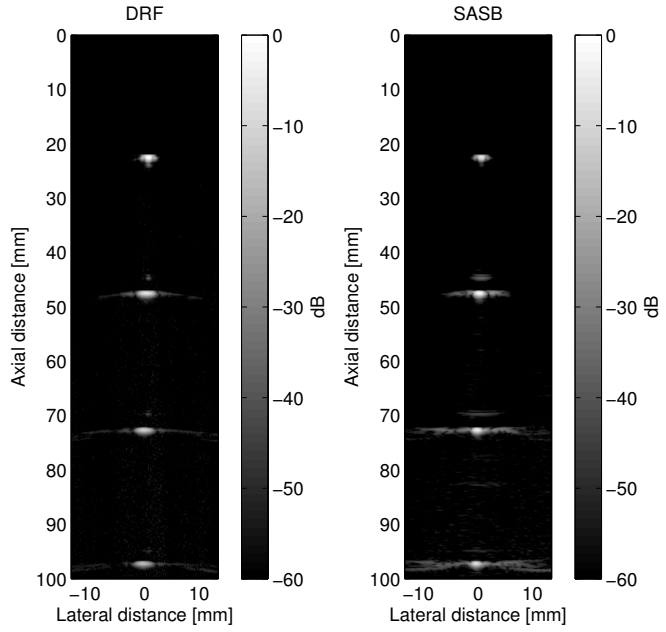

(a) DRF **(b)** SASB

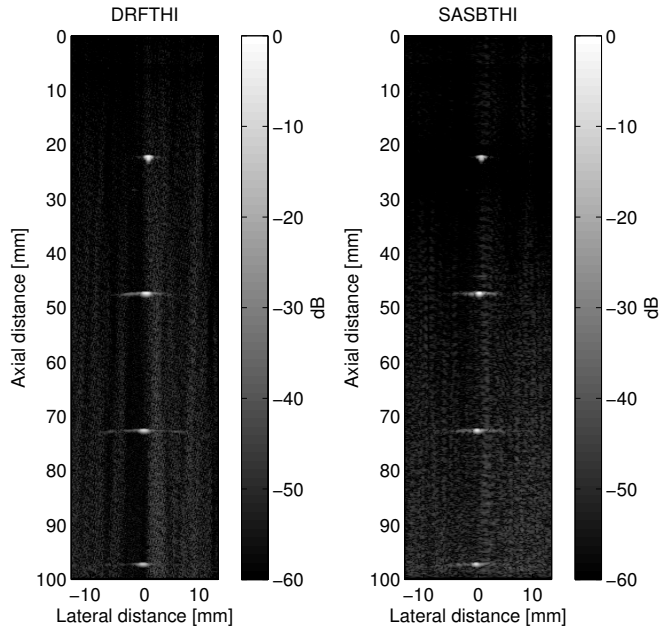

(c) DRFTHI **(d)** SASBTHI

Figure 5.14: B-mode images of wire phantom acquired using the BK 8804 linear array transducer and SARUS. The transmit focal point is at 25 mm and the F# is 3.

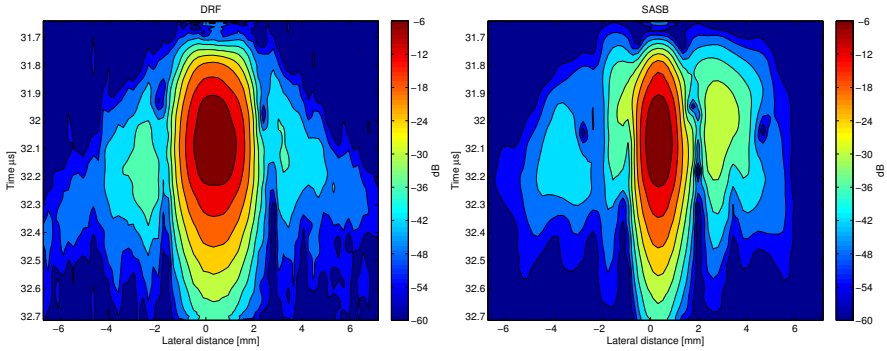

(a) DRF **(b)** SASB

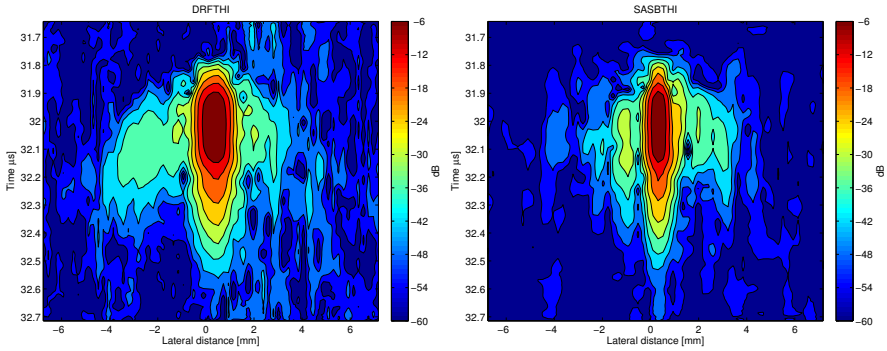

(c) DRFTHI **(d)** SASBTHI

Figure 5.15: Contour plots of the point spread functions for the wire at 22 mm depth. Focus point is at 25 mm and the F# is 3. The level between the contour lines is 6 dB.

that SASBTHI and DRFTHI produces almost the same FWOTM for all focal depths, however SASBTHI does generally produce the lowest FWOTM values. In the specific case, where the focal point is at 25 mm, SASBTHI produces a FWHM of 0.67 mm for the wire at 47.5 mm. In comparison, DRF, SASB, and DRFTHI produce values of 2.04 mm, 1.16 mm, and 1.12 mm which are 206%, 75%, and 69% higher respectively. For the FWOTM, DRF, SASB, and DRFTHI produce 158%, 61%, and 42% higher values than SASBTHI.

In Fig. 5.17, the lateral resolution for SASBTHI is shown for the different focal depths. Here, it is seen, that a focal depth of 25 mm produces almost completely uniform FWHM values. It is possible to achieve a lower resolution with a focal point at 10 mm, but here the resolution varies with imaging depth. In order to achieve the lowest and most depth invariant lateral resolution, the results suggest that a focal point near 25 mm should be used.

5.4.5 Section Conclusion

A novel SASBTHI technique was successfully implemented on SARUS. The results on resolution that were obtained using the linear array transducer show, that SASBTHI is quite capable of improving the resolution compared with DRFTHI. The technique was therefore be expanded to also function on convex array transducers and was ultimately used in a clinical trial to reveal the clinical relevance of the technique.

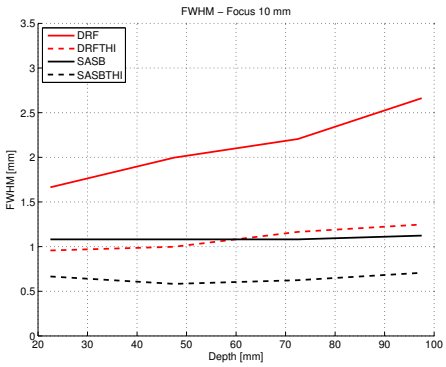

(a) Lateral FWHM, 10 mm focus

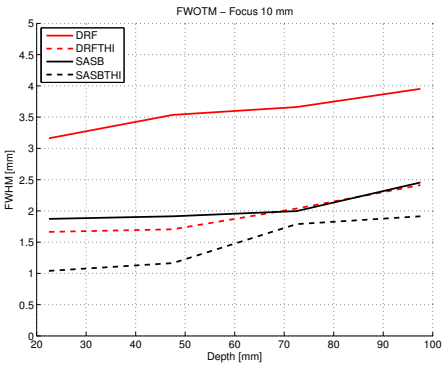

(b) Lateral FWOTM, 10 mm focus

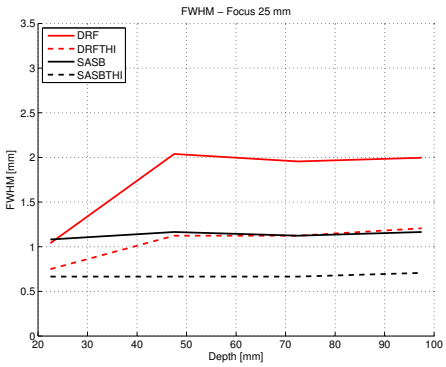

(c) Lateral FWHM, 25 mm focus

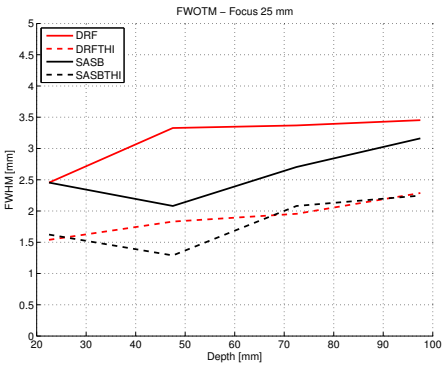

(d) Lateral FWOTM, 25 mm focus

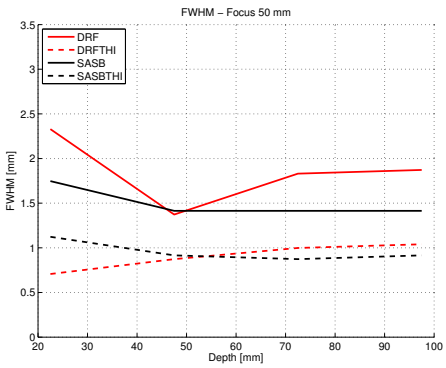

(e) Lateral FWHM, 50 mm focus

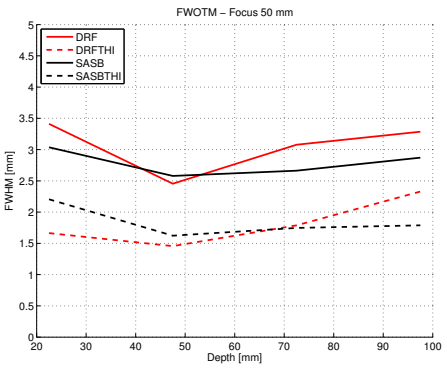

(f) Lateral FWOTM, 50 mm focus

Figure 5.16: Lateral resolution for DRF, SASB, DRFTHI, and SASBTHI for various focal depths using the BK 8804 linear array transducer and SARUS.

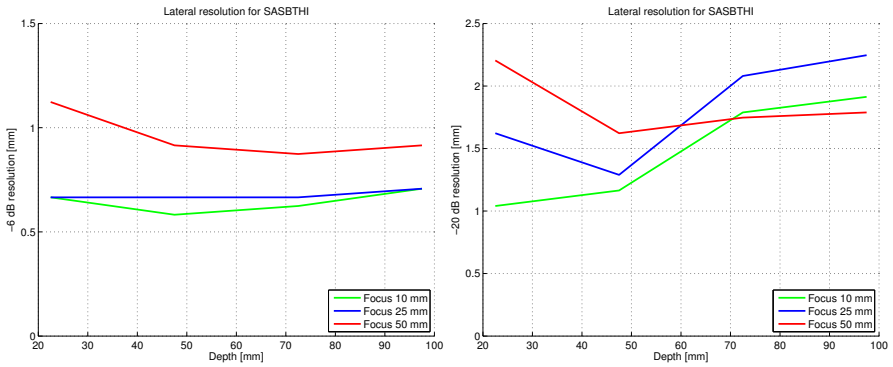

(a) Lateral FWHM for SASBTHI

(b) Lateral FWOTM for SASBTHI

Figure 5.17: Lateral resolution for SASBTHI with various focal depths.

5.5 SASBTHI on Convex Array Transducers

In order to optimize the settings for SASBTHI for a convex array transducer, a series of measurements on wire and speckle phantoms were conducted. The scope of these measurements was to find the optimal F#, virtual source position, and imaging line density for SASBTHI that will result in high and depth independent resolution, while maintaining low levels of side lobe energy and highest possible frame rate. A scaling technique was developed to equalize the gray scale throughout the image due to low signal strength at the virtual source. Finally, the optimized SASBTHI technique was compared to DRFTHI in a series of phantom and *in-vivo* scans.

5.5.1 Optimization of the F#

In this experiment, the effect of the transmit/receive F# on the lateral resolution and PSF of SASBTHI was studied. An implementation of SASBTHI was performed on the UltraView system with the BK 8820e convex array transducer. The scan parameters that went into the use case in the URI on UltraView are shown in Table 5.7. Several scans of a wire phantom was conducted using the setup. Here, the transmit/receive focal depth was varied between 50 mm and 90 mm in incremental steps of 10 mm. For all focal point positions, the F# was varied between 1 and 5 in incremental steps of 0.5. This produced at total of 45 B-mode images of the wire phantom.

For each scan setup, the FWHM was measured from the B-mode images of the wire phantom. In Fig. 5.18a, the lateral FWHM for the visible wires in the B-mode image as function of the F# for the focal point at 80 mm is shown. The objective in this study is to find the F# that will produce the highest

Table 5.7: Scan parameters for optimizing the F# in SASBTHI for the BK 8820e convex array transducer on the UltraView.

Scanner Parameters	SASBTHI
Transmit center frequency	2.14 MHz
Waveform cycles	1.5
Sampling frequency	17 MHz
Number of scanlines	192
Number of active elements	64
Focus Tx/Rx (mm)	[50:10:90]
Imaging depth (mm)	160
F# Tx/Rx	[1:0.5:5]
Apodization Tx	Boxcar
Apodization Rx	Gauss

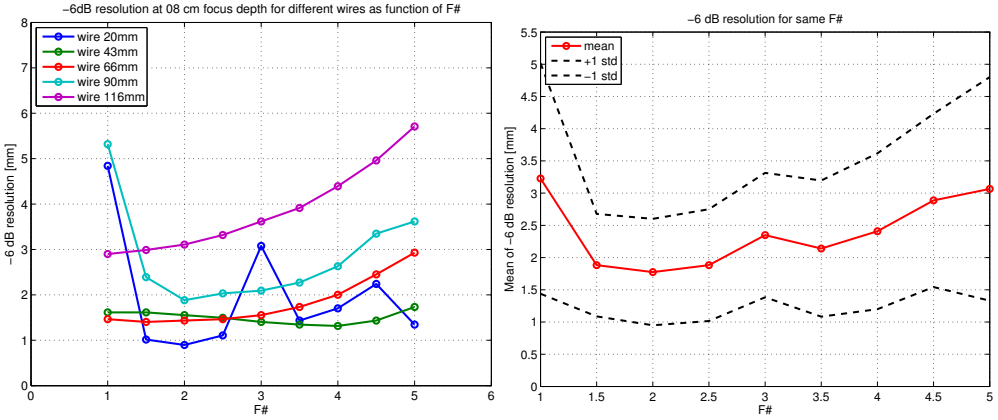

(a) Lateral FWHM as function of F#

(b) Mean of lateral FWHM as function of F#

Figure 5.18: The lateral resolution in SASBTHI for different wires and the mean of the lateral resolution as function of the F# . The focal depth is set to 80 mm.

resolution for all wires, but also to find the F# that is capable of producing the most uniform resolution. The figure shows that the wires at 20 mm, 66 mm, and 90 mm seem to have a local minimum FWHM near a F# of 2. The wire at 43 mm has a local minimum for F# of 4, while the wire at 116 mm has a local minimum for F# of 1. In Fig. 5.18b the mean of the FWHM values for all wires $\pm$ one standard deviation as function of the F# is shown. Here it is seen, that a F# of 2 produces overall the best resolution, because it presents the lowest mean FWHM with a low standard deviation.

The PSF was also measured for F# 's of 1, 3, and 5 to visualize the shape of the main lobe and the level of side lobe energy. The measured PSF's are shown in Fig. 5.19. Here it is seen, that the width of the main lobe is increased as the F# goes up, while the level of side lobe energy is increased as the F# goes down.

Of the three shown PSF's, a F# of 3 produces the best PSF in terms of a narrow main lobe and low levels of side lobe energy.

The study of the effect of the transmit/receive F# on the lateral resolution showed, that the highest and most depth invariant lateral resolution was achieved with a F# of 2. The study of the PSF's confirmed these results and showed that the F# should be near 3 to reduce the width of the main lobe while at the same time keeping the side lobe energy levels at a minimum. In the following studies, that are presented in this thesis, a F# of 2 was applied.

5.5.2 Optimization of the Virtual Source Position

The scope of these experiments was to find the optimal depth for the virtual source and imaging line density for SASBTHI that would result in high and depth independent resolution, while maintaining the highest possible frame rate. The wire phantom was scanned using different virtual source positions and line densities and the lateral resolution was measured. For each measurement a different virtual source position and line density was set. The virtual source position varied between 50 mm and 70 mm, while the line density varied between 192, 269, and 384 image lines per B-mode image as seen in Table 5.8. In total, 9 measurements were made with the different settings. All first stage image data were stored on the desktop PC and second stage beamforming was completed for each measurement.

Table 5.8: Scan parameters for SASBTHI optimization.

Scanner Parameters	SASBTHI
Transmit center frequency	2.14 MHz
Waveform cycles	1.5
Sampling frequency	17 MHz
Number of scanlines	[192, 269, 384]
Number of active elements	64
Focus Tx/Rx (mm)	[50, 60, 70]
Imaging depth (mm)	160
F# Tx/Rx	2
Apodization Tx	Boxcar
Apodization Rx	Gauss

Fig. 5.20 shows four examples of SASBTHI B-mode images of the wire phantom using different line densities and positions of the virtual source. In Fig. 5.20a and Fig. 5.20b, the position of the virtual souce is fixed, while the line density is increased from 192 lines to 384 lines. As can be seen from the images, the resolution is improved by the increased line density. This is particularly pronounced in the bottom of the image, where structures in the phantom are seen multiple times due to high levels of side

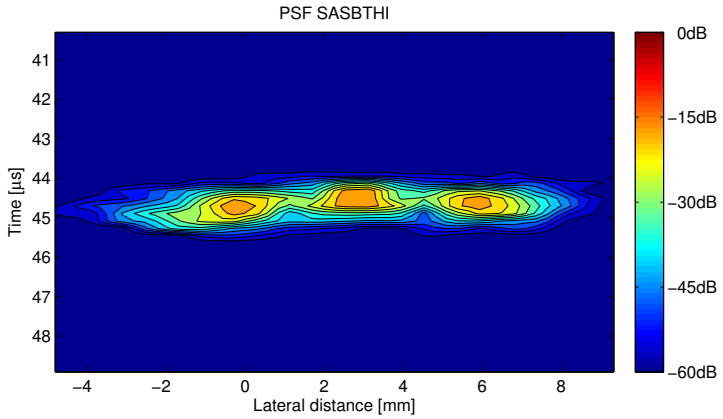

(a) F# 1

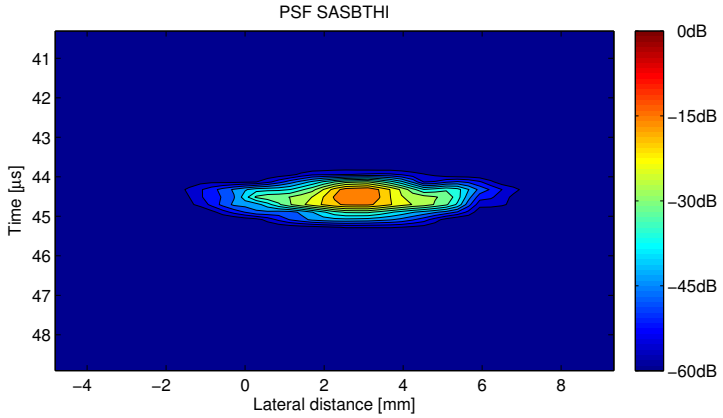

(b) F# 3

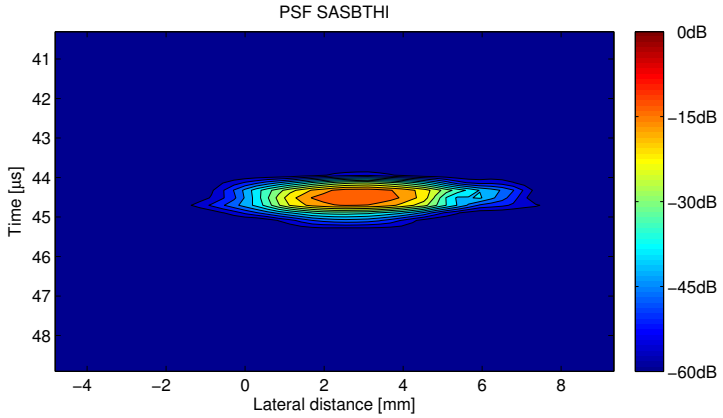

(c) F# 5

Figure 5.19: Contour plots if the point spread functions for the wire at 65 mm depth for different F# 's. The focal depth is set to 80 mm. The distance between the contour lines is 6 dB.

lobes in the image in Fig. 5.20a. This indicates, that the number of image lines should be maximized to improve resolution. In Fig. 5.20c and Fig. 5.20d, the line density is kept constant at 269 lines, but the position of the virtual source is moved from 50 mm depth to 70 m depth. Here it is seen, that moving the virtual source also affects the levels of side lobes. In Fig. 5.20d, where the virtual source is moved down to 70 mm, the amount of artifacts due to high levels of side lobes in the bottom of the image, is reduced. By moving the location of the virtual source from 50 mm to 70 mm in Fig. 5.20c and Fig. 5.20d, the level of side lobes at the top and bottom of the image shifts. This would indicate, that the level of side lobe energy increases with distance to the virtual source. It is seen, that the side lobes fan out from the position of the virtual source. This suggests, that the virtual source should be positioned near the half of the maximum imaging depth as to decrease the level of side lobes throughout the entire image.

The PSF's of SASBTHI using different line densities and virtual source positions are shown in Fig. 5.21 for the wire at 70 mm depth. Here, the findings in the previous B-mode images are confirmed. In Fig. 5.21a and Fig. 5.21b, the virtual source position is fixed, while the line density is changed from 192 lines to 384 lines. Here, the reduction in side lobe energy due to the increased line density is clearly visible. In Fig. 5.21c and Fig. 5.21d, the line density remains fixed at 269 lines per image, while the position of the virtual source is moved from 50 mm depth to 70 mm depth. Here the level of side lobes are reduced by moving the position of the virtual source down to 70 mm.

In Fig. 5.22, the lateral FWHM is shown for different positions of the virtual source and for varying line density. By increasing the number of lines in the image, in Fig. 5.22a to Fig. 5.22c, the lateral resolution for all positions of the virtual source becomes more uniform and more depth invariant. It is also seen from in the figures, that as the the number of image lines increases, the lateral resolution for all three positions of the virtual source become more identical. This indicates, that the lateral resolution in the image is less affected by the change of focus point as the line density increases. In all cases in Fig. 5.22, it is seen, that having the virtual source near 70 mm depth produces both the lowest and the most depth invariant FWHM values. Therefore, in order to keep the most depth invariant and best lateral resolution, the line density should be maximized, while the focus point and thereby the position of the virtual source should be at 70 mm depth.

5.5.3 Optimization of the Line Density

As described in section 5.5.2, increasing the line density in SASBTHI drastically reduces the energy levels of the side lobes. However, it also affects the time it takes to complete a B-mode frame. Table

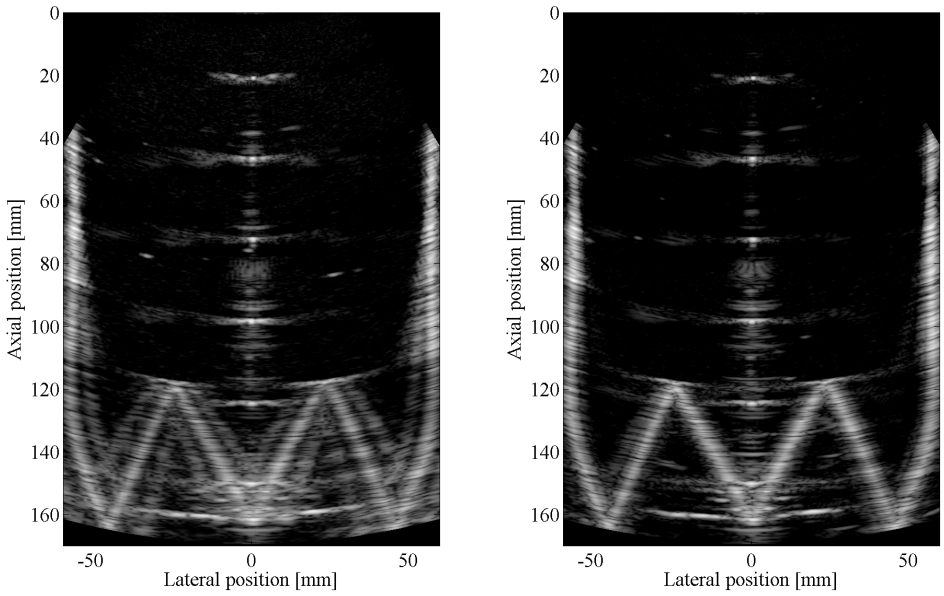

(a) 192 image lines, 70mm focus

(b) 384 image lines, 70mm focus.

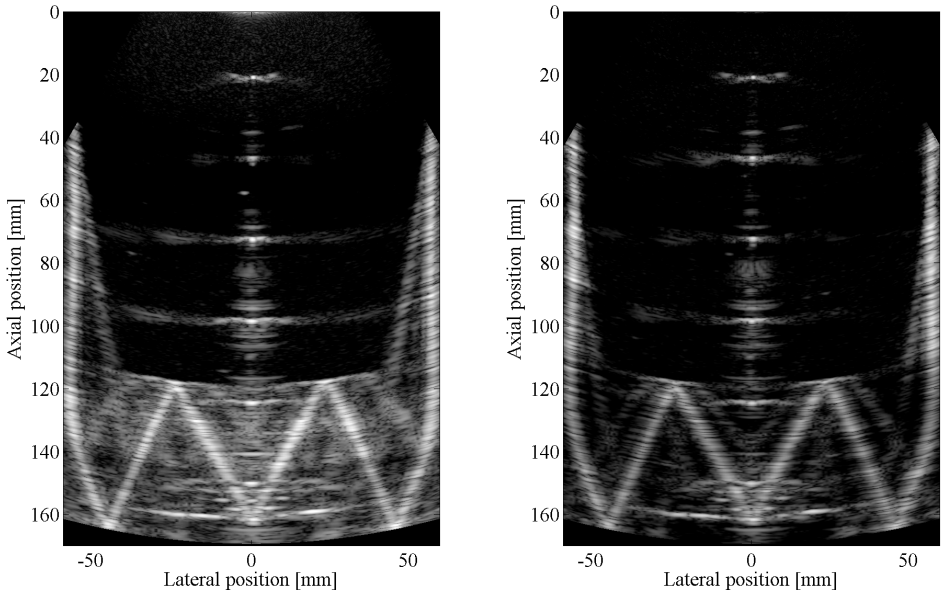

(c) 269 image lines, 50mm focus.

(d) 269 image lines, 70mm focus.

Figure 5.20: SASBTHI B-mode scans of wire phantom using varying number of image lines and transmit/receive focus depths.

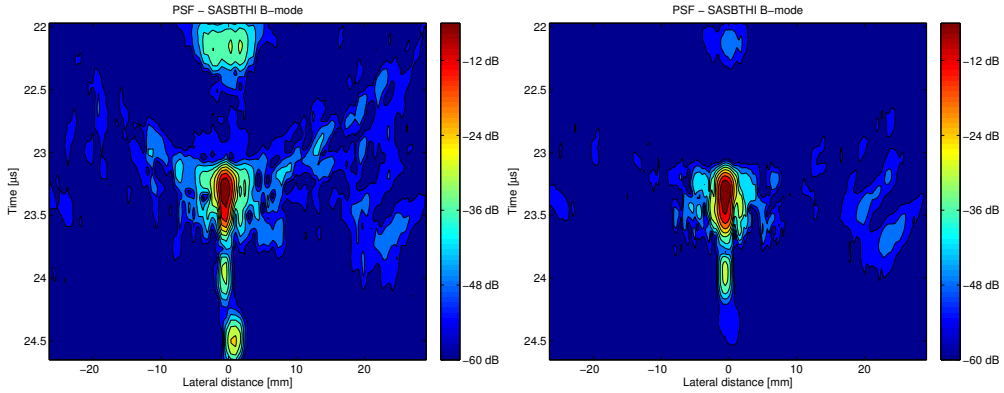

(a) 192 image lines, 70mm focus.

(b) 384 image lines, 70mm focus.

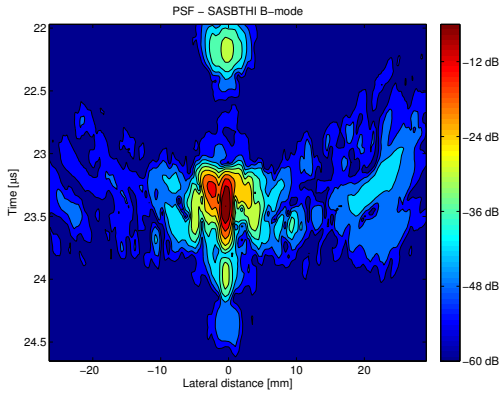

(c) 269 image lines, 50mm focus.

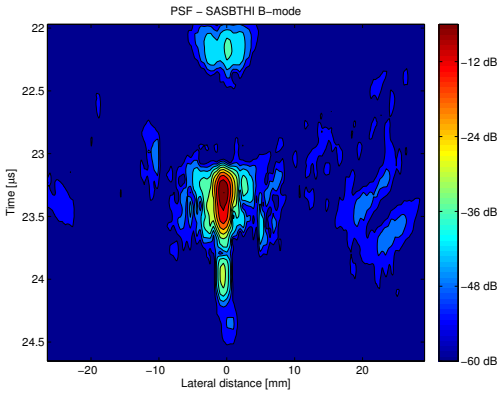

(d) 269 image lines, 70mm focus.

Figure 5.21: Contour plot of the point spread functions for SASBTHI using various number of image lines and transmit/receive focus depths. The level between the contour lines is 6 dB.

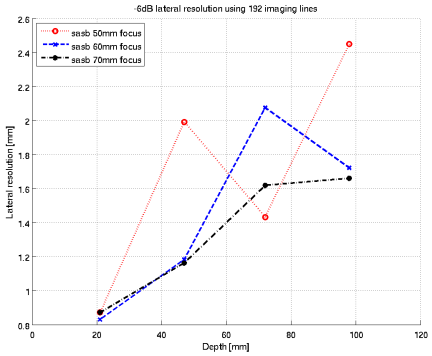

(a) 192 image lines.

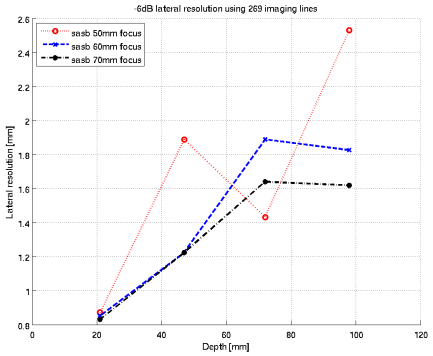

(b) 269 image lines.

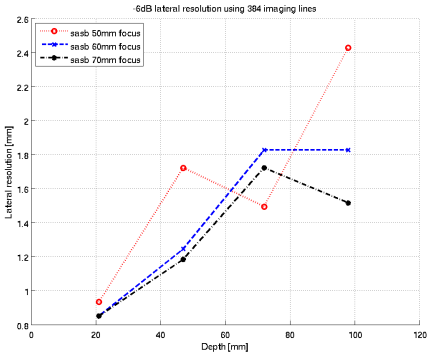

(c) 384 image lines.

Figure 5.22: Measured lateral FWHM for SASBTHI using 192 (5.22a), 269 (5.22b), and 384 (5.22c) image lines and transmit/receive focus depths.

5.9 shows the frame rates that can be accomplished for different line densities when the scan sequence on the UltraView is performing a duplex scan with both SASBTHI and DRFTHI with equal line density. While having 384 scan lines available improves both the spatial resolution and the levels of side lobes, the frame rate of the scan drops to just 3 frames per second. The display of continuously moving tissues in an *in-vivo* scan is disrupted by the low frame rate to a degree where finding and scanning the desired area is near impossible for the user. By decreasing the number of available imaging lines to 269, the frame rate is increased to 5 frames per second which shows a remarkably improvement to the eye of the user. For scans where only either SASBTHI or DRFTHI is required, the available frame rate can be doubled, because no duplex scan is needed. This will allow the use of maximum line density (384 scan lines per frame) without disrupting the display of moving tissues. In the usecase that was implemented for SASBTHI on the UltraView system, a line density of 269 was chosen, because the technique was supposed to run in a duplex sequence with DRFTHI for simultaneous acquisition in clinical scans. This forced the available frame rate in the scans to 5 frames per second as seen from Table 5.9.

Table 5.9: Available frame rates for B-mode SASBTHI/DRFTHI duplex scan for various line densities.

Scan lines	Frame rate
192	6 frames/s
269	5 frames/s
384	3 frames/s

5.5.4 Measurement of the Signal to Noise Ratio

The signal to noise ratio (SNR) of SASBTHI is measured using the optimized parameters for F#, virtual source position, and line density found in Sections 5.5.1, 5.5.2, and 5.5.3. Measurements were performed on a tissue mimicking phantom with no scatterers. The attenuation of the phantom was 0.5 $\frac{\text{dB}}{\text{mm}\cdot\text{MHz}}$ and the speed of sound was 1540 $\frac{\text{m}}{\text{s}}$, which is equivalent to the attenuation and speed of sound found in human tissue.

The SNR was found as the ratio of the signal power, S for depth d over the noise power, N

$$\text{SNR}(d) = \frac{S(d)}{N(d)} \tag{5.1}$$

Here, the signal power was found over M measurements as

$$S(d) = \left(\frac{1}{M} \sum_{m=1}^{M} x_m(d) \right)^2 \tag{5.2}$$

and the noise power as

$$N(d) = \frac{1}{M} \sum_{m=1}^{M} \left(x_m(d) - \frac{1}{M} \sum_{m=1}^{M} x_m(d) \right)^2 \tag{5.3}$$

where x is the signal value.

In total, 30 image frames or measurements was used to find the signal and noise powers.

The SNR shown in the following is expressed in terms of dB. The conversion into dB is found as

$$\text{SNR}_{dB} = 10 \cdot log_{10} \left(\text{SNR} \left(d \right) \right) \tag{5.4}$$

The resulting SNR curve for SASBTHI is shown compared to DRFTHI in Fig. 5.23. Here, the settings for DRFTHI are kept at the default values on the UltraView with a transmit focus at 85 mm. In the figure, the position of virtual source in SASBTHI is clearly visible at 70 mm depth as a dip in SNR. The dip in SNR is caused by the low number of first stage image lines that contribute to an imaging point near the virtual source and because of the geometrical shape of the transducer. As seen from Fig. 3.3a, an imaging point may be represented by several image lines. For an imaging point close to the virtual source, however, the point may only be represented in just one line. This will cause the energy in the second stage image to drop in the vicinity of the virtual source. Furthermore, because a convex array transducer is used, the first stage scan lines are not parallel to each other, but spread out like a fan with imaging depth. This further contributes to less first stage lines representing imaging points near the virtual source.

The SNR in Fig. 5.23 increases for both techniques with image depth for the first 50 mm due to buildup of harmonic signal strength. Since the harmonics in a waveform are progressively generated by distortion of the transmitted waveform, the 2nd harmonic will build up in signal strength as the distance the waveform has propagated increases. Just before the position of the virtual source, the 2nd harmonic is fully developed and a maximum in SNR is reached. After 100 mm depth, the 2nd harmonic energy decreases due to attenuation. For DRFTHI the maximal penetration depth defined as 0 dB SNR is met at 150 mm depth. For SASBTHI, 0 dB SNR is not reached with the given setup. It is also seen from the figure, that SNR for SASBTHI is generally of an order of 10 dB higher than DRFTHI for all depths. This is not surprising, since the image in SASBTHI is constructed by summing over several first stage image lines,

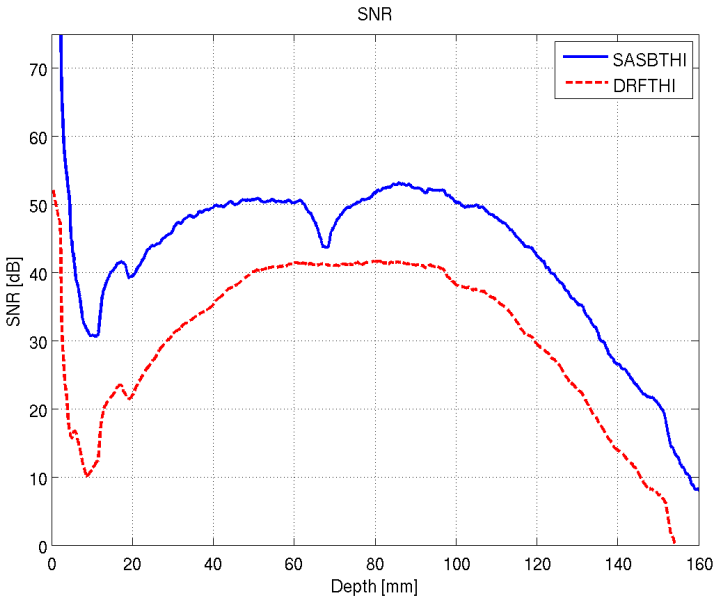

Figure 5.23: Signal to noise ratio for SASBTHI and DRFTHI.

whereas in DRFTHI, each line in the final image is constructed from a single emission. The difference in the number of input contributions to every line, greatly affects the SNR in the finished images, which is seen in the measurement.

5.5.5 Virtual Source Scaling

In Fig. 5.26a a SASBTHI scan of a cyst phantom is shown. A section of the phantom containing almost no cysts is scanned thereby producing a scan that shows the speckle pattern of SASBTHI. The image shows, apart from the cysts in the right hand side of the image, a darkened region across the image at the focal depth at 70 mm depth as well as a darkened region in the top 10 mm of the image. The dark region at the top of the image is caused by the lack of 2nd harmonic energy in the transmitted waveform. Since the harmonics in a waveform are progressively generated by distortion of the transmitted waveform, the 2nd harmonic will build up in signal strength as the distance the waveform has propagated increases. At the top of the image, the distance the waveform has propagated is small, causing the distortion of the waveform and the level of 2nd harmonic energy to be very low as well. This results in the dark region that is seen in the top of image in Fig. 5.26a. The dark region near the focal point is caused by the position of the virtual source due to low number of first stage image lines that contribute to an imaging point near the virtual source as described in Section 5.5.4.

In order to equalize these dark regions in the SASBTHI image, some sort of scaling must be done to the

image. By calculating the median of the energy across image lines in Fig. 5.26a for every sample depth, a map of the energy in the image can be drawn. The measured energy is inverted and low pass filtered to exclude rapid fluctuations in order to generate a set of virtual source scaling (VS-scaling) curves that can be used to equalize gain in the SASBTHI images.

As can be seen from the VS-scaling curve in Fig. 5.24a, the energy is enhanced primarily at the top of the image and to a lesser degree at the position of the virtual source at 70 mm. The scaling curve is extended to a matrix covering the same size of the image frame in terms of image lines, and samples. The VS-scaling matrix generated for imaging of the UltraView system is shown in Fig. 5.25. In Fig. 5.24b, the measured normalized inverted mean of the energy across the image lines after the application of VS-scaling is shown. It is seen, that the normalized energy is 1 for almost all sample depths in the image, showing that the VS-scaling has equalized the gray scale in the image. Fig. 5.26b shows the B-mode image of the cyst phantom with the median VS-scaling matrix applied. As can be seen from the image, the dark regions near the virtual source and at the top of the image have now been neutralized and a uniform gray level has been attained. In Fig. 5.31, an *in-vivo* scan of the liver of a healthy 31 year old male is shown with and without VS-scaling applied. The images were acquired using the UltraView and the URI with the optimized scan settings applied. The dark region of the virtual source is neutralized by VS-scaling and does not introduce any visual artifacts in the *in-vivo* image. The energy is also increased at the top of the image after VS-scaling to obtain a more uniform gray scale throughout the entire image.

A similar scaling curve based on a DRFTHI speckle scan is made for DRFTHI. Here, the scaling curve only adjusts for low 2nd harmonic energy at the top of the image.

5.5.6 SASBTHI Scan Parameters

In the following study of the performance of SASBTHI, the technique will be compared against DRFTHI. DRFTHI is the default scan technique defined by the manufacturer on the UltraView scanner and therefore the prime candidate for a golden standard technique to compare with. The UltraView scanner is set up to perform both SASBTHI and DRFTHI simultaneously in a duplex scan. For DRFTHI the default transmit waveform is a one-and-a-half cycle sinusoid waveform with center frequency of 2.14 MHz and 14 MHz sampling frequency. The 2nd harmonic component of the received signal used for DRFTHI should therefore have an expected center frequency of 4.28 MHz. A transmit focus of 85 mm and F# of 5.67 is applied for DRFTHI with an active aperture of 64 elements using boxcar transmit apodization. In receive, a dynamically expanding aperture is used with gauss apodization and an F# of 0.8. For SASBTHI, the optimized parameters for F#, virtual source position, and line density were applied. The size of the

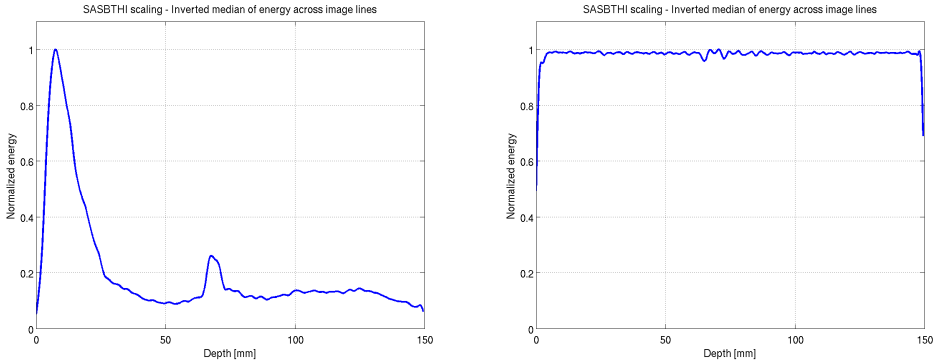

(a) VS-scaling curve.

(b) Normalized inverted median of energy after VS-scaling.

Figure 5.24: VS-scaling curve for SASBTHI using median VS-scaling. In 5.24, the VS-scaling curve is shown. It is calculated as the inverted median of energy across the image lines in a speckle phantom B-mode scan. In 5.24b, the normalized inverted median of energy across the image lines is shown for after the application the VS-scaling.

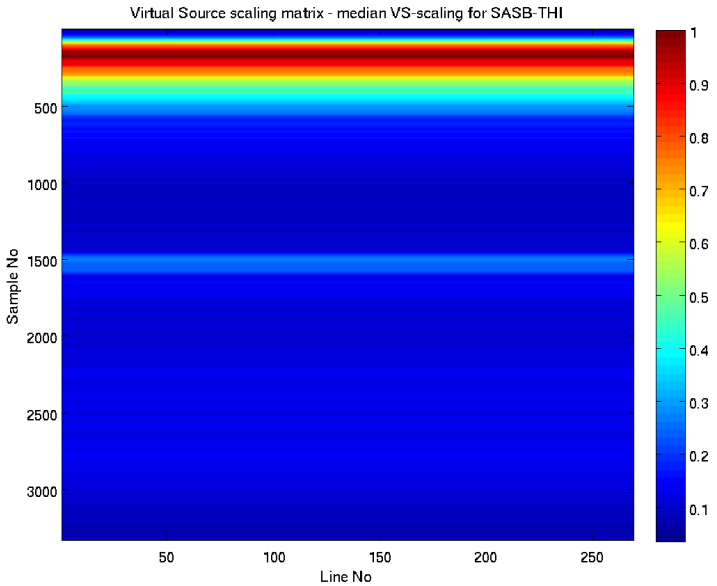

Figure 5.25: Median VS-scaling matrix for SASBTHI.

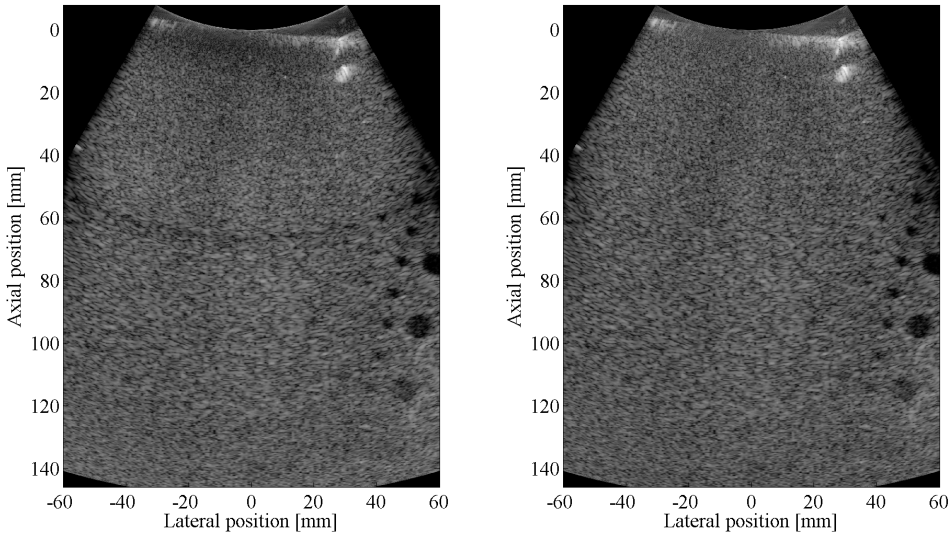

(a) No VS-scaling applied.

(b) Median VS-scaling applied.

Figure 5.26: B-mode speckle scan of tissue mimicking cyst phantom using SASBTHI. No VS-scaling is applied in 5.26a. Here, a dark region is visible at the position of the virtual source at 70 mm depth. A dark area is also seen in the top part of the image, where the 2nd harmonic signal strength is low. In the image in 5.26b, median VS-scaling is applied to correct for the regions with low signal strength. The top region and the virtual source region are now equal in gray scale compared to the rest of the image.

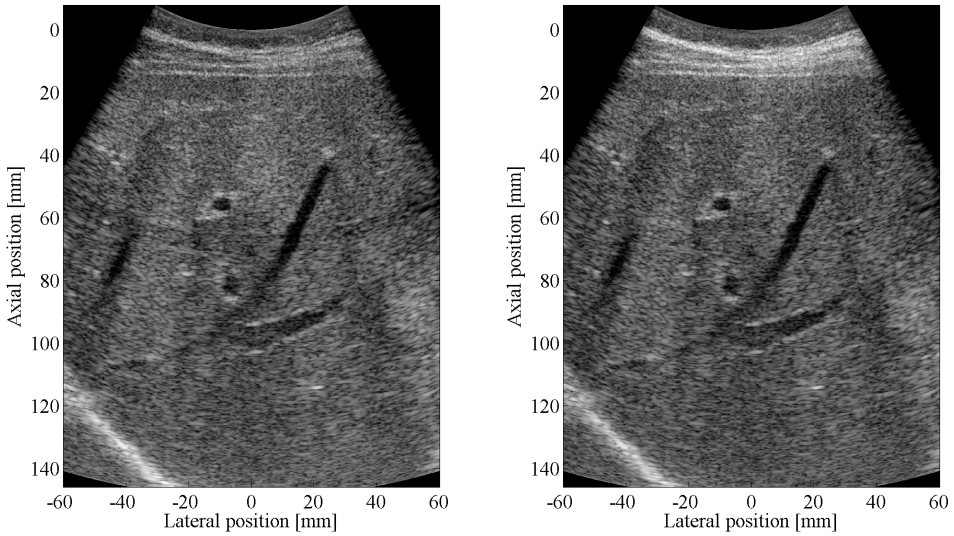

(a) No VS-scaling applied.

(b) Median VS-scaling applied.

Figure 5.27: B-mode *in-vivo* scan of liver tissue using SASBTHI without VS-scaling in 5.27a and with median Vs-scaling in 5.27b. The dynamic range in the images is 60 dB. It is seen from the images, that VS-scaling successfully equalizes the gray scale in the region near the virtual source to match the gray scale in the rest of the image. The region at the top of the image is amplified by VS-scaling to compensate for low 2nd harmonic signal strength.

transmit aperture, and the apodization profiles were the same as for DRFTHI. The scan parameters are shown in Table 5.10.

Table 5.10: Scan parameters for SASBTHI and DRFTHI for BK 8820e convex array transducer on UltraView.

Scanner Parameters	SASBTHI	DRFTHI
Transmit center frequency	2.14 MHz	2.14 MHz
Waveform cycles	1.5	1.5
Sampling frequency	17 MHz	17 MHz
No. scanlines	269	269
No. active elements	64	64
Focus Tx (mm)	70	85
Focus Rx (mm)	70	Dynamic
F# Tx	2	5.67
F# Rx	2	0.8
Apodization Tx	Boxcar	Boxcar
Apodization Rx	Gauss	Gauss

5.5.7 B-mode Images

A scan of the wire phantom was conducted using the SASBTHI/DRFTHI duplex scan sequence. The images are shown in Fig. 5.28. On close inspection of the images, it is found that SASBTHI produced a bit tighter main lobe, especially for the first wire near 20 mm depth. For the most of the image, the levels of side lobes are found to be lower for SASBTHI. This can be seen for the third wire at approximately 80 mm depth. However, at the bottom of the image, artifacts due to high levels of side lobes, are more pronounced for SASBTHI than for DRFTHI. The structures at the bottom of the phantom are more blurred for SASBTHI and multiple echoes from the structures are seen.

5.5.8 PSF's

The PSF's of the two techniques were visualized as contour plots in order to inspect the levels of side lobes. The PSF's for the wire at 70 mm depth are shown in Fig. 5.29. Here it is seen, that the width of the main lobe is approximately the same for the two techniques. The main lobe for SASBTHI is, however, a bit tighter at the -24 dB level. Below the -24 dB level, SASBTHI has remarkably lower levels of side lobes.

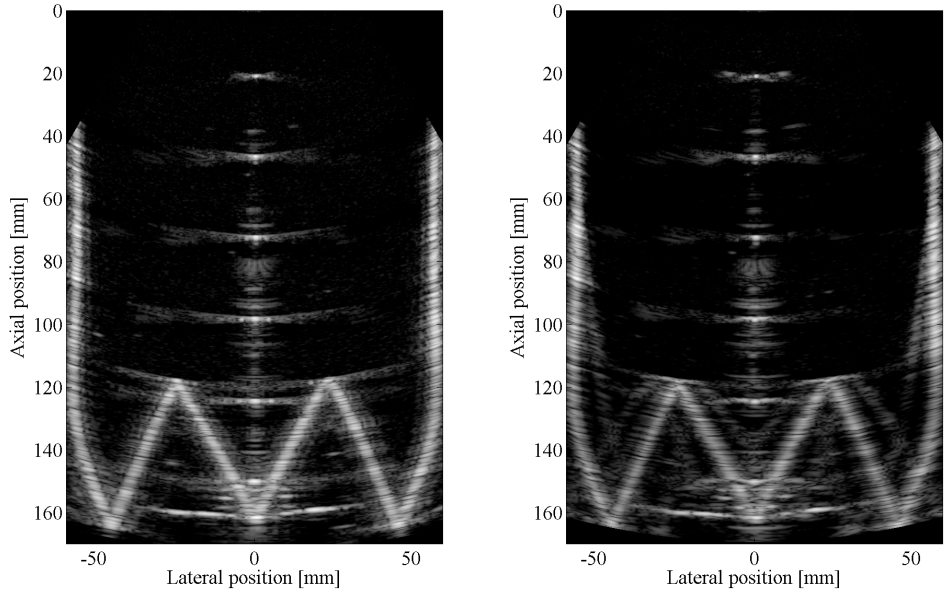

(a) DRFTHI, 269 image lines, 85 mm transmit focus

(b) SASBTHI, 269 image lines, 70mm transit/recieve source.

Figure 5.28: DRFTHI and SASBTHI B-mode scans of wire phantom using 269 image lines.

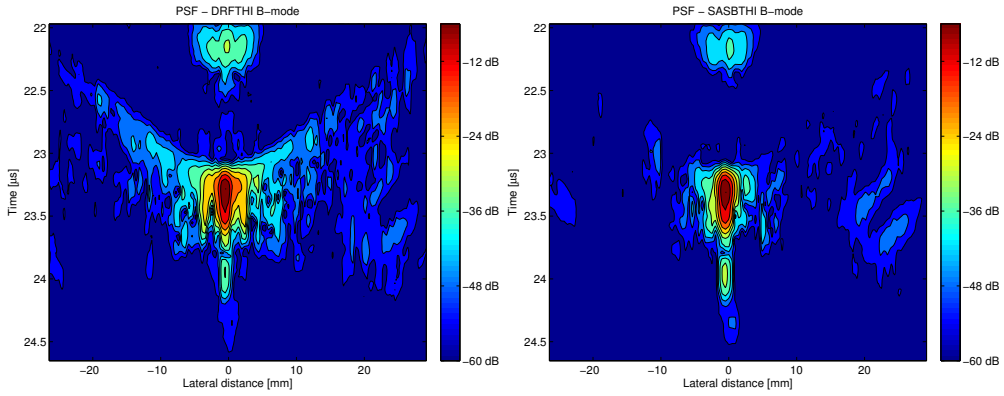

(a) DRFTHI PSF, 269 image lines, 85 mm transmit focus.

(b) SASBTHI PSF, 269 image lines, 70 mm transmit/receive focus.

Figure 5.29: Contour plot of the PSF's for DRFTHI and SASBTHI using 269 image lines.

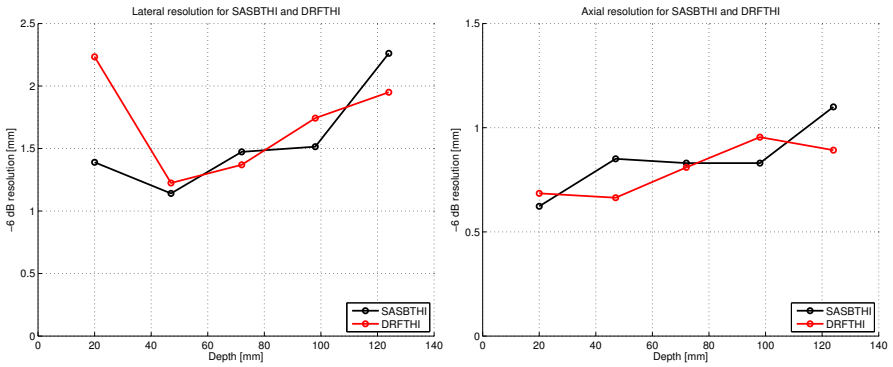

(a) Lateral FWHM **(b)** Axial FWHM

Figure 5.30: The lateral and axial resolution of SASBTHI and DRFTHI.

5.5.9 Resolution

In Fig. 5.30, the measured lateral and axial FWHM for the wires in the phantom is shown for both SASBTHI and DRFTHI. From Fig. 5.30a it is seen, that the lateral resolution of the two techniques is very similar, however, SASBTHI produces the best resolution at the top of the image, wheres DRFTHI produces better resolution at the bottom of the image. For SASBTHI, the mean of the FWHM values is 1.55 with a standard deviation of 0.42. For DRFTHI the mean FWHM is 1.70 with a standard deviation of 0.41. This shows, that the lateral resolution is generally 8% better for SASBTHI compared to DRFTHI. In Fig. 5.30b, the axial resolution is shown for the two techniques. Here, the resolution of the two techniques fluctuate around nearly the same mean FWHM value. For SASBTHI the mean axial FWHM is 0.84 mm and for DRFTHI the mean axial FWHM is 0.81 mm.

5.5.10 *In-vivo* B-mode images

An *in-vivo* scan of the liver of a healthy 31-year old volunteer was performed using UltraView and the SASBTHI/DRFTHI duplex use case. The compiled B-mode images are shown in Fig. 5.31. In both images several blood vessels can be identified. On close inspection, it is seen that the small vessels at (0;70) mm lateral and axial positions are more visible in the SASBTHI image. Furthermore, the delineation of the vessels branches in the image and of the dissected vessel at (-10;60) mm lateral and axial positions is sharper for SASBTHI. Also, the contrast in the vessel branches seem to be higher for SASBTHI. At the bottom left of the image the border of the liver tissue is seen as a white border. In DRFTHI, the delineation of the border is bit sharper than for SASBTHI. Overall, the two images are very similar and only small differences can be spotted. In the following chapter, the clinical value of SASBTHI will be studied in more detail.

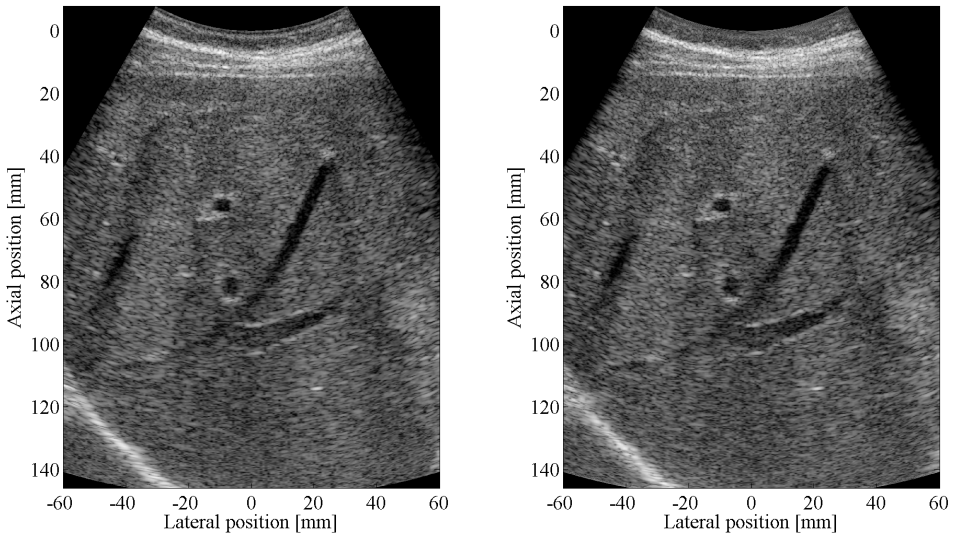

(a) DRFTHI. **(b)** SASBTHI.

Figure 5.31: B-mode *in-vivo* scan of liver tissue using DRFTHI and SASBTHI. The dynamic range in the images is 60 dB.

5.5.11 Section Conclusion

An implementation of SASBTHI was conducted on the UltraView system. Based on phantom measurements, the F#, virtual souce position, and line density was optimized. The SNR was measured for SASBTHI and DRFTHI and found to be higher for SASBTHI by an order of 10 dB. The results on resolution that were obtained using the convex array transducer showed, that SASBTHI is capable of improving the resolution compared to DRFTHI. The clinical value of SASBTHI should therefore be investigated in further studies.

CHAPTER

SIX

CLINICAL EVALUATION

The clinical relevance of SASBTHI is determined by a comparison with DRFTHI on simultaneously acquired *in-vivo* images using the UltraView and URI. The scope of the comparison is to reveal whether SASBTHI provides an improvement in image quality and whether SASBTHI provides an improvement in detecting pathology compared to DRFTHI. A clinical trial was conducted to collect *in-vivo* scan data, which was later evaluated by a panel of trained doctors. The hypothesis, the scan procedure, the evaluation procedure, and the results of the study are all described in detail in the following sections.

6.1 Hypothesis

The two techniques were evaluated against each other by a panel trained professionals in two separate double blinded trials using simultaneously acquired *in-vivo* data. In the first trial, each examiner was presented with videos of two simultaneous DRFTHI and SASBTHI scans that showed views with and without pathology. The examiner was asked to consider the following question in this study:

- Which of the two scans shown do you prefer?

In the second trial, the examiner was presented with videos of either a DRFTHI or a SASBTHI scan that that showed a view either with or without pathology. The examiner was asked to consider the following question:

- Do you see pathology in the scan?

The result of the first question will determine whether the examiner thought the image quality produced by SASBTHI is better than DRFTHI. Since each examiner may have his or her own personal preference when it comes to quality of an image, the outcome of the study is very subjective. Each examiner

may prefer different characteristics, such as color hue, penetration, delineation, and speckle pattern and may weigh them differently in importance. However, by comparing the techniques in this manner, no restrictions are made to which characteristics should be evaluated, and the clinical relevance in terms of image quality can be determined.

The result from the second study will determine, whether SASBTHI provides the doctor with more information on pathology. Again, the question is put in a way as to not restrict the examiner in what to look for. The personal preferences will differ within the panel, but a general comparison of the two techniques can easily be done in this manner. Collectively, the two questions from the two studies will determine the clinical relevance of SASBTHI compared to DRFTHI.

6.2 *In-vivo* Data Acquisition

In-vivo scans on voluntary patients with liver metastases were conducted at Copenhagen University Hospital, Rigshospitalet by two trained doctors. Subjects were all volunteers that had been submitted to liver biopsy later that same day, due to findings of pathology from CT scans and ultrasound scans.

Prior to receiving the patient, the two doctors, who performed the scans, had studied the position and size of the metastases from the CT scan. Once the volunteer was received, an ultrasound abdominal scan was performed using the UltraView scanner running in normal scan mode. Here, the position of metastases was verified. Next, the UltraView's URI mode was activated and a usecase for DRFTHI/SASBTHI in a duplex scan was loaded. In total, 8-10 scans were performed (4-5 with pathology, 4-5 without pathology) on the patient. Data was stored on the external computer and was uploaded to a data base for later beamforming and processing. The specific usecase used in the study was the same as illustrated in Fig. 5.3 in Section 5.1.2 and the settings the same as in Table 5.10 in Section 5.5.6.

A total of 25 patients with various liver metastases were selected. An inclusion/exclusion criterion of patients was defined. The criterion states, that patients are included into the study if the location of the metastasis can be confirmed by the CT scan and by the preceding ultrasound investigation. If the metastasis in the CT and ultrasound scans can not be located by the two doctors, the patient is excluded from the study. Of the total of 25 patients, 6 patients were excluded because the position of the metastases could not be determined by the preceding ultrasound investigation. This resulted in a group of 19 patients meeting the inclusion criterion.

6.3 *In-vivo* Data Comparisons

The clinical relevance of SASBTHI was evaluated against DRFTHI by a panel consisting of 3 trained doctors who were presented with the video sequences made from each scan. A total collection of 114 scans were examined in the trial with 57 of the sequences presenting the pathology and 57 not presenting any pathology. The video sequences were presented in the program IQap[31], which automatically and randomly selected two corresponding DRFTHI and SASBTHI video files from the collection of scans and presented the videos on screen next to each other. The program randomly selected on which side of the screen to present each imaging technique. The examiner did therefore not know which scan was being watched and which imaging technique was presented on either side of the screen. The entire collection of paired videos was presented twice with opposite left-right placement. Each examiner sat isolated during the entire scoring process and was not allowed to discuss the images with any other persons.

In the first evaluation, the image quality was scored. Here, the examiners were presented to paired video sequences of DRFTHI and SASBTHI scans with or without pathology. Each examiner was asked to score which of the two sequences was preferred based on a visual analog scale (VAS). The VAS was in the range of -50 to 50 corresponding to left view is best - left view is slightly better - no difference - right view slightly better - right view is best. No limitations as to which features of the image to look for was given to the examiners. An example of an evaluation of a scan sequence using IQap is shown in Fig. 6.1. Here, it is seen how the two techniques are displayed side by side and are played simultaneously. A set of controls are shown to the examiner at the bottom right corner. With these, the examiner, can pause frames, go forward and backwards frame by frame, resume play, and skip to the next sequence. The VAS scale is shown at the bottom of the screen. The examiner moves the marker on the bar to either side to indicate which technique is preferred.

In the second evaluation, the examiners were presented with a video of either a DRFTHI or a SASBTHI scan. No information was given to the examiner on which technique was being displayed or whether there was pathology or not in the scan. Here, the examiners were asked to decide whether or not there was pathology presented in the scan, again using a VAS. Fig. 6.2 shows an example of an evaluation of pathology using IQap. If the examiner finds pathology in the image, the bar in the image is moved to the top of the image. If no pathology is detected, the examiner moves the bar to the bottom.

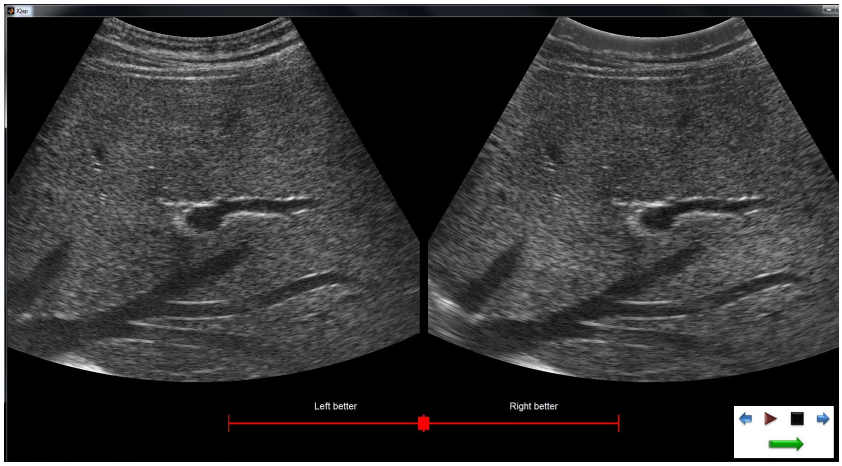

Figure 6.1: Example of an evaluation of image quality of a scan sequence using IQap.

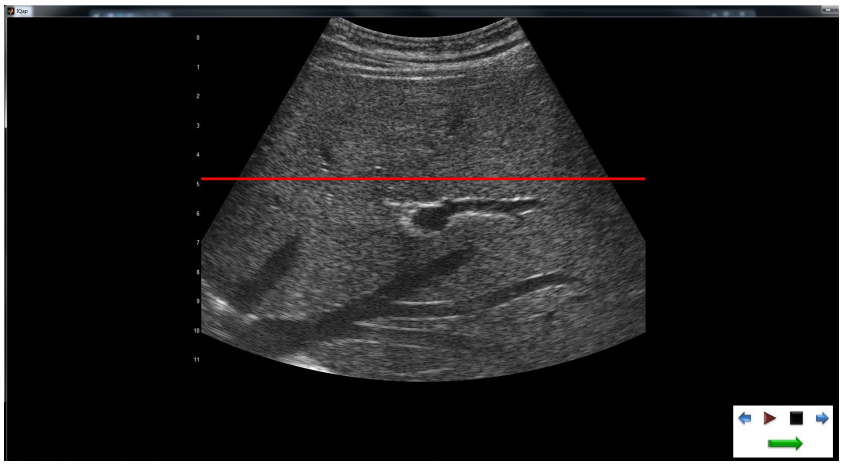

Figure 6.2: Example of an evaluation of pathology in a scan sequence using IQap.

6.4 Results

The results of the studies are presented in the following two sections. For the image quality study, the results are presented as a series of histograms of the VAS scores form the examiners. Statistical analyses are conducted on the results to investigate the strength of the results. In the pathology study, the results are expressed as the sensitivity and specificity for each of the techniques.

6.4.1 Image Quality

The results of the first evaluation are presented as histograms of the VAS scores for each examiner in Fig. 6.3. In the histograms, a positive VAS score indicates, that the examiners thought SASBTHI produced better images, and a negative VAS score, that DRFTHI produced better images. A VAS score of 0 indicates, that both techniques were equally favored. In the comparisons, the 114 video sequences were displayed twice to the examiner, therefore, the total number of VAS scores in each histogram is 228 (VAS1 and VAS2). For all three histograms in Fig. 6.3, the majority of outcomes are centered at a VAS score of 0, indicating that the examiners generally preferred both techniques equally. The mean of the VAS scores are shown in Table 6.1, where a slight trend towards a positive mean VAS score is seen for all three histograms. This could indicate, that SASBTHI produced slightly better images than DRFTHI, however, the standard deviation for the VAS scores is so great, that any definite conclusions are difficult to make.

Table 6.1: Mean VAS score and standard deviation of image quality.

Examiner	Mean VAS $\pm$ 1 std
Examiner 1	0.088 ± 2.261
Examiner 2	0.004 ± 1.121
Examiner 3	0.097 ± 7.621

A Wilcoxon signed rank test is performed on the VAS scores for each of the 3 examiners. Three types of test are performed. First, the Wilcoxon test is performed on the difference between each of the collections of VAS scores (VAS1 - VAS2). Here any left-right bias is studied for each of the examiners, by testing the null hypothesis (H_0), that VAS scores have zero median against the alternative that the distribution does not have zero median (H_1). In the second study, a Wilcoxon test is performed twice on each of the collections of VAS scores (VAS1 or VAS2). Here the null hypothesis, that each collection of VAS scores have zero median, is tested. Finally, the entire collection of 228 VAS scores from each examiner is tested using the Wilcoxon test. Here the null hypothesis, that all VAS scores have zero median, is tested.

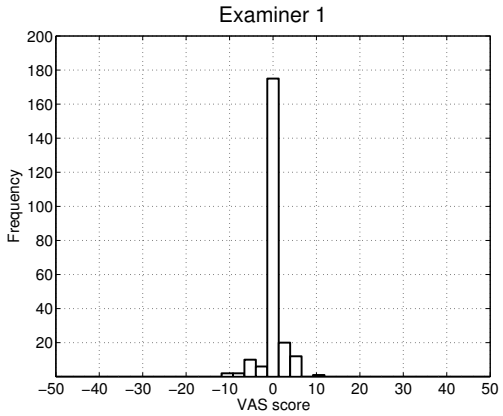

(a) Examiner 1

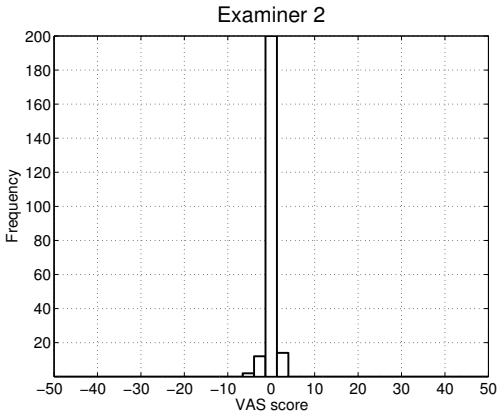

(b) Examiner 2

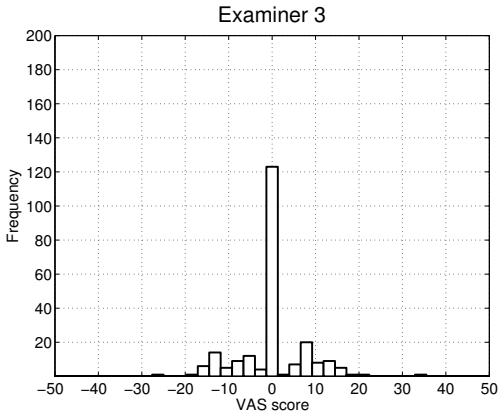

(c) Examiner 3

Figure 6.3: Histograms of the VAS scores from 3 examiners. A total of $2 \cdot 114$ sequences were scored. A positive VAS score favors SASBTHI, while a negative VAS score favors DRFTHI.

Table 6.2: Wilcoxon signed rank test - Examiner 1.

Data	Reject H_0	p-value
VAS1-VAS2	Yes	0.001
VAS1	Yes	0.01
VAS2	Failed	0.13
VAS1 and VAS2	Failed	0.53

Table 6.3: Wilcoxon signed rank test - Examiner 2.

Data	Reject H_0	p-value
VAS1-VAS2	Failed	0.31
VAS1	Failed	0.39
VAS2	Failed	0.74
VAS1 and VAS2	Failed	0.72

Table 6.4: Wilcoxon signed rank test - Examiner 3.

Data	Reject H_0	p-value
VAS1-VAS2	Failed	0.08
VAS1	Failed	0.20
VAS2	Failed	0.25
VAS1 and VAS2	Failed	0.91

Tables 6.2-6.4 show the results of the Wilcoxon tests for each of the examiners. It is noticed, that for examiner 1, the first Wilcoxon test on the difference of the VAS scores, rejects the H_0 hypothesis. This indicates, that the examiner had a left-right bias in this part of the study. The second Wilcoxon test shows the outcome from each of the collections of VAS scores. Here, it is seen that for VAS1, H_0 is rejected indicating, that the median of VAS1 is not zero, while for VAS2, H_0 is not rejected, indicating that the median of VAS2 is zero. For the last Wilcoxon test on the entire collection of VAS scores for examiner 1, the H_0 hypothesis is rejected, indicating that the median of all VAS scores from examiner 1 is zero

For the other two examiners, the Wilcoxon tests shows no left-right bias, and all tests failed to reject the H_0 hypothesis, indicating, that the VAS scores from each examiner has zero median.

Table 6.5: Wilcoxon signed rank test - All examiners.

Data	Reject H_0	p-value
All VAS scores	Failed	0.42

A Wilcoxon test is made on the accumulated VAS scores from all 3 examiners. The results are shown in Table 6.5. Here, H_0 hypothesis is failed to be rejected with a p-value of $p = 0.42$. This shows, that the hypothesis, that VAS scores have zero median could not be rejected, or in other words, that there was no statistical difference between the image quality of DRFTHI and SASBTHI.

6.4.2 Pathology test

The results of the second evaluation are shown in Table 6.6a for DRFTHI and Table 6.6b for SASBTHI. Here the results are shown as percentages indicating, in how many of the cases where pathology was present in the image did the examiner also see the pathology and vice versa. For DRFTHI, the amount of false positive cases, where the examiners found pathology present in the images, when there actually was no pathology present, is 18%. For SASBTHI, the amount of false positive cases is only 12%. The amount of false negative cases, where the examiners did not find the pathology that was present in the images, is 32% for DRFTHI and 36% for SASBTHI. Tables of the results of the pathology tests for each individual examiner can be found in Appendix A.

Table 6.6: Pathology test - All examiners

(a) DRFTHI

	No visual of pathology	Visual of pathology
No pathology in image	82	18
Pathology in image	32	68

(b) SASBTHI

	No visual of pathology	Visual of pathology
No pathology in image	88	12
Pathology in image	36	64

In Table 6.7, the sensitivity and specificity of the two techniques are shown. The sensitivity is defined as the ratio of the amount of cases where the examiner correctly detected pathology, over the total amount of cases where pathology was detected. The specificity is defined as the ratio of the amount of cases where the examiner correctly rejected presence of pathology, over the total amount of cases where pathology was rejected. In other words, sensitivity is the proportion of actual positives which are correctly identified as such, while the specificity is the proportion of negatives which are correctly identified as such. Tables of the results on sensitivity and specificity for each examiner can be found in Appendix B.

Table 6.7: Sensitivity and specificity for DRFTHI and SASBTHI.

	Sensitivity	Specificity
DRFTHI	0.79	0.72
SASBTHI	0.84	0.71

Here, it is seen, that SASBTHI has higher sensitivity than DRFTHI, which means, that the examiners were better to correctly detect pathology using SABTHI. The specificity is almost the same for the two techniques, indicating, that the examiners were equally good to correctly exclude pathology using either

technique.

6.5 Chapter Conclusion

A study of the clinical relevance of SASBTHI was performed. The study answered the two questions on whether SASBTHI provided improved image quality and whether SASBTHI made detection of pathology easier. Simultaneously acquired DRFTHI and SASBTHI scan data from 114 *in-vivo* scans on 19 patients was performed by trained doctors from Copenhagen University Hospital, Rigshospitalet. The collection of scan videos were evaluated by a panel consisting of three trained doctors who scored the videos in two double-blinded trials. The results of the trials show, that SASBTHI produced VAS mean values that were slightly better than DRFTHI, however there was no statistically difference between the image quality of SASBTHI and DRFTHI. In terms of increasing the detectability of pathology, SASBTHI produced a sensitivity of 0.84 which is better than the sensitivity of DRFTHI which is only 0.79. The specificity is found to be the same for the two techniques where values of 0.71 and 0.72 for SASBTHI and DRFTHI are obtained. In general, the study showed, that SASBTHI produces clinical images that have as good image quality and specificity as the golden standard (DRFTHI), while the sensitivity of SASBTHI is better than for DRFTHI.

CHAPTER

SEVEN

PROJECT CONCLUSIONS

The project was divided into three main topics.

1. THI on linear and convex array transducers
2. SASBTHI on linear and convex array transducers
3. The clinical relevance of SASBTHI

7.1 THI on Linear and Convex Array Transducers

A PI technique was implemented on SARUS for DRFTHI using a linear array transducer. The scope of the experiment was to investigate whether the newly developed SARUS could perform a 180° phase shift required for PI. Inspection of the pulse responses confirmed the systems capability of producing PI, however, harmonic leakage from the fundamental into the 2nd harmonic was present due to poor separation of the 2nd harmonic. A new implementation of DRFTHI was made on SARUS using a convex array transducer. Here the PI technique was exploited for fundamental, 2nd harmonic, and 3rd harmonic imaging. Matched filters were applied to reduce harmonic leakage for all three techniques. The results proved that THI could be performed on SARUS for both 2nd and 3rd harmonic imaging using PI, and that improvements of 43% and 56% in the FWHM could be obtained for 2nd and 3rd harmonic imaging, respectively. Significant experience with the PI technique, the effects of harmonic leakage in particular, and THI in general, was obtained during these studies.

7.2 SASBTHI on Linear and Convex Array Transducers

The experimental ultrasound system was used for a novel implementation of SASBTHI for a linear array transducer. The scope of the measurements was to investigate, whether the technique was feasible and to study how the technique compared to DRFTHI in terms of obtained resolution. Different positions of the virtual source was applied in a series of scans of a wire phantom. The measured resolution of the wires suggests, that SASBTHI is quite capable of improving the resolution compared to DRFTHI. An improvement of 69% in the lateral FWHM was accomplished using the linear array compared with DRFTHI. The technique was expanded for a convex array transducer and applied to the commercial ultrasound system UltraView. The use of a commercially available ultrasound system allows for the technique to be applied for future *in-vivo* imaging without the risk of violating clinical regulations. A thorough optimization study was performed, where the optimal F#, position of the virtual source, and line density were found. The SNR was measured for the optimized SASBTHI technique and for DRFTHI. The measurement showed, that the SNR for SASBTHI was generally 10 dB higher than DRFTHI, and that the noise floor was not met for a scan depth of up to 160 mm. A scaling technique was developed to equalize low signal strength at the position of the virtual source and at the top the images due to low 2nd harmonic signal strength. The scaling technique was applied for phantom scans and *in-vivo* scans where no artifacts caused by the scaling were found. Measurements of the resolution of SASBTHI confirmed previous findings, that SABTHI provides improved resolution compared to DRFTHI.

7.3 The clinical relevance of SASBTHI

The optimized implementation of SASBTHI was used in a small clinical trial to investigate whether SASBTHI improves image quality and makes detection of pathology easier. A total of 114 *in-vivo* scans were performed on 19 patients at Copenhagen University Hospital, Rigshospitalet by trained professionals. A duplex SASBTHI/DRFTHI usecase acquired scan data from the two techniques simultaneously. A double-blinded trial was performed where 3 trained examiners evaluated each pair of acquired scan sequences.

The statistical analysis showed that the mean of the VAS scores for image quality were slightly higher for SASBTHI, but were not statistically significant. A Wilcoxon analysis on the accumulated VAS scores for image quality showed, that the hypothesis that the median of the scores was zero could not be rejected. This indicates, that there is no statistically difference in the image quality and that SASBTHI produces equally as good images as DRFTHI.

The results on the detectability of pathology in the images shows that the sensitivity of SASBTHI is 0.84 which is 6% higher than DRFTHI sensitivity. The specificity for SASBTHI is found to be 0.71 which is virtually the same as for DRFTHI (0.72). This shows, that the examiners found it easier to correctly detect pathology in the images using SASBTHI and found excluding pathology equally easy in the SASBTHI and DRFTHI images.

7.4 Final Conclusion

The project investigated the field of THI and covered many aspects of the PI technique including the effects of harmonic leakage and the improvements in resolution using THI. Overall, the project showed, that SASB can be combined with THI to produce images which benefit from higher resolution compared to today's golden standard DRFTHI. In the clinical investigations, it was found that the image quality and specificity of SASBTHI was as good as DRFTHI, and that the sensitivity of SASBTHI was even higher.

As the hardware computational power in ultrasound systems increases, more and more synthetic aperture techniques will emerge. It is the author's expectation, that SASBTHI will be a valuable tool in the development of a hands free ultrasound system. The first stage beamformer in SASB reduces image RF data to image line data and is of such low complexity that it could eventually be implemented into the handle of the transducer. Image line data could then be transferred wirelessly to a stationary second stage beamformer on a computer or cluster engine. The benefits of increased resolution and reduced artifacts in THI can make SASBTHI the new default imaging technique on future ultrasound systems.

APPENDICES

APPENDIX

A

PATHOLOGY TEST

The following tables present additional data material on the pathology tests for SASBTHI and DRFTHI.

Table A.1: Pathology test - Examiner 1

(a) DRFTHI

	No visual of pathology	Visual of pathology
No pathology in image	59	41
Pathology in image	20	80

(b) SASBTHI

	No visual of pathology	Visual of pathology
No pathology in image	72	28
Pathology in image	28	72

Table A.2: Pathology test - Examiner 2

(a) DRFTHI

	No visual of pathology	Visual of pathology
No pathology in image	96	4
Pathology in image	54	46

(b) SASBTHI

	No visual of pathology	Visual of pathology
No pathology in image	96	4
Pathology in image	50	50

Table A.3: Pathology test - Examiner 3

(a) DRFTHI

	No visual of pathology	Visual of pathology
No pathology in image	91	9
Pathology in image	22	78

(b) SASBTHI

	No visual of pathology	Visual of pathology
No pathology in image	96	4
Pathology in image	30	70

APPENDIX

B

SENSITIVITY AND SPECIFICITY

The following tables present additional data material on the sensitivity and specificity of SASBTHI and DRFTHI.

Table B.1: Sensitivity and specificity for DRFTHI and SASBTHI - Examiner 1.

	Sensitivity	Specificity
DRFTHI	0.66	0.75
SASBTHI	0.72	0.72

Table B.2: Sensitivity and specificity for DRFTHI and SASBTHI - Examiner 2.

	Sensitivity	Specificity
DRFTHI	0.92	0.64
SASBTHI	0.93	0.66

Table B.3: Sensitivity and specificity for DRFTHI and SASBTHI - Examiner 3.

	Sensitivity	Specificity
DRFTHI	0.90	0.81
SASBTHI	0.95	0.76

APPENDIX

C

CLINICAL TRIAL DATA MATERIAL

The following figures presents the first B-mode image in each of the 114 image sequences presented to the examiners in the clinical trial.

(a) DRFTHI

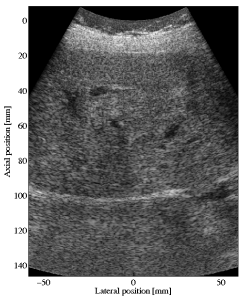

(b) SASBTHI

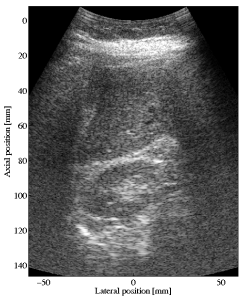

(c) DRFTHI

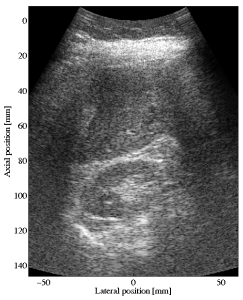

(d) SASBTHI

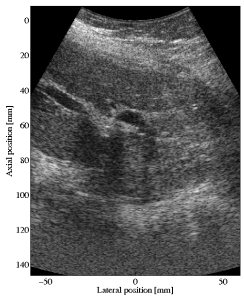

(e) DRFTHI

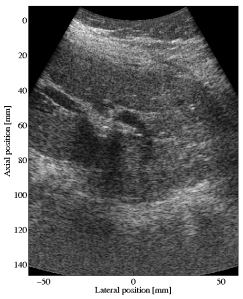

(f) SASBTHI

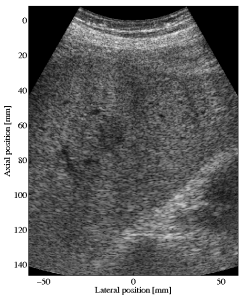

(g) DRFTHI

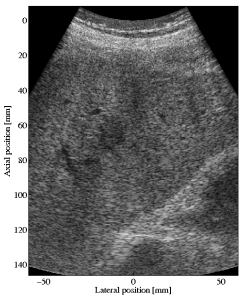

(h) SASBTHI

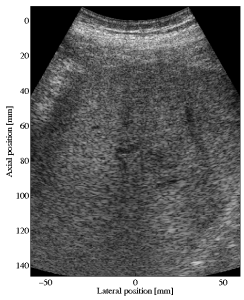

(i) DRFTHI

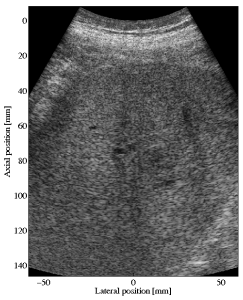

(j) SASBTHI

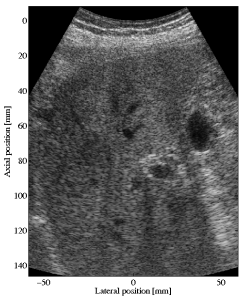

(k) DRFTHI

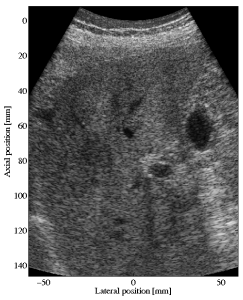

(l) SASBTHI

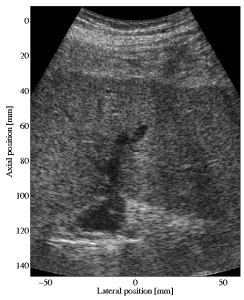

(a) DRFTHI

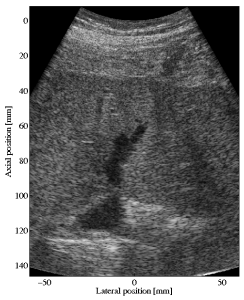

(b) SASBTHI

(c) DRFTHI

(d) SASBTHI

(e) DRFTHI

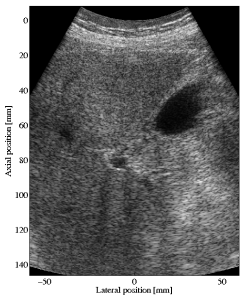

(f) SASBTHI

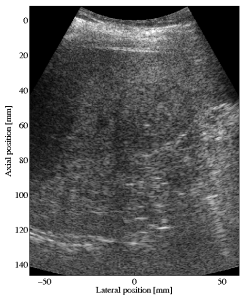

(g) DRFTHI

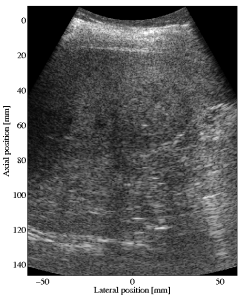

(h) SASBTHI

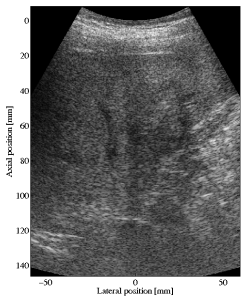

(i) DRFTHI

(j) SASBTHI

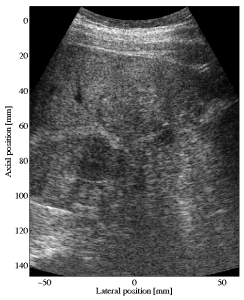

(k) DRFTHI

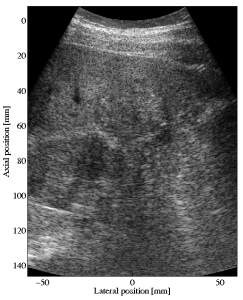

(l) SASBTHI

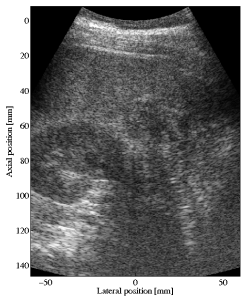

(a) DRFTHI

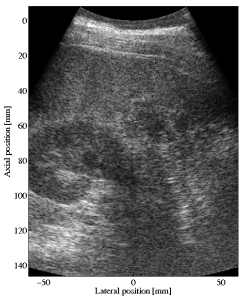

(b) SASBTHI

(c) DRFTHI

(d) SASBTHI

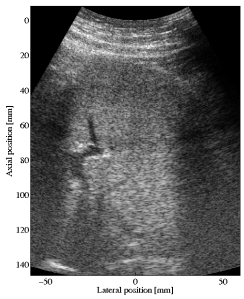

(e) DRFTHI

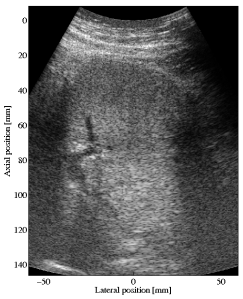

(f) SASBTHI

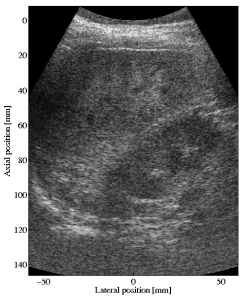

(g) DRFTHI

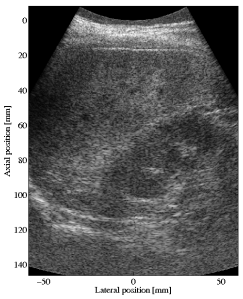

(h) SASBTHI

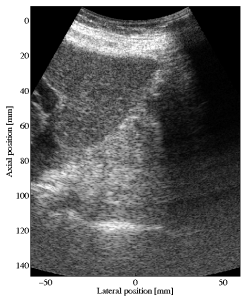

(i) DRFTHI

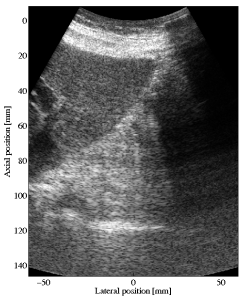

(j) SASBTHI

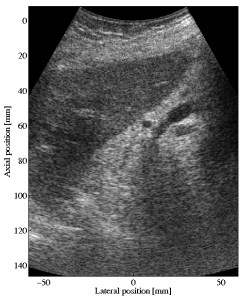

(k) DRFTHI

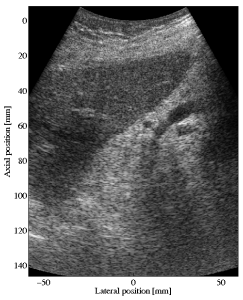

(l) SASBTHI

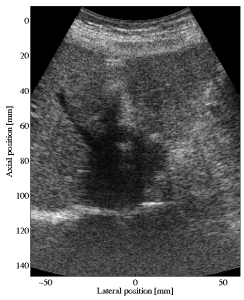

(a) DRFTHI

(b) SASBTHI

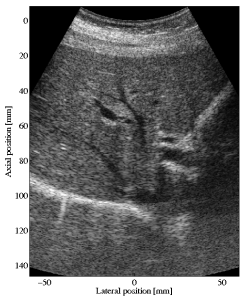

(c) DRFTHI

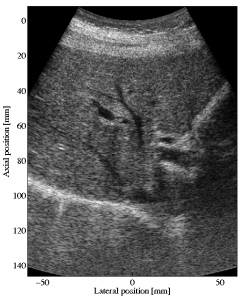

(d) SASBTHI

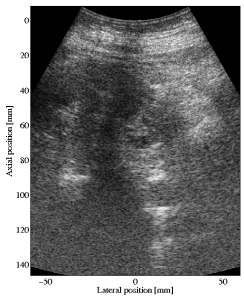

(e) DRFTHI

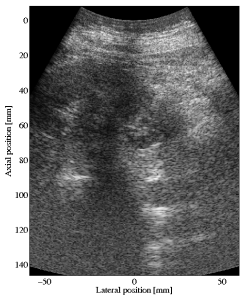

(f) SASBTHI

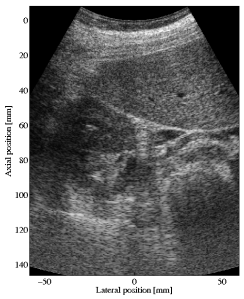

(g) DRFTHI

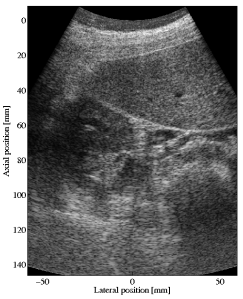

(h) SASBTHI

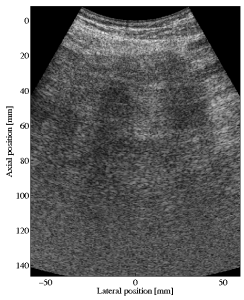

(i) DRFTHI

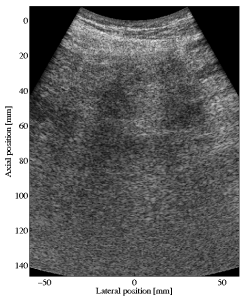

(j) SASBTHI

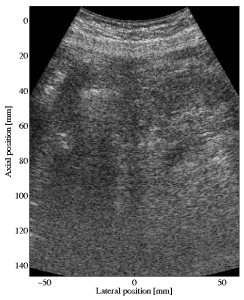

(k) DRFTHI

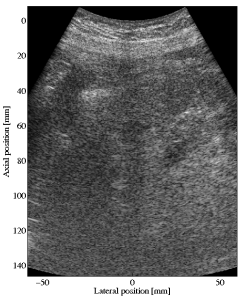

(l) SASBTHI

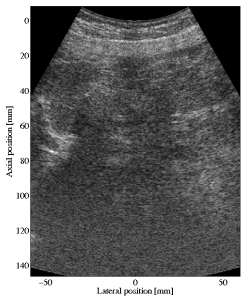

(a) DRFTHI

(b) SASBTHI

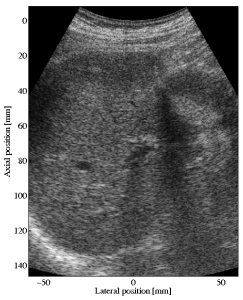

(c) DRFTHI

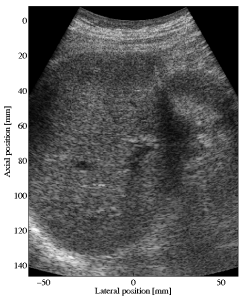

(d) SASBTHI

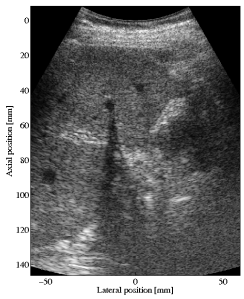

(e) DRFTHI

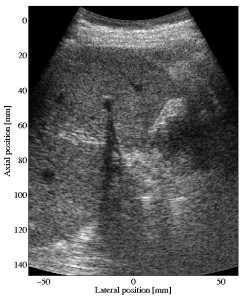

(f) SASBTHI

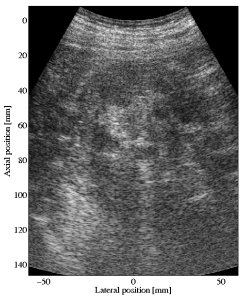

(g) DRFTHI

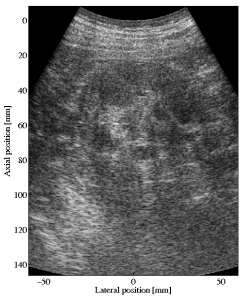

(h) SASBTHI

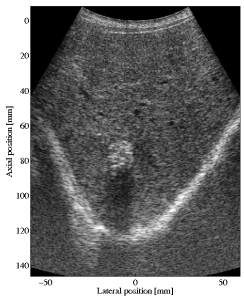

(i) DRFTHI

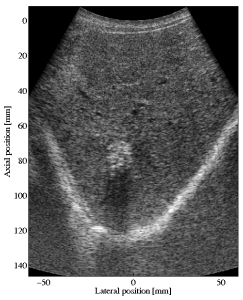

(j) SASBTHI

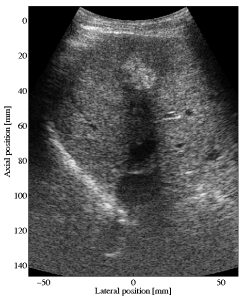

(k) DRFTHI

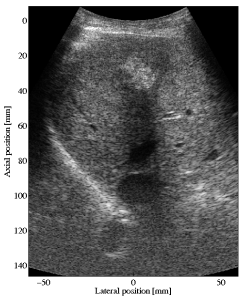

(l) SASBTHI

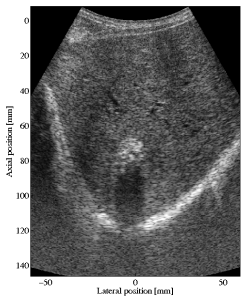

(a) DRFTHI

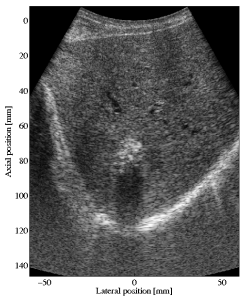

(b) SASBTHI

(c) DRFTHI

(d) SASBTHI

(e) DRFTHI

(f) SASBTHI

(g) DRFTHI

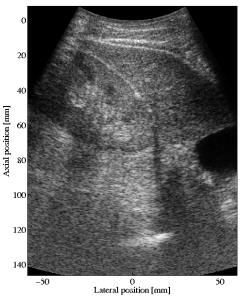

(h) SASBTHI

(i) DRFTHI

(j) SASBTHI

(k) DRFTHI

(l) SASBTHI

(a) DRFTHI

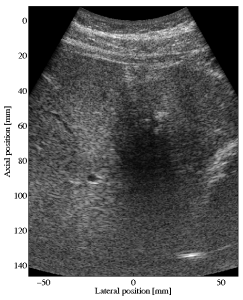

(b) SASBTHI

(c) DRFTHI

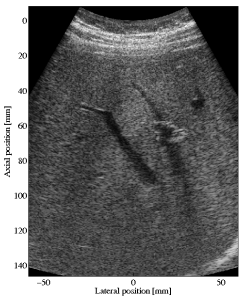

(d) SASBTHI

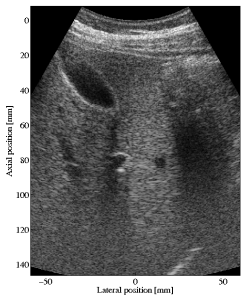

(e) DRFTHI

(f) SASBTHI

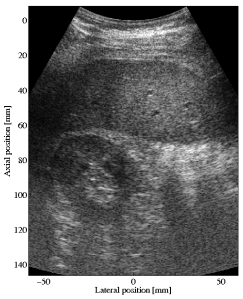

(g) DRFTHI

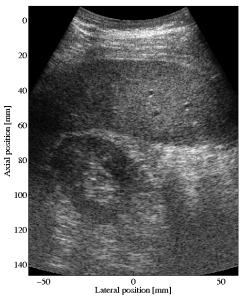

(h) SASBTHI

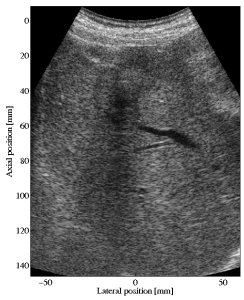

(i) DRFTHI

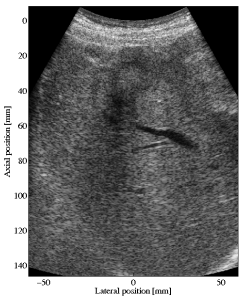

(j) SASBTHI

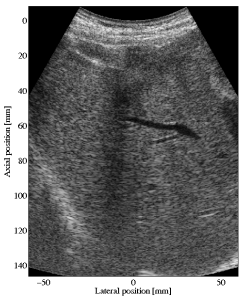

(k) DRFTHI

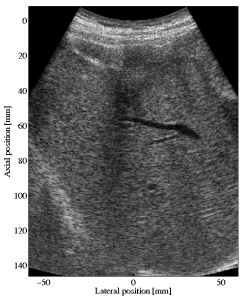

(l) SASBTHI

(a) DRFTHI

(b) SASBTHI

(c) DRFTHI

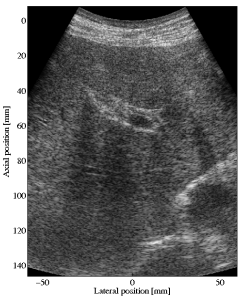

(d) SASBTHI

(e) DRFTHI

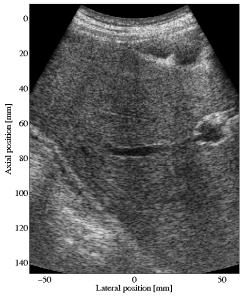

(f) SASBTHI

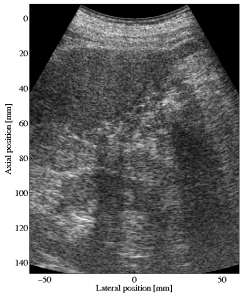

(g) DRFTHI

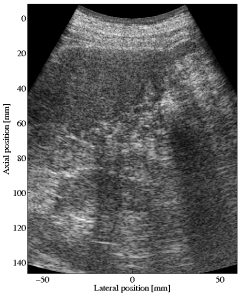

(h) SASBTHI

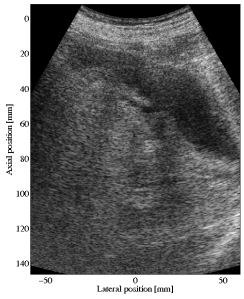

(i) DRFTHI

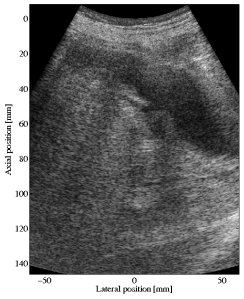

(j) SASBTHI

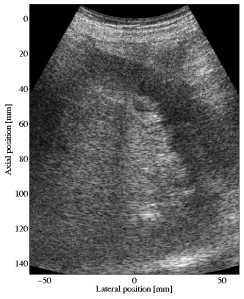

(k) DRFTHI

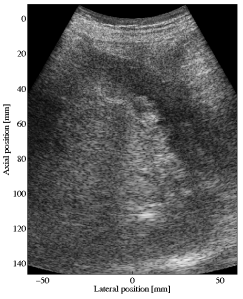

(l) SASBTHI

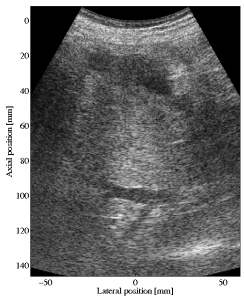

(a) DRFTHI

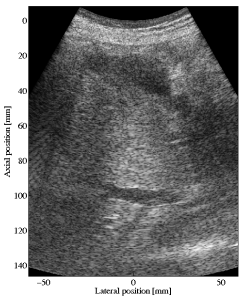

(b) SASBTHI

(c) DRFTHI

(d) SASBTHI

(e) DRFTHI

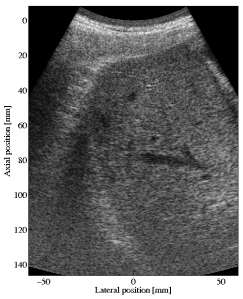

(f) SASBTHI

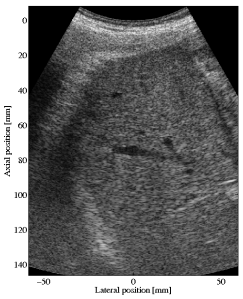

(g) DRFTHI

(h) SASBTHI

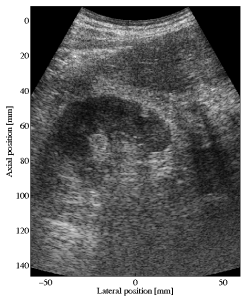

(i) DRFTHI

(j) SASBTHI

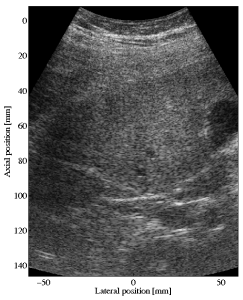

(k) DRFTHI

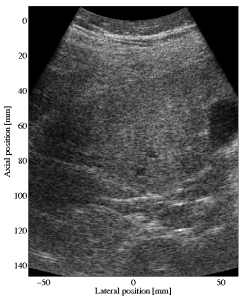

(l) SASBTHI

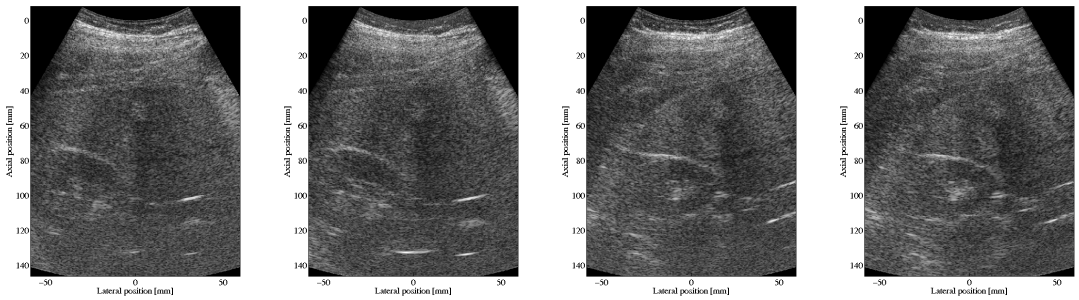

(a) DRFTHI **(b)** SASBTHI **(c)** DRFTHI **(d)** SASBTHI

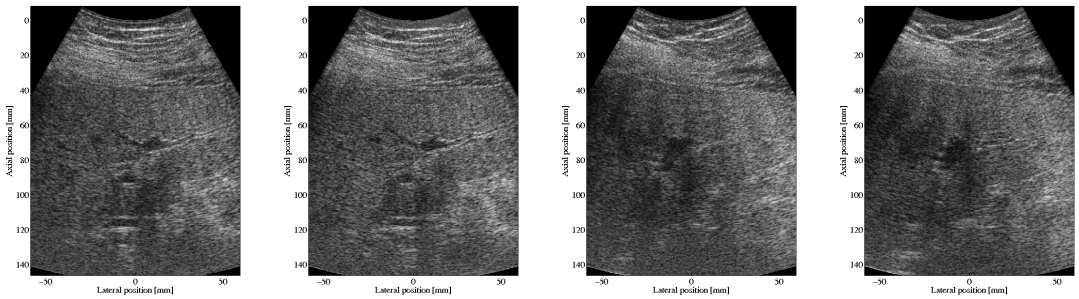

(e) DRFTHI **(f)** SASBTHI **(g)** DRFTHI **(h)** SASBTHI

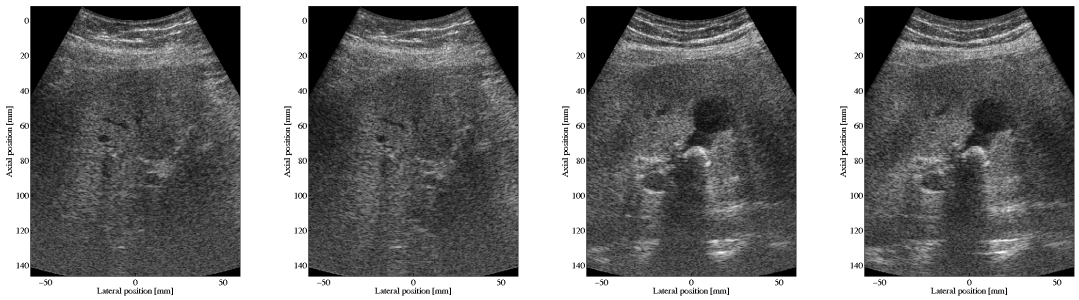

(i) DRFTHI **(j)** SASBTHI **(k)** DRFTHI **(l)** SASBTHI

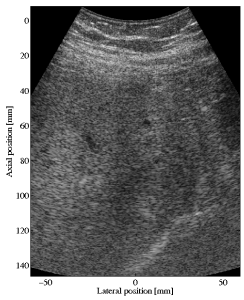

(a) DRFTHI

(b) SASBTHI

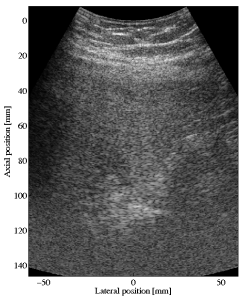

(c) DRFTHI

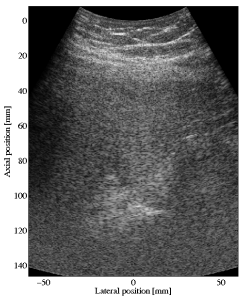

(d) SASBTHI

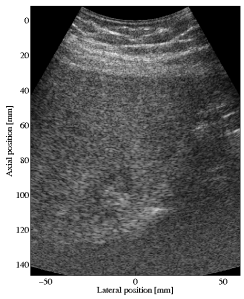

(e) DRFTHI

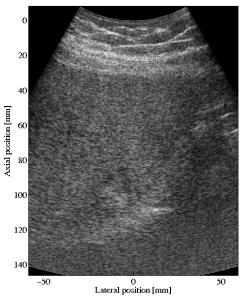

(f) SASBTHI

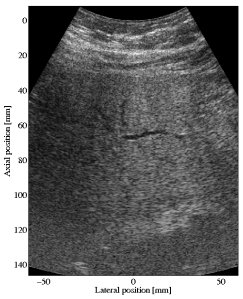

(g) DRFTHI

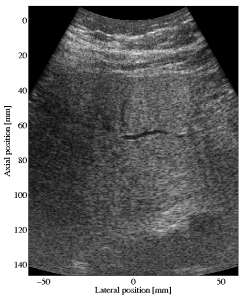

(h) SASBTHI

(i) DRFTHI

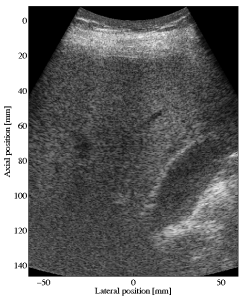

(j) SASBTHI

(k) DRFTHI

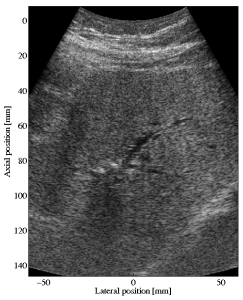

(l) SASBTHI

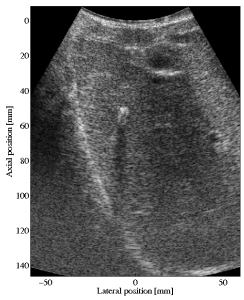

(a) DRFTHI

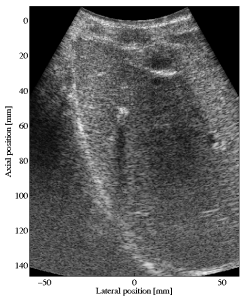

(b) SASBTHI

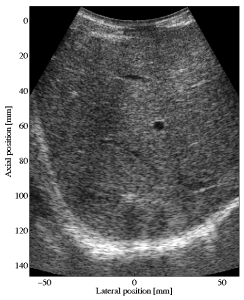

(c) DRFTHI

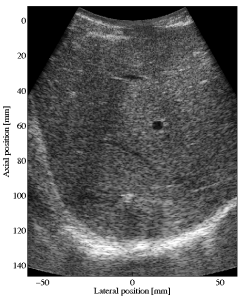

(d) SASBTHI

(e) DRFTHI

(f) SASBTHI

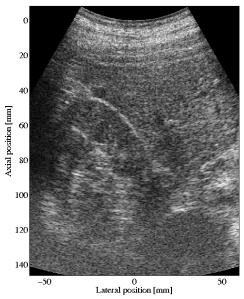

(g) DRFTHI

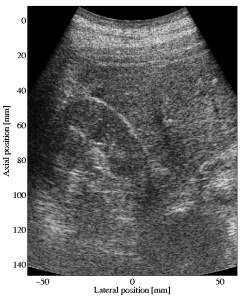

(h) SASBTHI

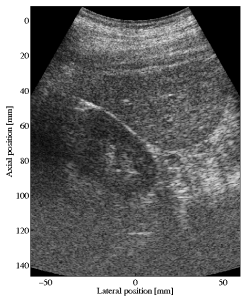

(i) DRFTHI

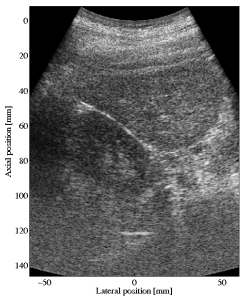

(j) SASBTHI

(k) DRFTHI

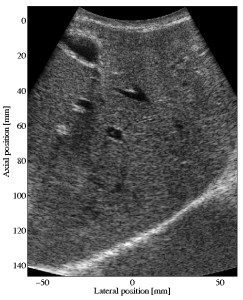

(l) SASBTHI

(a) DRFTHI

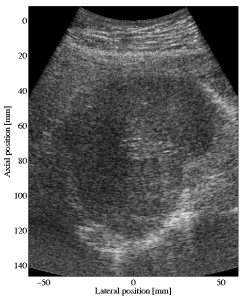

(b) SASBTHI

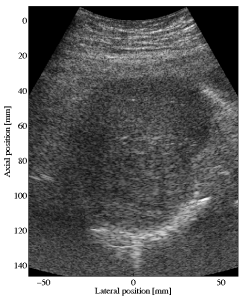

(c) DRFTHI

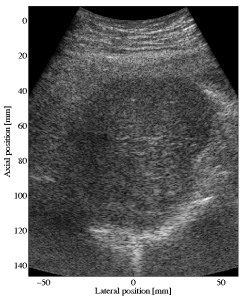

(d) SASBTHI

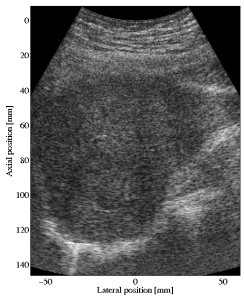

(e) DRFTHI

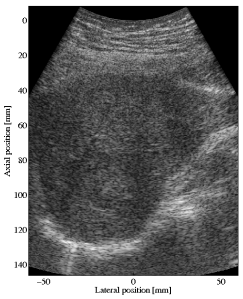

(f) SASBTHI

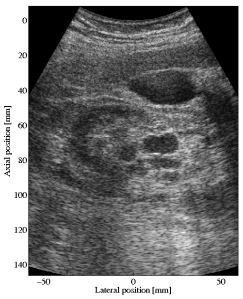

(g) DRFTHI

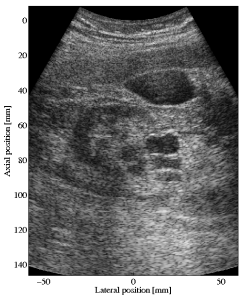

(h) SASBTHI

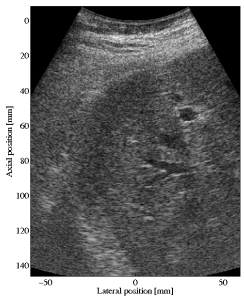

(i) DRFTHI

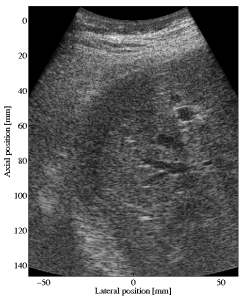

(j) SASBTHI

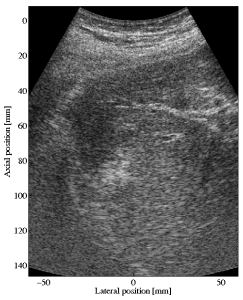

(k) DRFTHI

(l) SASBTHI

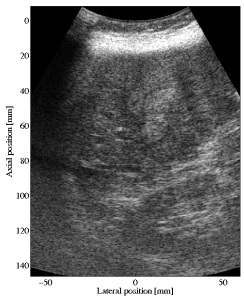

(a) DRFTHI

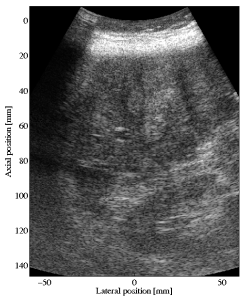

(b) SASBTHI

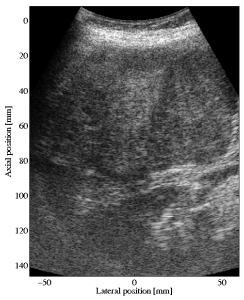

(c) DRFTHI

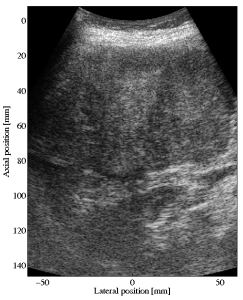

(d) SASBTHI

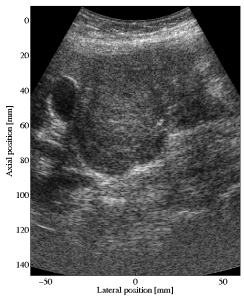

(e) DRFTHI

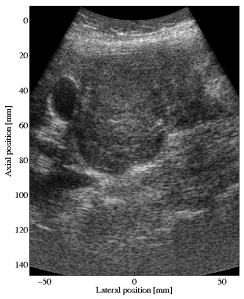

(f) SASBTHI

(g) DRFTHI

(h) SASBTHI

(i) DRFTHI

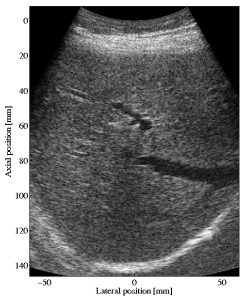

(j) SASBTHI

(k) DRFTHI

(l) SASBTHI

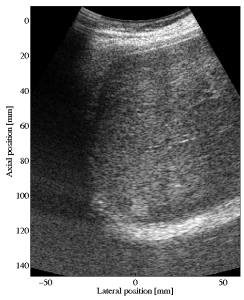

(a) DRFTHI

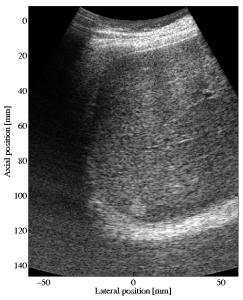

(b) SASBTHI

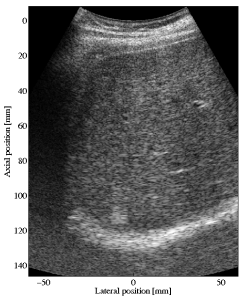

(c) DRFTHI

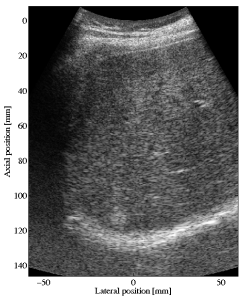

(d) SASBTHI

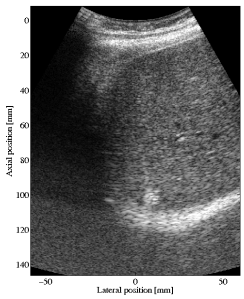

(e) DRFTHI

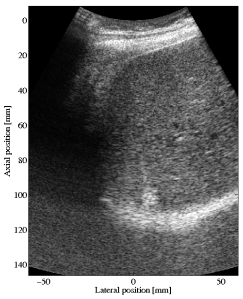

(f) SASBTHI

(g) DRFTHI

(h) SASBTHI

(i) DRFTHI

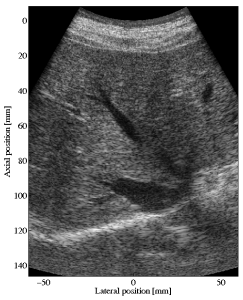

(j) SASBTHI

(k) DRFTHI

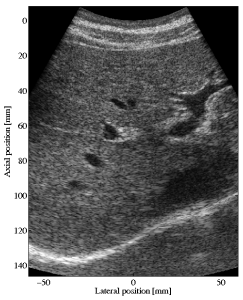

(l) SASBTHI

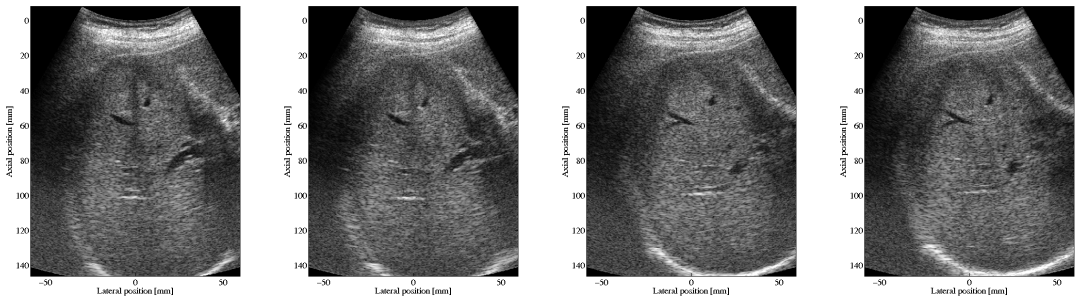

(a) DRFTHI **(b)** SASBTHI **(c)** DRFTHI **(d)** SASBTHI

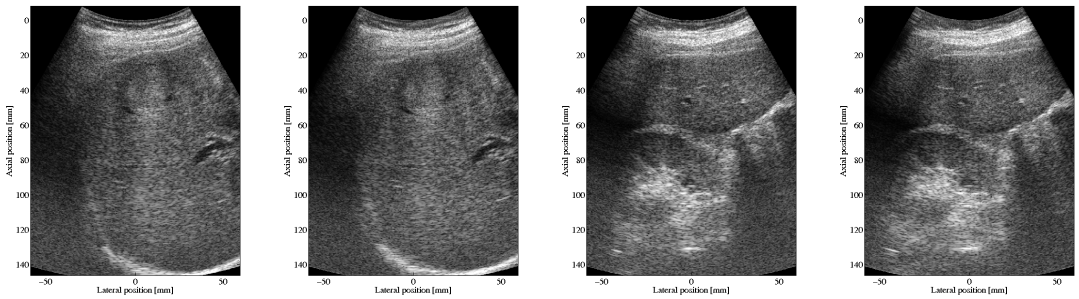

(e) DRFTHI **(f)** SASBTHI **(g)** DRFTHI **(h)** SASBTHI

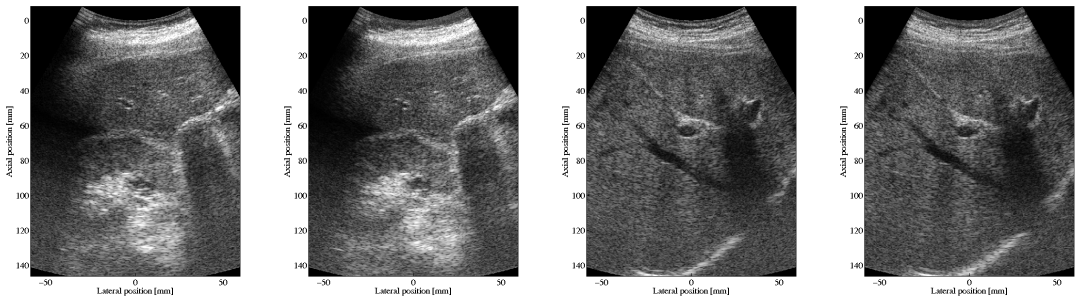

(i) DRFTHI **(j)** SASBTHI **(k)** DRFTHI **(l)** SASBTHI

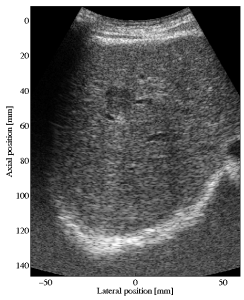

(a) DRFTHI

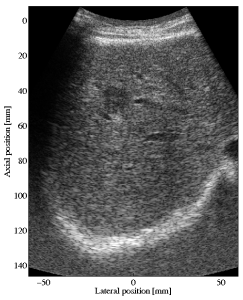

(b) SASBTHI

(c) DRFTHI

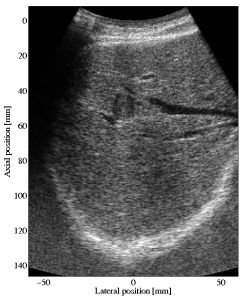

(d) SASBTHI

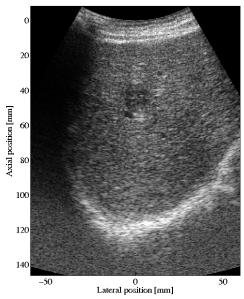

(e) DRFTHI

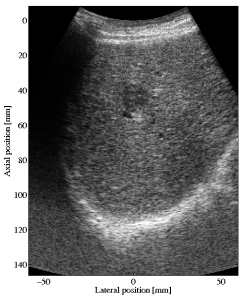

(f) SASBTHI

(g) DRFTHI

(h) SASBTHI

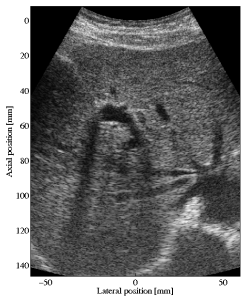

(i) DRFTHI

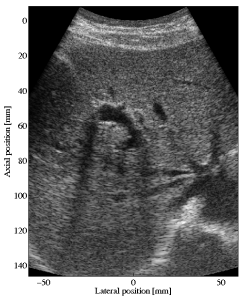

(j) SASBTHI

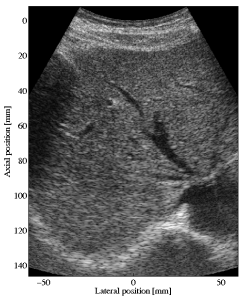

(k) DRFTHI

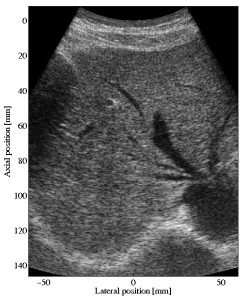

(l) SASBTHI

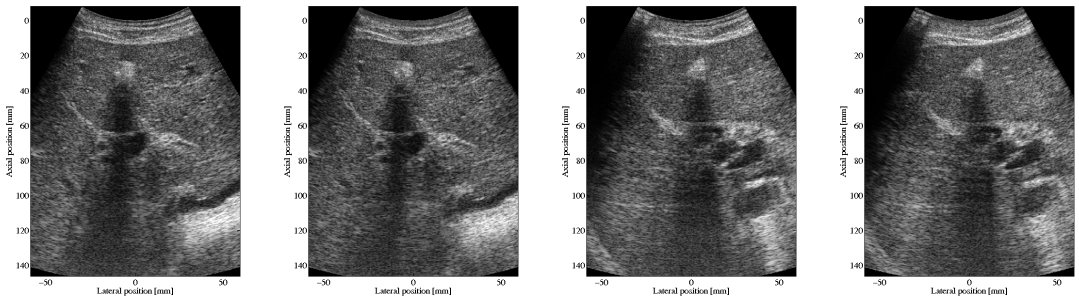

(a) DRFTHI **(b)** SASBTHI **(c)** DRFTHI **(d)** SASBTHI

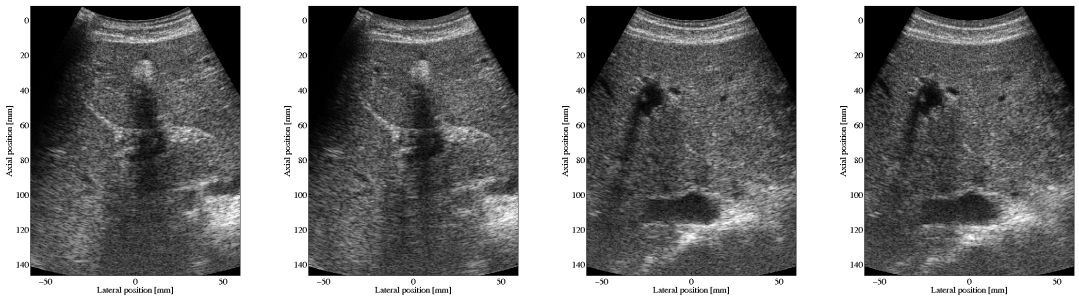

(e) DRFTHI **(f)** SASBTHI **(g)** DRFTHI **(h)** SASBTHI

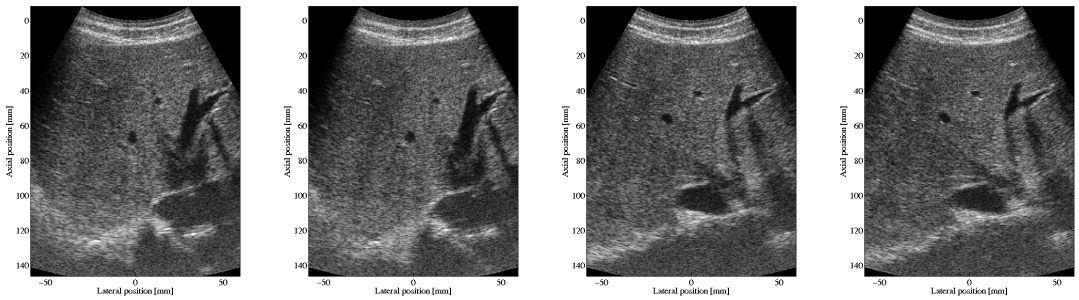

(i) DRFTHI **(j)** SASBTHI **(k)** DRFTHI **(l)** SASBTHI

BIBLIOGRAPHY

[1] M. A. Averkiou. Tissue harmonic imaging. In *Proc. IEEE Ultrason. Symp.*, volume 2, pages 1563–1572, 2000.

[2] M. A. Averkiou, D. N. Roundhill, and J. E. Powers. A new imaging technique based on the nonlinear properties of tissues. In *Proc. IEEE Ultrason. Symp.*, volume 2, pages 1561–1566, 1997.

[3] Michalakis A. Averkiou and Mark F. Hamilton. Measurements of harmonic generations in a focused finite-amplitude sound beam. *J. Acoust. Soc. Am.*, 98(6):3439–3442, 1995.

[4] M. Bae, H. Lee, S. B. Park, R. Yoon, M. H. Jeong, D. G. Kim, M. Jeong, and Y. Kim. A new ultrasonic synthetic aperture tissue harmonic imaging system. In *Proc. IEEE Ultrason. Symp.*, pages 1258–1261, 2008.

[5] M. H. Bae and M. K. Jeong. A study of synthetic-aperture imaging with virtual source elements in B-mode ultrasound imaging systems. In *IEEE Trans. Ultrason., Ferroelec., Freq. Contr.*, volume 47, pages 1510–1519, 2000.

[6] M. H. Bae, S. B. Park, H. W. Lee, S. G. Nam, and M. K. Jeong. A new extended range ultrasonic synthetic aperture tissue harmonic imaging system. In *Proc. IEEE Ultrason. Symp.*, volume 2011 IEEE INTERNATIONAL ULTRASONICS SYMPOSIUM (IUS), pages 401–404, 2012.

[7] R. T. Beyer. *Nonlinear Acoustics*. Department of the Navy, 1974.

[8] C. Bradley. Mechanisms of image quality improvement in tissue harmonic imaging. *Innovations in Nonlinear Acoustics, 17th Int. Symp. Nonlinear Acoustics*, pages 247–254, 2006.

[9] G. A. Brock-Fischer, M. D. Poland, and P. G. Rafter. Means for increasing sensitivity in non linear ultrasound systems us patent(5577505). US Patent, 1996.

[10] E. L. Carstensen, W. K. Law, N. D. McKay, and T. G. Muir. Demonstration of nonlinear acoustical effects at biomedical frequencies and intensities. *Ultrasound Med. Biol.*, 1980(6):359–368, 1980.

[11] C. S. Chapman and J. C. Lazenby. Ultrasound imaging system employing phase inversion subtraction to enhance the image. US Patent 5632277, 1997.

[12] R. Y. Chiao, L. J. Thomas, and S. D. Silverstein. Sparse array imaging with spatially-encoded transmits. In *Proc. IEEE Ultrason. Symp.*, pages 1679–1682, 1997.

[13] T. Christopher. Finite amplitude distortion-based inhomogeneous pulse echo ultrasonic imaging. *IEEE Trans. Ultrason., Ferroelec., Freq. Contr.*, 44(1):125–139, 1997.

[14] T. Christopher. Experimental investigation of finite amplitude distortion-based, second harmonic pulse echo ultrasonic imaging. *IEEE Trans. Ultrason., Ferroelec., Freq. Contr.*, 45(1):158–162, 1998.

[15] J. C. Curlander and R. N. McDonough. *Synthetic Aperture Radar: Systems and Signal Processing*. John Wiley & Sons, Inc., 1991.

[16] L. J. Cutrona, W. E. Vivian, E. N. Leith, and G. O. Hall. A high resolution radar combat-surveillance system. *IRE Trans. Mil. Elect.*, MIL-5(2):127–131, 1961.

[17] N. de Jong, R. Cornet, and C. T. Lancee. Higher harmonics of vibrating gas-filled microspheres. part one: Simulations. *Ultrasonics*, 1994(32):447–453, 1994.

[18] N. de Jong, R. Cornet, and C. T. Lancee. Higher harmonics of vibrating gas-filled microspheres. part two: Measurements. *Ultrasonics*, 1994(32):455–459, 1994.

[19] T. S. Desser, T. Jedrzejewicz, and C. B. Bradley. Native tissue harmonic imaging: Basic principles and clinical applications. *Ultrasound Quaterly*, 16:40–48, 2000.

[20] T. S. Desser, R. B. Jeffrey, M. J. Lane, and P. W. Ralls. Pictorial essay: Utility of tissue harmonic imaging in abdominal and pelvic ultrasonography. *J. Clin. Ultrasound*, 27:135–141, 1999.

[21] Y. Du, J. Rasmussen, H. Jensen, and J. A. Jensen. Second harmonic imaging using synthetic aperture sequential beamforming. In *Proc. IEEE Ultrason. Symp.*, pages 2261–2264, 2011.

[22] F. A. Duck. Nonlinear acoustics in diagnostic ultrasound. *Ultrasound Med. Biol.*, 28:1–18, 2002.

[23] F. A. Duck, A. C. Baker, and H. C. Starritt. *Ultrasound in Medicine*. Institute of Physics Publishing, 1998.

[24] C. H. Frazier and W. D. O'Brien. Synthetic aperture techniques with a virtual source element. *IEEE Trans. Ultrason., Ferroelec., Freq. Contr.*, 45:196–207, 1998.

[25] K. L. Gammelmark and J. A. Jensen. Multielement synthetic transmit aperture imaging using temporal encoding. *IEEE Trans. Med. Imag.*, 22(4):552–563, 2003.

[26] S. Gustavsson and J. Kortbek. Users guide for the beamformation toolbox ii, release 5.0. Technical report, Ørsted•DTU, Technical University of Denmark, Lyngby, Denmark, 2005.

[27] M. F. Hamilton and D. T. Blackstock. *Nonlinear Acoustics*. Academic Press, 1997.

[28] J. M. Hansen, M. C. Hemmsen, and J. A. Jensen. An object-oriented multi-threaded software beamformation toolbox. In *Proc. SPIE Med. Imag.*, volume 7968, pages 79680Y 1–9, March 2011.

[29] P. He. Simulation of ultrasound pulse propagation in lossy media obeying a frequency power law. *IEEE Trans. Ultrason., Ferroelec., Freq. Contr.*, 45(1):114–125, 1998.

[30] M. C. Hemmsen, J. M. Hansen, and J. A. Jensen. Synthetic Aperture Sequential Beamformation applied to medical imaging using a multi element convex array transducer. In *EUSAR*, page Accepted for publication, Apr. 2012.

[31] M. C. Hemmsen, M. M. Petersen, S. I. Nikolov, M. B., Nielsen, and J. A. Jensen. Ultrasound image quality assessment: A framework for evaluation of clinical image quality. In *Proc. SPIE Med. Imag.*, volume 76291, pages 76290C–12. Medical Imaging 2010: Ultrasonic Imaging, Tomography, and Therapy, 2010.

[32] V. F. Humphrey. Nonlinear propagation in ultrasonics fields: measurements, modelling and harmonic imaging. *Ultrasonics*, 38:267–272, 2000.

[33] V. F. Humphrey. Nonlinear acoustics and harmonic imaging. Short course given at the 2012 IEEE International Ultrasonics Symposium in Dresden, Germany, 2012.

[34] J. A. Jensen. Medical ultrasound imaging. *Prog. Biophys. Mol. Biol.*, 93:153–165, 2007.

[35] J. A. Jensen, M. Hansen, B. G. Tomov, S. I. Nikolov, and H. Holten-Lund. System architecture of an experimental synthetic aperture real time ultrasound system. In *Proc. IEEE Ultrason. Symp.*, pages 636–640, Oct. 2007.

[36] J. A. Jensen, H. Holten-Lund, R. T. Nielson, B. G. Tomov, M. B. Stuart, S. I. Nikolov, M. Hansen, and U. D. Larsen. Performance of SARUS: A Synthetic Aperture Real-time Ultrasound System. In *Proc. IEEE Ultrason. Symp.*, pages 305–309, Oct. 2010.

[37] J. A. Jensen, H. Holten-Lund, R. T. Nilsson, M. Hansen, U. D. Larsen, R. P. Domsten, B. G. Tomov, M. B. Stuart, S. I. Nikolov, M. J. Pihl, Y. Du, J. H. Rasmussen, and M. F. Rasmussen. SARUS: A synthetic aperture real-time ultrasound system. *IEEE Trans. Ultrason., Ferroelec., Freq. Contr.*, 60(9):1838–1852, 2013.

[38] M. Karaman, P. C. Li, and M. O'Donnell. Synthetic aperture imaging for small scale systems. *IEEE Trans. Ultrason., Ferroelec., Freq. Contr.*, 42:429–442, 1995.

[39] J. Kortbek. *Synthetic aperture sequential beamforming and other beamforming techniques in ultrasound imaging*. PhD thesis, Ørsted•DTU, Technical University of Denmark, 2800, Lyngby, Denmark, 2007.

[40] J. Kortbek, J. A. Jensen, and K. L. Gammelmark. Synthetic aperture sequential beamforming. In *Proc. IEEE Ultrason. Symp.*, pages 966–969, 2008.

[41] J. Kortbek, J. A. Jensen, and K. L. Gammelmark. Sequential beamforming for synthetic aperture imaging. *Ultrasonics*, 53(1):1–16, 2013.

[42] J. Kortbek, S. I. Nikolov, and J. A. Jensen. Effective and Versatile software Beamformation Toolbox. In *Proc. SPIE - Medical Imaging - Ultrasonic Imaging and Signal Processsing*, pages 651319,1–10, 2007.

[43] V. P. Kuznetsov. Equations of nonlinear Acoustics. *Sov. Phys. Acoust.*, 16:467–470, 1971.

[44] M. L. Li, W. J. Guan, and P. C. Li. Improved synthetic aperture focusing technique with application in high-frequency ultrasound imaging. *IEEE Trans. Ultrason., Ferroelec., Freq. Contr.*, 51(1):63–70, January 2004.

[45] T. G. Muir and E. L. Carstensen. Prediction of nonlinear acoustic effects at biomedical frequencies and intensities. *Ultrasound Med. Biol.*, 1980(6):345–357, 1980.

[46] S. I. Nikolov and J. A. Jensen. 3D synthetic aperture imaging using a virtual source element in the elevation plane. In *Proc. IEEE Ultrason. Symp.*, volume 2, pages 1743–1747, 2000.

[47] S. I. Nikolov and J. A. Jensen. Virtual ultrasound sources in high-resolution ultrasound imaging. In *Proc. SPIE - Progress in biomedical optics and imaging*, volume 3, pages 395–405, 2002.

[48] C. Passmann and H. Ermert. A 100-MHz ultrasound imaging system for dermatologic and ophthalmologic diagnostics. *IEEE Trans. Ultrason., Ferroelec., Freq. Contr.*, 43:545–552, 1996.

[49] A. D. Pierce. *Acoustics, An Introduction to Physical Principles and Applications*. Acoustical Society of America, New York, 1989.

[50] R. S Shapiro, J. Wagreich, R. B. Parsons, A. Stancato-Pasik, H. C. Yeh, and R. Lao. Tissue harmonic imaging sonography: Evaluation of image quality compared with conventional sonography. *American Journal of Roentgenology*, 171:1203–1206, 1998.

[51] C. W. Sherwin, J. P. Ruina, and D. Rawcliffe. Some early developements in synthetic aperture radar systems. *IRE Trans. Mil. Elect.*, MIL-6(2):111–115, 1962.

[52] D. H. Simpson, C. T. Chin, and P. N. Burns. Pulse inversion Doppler: a new method for detecting nonlinear echoes from microbubble contrast agents. *IEEE Trans. Ultrason., Ferroelec., Freq. Contr.*, 46(2):372–382, 1999.

[53] H. C. Starritt, F. A. Duck, A. J. Hawkins, and V. F. Humphrey. The development of harmonic distortion in pulsed finite-amplitude ultrasound passing through liver. *Phys. Med. Biol.*, 1986(31):1401–1409, 1986.

[54] H. C. Starritt, M. A. Perkins, F. A. Duck, and V. F. Humphrey. Evidence for ultrasonic finite-amplitude distortion in muscle using medical equipment. *J. Acoust. Soc. Am.*, 77:302–306, 1985.

[55] T. L. Szabo. *Diagnostic ultrasound imaging inside out*. Elsevier, 2004.

[56] F. Tranquart, N. Grenier, V. Eder, and L. Pourcelot. Clinical use of ultrasound tissue harmonic imaging. *Ultrasound Med. Biol.*, 25(6):889–894, 1999.

[57] Xander A. A. M. Verbeek, Léon A. F. Ledoux, Jean M. Willigers, Peter J. Brands, and Arnold P. G. Hoeks. Experimental investigation of the pulse inversion technique for imaging ultrasound contrast agents. *J. Acoust. Soc. Am.*, 107(4):2281–2290, 2000.

[58] B. Ward, A. C. Baker, and V. F. Humphrey. Nonlinear propagation applied to the improvement of resolution in diagnostoc medical ultrasound. *J. Acoust. Soc. Am.*, 101(1):143–154, 1997.

[59] P. J. Westervelt. Parametric acoustic array. *J. Acoust. Soc. Am.*, 35:535–537, 1963.

[60] J. Wu and J. Tong. Measurements of nonlinearity parameter b/a of contras agents. *Ultrasound Med. Biol.*, 20:195–201, 1994.

[61] D. Yun, J. Kim, and K. Y. Jhang. Imaging of contact acoustic nonlinearity using synthetic aperture technique. *Ultrasonics*, 53(2013):1349–1354, 2013.

PAPER I

Non-linear Imaging using an Experimental Synthetic Aperture Real Time Ultrasound Scanner

Joachim Rasmussen, Yigang Du, and Jørgen Arendt Jensen

Proceedings of the 15th Nordic-Baltic Conference on Biomedical Engineering and Medical Physics

Presented in Aalborg, Denmark, 2011

Non-linear Imaging Using an Experimental Synthetic Aperture Real Time Ultrasound Scanner

Joachim Rasmussen[1], Yigang Du[1,2], and Jørgen Arendt Jensen[1]

[1] Center for Fast Ultrasound Imaging, Department of Electrical Engineering, Technical University of Denmark, Kgs. Lyngby, Denmark

[2] BK Medical Aps, Mileparken 34, Herlev, Denmark

***Abstract*— This paper presents the first non-linear B-mode image of a wire phantom using pulse inversion attained via an experimental synthetic aperture real-time ultrasound scanner (SARUS). The purpose of this study is to implement and validate non-linear imaging on SARUS for the further development of new non-linear techniques. This study presents non-linear and linear B-mode images attained via SARUS and an existing ultrasound system as well as a Field II simulation. The non-linear image shows an improved spatial resolution and lower full width half max and -20 dB resolution values compared to linear B-mode imaging on the other systems. For the second scatterer at 47 mm depth the -20 dB resolution value for the non-linear SARUS image is 0.9907 mm and 1.1970 mm for the linear image from SARUS.**

***Keywords*— non-linear imaging, pulse inversion, synthetic aperture real time ultrasound scanner.**

I. Introduction

One way to improve the spatial resolution of a B-mode ultrasound image is to perform non-linear imaging. The pulse inversion (PI) technique [1] has for many years been an easy method to perform non-linear imaging. This technique acquires data in the same direction twice, where the second emitted pulse is phase shifted 180° compared to the first pulse. Adding the two received signals will cancel the 1st harmonic component of the received summed pulse due to the 180° phase shift. The 2nd harmonic component is phase shifted $2 \cdot 180°$ and will therefore add constructively and be amplified. The technique can thus isolate the 2nd harmonic component even for broad band signals.

While non-linear imaging benefits from a good spatial resolution and low side lobes, PI suffers from lower penetration depth and a loss in frame rate. At the Center for Fast Ultrasound Imaging (CFU) a new fast non-linear imaging technique aimed at solving these issues is being developed using the experimental synthetic aperture real-time ultrasound scanner (SARUS) [2]. The purpose of this paper is to document the first non-linear imaging attempts using PI on SARUS and compare the results to existing ultrasound imaging systems and simulations.

II. Pulse Inversion

In PI two consecutive waveforms, x_1 and x_2, that are identical except for a 180° phase shift are emitted [1],[3]. That is, $x_1=-x_2$ (see Fig. 1). The received signals, y_1 and y_2, contain higher order harmonics due to the non-linear propagation of sound waves in tissue. That is,

$$y_1 = a_1x_1+a_2x_1^2+\ldots \quad (1)$$

$$y_2= a_1x_2+a_2x_2^2+\ldots= a_1(-x_1)+a_2(-x_1)^2+\ldots, \quad (2)$$

where a_i are non-linear constants.

When the received waveforms, y_1 and y_2, are summed the out of phase odd number harmonics (1st, 3rd, …) cancel out while the even in phase harmonics (2nd, 4th, …) add. The amplitude of the even harmonics in the summed signal is twice that of the amplitude seen in either of the two received signals (see bottom of Fig. 2).

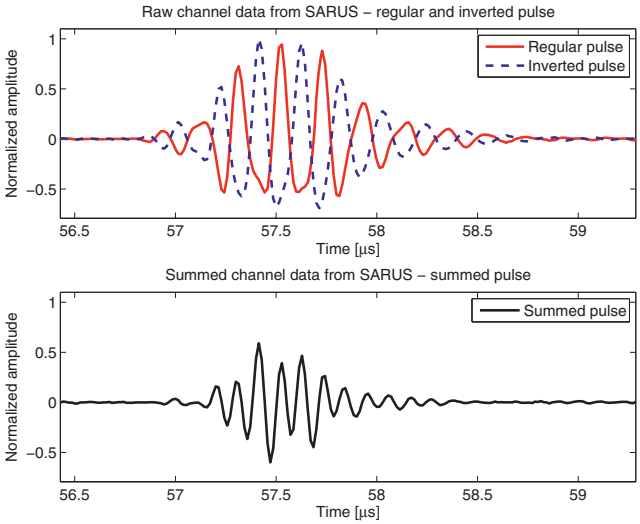

Fig. 1 Raw channel data from SARUS showing the normalized amplitude of the received regular pulse, the received inverted pulse, and the summed pulse used for PI imaging.

K. Dremstrup, S. Rees, M.Ø. Jensen (Eds.): 15th NBC on Biomedical Engineering & Medical Physics, IFMBE Proceedings 34, pp. 101–104, 2011.
www.springerlink.com

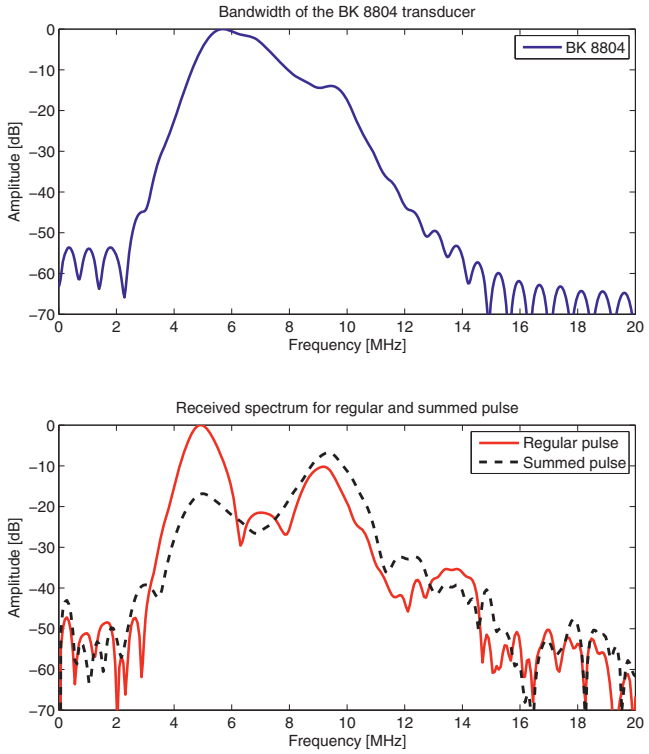

Fig. 2 Bandwidth of the BK 8804 transducer (top) and the spectrum of the received regular pulse and summed pulse (bottom). The fundamental frequency of 5 MHz is easily detected for the regular pulse as well as the 2nd harmonic component at 10 MHz. Both are well within the bandwidth of the transducer. For the summed pulse the fundamental frequency is suppressed by 17 dB while the 2nd harmonic component is enhanced by 4 dB compared to the 2nd harmonic component of the regular pulse.

III. Setup

A B-mode scan of a wire phantom using PI is performed using SARUS. Similar linear scans are performed on the ProFocus scanner from BK Medical and a Field II [4],[5] simulation of the scan is performed. The Full Width Half Max (FWHM) and -20 dB resolution values for each scatterer is measured in all images for comparison.

Transducer: A 192 element BK 8804 linear array transducer from BK Medical is used. The center frequency of this transducer is 7 MHz. Sixty-four active channels are used for both transmit and receive. Apodization for transmit is done using a Hamming function, whereas receive apodization is set to one for all 64 elements.

Phantom: A water-filled wire phantom containing 6 equidistant wires is used. The distance between each wire is 2.5 cm. The transducer is held in a fixed setup centered over the wires in the phantom with the surface of the transducer slightly submerged in water.

SARUS setup: For the SARUS scan 129 dual emissions are obtained to derive the non-linear image. The total collection of received data can be used for linear B-mode images (one for the regular pulse; one also for the inverted pulse) and one PI non-linear B-mode image (from the summed pulse).

Since the transducer of the system has a limited band width, the transmitted center frequency must be chosen such that it allows for the detection of the 2nd harmonic component in the received signal. From the bandwidth plot of the transducer in Fig. 2, a 5 MHz center frequency for the excitation pulse with a 10 MHz 2nd harmonic component is chosen. Both frequencies are well within the bandwidth of the BK 8804 transducer.

A fixed focal depth of 40 mm is used and the 64 channel received data are beam formed using the BFT3 toolbox [6].

ProFocus scanner setup: Twenty consecutive B-mode scans using 129 emissions with a 7 MHz center frequency are obtained using the ProFocus system from BK Medical. A fixed focal depth of 40 mm is set for all scans.

Field II setup: A simulation of a B-mode scan of the phantom is obtained using Field II with a 70 MHz sampling frequency, 5 MHz center frequency, 129 emissions, and a 40 mm fixed focal depth.

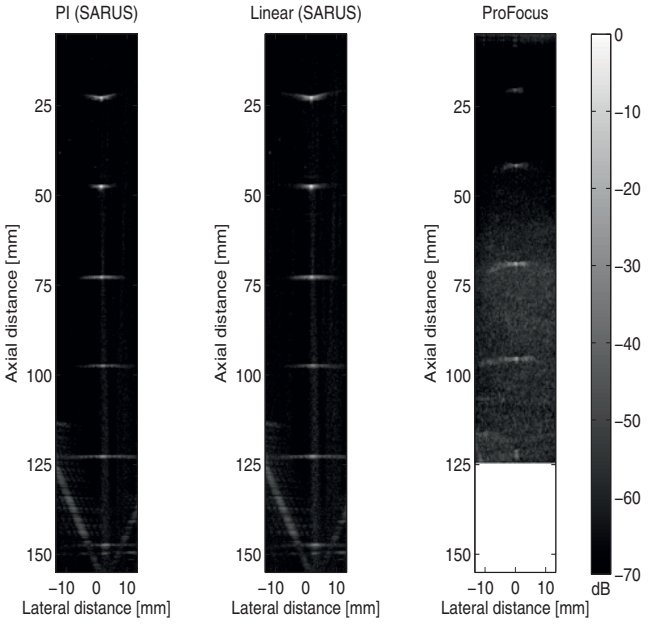

Fig. 3 B-mode images obtained from SARUS. Left shows the non-linear B-mode image of the wire phantom created via PI. Middle shows the same image obtained via linear B-mode imaging. Right shows the B-mode image obtained using the ProFocus scanner. Note that the ProFocus image depth is only 125 mm.

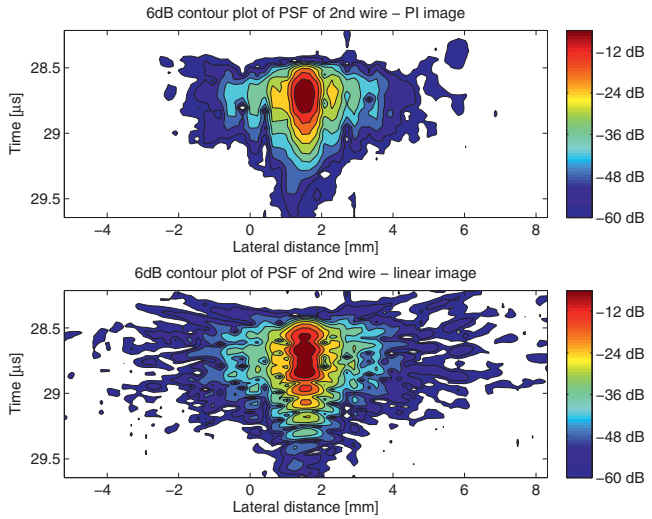

Fig. 4 Six dB contour plot of the PSF around the 2nd wire. Top shows the PSF for the non-linear PI B-mode image, bottom shows the PSF for the linear B-mode image.

IV. Results

B-mode images are obtained from all scans and from the Field II simulation. Fig. 3 shows the non-linear B-mode image from the PI scan, the linear B-mode image from a linear scan on the SARUS system, and a linear B-mode image from the ProFocus system. All 6 wires in the phantom are detectable in both the SARUS images as well as the structure of the bottom of the phantom at 150 mm depth. The ProFocus image depth is only 125 mm due to the settings on the system. Consequently, only the first 5 wires are seen and the bottom of the phantom can only just be perceived.

The point spread functions (PSF) for both the PI signal and the regular linear signal from the SARUS images around the 2nd wire in the phantom are shown in Fig. 4. In this figure it is clearly seen that the spatial resolution in the PI B-mode image is improved compared to the linear B-mode image. The PSF for the 2nd harmonic pulse has more narrow side lobes than the linear fundamental pulse.

Another quantitative measure for the spatial resolution of the B-mode image is the FWHM and -20 dB resolution values for each of the wires as shown in Fig. 5. From the top view of Fig. 5 it is seen that both SARUS imaging modalities have almost same FWHM values for all depths. The ProFocus system, however, has a lower FWHM resolution value than any of the other imaging system for the 4th wire indicating a better spatial resolution at this point.

In the bottom view of Fig. 5 it is seen that both imaging modalities on the SARUS system and the Field II simulation have generally lower -20 dB resolution values than the ProFocus system indicating an overall better spatial resolution. Especially at the 1st and 5th wire the ProFocus system is outperformed by all of the other imaging modalities. Furthermore, it is seen that SARUS PI and SARUS linear imaging have almost same resolution values except at the 4th and 6th wire where PI has lower -20 dB resolutions. At the 3rd wire the -20dB resolution of both SARUS modalities is lower than both Field II and ProFocus and at the 6th wire SARUS PI outperforms all other modalities.

On close inspection of the second wire at 47 mm depth, close to the focal point, the FWHM value of the non-linear SARUS image is found to be 0.7017 mm and the -20 dB resolution value to be 0.9907 mm. In comparison the FWHM of the linear SARUS image is 0.6604 mm and 1.1970 mm. These values indicate that although linear SARUS has lower FWHM value than non-linear SARUS, the shape of the PSF of the non-linear SARUS scatterer has more narrow side lobes due to the lower -20 dB resolution value. This is further verified by the PSF plot in Fig. 4 which also shows an improved spatial resolution of the non-linear image.

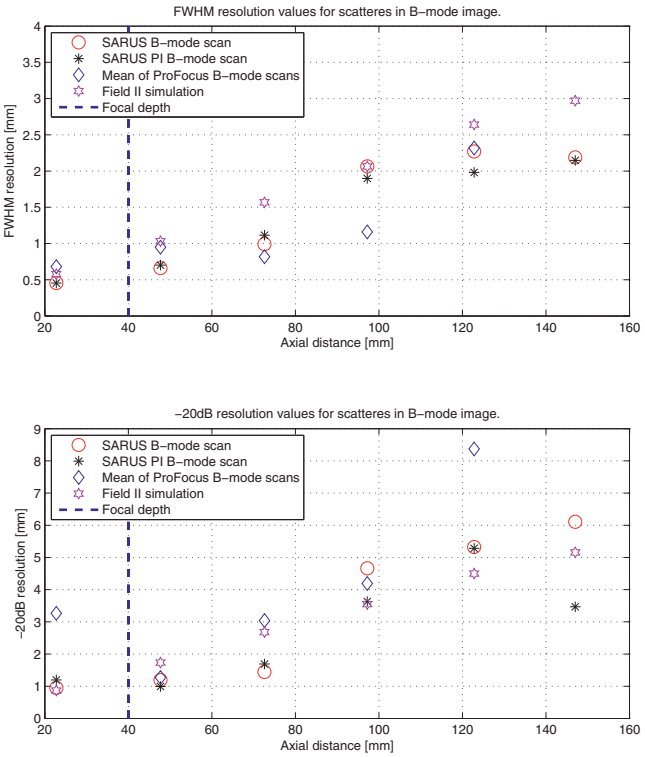

Fig. 5 FWHM (top) and -20 dB (bottom) resolution values for each wire in the phantom obtained using different imaging systems. Values for linear SARUS B-mode, PI SARUS B-mode, linear ProFocus, and Field II imaging are shown. Notice that only the first 5 wires of the phantom were imaged using the ProFocus system.

V. Discussion

From the results in Fig. 5 it is seen that the imaging modalities on SARUS generally has lower -20 dB resolution values than the ProFocus system. The very high -20 dB resolution values for the 1st and 5th wire in the ProFocus image could indicate a poor spatial resolution of the wire. While this is the case for the 5th wire the spatial resolution of the 1st wire in the image is in fact not as bad as indicated. This is due to the shape of the PSF around the 1st wire. Here the PSF takes a very pointy appearance with a very high maximum value and steep slopes, but with very wide low-level side lobes. This leads to a high -20 dB resolution value while the spatial resolution remains good. Accordingly, had the PSF taken the appearance of a hump with low maximum value, but with narrow side lobes, the -20 dB resolution value would be lower but the spatial resolution poor. When determining the spatial resolution of an imaging modality the FWHM and -20dB resolution values cannot be used alone, but must be compared to the actual image of the scanning before conclusions can be made.

Both SARUS imaging modalities have low FWHM and -20 dB resolution values compared to both Field II and ProFocus. In addition, in close comparison of the two SARUS B-mode images in Fig. 3, it is seen that the spatial resolution of the wires in the non-linear B-mode image is better than in the linear B-mode image. The low attenuation in the images is a result of the water filled phantom that is used. Had the phantom been filled with a substance that mimics human tissue, the attenuation would have made detection of deep wires harder.

VI. Pros and cons for non-linar imaging

While non-linear imaging using PI has the benefits of improved spatial resolution and low side lobes, it also has some drawbacks. First of all, two emissions need to be received in order to derive the summed pulse used in PI. This reduces the frame rate of the imaging system by a factor 2 compared to linear B-mode imaging. The dual emissions also increase the amount of data the processor of the imaging system must be able to handle without further loosing frame rate. The loss of frame rate could prove very disadvantageous, if the scan is made on non-stationary tissues. Here any tissue motion may lead to a phase change in the paired received signals severely reducing the 2nd harmonic component of the summed pulse.

Secondly, the transducer must function optimally over a broad spectrum to be able to transmit and receive a maximum energy at the fundamental and 2nd harmonic center frequency. If there is an energy loss at either frequencies the signal to noise ratio (SNR) in the image will decrease.

Thirdly, the attenuation of the 2nd harmonic signal is much higher than the attenuation of the fundamental signal. This is because only a fraction of the transmitted signal is converted to the 2nd harmonic component. Further, the attenuation is proportional in dB to the frequency of the signal leading to a higher attenuation of the 2nd harmonic component compared to the fundamental wave. In all this leads to a much lower SNR of the 2nd harmonic component.

VII. Conclusion

Non-linear B-mode imaging has successfully been accomplished using SARUS. The spatial resolution of the image is determined to be better than both the linear B-mode image from SARUS, the B-mode images from the ProFocus system, and from the Field II simulation.

Acknowledgement

This work was supported by grant 024-2008-3 from the Danish Advanced Technology Foundation and BK Medical Aps, Denmark.

References

1. Chapman C S and Lazenby J C (1997) Ultrasound imaging system employing phase inversion subtraction to enhance the image. Official Gazette of the United States Patent and Trademark Office Patents, Vol. 1198, Issue 4, pp. 2249.
2. Jensen J A, Tomov B G, Nikolov S I, Hansen M and Holten-Lund H (2007) System architecture of an experimental synthetic aperture real-time ultrasound system. Proceedings IEEE Ultrasonics Symposium, 2007, pp. 636-640.
3. Jiang P, Mao Z and Lazenby J C (1998) A new tissue harmonic imaging scheme with better fundamental frequency cancellation and higher signal-to-noise ratio. Proceedings IEEE Ultrasonics Symposium, 1998, Vol. 2, pp. 1589-1594.
4. Jensen J A (1996) Field: A program for simulating ultrasound systems. 10th Nordic-Baltic Conference on Biomedical Imaging vol. 4 supplement 1, part 1:351-353.
5. Jensen J A and Svendsen N B (1992) Calculation of pressure fields from arbitrarily shaped, apodized, and excited ultrasound transducers. IEEE Trans. Ultrason., Ferroelec., Freq. Contr., 39:262-267.
6. Hansen J M, Hemmsen M C and Jensen J A (2011) An object-oriented multi-threaded software beam formation toolbox. SPIE, Medical Imaging, Ultrasonic Imaging and Signal Processing, 2011.

Corresponding author: Joachim Rasmussen
Institute: Technical University of Denmark
Street: Oersteds Plads 349
City: Kgs. Lyngby
Country: Denmark
Email: jr@elektro.dtu.dk

PAPER II

Third Harmonic Imaging using Pulse Inversion

Joachim Rasmussen, Yigang Du, and Jørgen Arendt Jensen

Proceedings of the IEEE International Ultrasonics Symposium

Presented in Orlando, Florida, United States, 2011

10.1109/ULTSYM.2011.0563

Third Harmonic Imaging using Pulse Inversion

Joachim Hee Rasmussen, Yigang Du and Jørgen Arendt Jensen
Center for Fast Ultrasound Imaging, Dept. of Elec. Eng. Bldg. 349,
Technical University of Denmark, DK-2800 Kgs. Lyngby, Denmark

***Abstract*—The pulse inversion (PI) technique can be utilized to separate and enhance harmonic components of a waveform for tissue harmonic imaging. While most ultrasound systems can perform pulse inversion, only few image the 3rd harmonic component. PI pulse subtraction can isolate and enhance the 3rd harmonic component for imaging on any ultrasound system capable of PI. PI was used to perform 3rd harmonic B-mode scans of a water-filled wire phantom on an experimental ultrasound system. The 3rd harmonic scans were compared to fundamental and 2nd harmonic scans on the same system. The 3rd harmonic image showed a 46% improvement in the lateral FWHM resolution compared to fundamental B-mode imaging at 75 mm depth and a 28% improvement compared to 2nd harmonic B-mode imaging. The axial FWHM resolution was improved by 35% and 30% for 3rd harmonic imaging compared to fundamental and 2nd harmonic imaging respectively. The improvements in spatial resolution and the fact that PI can isolate the 3rd harmonic suggest that it is advantageous to implement 3rd harmonic imaging on ultrasound systems capable of PI.**

I. Introduction

Tissue harmonic imaging is a technique widely used in commercial ultrasound systems to improve spatial resolution. In harmonic B-mode imaging, however, an overlap is often seen between the harmonic components in the received RF signal, making separation of a single harmonic band difficult. The harmonics are often hidden in the spectrum by overlaps between neighboring harmonics, sum and difference harmonics, and noise. Contributions from neighboring harmonics could therefore, be included in the harmonic B-mode image even after filtration, thus degrading the spatial resolution of the final harmonic image. Pulse inversion (PI) [1][2] can be used to suppress the neighboring harmonic components for a more efficient isolation of a specific harmonic. Ultrasound systems today employ PI but use this often only to image the 2nd harmonic component. PI however, is fully capable of isolating the 3rd harmonic component on the ultrasound system. The purpose of this paper is to perform 3rd harmonic imaging on an ultrasound system capable of PI and investigate whether 3rd harmonic imaging is advantageous over 2nd harmonic and fundamental imaging.

II. Theory

A. Pulse Inversion

A PI technique can be used to isolate and enhance the 2nd and 3rd harmonics from their neighboring harmonic components. In this technique two pulses (regular pulse, $180°$ phase shifted pulse) are transmitted in turn. While a $180°$ phase shift can be detected for the fundamental component of the received signal a corresponding $360°$ and $540°$ phase shift can be seen for the 2nd and 3rd harmonic components respectively [3][4]. To suppress the odd order harmonics each correlated pair (regular and phase shifted) of the received responses are summed. Harmonic components that are in phase (all even harmonics) will double in amplitude, while out of phase components (all odd harmonics) will cancel out (see Fig. 1). This separates and enhances the 2nd harmonic component, which in turn then can be filtered and used for imaging. To suppress the even order harmonics the pairs of received responses are subtracted, thus causing all odd harmonics to double in amplitude and even harmonics to cancel out. In this manner the 3rd harmonic component can be isolated and enhanced for imaging.

B. Waveform Bandwidth

The bandwidth of the transmitted pulse can also be used to reduce overlap between the harmonic components. When transmitting a pulse with a narrow bandwidth the harmonic components are more easily separable compared to wide bandwidth transmit waveforms [4][5]. The disadvantage in using narrow bandwidth waveforms is that the axial resolution is reduced [3][6]. The task is therefore, to weight the importance of a good separation of harmonics over changes in axial resolution when selecting a waveform bandwidth.

III. Experimental Setup

A B-mode scan of a wire phantom is performed by PI on an experimental synthetic aperture real-time ultrasound system (SARUS) [7][8]. This scanner is capable of performing PI and 2nd harmonic imaging [9] and is therefore also capable of performing 3rd harmonic imaging. SARUS is used to record raw channel data from a commercially available 192 element convex transducer (BK8820e). Images are made for purely linear B-mode, 2nd harmonic B-mode, and 3rd harmonic B-mode of a water filled wire phantom. The phantom contains 6 equidistant wires spaced 25 mm apart. The transducer is held in a fixed position centered over the wires in the phantom with the surface of the transducer slightly submerged in water. Sixty-five active channels in a sliding aperture are used for transmit and 192 channels for receive. Apodization in both transmit and receive is set to be a Hamming function. A fixed focal depth of 65 mm is used - this is also the elevation focus of the convex transducer. For each position of the aperture two emissions, one regular and one inverted are performed. In total 32 dual emissions are recorded for each frame in

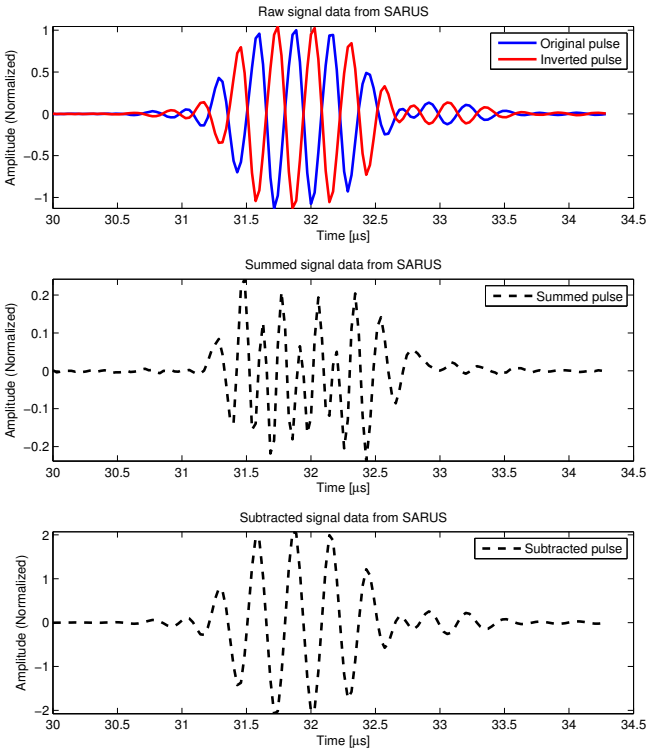

Figure 1. Data received from SARUS. Top plot shows the received pulses (normal and inverted). Middle plot shows the resulting pulse after pulse summation. Bottom plot shows the resulting pulse after pulse subtraction. All data have been normalized to the original pulse in the top plot.

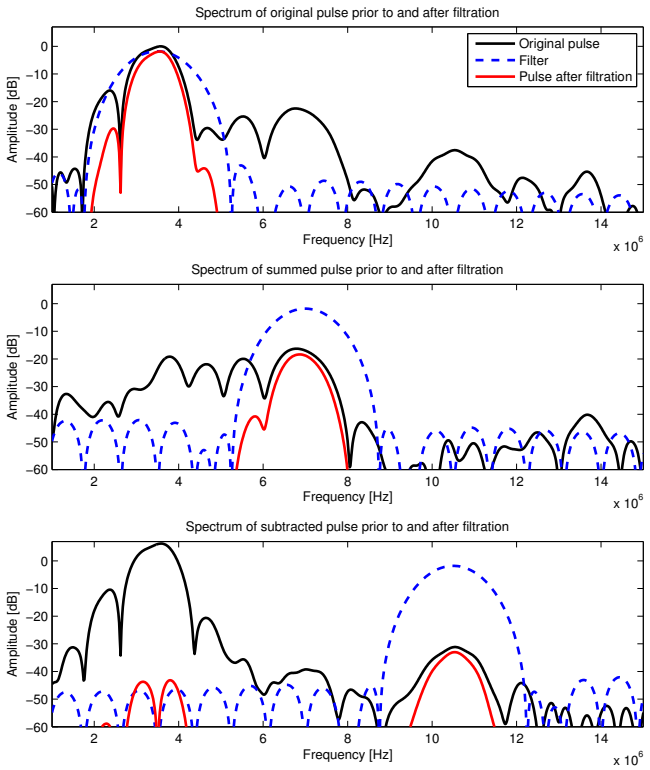

Figure 2. Spectrum of received RF signals. Top figure shows the spectrum of the fundamental signal prior to and after matched filtration. Middle shows the summed pulse used for 2nd harmonic imaging before and after filtration. Bottom figure shows the subtracted pulse used in 3rd harmonic imaging before and after matched filtering.

the image. The collection of data in a frame can be used for two regular B-mode images (one for the regular pulse; one also for the inverted pulse), one 2nd harmonic B-mode image (from the summed pulse), and one 3rd harmonic B-mode image (from the subtracted pulse). The Full Width at Half Maximum (FWHM (-6 dB)) and the Full Width at One Tenth Maximum (FWOTM (-20 dB)) values of the scatterers in the image are measured for fundamental, 2nd harmonic, and 3rd harmonic imaging and the values are compared.

Since the transducer of the system only has a limited 2-way frequency response the center frequency of the transmitted signal must be chosen such that it allows for the detection of both the 2nd and 3rd harmonic component in the received signal. On the other hand, the center frequency must also be chosen such that the transducer is able to transmit enough energy to induce the non-linear response. In this case a center frequency of 3.5 MHz for the 4 cycle excitation pulse is set. This means that the 2nd and 3rd harmonic components will be found at 7 MHz and 10.5 MHz respectively. All data is filtered using a matched filter having the same peak frequency as the harmonic component at hand. Image data is then beamformed using the Beamformation Toolbox 3 (BFT3) [10].

IV. Results

The amplitude spectrum of the received waveforms in Fig. 2 shows the harmonic components in the original pulse at 3.5 MHz, 7 MHz, and 10.5 MHz as predicted. The pulse summation reduces the fundamental and 3rd harmonic components and enhances the 2nd harmonic component. The pulse subtraction reduces the 2nd harmonic while enhancing the fundamental and 3rd components. The blue dashed line in Fig. 2 shows the amplitude of the matched filter used to separate the harmonic component.

Fig. 3 shows the 3rd harmonic B-mode image of the first 4 wires of the phantom after scanline conversion. Because only a fraction of the transmitted energy is converted into 3rd harmonic energy, the signal to noise ratio (SNR) is low compared to e.g. fundamental B-mode imaging [6]. However, in spite of the lower SNR the 4 wires are clearly seen in the B-mode image. Fig. 4 shows the point spread functions (PSF) of the linear, 2nd, and 3rd harmonic components for the 3rd wire in the phantom (at 75 mm depth). From this plot it is seen that the side lobe energy decreases for 2nd and 3rd harmonic imaging and that the main lobe of the PSF is much narrower for the harmonic components compared to the fundamental component. The FWHM and FWOTM values for the first 3 wires in the phantom are measured and shown in Table I and Table II. The tables show that lateral FWHM for

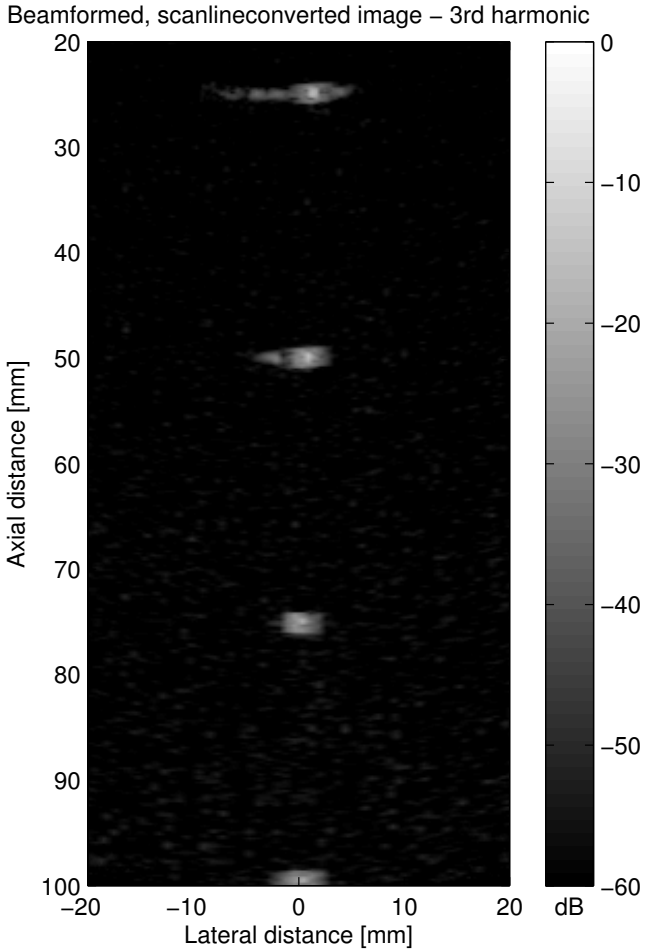

Figure 3. 3rd harmonic B-mode image of the wire phantom using the convex transducer. The image has 60 dB dynamic range.

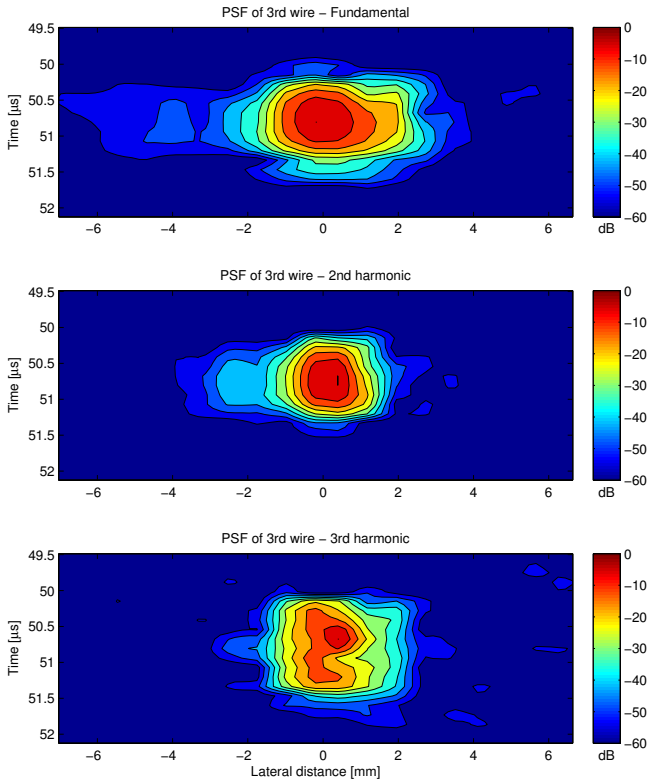

Figure 4. The point spread functions (PSF) of the fundamental pulse (top), 2nd harmonic pulse (middle), and 3rd harmonic pulse (bottom). The PSFs are displayed with 6dB contour lines.

the 3rd harmonic component is lower than FWHM for both fundamental and 2nd harmonic components. Third harmonic axial FWHM is only reduced for the 3rd wire in the phantom. The lateral FWOTM values for the 3rd harmonic component are lower than those for the fundamental component but only the value for the first wire is lower than the value of the 2nd harmonic component. For the axial FWOTM values the 3rd harmonic component shows no improvement compared to the other imaging methods.

V. Discussion

The reduction in the FWHM and FWOTM values seen for the harmonic components in Table I and Table II show that the spatial resolution is improved. There is a 46% reduction in the lateral FWHM resolution between the fundamental and 3rd harmonic components at 75 mm depth and a 28% reduction in the lateral FWHM resolution between the 2nd and 3rd harmonic components at that same depth. The axial FWHM

Table I
FWHM values for wires at 25 mm, 50 mm, and 75 mm depth.

Depth	Direction	Fundamental	2nd harmonic	3rd harmonic
25 mm	Lateral [mm]	2.19	1.25	0.86
	Axial [mm]	0.94	0.86	0.98
50 mm	Lateral [mm]	2.70	1.21	0.70
	Axial [mm]	0.94	0.94	1.02
75 mm	Lateral [mm]	2.03	1.52	1.09
	Axial [mm]	1.02	0.94	0.66

Table II
FWOTM values for wires at 25 mm, 50 mm, and 75 mm depth.

Depth	Direction	Fundamental	2nd harmonic	3rd harmonic
25 mm	Lateral [mm]	4.22	2.19	1.72
	Axial [mm]	1.48	1.29	2.54
50 mm	Lateral [mm]	4.61	2.07	3.24
	Axial [mm]	1.45	1.41	1.99
75 mm	Lateral [mm]	4.53	2.46	3.40
	Axial [mm]	1.48	1.48	2.34

resolution for the 3rd harmonic component is reduced by 35% and 30% compared to the fundamental and 2nd harmonic components respectively. The increase in 3rd harmonic axial FWOTM results from the bandwidth of the matched filter that is used prior to imaging. It is necessary to choose a filter with a bandwidth that is capable of isolating the individual harmonics while still attaining a low axial resolution. In this specific case the bandwidth of the filter was chosen such that there was no harmonic overlap between the 2nd and 3rd harmonics and the axial FWHM resolution changed as little as possible compared to fundamental and 2nd harmonic axial FWHM resolution.

Since the results show that 3rd harmonic imaging does improve the lateral resolution compared to both fundamental and 2nd harmonic imaging, it could prove advantageous to implement 3rd harmonic imaging on ultrasound systems capable of PI. The only changes needed on the 2nd harmonic PI systems is a pulse subtraction technique. By this simple method the system could perform both 2nd and 3rd harmonic imaging from the same set of RF data.

While harmonic imaging using PI has the benefits of improved spatial resolution and low side lobes, PI also has some drawbacks. First of all, two emissions need to be received for every image line to derive the summed and subtracted pulses used in PI. This reduces the frame rate of the imaging system by a factor of 2 compared to linear B-mode imaging. The dual emissions also increase the amount of data the processor of the imaging system must be able to handle without further loosing frame rate. The loss of frame rate could prove very disadvantageous, if the scan is made on non-stationary tissues. Here any tissue motion may lead to a phase change in the paired received signals and severely reduce the harmonic components of the summed and subtracted pulses. Secondly, the transducer must function optimally over a broad spectrum to be able to transmit and receive a maximum energy at the fundamental, 2nd harmonic, and 3rd harmonic center frequency. If there is an energy loss at either frequencies the signal to noise ratio (SNR) in the image will radically decrease reducing the penetration depth of the harmonic component. Since the attenuation of the harmonic components also is much higher than that of the fundamental component the importance of selecting the optimal center frequency is imperative.

VI. Conclusion

Third harmonic B-mode imaging has successfully been accomplished using SARUS. The lateral resolution of the 3rd harmonic image is determined to be higher than that of 2nd harmonic and fundamental B-mode imaging.

VII. Acknowledgements

This work was supported by grant 024-2008-3 from the Danish Advanced Technology Foundation and BK Medical Aps, Denmark.

References

[1] C. S. Chapman and J. C. Lazenby, "Ultrasound imaging system employing phase inversion subtraction to enhance the image," *US Patent*, vol. 5632277, 1997.

[2] D. H. Simpson, C. T. Chin, and P. N. Burns, "Pulse inversion Doppler: a new method for detecting nonlinear echoes from microbubble contrast agents," *IEEE Trans. Ultrason., Ferroelec., Freq. Contr.*, vol. 46, no. 2, pp. 372–382, 1999.

[3] J. A. Jensen, "Medical ultrasound imaging," *Progress in Biophysics and Molecular Biology*, vol. 93, pp. 153–165, 2007.

[4] M. A. Averkiou, "Tissue harmonic imaging," in *Proc. IEEE Ultrason. Symp.*, vol. 2, 2000, pp. 1563–1572.

[5] C. Shen and P. Li, "Harmonic leakage and image quality degradation in tissue harmonic imaging," *IEEE Trans. Ultrason., Ferroelec., Freq. Contr.*, vol. 48, pp. 728–736, 2001.

[6] A. Bouakaz and N. de Jong, "Native tissue imaging at superharmonic frequencies," *IEEE Trans. Ultrason., Ferroelec., Freq. Contr.*, vol. 50, pp. 496–506, 2003.

[7] J. A. Jensen, M. Hansen, B. G. Tomov, S. I. Nikolov, and H. Holten-Lund, "System architecture of an experimental synthetic aperture real time ultrasound system," in *Proc. IEEE Ultrason. Symp.*, Oct. 2007, pp. 636–640.

[8] J. A. Jensen, H. Holten-Lund, R. T. Nielson, B. G. Tomov, M. B. Stuart, S. I. Nikolov, M. Hansen, and U. D. Larsen, "Performance of SARUS: A Synthetic Aperture Real-time Ultrasound System," in *Proc. IEEE Ultrason. Symp.*, Oct. 2010, pp. 305–309.

[9] J. Rasmussen, Y. Du, and J. A. Jensen, "Non-linear imaging using an experimantal synthetic aperture real time ultrasound scanner," *IFMBE Proceedings*, vol. 34, pp. 101–104, 2011.

[10] J. M. Hansen, M. C. Hemmsen, and J. A. Jensen, "An object-oriented multi-threaded software beam formation toolbox," in *Proc. SPIE - Medical Imaging - Ultrasonic Imaging and Signal Processsing*, vol. 7968, 2011, p. 79680Y.

PAPER III

Implementation of Tissue Harmonic Synthetic Aperture Imaging on a Commercial Ultrasound System

Joachim Hee Rasmussen, Martin Christian Hemmsen,
Signe Sloth Madsen, Peter Møller Hansen,
Michael Bachmann Nielsen, and Jørgen Arendt Jensen

Proceedings of the IEEE International Ultrasonics Symposium

Presented in Dresden, Germany, 2012

10.1109/ULTSYM.2012.0030

Implementation of Tissue Harmonic Synthetic Aperture Imaging on a Commercial Ultrasound System

Joachim Hee Rasmussen[a], Martin Christian Hemmsen[a], Signe Sloth Madsen[b], Peter Møller Hansen[b], Michael Bachmann Nielsen[b], and Jørgen Arendt Jensen[a]

[a]Center for Fast Ultrasound Imaging, Dept. of Elec. Eng., Bldg. 349, Technical University of Denmark, DK-2800 Kgs. Lyngby, Denmark
[b]Department of Radiology, Rigshospitalet, DK-2100 Copenhagen, Denmark

***Abstract*—This paper presents an imaging technique for synthetic aperture (SAI) tissue harmonic imaging (THI) on a commercial ultrasound system. Synthetic aperture sequential beamforming (SASB) is combined with a pulse inversion (PI) technique on a commercial BK 2202 UltraView system. An interleaved scan sequence that performs dynamic receive focused (DRF) imaging and SASB, both using PI, is implemented. From each acquisition four images can be created: DRF image, SASB image, tissue harmonic DRF image (DRF-THI), and tissue harmonic SASB image (SASB-THI). For SASB imaging, a fixed transmit and receive focus at 80 mm and an F# of 3 is applied. For DRF imaging, default scanner settings are used, which are a focus at 85 mm and F# of 5.7 in transmit and a dynamic receive aperture with an F# of 0.8. In all cases a 2.14 MHz one-and-a-half cycle excitation transmit waveform is used. A BK 8820e 192 element convex array transducer is used to conduct scans of wire phantoms. The -6 dB and -20 dB lateral resolution is measured for each wire in the phantom. Results show that the -6 dB lateral resolution for SASB-THI is as good as for DRF-THI except at the point of the virtual source. SASB-THI even shows 7% reduction in -6 dB lateral resolution for the deepest wire at 100 mm. The -20 dB resolution for SASB-THI at [25, 50, 75, 100] mm was reduced by [5, 0 -34, 11] % compared to DRF-THI, which shows, that except for the point of the virtual source, the lateral resolution was improved by SASB-THI. A successful implementation of SASB-THI was achieved on a commercial system, which can be used for future pre-clinical trials.**

I. Introduction

In ultrasound B-mode imaging, several techniques to improve spatial resolution have been developed over the past decades. Tissue harmonic imaging has long been used to image difficult regions with an increased contrast and resolution. One of the most common THI techniques is the pulse inversion (PI) scheme, which is implemented in many ultrasound systems today. The PI technique can be combined with a variety of focusing techniques. One focusing technique, that obtains high and depth independent spatial resolution is synthetic aperture imaging (SAI). This paper presents an imaging technique for synthetic aperture tissue harmonic imaging (SAI-THI) on a commercial ultrasound system. A parameter study is presented which shows the optimal positions for focal depth and F# for SAI-THI. Furthermore, a comparison of the spatial resolution between SAI-THI and a common THI technique is presented. Finally, a simultaneously acquired in-vivo image using the two techniques is presented and compared.

II. Theory

A. Pulse Inversion

In THI the purpose is to image a single harmonic component of a pulse response, instead of the fundamental component. A PI technique can be used to isolate the 2nd harmonic component from its neighboring harmonic components and enhance it [1], [2]. In this technique two pulses (regular pulse, 180° phase shifted pulse) are transmitted in turn. While a 180° phase shift can be detected for the fundamental component of the received signal, a corresponding 360° and 540° phase shift can be seen for the 2nd and 3rd harmonic components respectively [3], [4]. To suppress the odd order harmonics, each correlated pair (regular and phase shifted) of the received responses are summed. Harmonic components that are in phase (all even harmonics) will double in amplitude, while out of phase components (all odd harmonics) will cancel out (see Fig. 1). This separates and enhances the 2nd harmonic component, which in turn then can be filtered and used for imaging.

B. Synthetic Aperture Sequential Beamforming

Traditionally, SAI utilizes only one active transducer element in transmit. Because the transmitted acoustic energy in this case is very low, SAI is not capable of producing harmonic components for THI. Synthetic aperture sequential beamforming (SASB) is a SAI technique, which uses virtual sources and a dual stage beamforming approach to significantly reduce the computational load compared to SAI [5], [6]. A fixed transit and receive focal point is used in the first stage beamformer to create a set of focused scan lines. Each image point is potentially represented in several scan lines and can be used to improve resolution (see Fig. 2). The second stage beamformer combines the contributing first stage scan lines into an image, which has higher and more depth independent

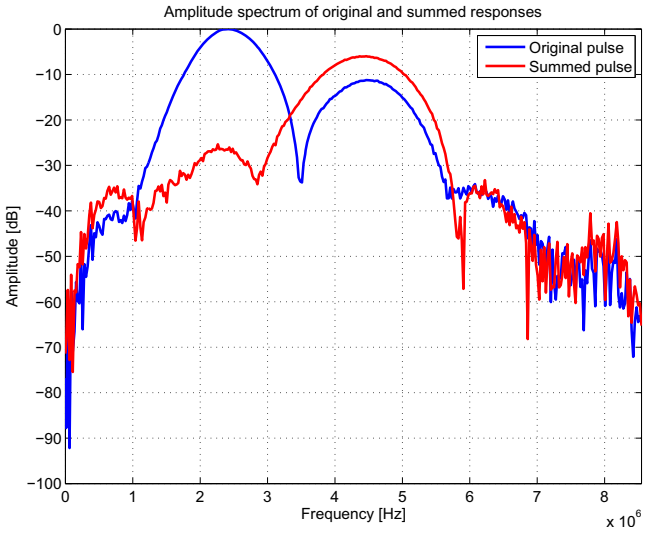

Figure 1. Spectrum of received RF signals. The blue curve shows the spectrum of a received response, while the red curve shows the spectrum after pulse summation with the inversed response. The 2nd harmonic component at 4.24 MHz is enhanced by approximately 6 dB, while the fundamental component at 2.14 MHz is attenuated by approximately 25 dB.

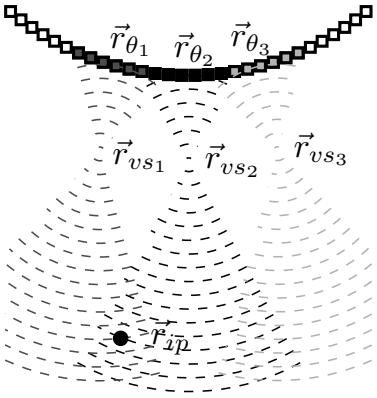

Figure 2. Three emissions for first stage SASB. A scan line is created with reference $r\theta$ and a virtual source at r_{vs} in each emission. The dotted lines show the image information at spatial positions that are found in each focused scan line. A single image point, r_{ip} may be represented in several focused scan lines as shown by the black dot. The second stage beamformer determines which scan lines contain information from the same point and sums the contributions into one image. Figure taken from [6]

lateral resolution (see Fig. 3). The advantage of SASB, besides the improvements in lateral resolution, is that the transmitted acoustic energy is sufficient to produce harmonic components for THI [7]. A combination of SASB and THI can therefore be implemented on a commercial ultrasound system.

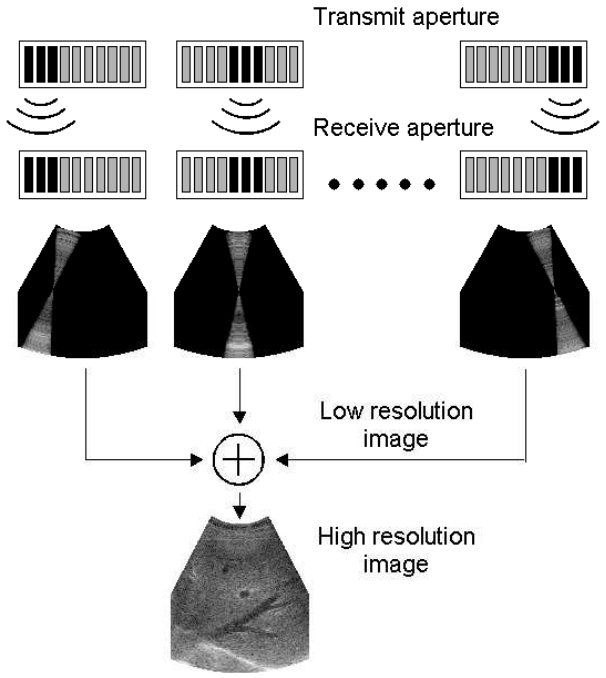

Figure 3. Schematic illustration of the dual stage beamformer. A number of acquisitions using fixed focus in transmit and receive are obtained. The received responses are beamformed along the scan line direction using the delay profile used in transmit (first stage beamforming). The resulting image data is then beamformed again (second stage beamforming) using a focus at each pixel in the image. This produces a set of low resolution images which are then summed coherently to form a single high resolution image. Figure taken from [6]

III. Tissue Harmonic Synthetic Aperture Imaging on Commercial Ultrasound System

A tissue harmonic SASB (SASB-THI) scan sequence is implemented on a commercial ultrasound system. A BK 2202 UltraView ultrasound system (UltraView) is equipped with a research interface that allows the user to adjust and control many scan parameters such as focal depth, F#, excitation waveform, etc. The research interface also allows the user to access and extract image IQ-data. The system has a collection of pre-defined settings for different imaging techniques. The default imaging technique, when conducting abdominal scans, is dynamic receive focusing tissue harmonic imaging (DRF-THI). This technique is used as a golden standard to compare SASB-THI against. In this case, the research interface is used to conduct a PI scan sequence using both DRF and SASB imaging simultaneously and extract DRF beamformed and SASB first stage image data. A 192 element BK 8820e convex array transducer is used. The default settings for DRF and DRF-THI can be found in Table I. A fixed focus is used for SASB for both transmit and receive, while an expanding aperture is used for DRF imaging. Transmit apodization for SASB and DRF is a Boxcar, while receive apodization is a Gauss for both. A total of 192 image lines each with two emissions (one for each PI pulse) is made for both SASB and DRF imaging. The scan sequence is such that 2x192 emissions

are made first for every scan line for SASB with the PI emissions interleaved. Next, a second set of 2x192 emissions are made for all DRF scan lines. This ensures minimum tissue movement between the PI emissions. A one-and-a-half cycle excitation pulse with center frequency of 2.14 MHz is used for both techniques. The collection of data acquired in one frame can be used for two linear B-mode images (one using SASB; one using DRF) and two 2nd harmonic B-mode images (SASB-THI and DRF-THI)

A. Parameter Study

A series of experiments is conducted in order to determine the optimal position of the focal point and value of the F# for SASB-THI. Measurements of the lateral resolution and point spread functions are conducted using SASB-THI on a water filled phantom with 6 equidistant wires. The focal points are varied from 50-120 mm in steps of 10 mm and the F# from 1.0-5.0 in steps of 0.5. For each combination of settings the -6 dB lateral resolution (FWHM) is measured and plotted as function of depth for each applied F#. Fig. 4 shows the measured FWHM values for each wire for every applied F# at 80 mm focal depth. The plot can be used to determine which focal depth and which F# can produce the best lateral resolution. The best lateral resolution is found where the FWHM values are low (good lateral resolution) and do not vary much with depth (depth independent lateral resolution). As seen from Fig. 4, the FWHM generally increases more with image depth as the F# increases. An F# of 2 produces the lowest and most constant scores of FWHM in this plot and could potentially be the best F# at this focal depth. However, the level of side lobes must also be taken into account when choosing a low F#.

Fig. 5 shows the point spread functions at 65 mm depth in the wire phantom for different F# 's. It is seen from the plots that the value of F# has great influence on the shape of the PSF. A low F# results in narrow main lobe with high levels of side lobes, while a high F# results in more wide main lobe and no side lobes. This is because the F# determines the width of the apodization curve applied in transmit and receive. In transmit, the apodization curve is always a Boxcar, while in receive, a Gauss curve is used. When a low F# is applied, the Gauss apodization curve that is used in receive, exceeds the actual width of the active aperture causing the edges of the Gauss curve to be cut off. In case of a very low F#, a greater part of the Gauss curve is cut off, causing the apodization curve to take the shape of a square or Boxcar, resulting in higher levels of side lobes. At higher values of the F# , the Gauss apodization curve fits the active aperture and side lobes are reduced. The difference is clearly seen in the top and bottom plot of Fig. 5, where F#'s are 1.0 and 5.0 respectively. In the top plot, the PSF has a very narrow main lobe, but also has distinct side lobes, while the PSF in the bottom has a wider main lobe, and no side lobes. The PSF for F# of 3.0 is shown in the middle plot of Fig. 5. Here, a compromise between main lobe width and levels of side lobes has been made to achieve optimal spatial resolution without artifacts from side lobes.

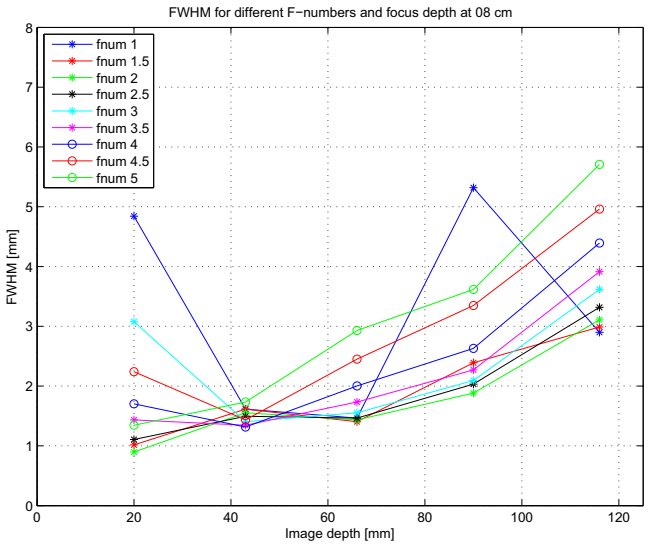

Figure 4. The -6 dB lateral resolution (FWHM) measured for wires in wire phantom using different values of F#. The transmit and receive focal point is set to 80 mm in all cases. The best value for F# is the one that results in low and almost uniform FWHM. This must however, be held against the level of side lobes in each case, because lower F#'s result in higher levels of side lobes.

B. Performance study

This study is conducted in order to determine the performance of SASB-THI compared to DRF-THI on the UltraView system. This is done by measurements and comparisons of the lateral resolution and by visual inspection of B-mode images of wire phantoms and in-vivo B-mode images. The settings used for DRF-THI and SASB-THI are shown in Table I. The settings chosen for DRF-THI are the default settings applied by the UltraView system, while the settings for SASB-THI where determined from the results in Sec. III-A.

One frame of the wire phantom and one *in-vivo* frame is acquired using the scan sequence on the system. DRF and first stage SASB image data are separated and extracted from the frame, inverted image lines are summed (pulse summation), and SASB data are beamformed on an external PC. For the wire phantom scan, the FWHM and -20 dB lateral resolution (FWOTM) for each visible wire is measured. For the *in-vivo* scan, a visual comparison between the two images is made.

1) Comparison of Lateral Resolution: Fig. 6 shows the measured lateral resolutions for all four image techniques on the wire phantom. It is seen from the figures, that THI generally produces better lateral resolution for both SASB and DRF. It is also seen that, SASB-THI produces almost the same lateral resolution as DRF-THI except near the focal point, where the lateral resolution of SASB-THI is worse than DRF-THI. However, SASB-THI shows a 7% reduction in FWHM

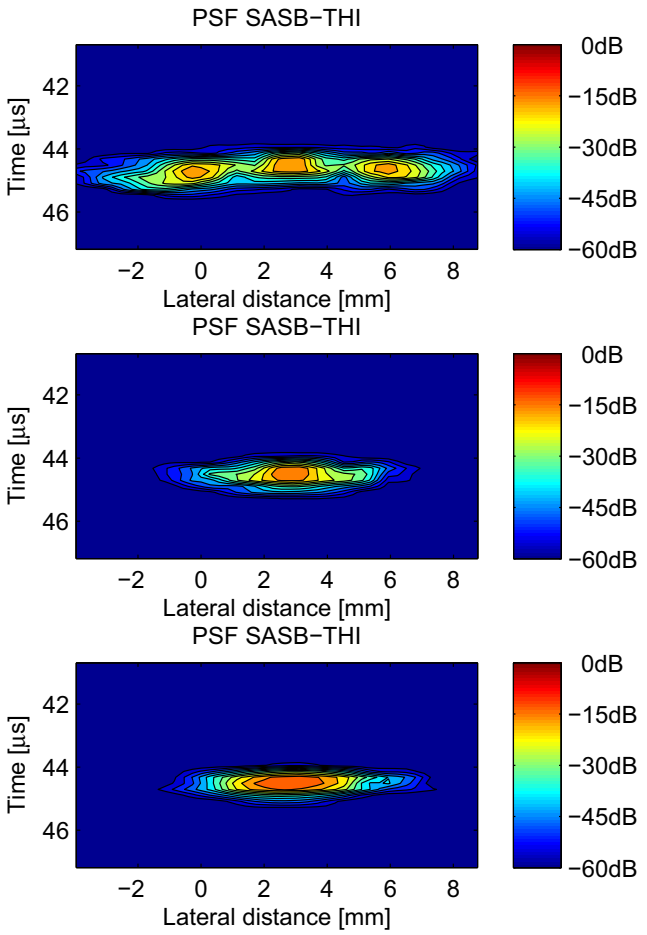

Figure 5. Point spread function (PSF) for wire at 65 mm depth using SASB-THI illustrated in 6 dB contour plot. Focus is set to 80 mm and F# is 1.0, 3.0, and 5.0 from top to bottom respectively.

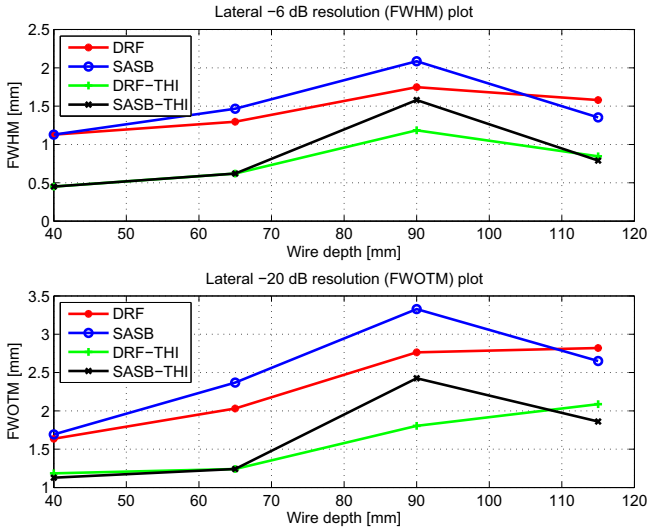

Figure 6. Lateral -6 dB resolution (FWHM) and -20 dB resolution (FWOTM) of visible wires.

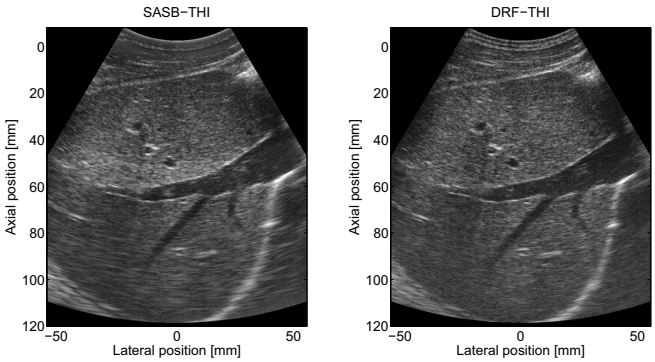

Figure 7. *In-vivo* image of liver tissues of a 29-year old healthy male volunteer. Left image shows SASB-THI, right image shows DRF-THI.

Table I
PARAMETERS USED FOR SASB AND DRF ON THE ULTRAVIEW RESEARCH INTERFACE SCANNER.

Scanner Parameters	Value	
Speed of sound	1492 m/s	
Transmit center frequency	2.14 MHz	
Sampling frequency	17 MHz	
Cycles	1.5	
Scanlines	192	
Emissions per scanline	2	
Active elements	64	
Imaging Setup	DRF	SASB
Focus Tx/Rx (mm)	85/dynamic	80/80
F# Tx/Rx	5.67/0.8	3/3
Apodization Tx/Rx	Boxcar/Gauss	Boxcar/Gauss

for the deepest wire at 100 mm. The FWOTM for SASB-THI at [25, 50, 75, 100] mm is reduced by [5, 0 -34, 11] % compared to DRF-THI, which shows, that except for the point of the virtual source, the FWOTM is improved by SASB-THI.

2) Comparison of in-vivo Images: Two simultaneously acquired *in-vivo* images are shown in Fig. 7. The images show a section of liver tissue with blood vessels of a 29-year old healthy male volunteer. The left *in-vivo* image shows the acquired SASB-THI image, while the right image shows DRF-THI. The two images are very similar in appearance. A slightly better penetration depth is acquired using SASB-THI and the edges of the large vessel are more sharp.

IV. DISCUSSION

The results show as predicted, that non-linear imaging is possible using SASB. The lateral resolution of SASB-THI is improved compared to linear SASB. The lateral resolution of SASB-THI is close to the same as for DRF-THI except at the

focal point. These results do not show as good improvements to the lateral resolution as the study by Du et. al. [7] showed. This is mainly because, Du et. al. used a linear transducer for SASB-THI, whereas in this study, a convex array transducer is used. The difference between the shape of the transducer has a direct effect on the positions and density of the virtual sources in SASB. Because the image lines spread out with depth using the convex array transducer, fewer image lines are used in the second stage beamformed SASB image at the point of the virtual source. This means that the resolution around the virtual source is not as good with a convex array transducer compared to a linear array transducer.

Furthermore, in the study by Du et al [7], transmit apodization was used. Here, a Hanning was used in transmit which resulted in low levels of side lobes. On the UltraView, no transmit apodization (besides Boxcar) is possible. This causes the level of side-lobes to be greater. But in the case of comparing SASB-THI to DRF-THI on the UltraView, no transmit apodization was used in both cases. This makes the comparison between the two fair, but improvements in the two imaging techniques can be made by applying transmit apodization.

The strengths of this study are, that a commercial ultrasound system is used and that the scan sequence created for this study performs both SASB-THI and DRF-THI simultaneously. The commercial platform allows the testing of SASB-THI in pre-clinical trials on volunteers and patients. Because SASB-THI and DRF-Image data are acquired simultaneously, comparison of clinical data is much more straight forward. There is only a minimum of time delay between each frame of the two techniques, so the scan geometry is always the same in the two images. Performance evaluations of the two techniques can be made by professional radiologists in double blinded studies as in the study by Hemmsen et. al. [6].

V. Conclusion

SASB-THI has been successfully implemented on a commercial ultrasound system in a scan sequence that also acquires DRF-THI simultaneously. Lateral -6 dB resolution for SASB-THI is close to identical to DRF-THI and better than both SASB and DRF. Lateral -20 dB resolution is also improved, except at the point of the virtual source. The implementation of SASB-THI on a commercial ultrasound system allows for *in-vivo* data to be acquired simultaneously with DRF-THI for performance comparisons.

VI. Acknowledgements

This work was supported by grant 024-2008-3 from the Danish Advanced Technology Foundation and BK Medical Aps, Denmark.

References

[1] C. S. Chapman and J. C. Lazenby, "Ultrasound imaging system employing phase inversion subtraction to enhance the image," *US Patent*, vol. 5632277, 1997.

[2] D. H. Simpson, C. T. Chin, and P. N. Burns, "Pulse inversion Doppler: a new method for detecting nonlinear echoes from microbubble contrast agents," *IEEE Trans. Ultrason., Ferroelec., Freq. Contr.*, vol. 46, no. 2, pp. 372–382, 1999.

[3] J. A. Jensen, "Medical ultrasound imaging, progress in biophysics and molecular biology," *Progress in Biophysics and Molecular Biology*, p. Submitted, 2006.

[4] M. A. Averkiou, "Tissue harmonic imaging," in *Proc. IEEE Ultrason. Symp.*, vol. 2, 2000, pp. 1563–1572.

[5] J. Kortbek, J. A. Jensen, and K. L. Gammelmark, "Synthetic aperture sequential beamforming," in *Proc. IEEE Ultrason. Symp.*, 2008, pp. 966–969.

[6] M. Hemmsen, P. M. Hansen, T. Lange, J. M. Hansen, K. L. Hansen, M. B. Nielsen, and J. A. Jensen, "In vivo evaluation of synthetic aperture sequential beamforming," *Ultrasound Med. Biol.*, vol. 38, no. 4, p. 708Ű716, 2012.

[7] Y. Du, J. Rasmussen, H. Jensen, and J. A. Jensen, "Second harmonic imaging using synthetic aperture sequential beamforming," *IEEE Trans. Ultrason., Ferroelec., Freq. Contr.*, pp. 2261–2264, 2011.

PAPER IV

Preliminary Study of Synthetic Aperture Tissue Harmonic Imaging on In-vivo Data

Joachim Hee Rasmussen, Martin Christian Hemmsen,
Signe Sloth Madsen, Peter Møller Hansen,
Michael Bachmann Nielsen, and Jørgen Arendt Jensen

Proceedings of SPIE : Medical Imaging 2013: Ultrasonic Imaging, Tomography, and Therapy

Presented in Orlando, Florida, United States, 2013

Preliminary study of synthetic aperture tissue harmonic imaging on in-vivo data

Joachim Hee Rasmussen[a], Martin Christian Hemmsen[a], Signe Sloth Madsen[b], Peter Møller Hansen[b], Michael Bachmann Nielsen[b] and Jørgen Arendt Jensen[a]

[a]Center for Fast Ultrasound Imaging, Technical University of Denmark, 2800 Lyngby, Denmark
[b]Department of Radiology, Copenhagen University Hospital, Rigshospitalet, 2100 Copenhagen, Denmark

ABSTRACT

A method for synthetic aperture tissue harmonic imaging is investigated. It combines synthetic aperture sequential beamforming (SASB) with tissue harmonic imaging (THI) to produce an increased and more uniform spatial resolution and improved side lobe reduction compared to conventional B-mode imaging. Synthetic aperture sequential beamforming tissue harmonic imaging (SASB-THI) was implemented on a commercially available BK 2202 Pro Focus UltraView ultrasound system and compared to dynamic receive focused tissue harmonic imaging (DRF-THI) in clinical scans. The scan sequence that was implemented on the UltraView system acquires both SASB-THI and DRF-THI simultaneously. Twenty-four simultaneously acquired video sequences of *in-vivo* abdominal SASB-THI and DRF-THI scans on 3 volunteers of 4 different sections of liver and kidney tissues were created. Videos of the *in-vivo* scans were presented in double blinded studies to two radiologists for image quality performance scoring. Limitations to the systems transmit stage prevented user defined transmit apodization to be applied. Field II simulations showed that side lobes in SASB could be improved by using Hanning transmit apodization. Results from the image quality study show, that in the current configuration on the UltraView system, where no transmit apodization was applied, SASB-THI and DRF-THI produced equally good images. It is expected that given the use of transmit apodization, SASB-THI could be further improved.

Keywords: Non-linear imaging, Second harmonic imaging, Tissue harmonic imaging, Synthetic aperture imaging, Virtual sources, In-vivo evalutaion

1. INTRODUCTION

Tissue harmonic imaging (THI) has been combined with a variety of imaging techniques to further improve image quality. Tissue harmonic imaging (THI) benefits from improved spatial resolution, lower side lobe levels, less reverberation, and a more narrow beam profile compared to regular B-mode imaging.[1,2] As a transmitted ultrasound waveform travels through tissues, the waveform gets distorted by the nonlinear properties of the different tissues. These non-linear properties cause the speed of sound in the tissues to change due to the difference in acoustic pressure in the peaks and troughs of the transmitted waveform.[3] This causes the high pressure peaks to travel faster than the relatively low pressure troughs. As the waveform gets distorted, higher harmonics are generated in the waveform. The strength of these harmonics is dependent on the strength of the emitted ultrasound field. It is therefore important to emit a field intense enough to ensure good development of harmonic waveforms.

One approach to obtain tissue harmonic imaging (THI) is by using a pulse inversion scheme.[4,5] Here, two identical, but individually phase inverted excitation pulses, are transmitted for every line in the B-mode image. By summing the responses, the second harmonic waveform is enhanced, while neighboring harmonic components (the fundamental and third harmonic waveforms) are attenuated.

THI has long been combined with various focusing techniques, including dynamic receive focusing (DRF) to further improve image quality. Synthetic aperture imaging (SAI) is a focusing technique that generates focused

Further author information: Joachim Hee Rasmussen: E-mail: jr@elektro.dtu.dk, Telephone: (+45) 45 25 39 02

Medical Imaging 2013: Ultrasonic Imaging, Tomography, and Therapy, edited by Johan G. Bosch, Marvin M. Doyley,
Proc. of SPIE Vol. 8675, 867512 · © 2013 SPIE · CCC code: 1605-7422/13/$18 · doi: 10.1117/12.2006363

images in both transmit and receive.[6–8] In the synthetic aperture focusing technique (SAFT)[9] an active aperture of a single element is used in transmit and receive. For every position of the active aperture, a low resolution image is constructed and in the end all low resolution images are combined to create one high resolution image. Naturally, because only one element is used, the signal-to-noise ratio (SNR) is very poor using this technique. Also, because a full low resolution image has to be beamformed for every line, the computational load and beamforming is extensive. Several SAI techniques have been suggested to improve SNR, including the use of multi-element transmit and receive aperture as suggested by Karaman et al.[10] Here a group of elements are used in transmit to increase the SNR. By focusing multiple elements in a single point in transmit, a virtual source is created as first described by Passmann and Ermert[11] and further investigated by Frazier and O'Brien,[12] Nikolov and Jensen,[13,14] and Bae and Jeong.[15]

The use of several electronically focused elements in the aperture for generating virtual sources causes the ultrasound energy field to be focused. This causes development of higher harmonic ultrasound waveforms as described in THI. Depending on the magnitude of the emitted field, a tissue harmonic image using SAI could be generated by isolating and imaging the second harmonic waveform of the received response. Such a technique was first suggested by Bae et al[16] in 2008 to generate a fully focused, high resolution image. Still, the major drawback, however, is the computational load required to produce SAI.

Synthetic aperture sequential beamforming (SASB) is a technique that utilizes a two step beamformer to significantly reduce computational processing load compared to traditional SAI.[17,18] In SASB, a set of image lines are first obtained and beamformed using a fixed focus in both transmit and receive. Secondly, the image data are beamformed using the fixed focus points as virtual sources to obtain the final synthetic aperture image. The advantage of SASB, besides the reduction in computational load, is that the lateral resolution remains higher and more uniform over depth compared to regular dynamic receive focusing (DRF).[19] The use of virtual sources in SASB has been shown to create an acoustic field intense enough to generate harmonics for THI.[20,21]

The purpose of this study is to implement SASB-THI on a commercial system and optimize the technique for clinical imaging. Furthermore, the purpose is to show if there is a difference between SASB-THI and DRF-THI on *in-vivo* image data acquired simultaneously for the two techniques. Finally, the purpose of this study is to show how SASB-THI on the commercial system can be further improved by use of transmit apodization.

2. METHODS

First stage SASB images can be generated using basically any ultrasound system capable of fixed transmit and receive focusing. If the ultrasound system is furthermore capable of pulse inversion, the system may be used to generate first stage SASB-THI. Instead of having only one emission for every fixed focus SASB line in the image, the two phase inverted excitation pulses are emitted for the same line position with the same fixed focus. The two pulses should be emitted interchangeably to minimize tissue movement between the two responses, which would compromise the final summed image.

2.1 Implementation on commercial ultrasound system

A commercially available BK 2202 Pro Focus UltraView (BK-Medical, Herlev, Denmark) ultrasound scanner was used for scanning. The scan sequence performed both SASB-THI and DRF-THI simultaneously. On the UltraView scanner, a DRF-THI setup is the default imaging technique, when performing abdominal scans. All settings for DRF-THI have been optimized for clinical scans by the manufacturer, which makes DRF-THI the obvious candidate for a golden standard to evaluate SASB-THI against. The DRF-THI scheme implemented in this case also uses the pulse inversion technique to obtain the second harmonic component for imaging.

The scan sequence was designed to minimize time delay between the pairs of excitation waveforms (regular and phase inverted waveforms). Each frame consisted of both a SASB-THI frame and a DRF-THI frame. First,

the SASB-THI frame was acquired, where for each image line, the waveform pairs were transmitted interchangeably. Secondly, the DRF-THI frame was acquired in much the same manner with transmit of the regular and phase inverted waveforms interleaved. In this manner, tissue motion between the regular and phase inverted excitation waveforms was kept at a minimum. Any tissue motion would effectively compromise the success of second harmonic waveform enhancement and separation using pulse inversion. The whole scan sequence was then repeated to acquire a collection of frames. An illustration showing the scan sequence on the UltraView system is shown in Fig. 1A.

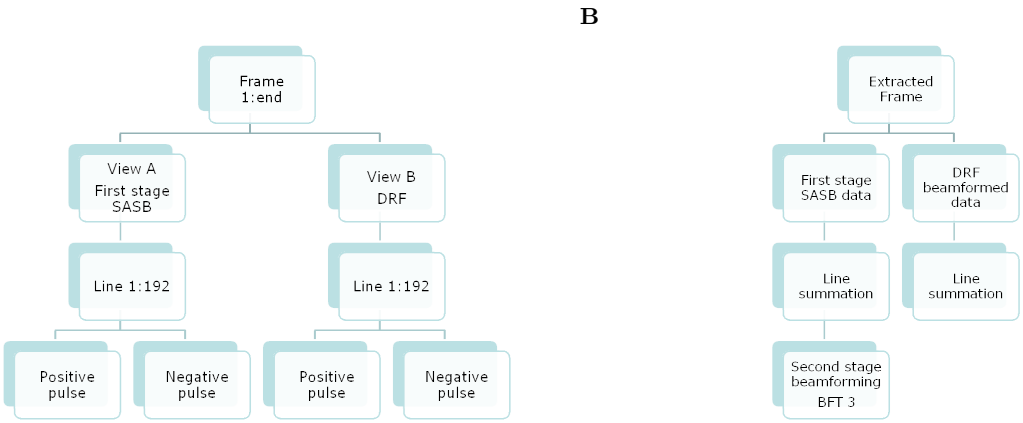

Figure 1. Graphical visualization of **A)** the scan sequence on the UltraView system and **B)** post processing steps.

The scanner was equipped with a UA2227 research interface (BK-Medical) that allows first stage image data to be acquired from the scanner and stored on a PC. For SASB-THI a 64 element fixed aperture with focus at 80 mm was used in transmit and receive with an F-number of 3. For DRF-THI a 64 element fixed aperture with focus of 85 mm and an F-number of 5.3 was used in transmit, while a 64 dynamic receive aperture and an F-number of 0.8 was used in receive. Limitations in the scanner's transmit stage prevent user defined transmit apodization to be applied, and so for both SASB-THI and DRF-THI the default transmit apodization was a 64 element boxcar. This can affect the quality of the final image as artifacts such as e.g. side lobes are more pronounced when no apodization is used. In receive, however, apodization is possible. Here, a Gauss window was applied for both SASB-THI and DRF-THI.

A one-and-a-half cycle excitation pulse with a center frequency of 2.14 MHz and its phase inverted copy were used for both SASB-THI and DRF-THI. The scanner was fitted with a 192 element convex array transducer (BK 8820e, BK-Medical) commonly used in abdominal tissue harmonic scans. This transducer has a center frequency of 3.5 MHz and recommended operational frequency range of 2-6 MHz. This ensured that transmission of the 2.14 MHz excitation pulse and reception of the 4.28 MHz second harmonic response both were well within the operational range of the transducer. The scanner was connected via a X64-CL Express camera link (Dalsa, Waterloo, Ontario, Canada) to a PC. Data were acquired on the PC using an acquisition routine that was run in MATLAB (MathWorks, Natick, MA, USA).

Abdominal *in-vivo* scans were made on 3 healthy volunteers by radiologists from Copenhagen University Hospital, Rigshospitalet. Four scan positions of liver and kidney tissues were imaged twice for each volunteer. The scan procedure was as follows. The scan sequence was loaded and initialized on the scanner and the data acquisition was initialized in MATLAB on the data acquisition PC. The radiologist found a good view of liver or kidney tissues on one of the scan locations. A sequence of 50 frames was then acquired from the scanner and stored on the PC. Pulse summation was performed on the pairs of corresponding first stage image lines and the acquired first stage SASB-THI data were beamformed using the BFT3 toolbox[22] to produce second stage image

data. Both the second stage SASB-THI data and DRF-THI data were then stored and compiled into video sequence files, which were also stored. The pulse summation, beamforming, video compiling, and data storing were performed using BFT3 in a MATLAB routine. An illustration showing the post processing steps for data extraction and beamforming is shown in Fig. 1B.

The performance of SASB-THI was evaluated against DRF-THI by two radiologists who were presented to the two video sequences made from each scan. The video sequences were presented in the program IQap,[23] which automatically and randomly selected two corresponding video files from the collection of scans and presented the videos on screen next to each other. The program randomly selected on which side of the screen to present each imaging technique. The viewing radiologist did therefore not know which scan was being watched and which imaging technique was presented on either side of the screen. The radiologist was asked to score which of the shown sequences was the best based on spatial resolution, image contrast, noise, and unwanted artifacts on a visual analog scale (VAS). The VAS was in the range of -50 to 50 corresponding to left view is best - left view is slightly better - no difference - right view slightly better - right view is best. An example of how a video sequence was presented to the radiologist is shown in Fig. 2.

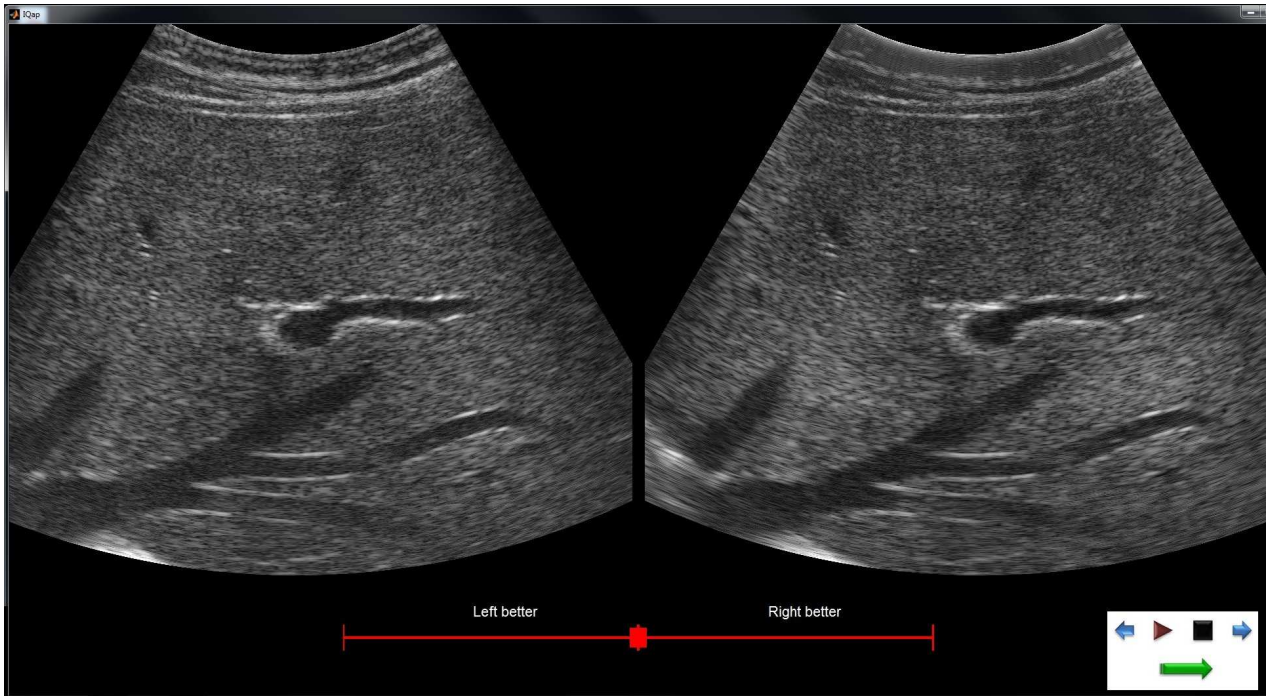

Figure 2. Visualization of an image pair for overall image quality evaluation. The VAS is shown in the bottom and the control panel for navigating the sequences are shown in the lower right corner. In this case, DRF-THI is shown on the left and SASB-THI is shown on the right.

3. RESULTS

A total of 24 sets of videos from 2x4 scans on 3 volunteers were made using SASB-THI and DRF-THI. Examples of images using the two techniques are shown in Fig. 3 and Fig. 4. Note, that in all examples in Fig. 3 and Fig. 4 the scan geometry is the same using the two techniques. This makes comparison of the two techniques much more straightforward as differences in scan geometry do not need to be taken into account. Fig 3A and Fig. 3B show three large arteries through the liver imaged on two different volunteers. Fig 4A and Fig. 4B show a section of a kidney plus a lobe of the liver from the same two volunteers. In all cases SASB-THI is shown on the left and DRF-THI on the right.

A

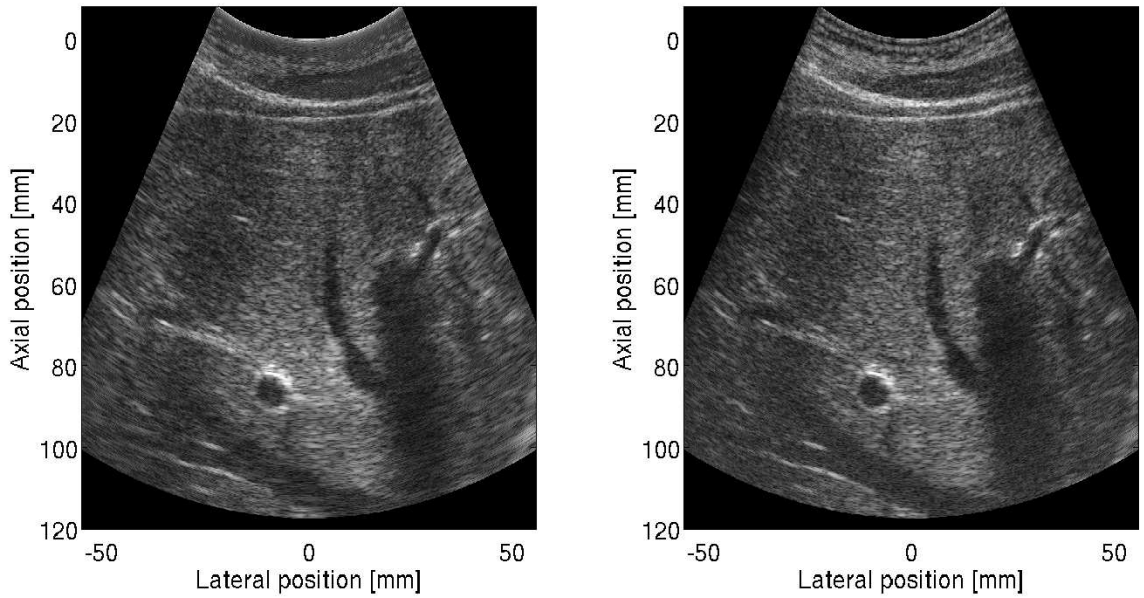

B

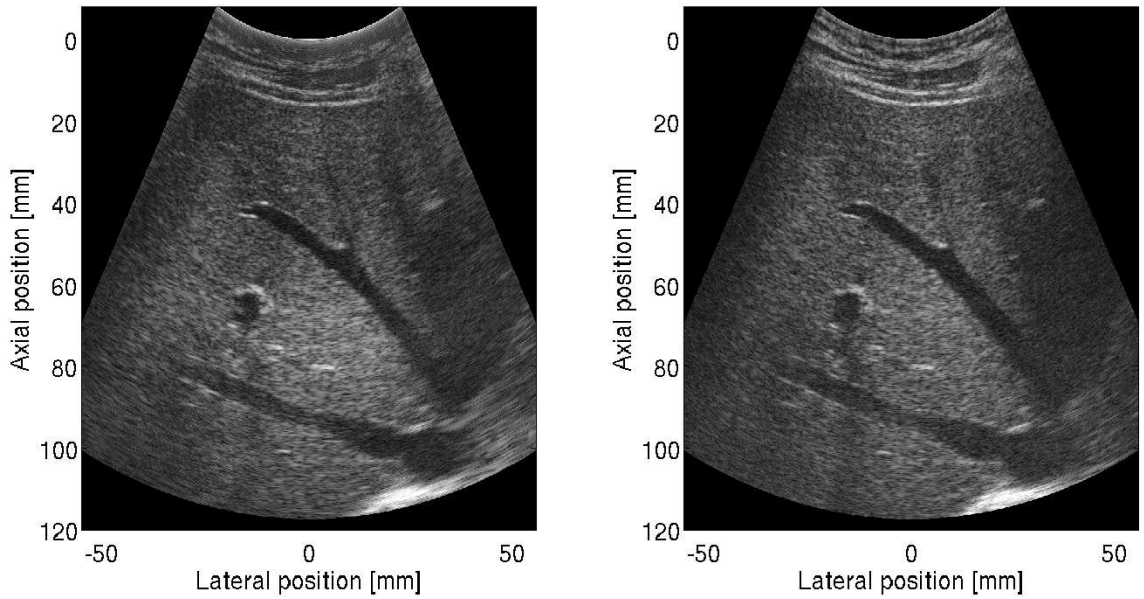

Figure 3. Clinical images acquired using the scan sequence on the UltraView system. Images show both scan techniques (SASB-THI and DRF-THI) from one scan location (liver) on two different volunteers. In both cases SASB-THI is shown on the left and DRF-THI on the right.

A

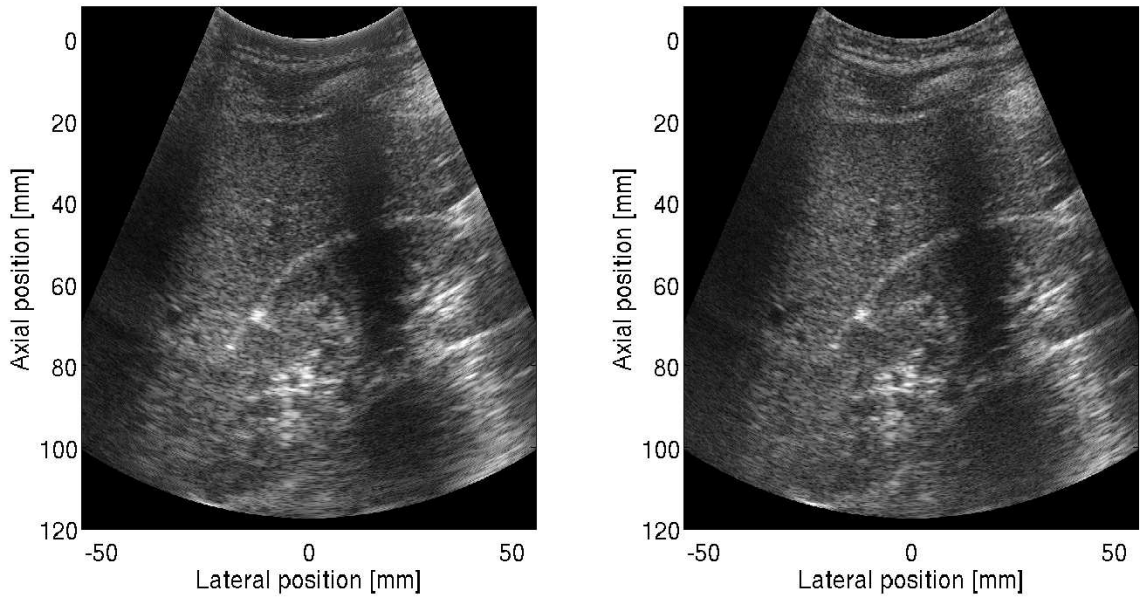

B

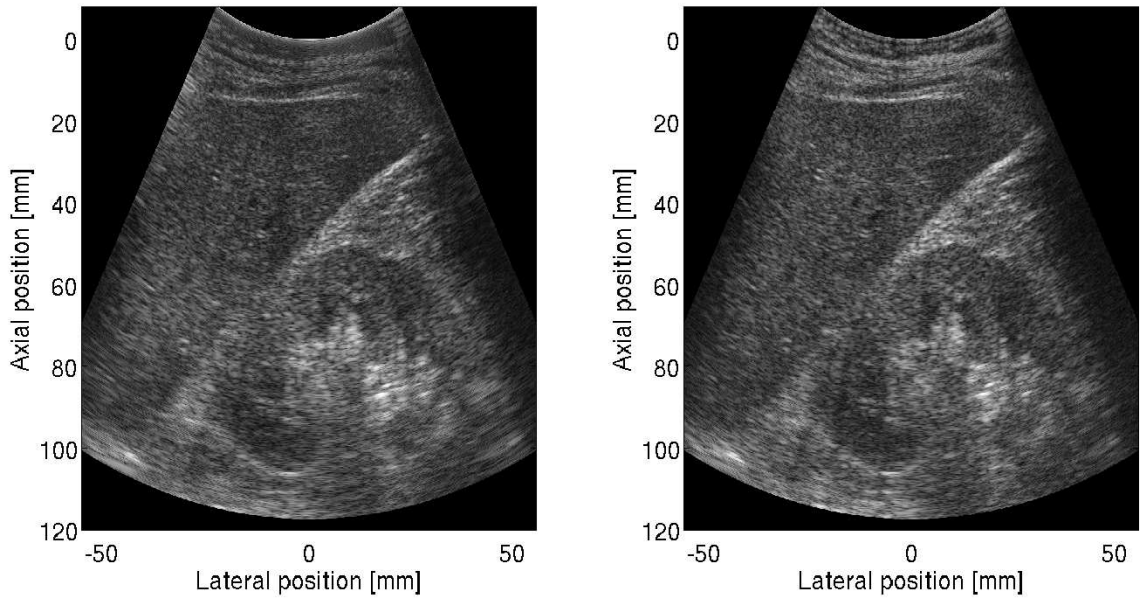

Figure 4. Clinical images acquired using the scan sequence on the UltraView system. Images show both scan techniques (SASB-THI and DRF-THI) from one scan location (kidney and liver lobe) on two different volunteers. In both cases SASB-THI is shown on the left and DRF-THI on the right.

It is seen from Fig. 3 and Fig. 4 that there is very little difference in the image quality in the two scan techniques. Both resolution and contrast in the two images from all scans are almost identical. Visual artifacts from e.g. ribs are present and are equally pronounced in both images in Fig. 3A, Fig. 3B, and Fig. 4A. Penetration depth is also the same for the two techniques.

The video sequences were presented to the two radiologist (A and B) twice in a double blinded study for scoring and the VAS scores were collected. In both cases, a positive VAS score favors DRF-THI over SASB-THI meaning DRF-THI produced better images compared to SASB-THI.

The histograms of the VAS scores from both radiologists are shown in Figure 5. The accumulated median of all VAS scores from radiologist A was +6 with the 25% and 75% quantiles at +5 and +9. The accumulated median of all VAS scores from radiologist B was +2 with the 25% and 75% quantiles at 0 and +4. These results show that the radiologists found the two techniques to be very similar in terms of image quality.

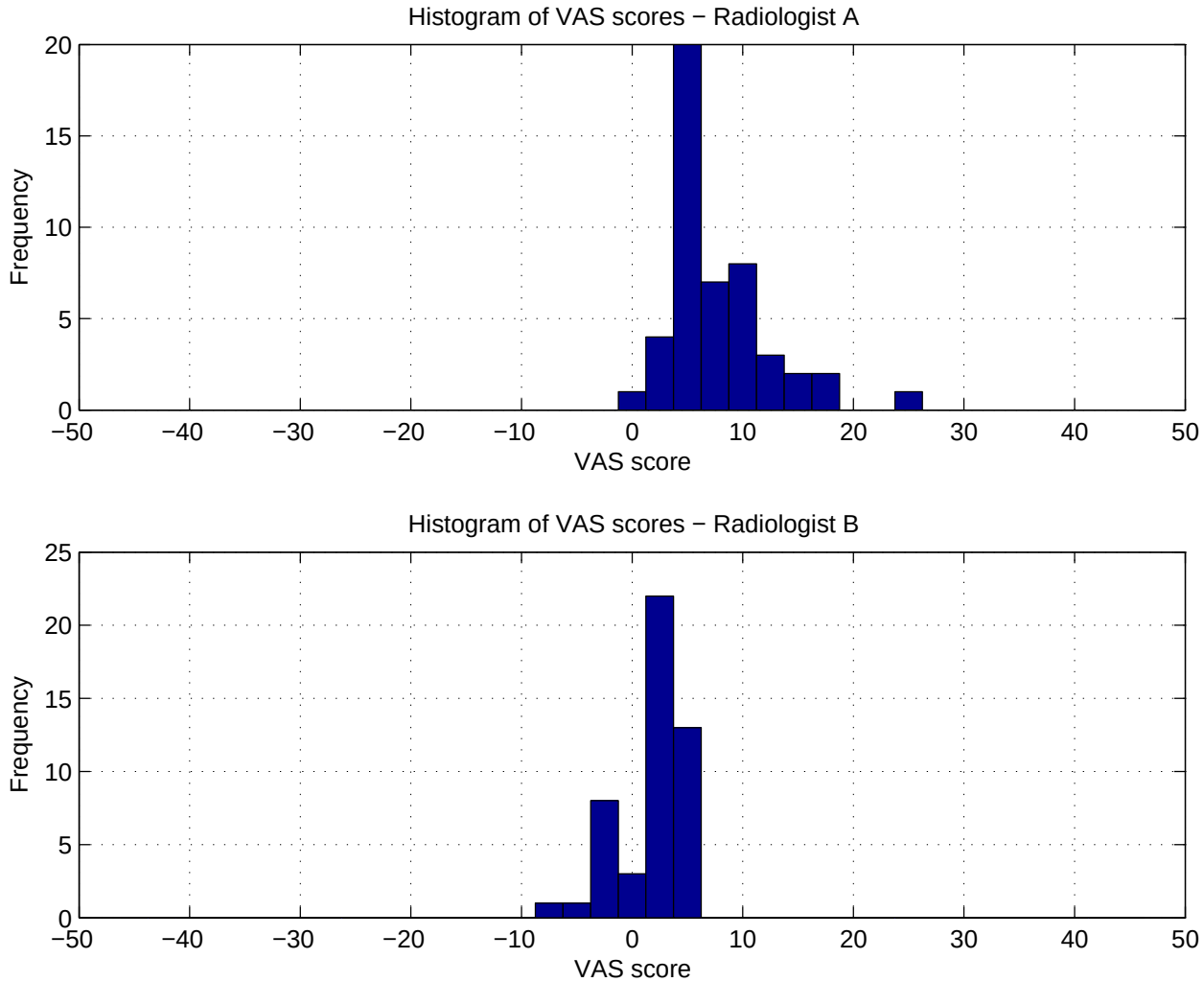

Figure 5. Histogram of VAS scores from Radiologist A and B. A negative VAS score indicates SASB-THI was preferred, a positive VAS score that DRF-THI was preferred. VAS scores are in the interval -50 to 50 corresponding to left view is best - left view is slightly better - no difference - right view slightly better - right view is best.

4. DISCUSSION AND CONCLUSION

A synthetic aperture tissue harmonic imaging technique was implemented successfully on a commercially available ultrasound system. The technique was used to perform *in-vivo* clinical investigations and was compared to DRF-THI, which is the common imaging technique in abdominal investigations. Since SASB-THI data were acquired simultaneously with DRF-THI data, variations in positions of the transducer during scans was excluded and therefore allowed for a fair comparison of the two techniques. DRF-THI was chosen as a golden standard to compare SASB-THI against since DRF-THI on the commercial system was already optimized for *in-vivo* scans by the manufacturer.

Visual comparison of the two scan techniques showed only very little differences in terms of resolution, contrast and penetration depth. Visual artifacts such as shadowing were present using both techniques, but were equally pronounced. Videos of the *in-vivo* scans performed on volunteers were shown to and scored by two radiologists in a double blinded study to exclude bias. Statistical investigations showed that the radiologists found that both techniques performed close to equally good in terms of image quality.

The first stage beamformer in SASB is of very low complexity as it only requires one delay profile. The second stage beamformer applies the output lines from the first stage beamformer rather than channel rf-data and dynamically focuses the image. This way of beamforming reduces the amount of computational calculations compared to traditional SAI and DRF imaging.

The results suggest, that in the scan sequence on the UltraView system, SASB-THI can produce images that are as good as DRF-THI, while reducing the amount of computational calculations.

The transmit stage on the UltraView system did not permit application of transmit apodization. It is hypothesized, that improvements to the reduction of side lobes in SASB-THI could be made by applying user defined transmit apodization. Fig. 6 show contour plots of the point spread functions for SASB simulation using Field II[24, 25] with either boxcar transmit apodization or Hanning transmit apodization. Here, it is seen how transmit apodization can reduce the level of side lobes in SASB. It is expected that the improvements in side lobes for SASB also apply for SASB-THI. The limitations to the transmit stage on UltraView suggests that further studies using a system capable of transmit apodization should be made on *in-vivo* image data. It is expected, that the application of transmit apodization will further improve the image quality of clinical images using SASB-THI.

ACKNOWLEDGMENTS

This work was supported by grant 024-2008-3 from the Danish Advanced Technology Foundation and BK Medical Aps, Denmark

REFERENCES

[1] B. Ward, A. C. Baker, and V. F. Humphrey, "Nonlinear propagation applied to the improvement of resolution in diagnostoc medical ultrasound," *J. Acoust. Soc. Am.* **101**(1), pp. 143–154, 1997.

[2] T. Christopher, "Finite amplitude distortion-based inhomogeneous pulse echo ultrasonic imaging," *IEEE Trans. Ultrason., Ferroelec., Freq. Contr.* **44**(1), pp. 125–139, 1997.

[3] R. T. Beyer, *Nonlinear Acoustics*, Department of the Navy, 1974.

[4] C. S. Chapman and J. C. Lazenby, "Ultrasound imaging system employing phase inversion subtraction to enhance the image," *US Patent* **5632277**, 1997.

[5] D. H. Simpson, C. T. Chin, and P. N. Burns, "Pulse inversion Doppler: a new method for detecting nonlinear echoes from microbubble contrast agents," *IEEE Trans. Ultrason., Ferroelec., Freq. Contr.* **46**(2), pp. 372–382, 1999.

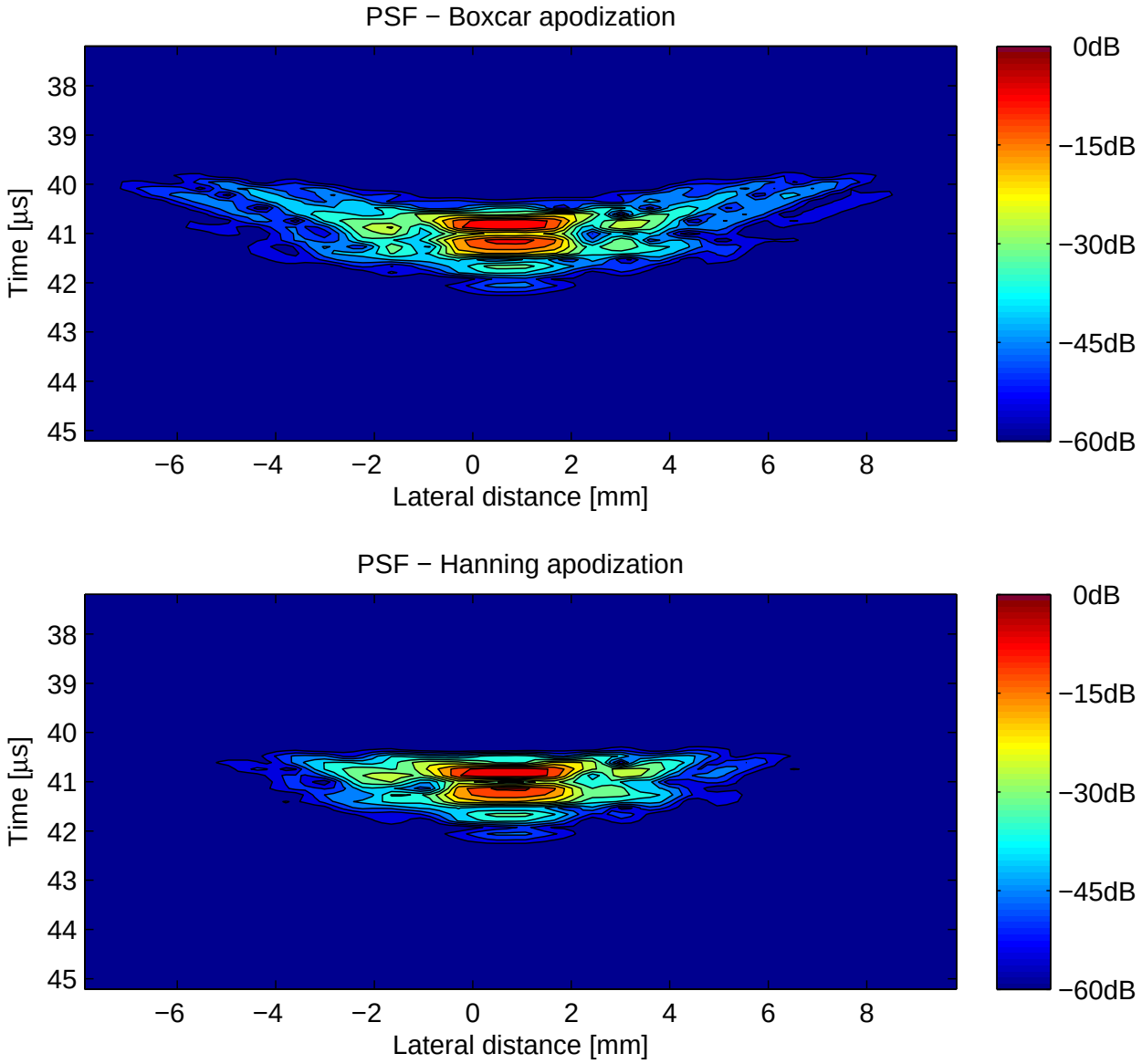

Figure 6. Simulated point spread functions for SASB using boxcar apodization (top) and Hanning apodization (bottom).

[6] L. J. Cutrona, W. E. Vivian, E. N. Leith, and G. O. Hall, "A high resolution radar combat-surveillance system," *IRE Trans. Mil. Elect.* **MIL-5**(2), pp. 127–131, 1961.

[7] C. W. Sherwin, J. P. Ruina, and D. Rawcliffe, "Some early developements in synthetic aperture radar systems," *IRE Trans. Mil. Elect.* **MIL-6**(2), pp. 111–115, 1962.

[8] J. C. Curlander and R. N. McDonough, *Synthetic Aperture Radar: Systems and Signal Processing*, John Wiley & Sons, Inc., 1991.

[9] R. Thomson, "Transverse and longitudinal resolution of the synthetic aperture focusing technique," *Ultrasonics* **22**, pp. 9–15, 1984.

[10] M. Karaman, P. C. Li, and M. O'Donnell, "Synthetic aperture imaging for small scale systems," *IEEE Trans. Ultrason., Ferroelec., Freq. Contr.* **42**, pp. 429–442, 1995.

[11] C. Passmann and H. Ermert, "A 100-MHz ultrasound imaging system for dermatologic and ophthalmologic diagnostics," *IEEE Trans. Ultrason., Ferroelec., Freq. Contr.* **43**, pp. 545–552, 1996.

[12] C. H. Frazier and W. D. O'Brien, "Synthetic aperture techniques with a virtual source element," *IEEE Trans. Ultrason., Ferroelec., Freq. Contr.* **45**, pp. 196–207, 1998.

[13] S. I. Nikolov and J. A. Jensen, "Virtual ultrasound sources in high-resolution ultrasound imaging," in *Proc. SPIE - Progress in biomedical optics and imaging*, **3**, pp. 395–405, 2002.

[14] S. I. Nikolov and J. A. Jensen, "3D synthetic aperture imaging using a virtual source element in the elevation plane," in *Proc. IEEE Ultrason. Symp.*, **2**, pp. 1743–1747, 2000.

[15] M. H. Bae and M. K. Jeong, "A study of synthetic-aperture imaging with virtual source elements in B-mode ultrasound imaging systems," in *IEEE Trans. Ultrason., Ferroelec., Freq. Contr.*, **47**, pp. 1510–1519, 2000.

[16] M. Bae, H. Lee, S. B. Park, R. Yoon, M. H. Jeong, D. G. Kim, M. Jeong, and Y. Kim, "A new ultrasonic synthetic aperture tissue harmonic imaging system," in *Proc. IEEE Ultrason. Symp.*, pp. 1258–1261, 2008.

[17] J. Kortbek, J. A. Jensen, and K. L. Gammelmark, "Synthetic aperture sequential beamforming," in *Proc. IEEE Ultrason. Symp.*, pp. 966–969, 2008.

[18] J. A. Jensen, J. Kortbek, S. I. Nikolov, M. C. Hemmsen, and B. Tomov, "Implementation of synthetic aperture imaging in medical ultrasound: The dual stage beamformer approach," in *EUSAR*, 2010.

[19] M. C. Hemmsen, J. M. Hansen, and J. A. Jensen, "Synthetic Aperture Sequential Beamformation applied to medical imaging using a multi element convex array transducer," in *EUSAR*, p. Accepted for publication, Apr. 2012.

[20] Y. Du, J. Rasmussen, H. Jensen, and J. A. Jensen, "Second harmonic imaging using synthetic aperture sequential beamforming," in *Proc. IEEE Ultrason. Symp.*, pp. 2261–2264, 2011.

[21] J. H. Rasmussen, M. C. Hemmsen, S. S. Madsen, P. M. Hansen, M. B. Nielsen, and J. A. Jensen, "Implementation of tissue harmonic synthetic aperture imaging on a commercial ultrasound system," in *Proc. IEEE Ultrason. Symp.*, p. Accepted, 2012.

[22] J. M. Hansen, M. C. Hemmsen, and J. A. Jensen, "An object-oriented multi-threaded software beamformation toolbox," in *Proc. SPIE Med. Imag.*, **7968**, p. 79680Y, March 2011. Lake Buena Vista (Orlando), Florida, USA.

[23] M. C. Hemmsen, M. M. Petersen, S. I. Nikolov, M. B., Nielsen, and J. A. Jensen, "Ultrasound image quality assessment: A framework for evaluation of clinical image quality," in *Proc. SPIE Med. Imag.*, **76291**, pp. 76290C–12, Medical Imaging 2010: Ultrasonic Imaging, Tomography, and Therapy, 2010.

[24] J. A. Jensen and N. B. Svendsen, "Calculation of Pressure Fields from Arbitrarily Shaped, Apodized, and Excited Ultrasound Transducers," *IEEE Trans. Ultrason., Ferroelec., Freq. Contr.* **39**, pp. 262–267, 1992.

[25] J. A. Jensen, "Field: A program for simulating ultrasound systems," *Med. Biol. Eng. Comp.* **10th Nordic-Baltic Conference on Biomedical Imaging, Vol. 4, Supplement 1, Part 1**, pp. 351–353, 1996.

PAPER V

Tissue Harmonic Synthetic Aperture Imaging

Joachim Hee Rasmussen, Yigang Du, Martin Christian Hemmsen, and Jørgen Arendt Jensen

Journal of the Acoustical Society of America

In review 2013

Tissue Harmonic Synthetic Aperture Ultrasound Imaging

Joachim Hee Rasmussen,[a)] Martin Christian Hemmsen, and Jørgen Arendt Jensen

Center for Fast Ultrasound Imaging,

Department of Electrical Engineering,

Technical University of Denmark,

Ørsteds Plads,

Bldg. 349,

DK-2800 Kgs. Lyngby,

Denmark

Yigang Du

Department of Electronic and Computer Engineering,

The Hong Kong University of Science and Technology,

Hong Kong,

China

(Dated: November 24, 2013)

Abstract

A method for tissue harmonic synthetic aperture imaging is presented. Investigations of spatial resolution, level of side lobes, and the degree of resolution depth independence was performed on a wire phantom using a linear array transducer (BK8804) and the experimental ultrasound system SARUS. Scans using synthetic aperture sequential beamforming SASB, tissue harmonic SASB (SASBTHI), dynamic receive focus (DRF), and tissue harmonic DRF (DRFTHI) were performed. The -6 dB resolution for DRF, SASB and DRFTHI was 206 %, 75 %, and 69 % wider than SASBTHI at 47.5 mm imaging depth (transmit focus of 25 mm). SASBTHI produced a more depth invariant spatial resolution compared to the other techniques. The highest spatial resolution was achieved for SASBTHI using a focus depth of 10 mm, while the most depth invariant spatial resolution was achieved using a focus depth of 25 mm. An implementation of SASBTHI and DRFTHI was made on a commercially available ultrasound system (BK Pro Focus UltraView). *In-vivo* B-mode scans of the liver of a 29-years old healthy male were produced and compared. No visual differences were found in the two techniques. Limitations in the transmit stage suggest that improvements could be made to the image quality of SASBTHI, if transmit apodization is applied.

PACS numbers: 43.80.Qf, 43.80.Vj, 43.35.Yb, 43.35.Bf

Keywords: Medical ultrasound, Tissue harmonic imaging, Synthetic aperture imaging, Experimental measurements

I. INTRODUCTION

Tissue harmonic imaging (THI) can be used in ultrasound investigations to image difficult regions of the human body and to generally improve the image quality. Synthetic aperture imaging (SAI) is a focusing technique that generates focused images in both transmit and receive. The scope of this study is to investigate a method for generating fully focused, high resolution B-mode images using tissue harmonic synthetic aperture imaging.

THI benefits from improved spatial resolution, lower side lobe levels, less reverberation, and a narrower beam profile compared to regular B-mode imaging[1–3]. The narrow beam profile of THI is used in many thoracic investigations to image tissues such as the heart valves that lie close to e.g. air filled regions in the lungs or bone in the rib cage that would otherwise interfere and obscure the final image. The higher spatial resolution of THI is also used in many abdominal investigations to image small objects in e.g. the gall bladder or kidneys. In many abdominal scans THI is used to penetrate fatty tissues that surround the area of interest. Recent years have seen an increase in the use of THI and in many cases THI has become the default setting on scanners when performing abdominal scans.

The concept in THI is to transmit a waveform with a fundamental frequency and receive and image the response at a different harmonic frequency. Inherent to THI is that only a fraction of the transmitted fundamental waveform energy is transformed into harmonics. The amplitude of the harmonic waveform is dependent on the magnitude of the emitted acoustic field. It is therefore important in THI to emit a field intense enough to ensure good development of harmonic waveforms.

Tissue harmonic imaging (THI) has been combined with a variety of focusing techniques,

[a)]Author to whom correspondence should be addressed. Electronic mail: jr@elektro.dtu.dk

including dynamic receive focusing (DRF) to further improve image quality. Synthetic aperture imaging (SAI) is a focusing technique that generates focused images in both transmit and receive[4–6]. In the synthetic aperture focusing technique (SAFT)[7] an active aperture of a single element is used in transmit and receive. For every position of the active aperture, a low resolution image is constructed and in the end all low resolution images are combined to create one high resolution image. Naturally, because only one element is used, the signal-to-noise ratio (SNR) is very poor using this technique. Also, because a full low resolution image has to be beamformed for every line, the computational load and beamforming is extensive. Several SAI techniques have been suggested to improve SNR, including the use of multi-element transmit and receive aperture as suggested by Karaman et al.[8]. Here a group of elements are used in transmit to increase the SNR. By focusing multiple elements in a single point in transmit, a virtual source is created as first described by Passmann and Ermert[9] and further investigated by Frazier and O'Brien[10], Nikolov and Jensen[11,12], Gammelmark and Jensen[13], and Bae and Jeong[14].

The use of several electronically focused elements in the aperture for generating virtual sources causes the emitted ultrasound energy field to increase in intensity. This causes development of higher harmonic ultrasound waveforms as described in THI. Depending on the magnitude of the emitted field, SAI could be combined with THI by isolating and imaging the second harmonic waveform of the received response. Such a technique has been suggested by Li et al.[15] for a single element transducer and by Bae et al.[16] for a multi element array transducer. In both studies, however, the computational load required to produce SAI is still a major drawback.

Synthetic aperture sequential beamforming (SASB) is a technique that utilizes a two step beamformer to significantly reduce computational processing load compared to traditional SAI[17,18]. In SASB, a set of image lines are first obtained and beamformed using a fixed focus in both transmit and receive. Secondly, the image data are beamformed

using the fixed focus points as virtual sources to obtain the final synthetic aperture image. The advantage of SASB, besides the reduction in computational load, is that the lateral resolution remains higher and more uniform over depth compared to regular dynamic receive focusing (DRF)[19]. The use of virtual sources in SASB has been shown to create an acoustic field intense enough to generate harmonics for THI[20,21].

By combining THI with a SAI technique such as SASB, which is capable of generating harmonics for THI, the final image could potentially be improved by both techniques. The improvements could be increased spatial resolution, reduced reverberation artifacts, reduced side lobe levels, and a narrower beam profile from THI along with a range independent fully focused image in both transmit and receive from SASB.

This paper presents a method for tissue harmonic synthetic aperture imaging on an experimental ultrasound system for a linear array transducer. Spatial resolution, side lobe levels, and the degree of depth independence is investigated for different settings of focal depth via measurements on wire phantom. An implementation tissue harmonic synthetic aperture imaging on a commercial available ultrasound system is presented for a convex array transducer. A comparison is made to dynamic receive focus tissue harmonic imaging on clinical *In-vivo* data and the effect of transmit apodization on side lobes is studied.

II. THEORY

A. Pulse Inversion

In THI, the purpose is to image the second harmonic frequency band of a pulse response, instead of the transmitted fundamental frequency. As a transmitted ultrasound waveform travels through a medium, the waveform gets distorted due to the nonlinear properties of the medium[22,23]. The speed at which the waveform travels (the speed of sound) depends on the instantaneous acoustic pressure within the waveform. Because there is a pressure

difference between the high pressure peaks and the relatively low pressure troughs of the waveform, different parts of the waveform travels at different speeds[24]. This causes the high pressure peaks to travel a higher speed of sound than the relatively low pressure troughs. As the waveform gets continuously distorted, higher harmonics are generated in the waveform. The strength of these harmonics is dependent on the acoustic pressure of the emitted ultrasound field. It is therefore important to emit a field intense enough to ensure good development of harmonic waveforms.

In THI it is also important to ensure good separation of the desired harmonic frequency from unwanted neighboring frequencies, since these will influence the spatial resolution. Several techniques exist to separate and enhance harmonic frequencies such as matched filtering, power modulation, and pulse inversion (PI)[25–27]. In PI, two identical but phase shifted pulses (0° phase shifted and 180° phase shifted pulse) are transmitted in turn for the same transducer geometry. Under the assumption that there has been no motion in the medium in the time between the two waveforms were transmitted, differences in the responses are purely a result from how the waveforms were distorted by the medium. For the received pair of responses, a 180° phase shift between the two waveforms can be detected at the fundamental frequency. However, for the 2nd and 3rd harmonic frequencies, a corresponding 360° and 540° phase shift can be detected in the pair of waveforms respectively[28,29]. If the two responses are summed, all signals that are perfectly in phase will double in signal strength, while all signals that have opposite phases will cancel out. To suppress the odd order harmonics then, each pair (regular and phase shifted) of the received responses are summed (see Fig. 1). The harmonic frequencies that are in phase (all even harmonics) will double in amplitude, while out of phase harmonic frequencies (all odd harmonics) will cancel out (see Fig. 2). This separates and enhances the 2nd harmonic frequency, which in turn then can be extracted using a matched filter and used for imaging.

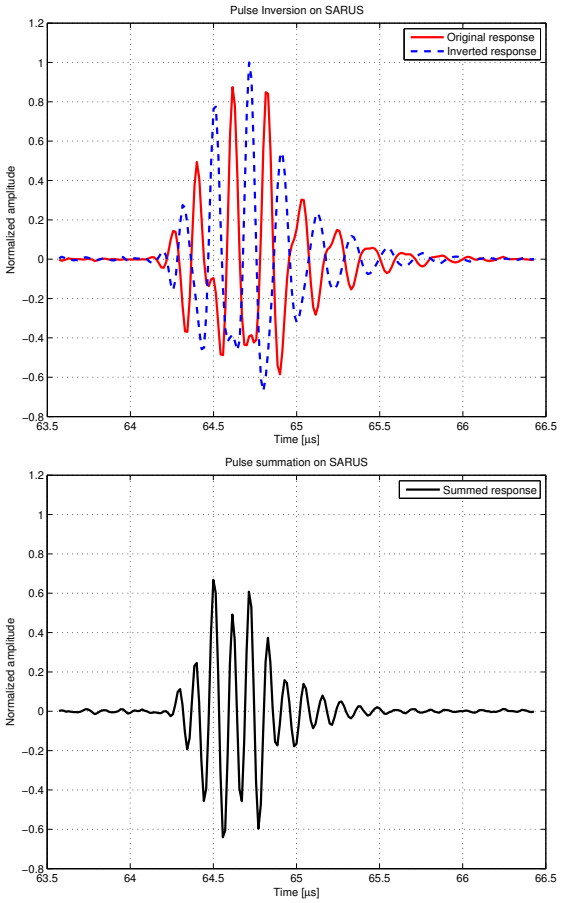

Figure 1. (Color online) The two received responses from the transmitted pulses are shown in the top figure. Note the 180° shift in phase between the two received responses. The summed response in the bottom figure shows the resulting response after pulse summation of the two received responses (original and phase inverted). All data have been normalized to the maximum amplitude of the original pulse in the top plot.

B. Synthetic Aperture Sequential Beamforming

Traditionally, SAI utilizes only one active transducer element in transmit (see Fig. 3A). Because the transmitted acoustic energy in this case is very low, SAI is not capable of producing harmonic components for THI. Synthetic aperture sequential beamforming (SASB) is a SAI technique, which uses virtual sources and a dual stage beamforming approach to significantly reduce the computational load compared to SAI[30,31]. A fixed transmit and

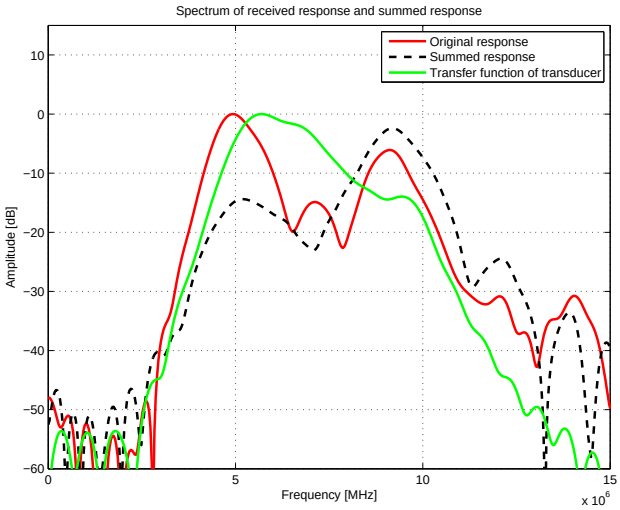

Figure 2. (Color online) Spectrum of received RF signals and response of transducer. The spectrum of a received response (positive pulse emission) is shown along with the spectrum of the response after pulse summation (summation of positive and negative pulse emission responses). The 2nd harmonic frequency near 10 MHz is enhanced by approximately 6 dB, while the fundamental frequency at 5 MHz is attenuated by approximately 15 dB. Both the fundamental frequency and the 2nd harmonic frequency lie within the transfer function of the transducer (BK8804).

receive focal point is used in the first stage beamformer to create a set of focused scan lines with reference r_θ and a virtual source at r_{vs} in each emission. The dotted lines in Fig. 4 show the image information at spatial positions that are found in each focused scan line. A single image point, r_{ip} may be represented in several focused scan lines as shown by the black dot. The overlapping contributions from the first stage image lines can be used to improve resolution. The first stage image data is therefore beamformed again (second stage beamforming) using a focus at each pixel in the image. This produces a set of low resolution images, which are then summed coherently to form a single depth invariant high resolution image (see Fig. 3B). The advantage of SASB, besides the improvements in lateral resolution, is that the transmitted acoustic energy is sufficient to produce harmonic components for THI[20]. A combination of SASB and THI can therefore be implemented.

A Schematic illustration of SAI.

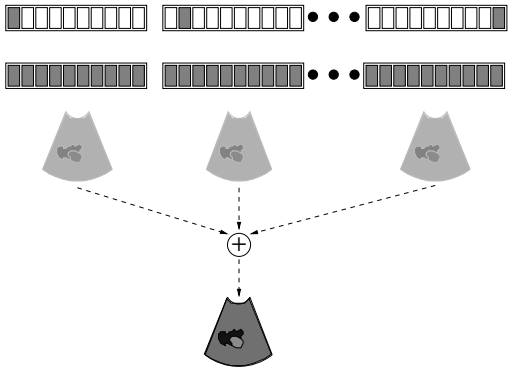

B Schematic illustration of SASB.

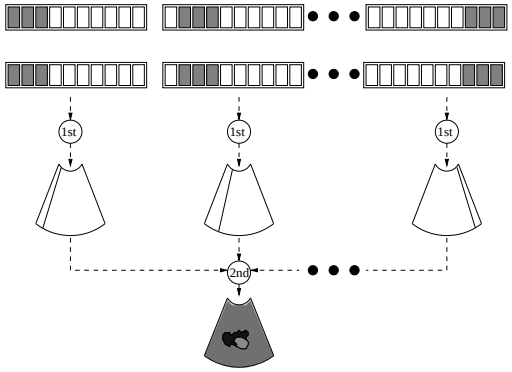

Figure 3. Concept illustrations of SAI and SASB. In SAI, a single element is used in transmit, while all elements are used in receive. Low resolution images are generated and summed. In SASB, a fixed group of elements are used in transmit and receive. A fixed focus image is generated using the first stage beamformer. The first stage image lines are used as input for the second stage beamformer using the focus point as a virtual source.

C. Methods

The experimental ultrasound system SARUS[32,33] was used to implement scan sequences for synthetic aperture sequential beamforming tissue harmonic imaging (SASBTHI) and dynamic receive focus tissue harmonic imaging (DRFTHI). The system allows for user defined scan sequences, raw channel acquisition, and is capable of performing both synthetic aperture imaging and tissue harmonic imaging[20,34]. For both SASBTHI and DRFTHI, scan sequences for a 192 element linear array transducer (BK8804, BK Medical Aps., Herlev,

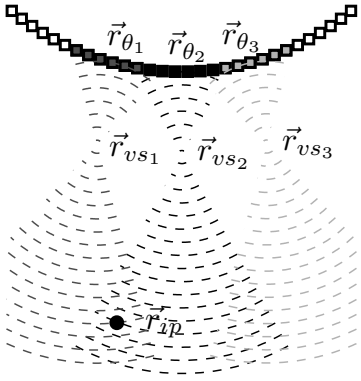

Figure 4. Three emissions for first stage SASB. A single image point, r_{ip} is represented in several focused scan lines. Figure taken from[31].

Denmark) were implemented. A two cycle 5 MHz transmit waveform was used with a 64 element fixed Hanning apodized sub-aperture for both SASBTHI and DRFTHI. For SASBTHI, receive apodization was a Hanning on a 64 element fixed sub-aperture with focal point for first stage beamforming at 10 mm, 25 mm, and 50 mm in three experiments. For the DRFTHI measurements, transmit foci at 10 mm, 20 mm, and 50 mm were used, while dynamic receive focus and an expanding aperture was used with a fixed F# of 3 (see Table I).

A water-filled wire phantom was scanned using SATHI and DRFTHI. Radio frequency (RF) data was recorded using SARUS and stored. The collection of RF data from one experiment contained RF data pairs for every scanline position (regular response and phase shifted response). These data can be used to compile both a tissue harmonic image (using pulse summation on the correlated RF data pairs) and a linear image (using only one of the responses from each RF data pair). For the linear images (DRF and SASB), the fundamental frequency was isolated using matched filters (5 MHz center frequency). For the tissue harmonic images (DRFTHI and SASBTHI), the second harmonic frequency was extracted using pulse summation and matched filters (10 MHz center frequency) using Matlab (MathWorks, Natick, MA, USA). Beamforming of RF data was performed using a beam-

formation toolbox[35,36] in Matlab. For the RF SASB data, first stage SASB beamforming was conducted using the fixed focus in transmit and receive. Next, the second stage SASB beamforming was conducted using the first stage image lines as input data with the focal point as a virtual source. For the DRF RF data, dynamic beamforming was applied in receive.

B-mode images were produced using three transmit focal points, for both linear imaging and tissue harmonic imaging, using SASB and DRF focusing, giving a total of 12 B-mode images (3x2x2). In each case, the -6 dB lateral resolution (FWHM) and the -20 dB lateral resolution (FWOTM) was measured for all visible wires in the image. Furthermore, the point spread function (PSF) of each technique was measured at a single wire depth.

D. Results

The B-mode images generated from the four techniques are shown in Fig. 5 for a focus depth of 25 mm. In the THI images (DRFTHI and SASBTHI), the level of noise in the images is higher than in the linear images (DRF and SASB). The pulse inversion technique can potentially achieve an enhancement of maximum 6 dB for the second harmonic frequency. From the spectrum of the received responses in Fig. 2, the amplitude of the second harmonic is measured to be -6 dB before pulse summation and -2.4 dB after pulse summation, resulting in a gain of 3.6 dB. The difference in maximum amplitude between the fundamental frequency in the linear images and the second harmonic frequency in the THI images is measured to be 2.4 dB. The signal to noise ratio (SNR) in the THI images (Fig. 5C and Fig. 5D) is therefore less than in the linear images (Fig. 5A and Fig. 5B). This is due to several reasons. Because only a fraction of the transmitted energy at the fundamental frequency is converted into the second harmonic frequency, the SNR is lower for THI. Also, because the transfer function of the transducer is limited, transmit and receive might be more efficient at the fundamental frequency than at the second harmonic frequency (see Fig. 2). Finally, imperfections in how accurately the inverted waveforms were transmit-

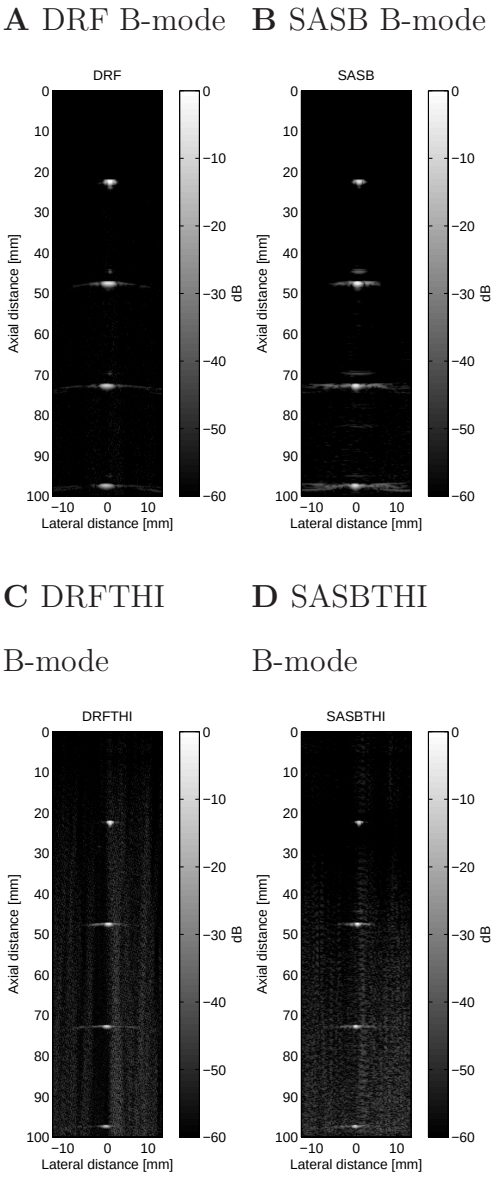

Figure 5. (Color online) B-mode images of wire phantom, transmit focus is at 25 mm depth

ted, could reduce the enhancement of the second harmonic frequency after pulse summation.

The -6 dB lateral resolution (FWHM) and -20 dB lateral resolution (FWOTM) was measured for each visible wire in the phantom using different transmit focal points (at 10 mm, 25 mm, and 50 mm). Table II shows the measured FWHM for all wires for DRF, DRFTHI, SASB, and SASBTHI. As seen from the table, SASB generally produce lower FWHM values than DRF. Furthermore, THI FWHM is lower than linear imaging. SAS-

BTHI produces a FWHM value of 0.67 mm for a wire depth of 47.5 mm when the transmit focus is at 25 mm. In comparison, DRF, SASB, and DRFTHI produce a FWHM value of 2.04 mm, 1.16 mm, and 1.12mm which are 206 %, 75 %, and 69 % higher than the SASBTHI FWHM. In Table III the measured FWOTM values are shown. Again it is seen, that SASB FWOTM is better than DRF, and THI FWOTM is better than linear imaging. Here, DRF, SASB, and DRFTHI produce 158%, 61%, and 42% higher FWOTM value for a wire depth of 47.5 mm, when the transmit focus is at 25 mm compared to SASBTHI, respectively.

Fig. 6A shows the measured FWHM values using DRF, DRFTHI, SASB, and SASBTHI, while Fig. 6B shows the measured FWOTM values. The THI images overall produce better lateral resolution compared to the linear images. SASB produces more uniform and depth independent resolution compared to DRF. The slope of the FWHM curves for SASB is almost flat, indicating that the lateral resolution of the wires using SASB does not change very much with imaging depth. In comparison, the slope of the FWHM curves for DRF change much more indicating that the lateral resolution here varies with imaging depth. For SASBTHI and DRFTHI, a similar trend is seen. Again SASBTHI produces more uniform FWHM compared to DRFTHI, and the FWHM values of SASTHI are close to half of those for SASB. Finally, it is seen, that SASBTHI outperforms all other imaging techniques in terms of lateral resolution, when a transmit focus of 10 mm or 25 mm is applied.

The point spread function for all techniques for a wire located at 47.5 mm depth is shown in Fig. 7. The side lobe levels are reduced by SASBTHI compared to the other imaging techniques and SASBTHI produces the highest lateral resolution. The lateral width of the PSF for SASBTHI is more narrow than all the other PSFs, and SASBTHI also improves the axial resolution. The axial length of the PSF is shorter for SASBTHI than for DRF, SASB, and DRFTHI. In general, SASBTHI produces the best spatial resolution of the four techniques.

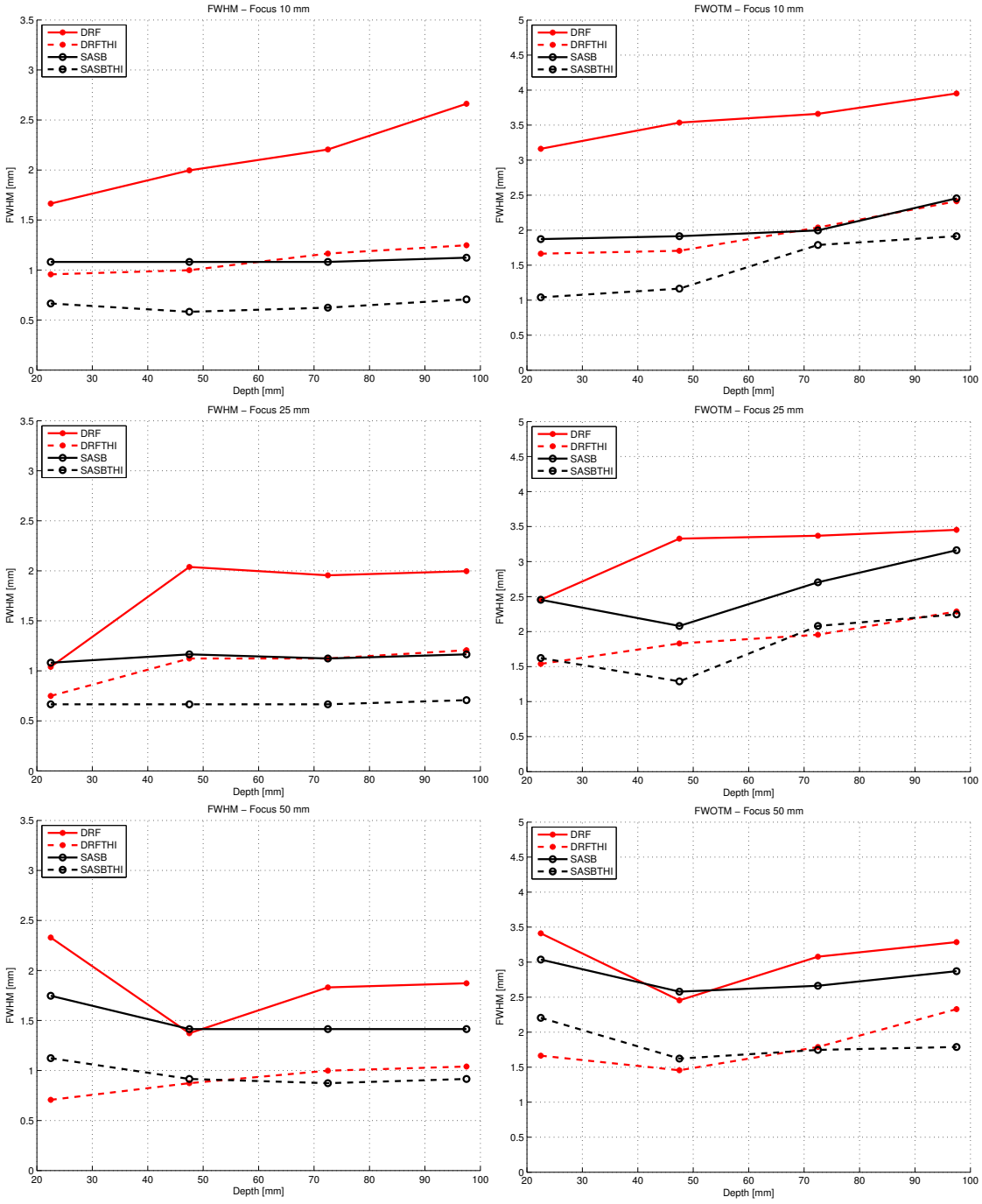

Figure 6. (Color online) Measured -6 dB lateral resolution (FWHM) and -20 dB lateral resolution (FWOTM) using different focus depths (10 mm, 25 mm, and 50 mm)

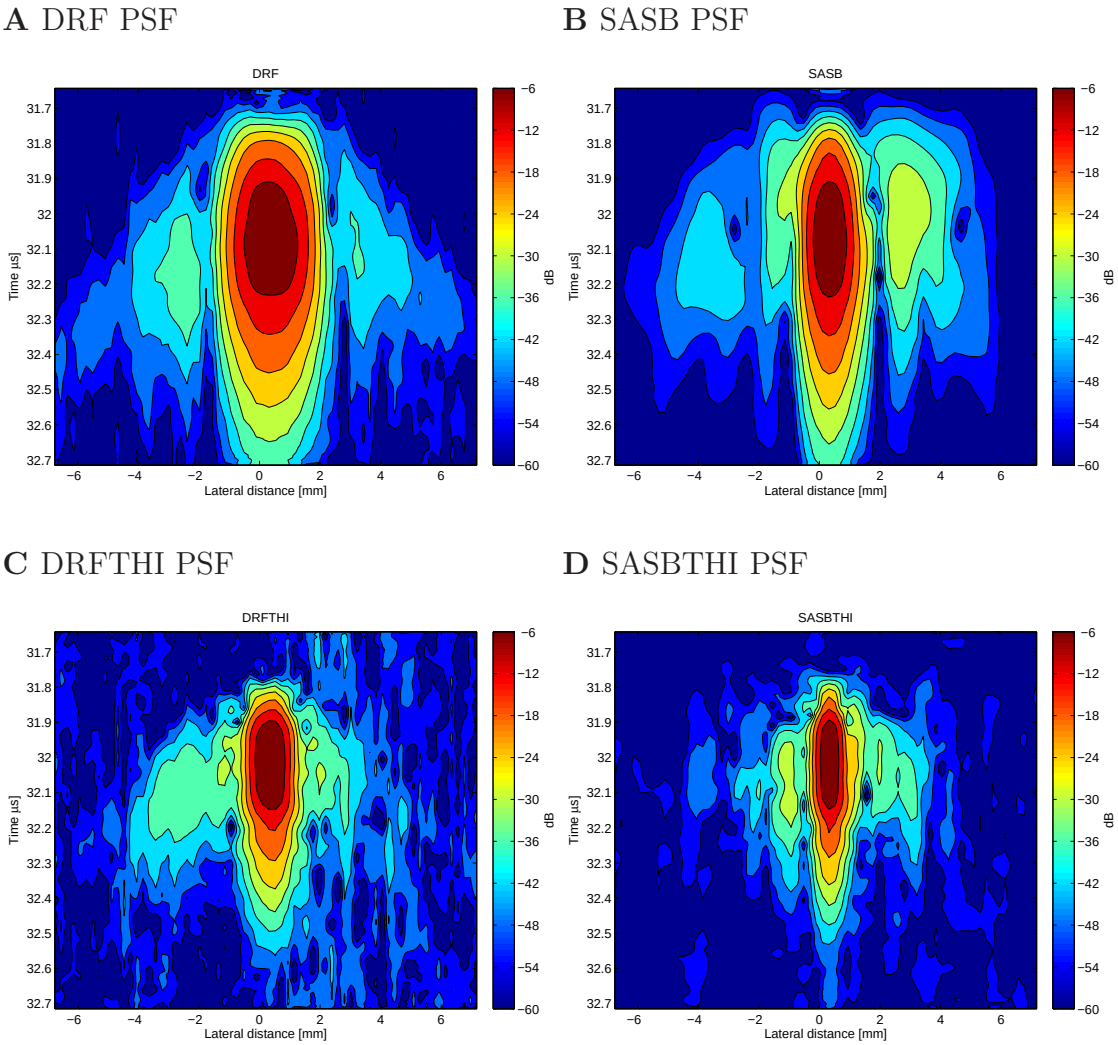

Figure 7. (Color online) Point spread function (PSF) for wire at 47.5 mm depth for DRF, SASB, DRFTHI, and SASBTHI. Transmit focus depth is at 25 mm.

III. DISCUSSION

Investigations of the FWHM and FWOTM show that SASBTHI generally produces higher lateral resolution compared to DRF, SASB, and DRFTHI. The FWHM for DRF, SASB, and DRFTHI are 206 %, 75 %, and 69 % higher than the SASBTHI FWHM respectively, at 47.5 mm imaging depth when the focus is at 25 mm. The results also show, that SASBTHI is able to maintain a more depth independent lateral resolution than all the other techniques in this study. Best results in terms of lowest possible FWHM and

FWOTM were attained when a focal depth of 10 mm was applied for SASBTHI ([0.67 0.58 0.62 0.70] mm for FWHM and [1.04 1.16 1.79 1.91] mm for FWOTM). Having the focus point close to the transducer produced highest lateral resolution, but not the most depth invariant resolution. This was accomplished using a focus depth of 25 mm ([0.67 0.67 0.66 0.70] mm for FWHM and [1.62 1.29 2.08 2.24] mm for FWOTM).

An implementation of SASBTHI and DRFTHI was made on a commercially available ultrasound system (BK 2202 Pro Focus UltraView, BK Medical Aps., Herlev, Denmark) for *In-vivo* imaging comparisons. A scan sequence that allowed simultaneous acquisitions of DRFTHI data and first stage SASBTHI data was used. Second stage beamforming for SASBTHI was performed using the BFT3 toolbox[37] on an external PC running MATLAB. A B-mode scan of the liver of a healthy 29-years old male was conducted using a 192 element convex array transducer (BK 8820e, BK Medical Aps. Herlev, Denmark) typically applied in abdominal investigations using DRFTHI. For SASBTHI a 64 element fixed aperture with a focus at 80 mm was used in transmit and receive with an F# of 3. For DRFTHI, settings predefined by the manufacturer was used to ensure optimal performance. Here, a 64 element fixed aperture with a focus of 85 mm and an F# of 5.3 was used in transmit, while a 64 dynamic receive aperture and an F# of 0.8 was used in receive. Limitations in the scanner's transmit stage prevent user defined transmit apodization to be applied, and so for both SASBTHI and DRFTHI the default transmit apodization was a 64 element boxcar. A one-and-a-half cycle excitation pulse with a center frequency of 2.14 MHz and its phase inverted copy were used for both SASBTHI and DRFTHI. Examples of the *In-vivo* B-mode images are shown in Fig. 8.

Visual comparison of the *In-vivo* B-mode images show no difference in terms of image quality, although SASBTHI performs better in terms of spatial resolution and resolution depth independence compared to DRFTHI. The reasons for this is the limitations of the transmit stage on the ultrasound system. On the UltraView system, no transmit

A DRFTHI - *In-vivo* imaging **B** SASBTHI - *In-vivo* imaging

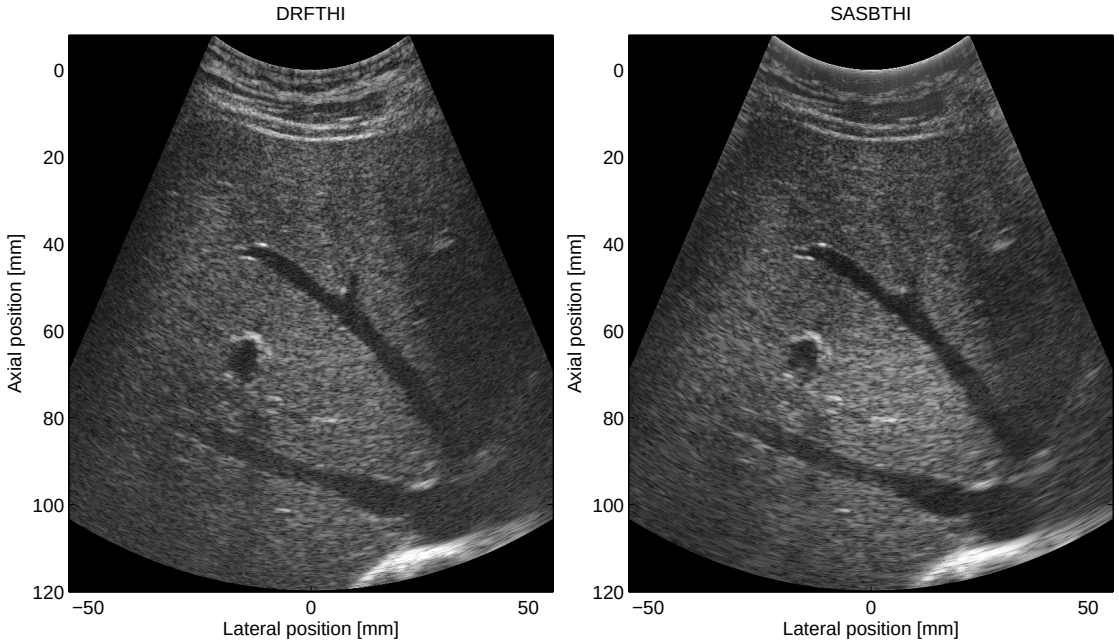

Figure 8. (Color online) *In-vivo* image of liver from a healthy 29 years old male. Images are shown with 60 dB dynamic range. Acquisitions are made using DRFTHI and SASBTHI simultaneously on the BK 2202 UltraView scanner.

apodization (besides Boxcar) is possible. This causes the level of side-lobes to be greater than when Hanning apodization is applied. Fig. 9 show the PSF for SASBTHI using the linear BK 8804 transducer on SARUS when either Boxcar or Hanning apodization is applied. For Boxcar apdization, the lateral FWOTM is measured to be 1.96 mm, while for Hanning apodization, the FWOTM is 1.91 mm. This shows that side lobes are reduced by transmit apodization and could therefore potentially improve SASBTHI on the UltraView system, if the transmit stage would permit user defined apodization.

A Boxcar apodization **B** Hanning apodization

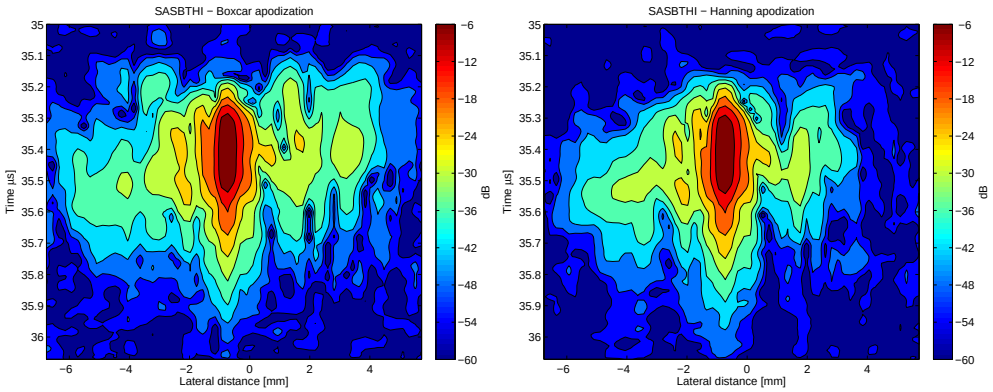

Figure 9. (Color online) Point spread function (PSF) for wire at 47.5 mm depth for SASBTHI using either Boxcar apodization or Hanning apodization. Transmit focus depth is at 25 mm.

IV. CONCLUSION

A method for tissue harmonic synthetic aperture imaging has been suggested. Investigations of spatial resolution, level of side lobes, and the degree of resolution depth independence was performed on a wire phantom using a linear array transducer and an experimental ultrasound system. Results show that the spatial resolution of SASBTHI is higher and is less affected by imaging depth compared to DRF, DRFTHI and SASB. Finally, an implementation of SASBTHI and DRFTHI was made on a commercially available ultrasound system. *In-vivo* B-mode scans were made and compared. No visual differences were found in the two techniques, however, limitations in the transmit stage and the choice of transducer suggest that improvements could be made to the image quality of SASBTHI if transmit apodization is applied.

Acknowledgment

This work is supported by grant 024-2003-3 from the Danish Advanced Technology Foundation and by BK Medical Aps, Herlev, Denmark.

References

[1] B. Ward, A. C. Baker, and V. F. Humphrey, "Nonlinear propagation applied to the improvement of resolution in diagnostoc medical ultrasound", J. Acoust. Soc. Am. **101**, 143–154 (1997).

[2] T. Christopher, "Finite amplitude distortion-based inhomogeneous pulse echo ultrasonic imaging", IEEE Trans. Ultrason., Ferroelec., Freq. Contr. **44**, 125–139 (1997).

[3] M. A. Averkiou and M. F. Hamilton, "Measurements of harmonic generations in a focused finite-amplitude sound beam", J. Acoust. Soc. Am. **98**, 3439–3442 (1995).

[4] L. J. Cutrona, W. E. Vivian, E. N. Leith, and G. O. Hall, "A high resolution radar combat-surveillance system", IRE Trans. Mil. Elect. **MIL-5**, 127–131 (1961).

[5] C. W. Sherwin, J. P. Ruina, and D. Rawcliffe, "Some early developements in synthetic aperture radar systems", IRE Trans. Mil. Elect. **MIL-6**, 111–115 (1962).

[6] J. C. Curlander and R. N. McDonough, *Synthetic Aperture Radar: Systems and Signal Processing* (John Wiley & Sons, Inc.), 1–647 (1991).

[7] R. Thomson, "Transverse and longitudinal resolution of the synthetic aperture focusing technique", Ultrasonics **22**, 9–15 (1984).

[8] M. Karaman, P. C. Li, and M. O'Donnell, "Synthetic aperture imaging for small scale systems", IEEE Trans. Ultrason., Ferroelec., Freq. Contr. **42**, 429–442 (1995).

[9] C. Passmann and H. Ermert, "A 100-MHz ultrasound imaging system for dermatologic and ophthalmologic diagnostics", IEEE Trans. Ultrason., Ferroelec., Freq. Contr. **43**, 545–552 (1996).

[10] C. H. Frazier and W. D. O'Brien, "Synthetic aperture techniques with a virtual source element", IEEE Trans. Ultrason., Ferroelec., Freq. Contr. **45**, 196–207 (1998).

[11] S. I. Nikolov and J. A. Jensen, "Virtual ultrasound sources in high-resolution ultrasound imaging", in *Proc. SPIE - Progress in biomedical optics and imaging*, volume 3, 395–405 (2002).

[12] S. I. Nikolov and J. A. Jensen, "3D synthetic aperture imaging using a virtual source

element in the elevation plane", in *Proc. IEEE Ultrason. Symp.*, volume 2, 1743–1747 (2000).

[13] K. L. Gammelmark and J. A. Jensen, "Multielement synthetic transmit aperture imaging using temporal encoding", IEEE Trans. Med. Imag. **22**, 552–563 (2003).

[14] M. H. Bae and M. K. Jeong, "A study of synthetic-aperture imaging with virtual source elements in B-mode ultrasound imaging systems", in *IEEE Trans. Ultrason., Ferroelec., Freq. Contr.*, volume 47, 1510–1519 (2000).

[15] M. L. Li, W. J. Guan, and P. C. Li, "Improved synthetic aperture focusing technique with application in high-frequency ultrasound imaging", IEEE Trans. Ultrason., Ferroelec., Freq. Contr. **51**, 63–70 (2004).

[16] M. Bae, H. Lee, S. B. Park, R. Yoon, M. H. Jeong, D. G. Kim, M. Jeong, and Y. Kim, "A new ultrasonic synthetic aperture tissue harmonic imaging system", in *Proc. IEEE Ultrason. Symp.*, 1258–1261 (2008).

[17] J. Kortbek, J. A. Jensen, and K. L. Gammelmark, "Sequential beamforming synthetic aperture imaging", Ultrasonics **53**, 1–16 (2013).

[18] J. A. Jensen, J. Kortbek, S. I. Nikolov, M. C. Hemmsen, and B. Tomov, "Implementation of synthetic aperture imaging in medical ultrasound: The dual stage beamformer approach", in *EUSAR*, 434–437 (2010).

[19] M. C. Hemmsen, J. M. Hansen, and J. A. Jensen, "Synthetic Aperture Sequential Beamformation applied to medical imaging", in *EUSAR*, 34–37 (2012).

[20] Y. Du, J. Rasmussen, H. Jensen, and J. A. Jensen, "Second harmonic imaging using synthetic aperture sequential beamforming", in *Proc. IEEE Ultrason. Symp.*, 2261–2264 (2011).

[21] J. H. Rasmussen, M. C. Hemmsen, S. S. Madsen, P. M. Hansen, M. B. Nielsen, and J. A. Jensen, "Implementation of tissue harmonic synthetic aperture imaging on a commercial ultrasound system", in *Proc. IEEE Ultrason. Symp.*, 121–125 (2012).

[22] J. A. Shooter, T. G. Muir, and D. T. Blackstock, "Acoustic saturation of spherical waves in water", J. Acoust. Soc. Am. **55**, 54–62 (1974).

[23] H. C. Starritt, M. A. Perkins, F. A. Duck, and V. F. Humphrey, "Evidence for ultrasonic finite-amplitude distortion in muscle using medical equipment", J. Acoust. Soc. Am. **77**, 302–306 (1985).

[24] R. T. Beyer, *Nonlinear Acoustics* (Department of the Navy), 91–165 (1974).

[25] C. S. Chapman and J. C. Lazenby, "Ultrasound imaging system employing phase inversion subtraction to enhance the image", US Patent 5632277 (1997).

[26] D. H. Simpson, C. T. Chin, and P. N. Burns, "Pulse inversion Doppler: a new method for detecting nonlinear echoes from microbubble contrast agents", IEEE Trans. Ultrason., Ferroelec., Freq. Contr. **46**, 372–382 (1999).

[27] X. A. A. M. Verbeek, L. A. F. Ledoux, J. M. Willigers, P. J. Brands, and A. P. G. Hoeks, "Experimental investigation of the pulse inversion technique for imaging ultrasound contrast agents", J. Acoust. Soc. Am. **107**, 2281–2290 (2000).

[28] J. A. Jensen, "Medical ultrasound imaging", Progress in Biophysics and Molecular Biology **93**, 153–165 (2007).

[29] M. A. Averkiou, "Tissue harmonic imaging", in *Proc. IEEE Ultrason. Symp.*, volume 2, 1563–1572 (2000).

[30] J. Kortbek, J. A. Jensen, and K. L. Gammelmark, "Synthetic aperture sequential beamforming", in *Proc. IEEE Ultrason. Symp.*, 966–969 (2008).

[31] M. Hemmsen, P. M. Hansen, T. Lange, J. M. Hansen, K. L. Hansen, M. B. Nielsen, and J. A. Jensen, "In vivo evaluation of synthetic aperture sequential beamforming", Ultrasound Med. Biol. **38**, 708–716 (2012).

[32] J. A. Jensen, M. Hansen, B. G. Tomov, S. I. Nikolov, and H. Holten-Lund, "System architecture of an experimental synthetic aperture real time ultrasound system", in *Proc. IEEE Ultrason. Symp.*, 636–640 (2007).

[33] J. A. Jensen, H. Holten-Lund, R. T. Nielson, B. G. Tomov, M. B. Stuart, S. I. Nikolov, M. Hansen, and U. D. Larsen, "Performance of SARUS: A Synthetic Aperture Real-time Ultrasound System", in *Proc. IEEE Ultrason. Symp.*, 305–309 (2010).

[34] J. Rasmussen, Y. Du, and J. A. Jensen, "Non-linear imaging using an experimantal syn-

thetic aperture real time ultrasound scanner", IFMBE Proceedings **34**, 101–104 (2011).

[35] J. Kortbek, S. I. Nikolov, and J. A. Jensen, "Effective and Versatile software Beamformation Toolbox", in *Proc. SPIE - Medical Imaging - Ultrasonic Imaging and Signal Processsing*, 651319,1–10 (2007).

[36] S. Gustavsson and J. Kortbek, "Users guide for the beamformation toolbox ii, release 5.0", Technical Report, Ørsted•DTU, Technical University of Denmark, Lyngby, Denmark, 1–16 (2005).

[37] J. M. Hansen, M. C. Hemmsen, and J. A. Jensen, "An object-oriented multi-threaded software beamformation toolbox", in *Proc. SPIE Med. Imag.*, volume 7968, 79680Y 1–9 (2011).

Table I. Scan parameters for SASBTHI and DRFTHI for linear array transducer on SARUS.

Scanner Parameters	SASBTHI	DRFTHI
Transmit center frequency	5.0 MHz	5.0 MHz
Waveform cycles	2	2
Sampling frequency	70 MHz	70 MHz
No. scanlines	128	128
No. emissions per scanline	2	2
No. active elements	64	64
Focus Tx (mm)	[10, 25, 50]	[10, 25, 50]
Focus Rx (mm)	[10, 25, 50]	Dynamic
F-number Tx/Rx	3	3
Apodization Tx/Rx	Hanning	Hanning

Table II. Measured -6 dB lateral resolution (FWHM) for DRF, DRFTHI, SASB, and SASBTHI for focal depths of 10mm, 25mm, and 50 mm.

FWHM [mm]					
Focus depth [mm]	Wire depth [mm]	DRF	DRFTHI	SASB	SASBTHI
10	22.5	1.66	0.96	1.08	0.67
	47.5	2.00	1.00	1.08	0.58
	72.5	2.20	1.16	1.08	0.62
	97.5	2.66	1.25	1.12	0.71
25	22.5	1.04	0.75	1.08	0.67
	47.5	2.04	1.12	1.16	0.67
	72.5	1.96	1.12	1.12	0.66
	97.5	2.00	1.21	1.16	0.71
50	22.5	2.33	0.71	3.04	2.20
	47.5	1.37	0.87	2.58	1.62
	72.5	1.83	1.00	2.66	1.75
	97.5	1.87	1.04	2.87	1.79

Table III. Measured -20 dB lateral resolution (FWOTM) for DRF, DRFTHI, SASB, and SASBTHI for focal depths of 10mm, 25mm, and 50 mm.

FWOTM [mm]					
Focus depth [mm]	Wire depth [mm]	DRF	DRFTHI	SASB	SASBTHI
10	22.5	3.16	1.66	1.87	1.04
	47.5	3.54	1.71	1.91	1.16
	72.5	3.66	2.04	2.00	1.79
	97.5	3.95	2.41	2.45	1.91
25	22.5	2.45	1.54	2.45	1.62
	47.5	3.33	1.83	2.08	1.29
	72.5	3.37	1.96	2.70	2.08
	97.5	3.45	2.29	3.16	2.25
50	22.5	3.41	1.67	1.75	1.12
	47.5	2.45	1.46	1.41	0.92
	72.5	3.08	1.78	1.41	0.87
	97.5	3.29	2.33	1.41	0.92

List of Figures

PAPER VI

Tissue Harmonic Synthetic Aperture Imaging Optimized for Duplex *In-Vivo* Imaging

Joachim Hee Rasmussen, Martin Christian Hemmsen,
Andreas Hjelm Brandt, Peter Møller Hansen,
Michael Bachmann Nielsen, and Jørgen Arendt Jensen

IEEE Transactions on Ultrasonics, Ferroelectrics and Frequency Control

Draft

Tissue Harmonic Synthetic Aperture Imaging Optimized for Duplex *In-Vivo* Imaging

Joachim Hee Rasmussen, *Student Member, IEEE*, Martin Christian Hemmsen, Andreas Hjelm Brandt, Peter Møller Hansen, Michael Bachmann Nielsen, and Jørgen Arendt Jensen, *Fellow, IEEE*

Abstract

This paper presents an implementation of a tissue harmonic synthetic aperture imaging technique optimized for *in-vivo* imaging on a commercial ultrasound system equipped with 192 element convex array transducer. Synthetic aperture imaging was performed using tissue harmonic synthetic aperture sequential beamforming (SASBTHI), with a virtual source position at 70 mm, a F# of 2 in transmit and receive and 269 image lines. A scan sequence that can perform a simultaneous SASBTHI and tissue harmonic dynamic receive focused imaging (DRFTHI) in duplex scan was developed. Line density and position of the virtual source for SASBTHI were optimized for the duplex scan sequence based on lateral resolution, side lobe levels, and frame rates. A scaling curve was developed to compensate for low distribution of contributing image lines near the virtual source and for low 2nd harmonic signal strength and a the top of the image. The scaling curve equalized the gray scale throughout the image and between the SASBTHI and DRFTHI images. Measurements of the -6 dB lateral resolution on a wire phantom showed that SASBTHI produced up to 20% higher resolution than DRFTHI except near the position of the virtual source where DRFTHI produced 0.1 mm higher resolution. In general, DRFTHI produced the most depth invariant lateral resolution of the two techniques, however it is expected that the resolution in SASBTHI can be made more depth invariant by increasing the line density. For 47 mm and 72 mm image depths DRFTHI produced approximately 1.5 mm better 20 dB cystic resolution than SASBTHI. An *in-vivo* scan of the liver of a healthy 31 year-old male was acquired using the duplex scan sequence. No visible differences were seen in the two images indicating, that SASBTHI performs as good as DRFTHI in the suggested setup.

I. Introduction

Tissue harmonic imaging (THI) can be used in ultrasound investigations to image difficult regions of the human body and to generally improve the image quality. Synthetic aperture imaging (SAI) is a focusing technique that generates focused images in both transmit and receive. The scope of this study is to optimize a tissue harmonic synthetic aperture imaging technique for clinical *in-vivo* imaging. The technique will be executed in a duplex scan

Joachim Hee Rasmussen is with the Department of Electrical Engineering, Center for Fast Ultrasound, Technical University of Denmark. e-mail: jr@elektro.dtu.dk.

This work is supported by grant 24-2008-3 from the Danish Advanced Technology Foundation and by BK Medical Aps, Herlev, Denmark.

sequence with the default imaging technique, implemented on a commercially available ultrasound system.

THI benefits from improved spatial resolution, lower side lobe levels, less reverberation, and a more narrow beam profile compared to regular B-mode imaging [1]–[3]. This leads to THI often being the default scan setting on many ultrasound systems today. In thoracic investigations for example, the narrow beam profile of THI is used to image e.g. the heart valves that lie close to air filled regions in the lungs or bone in the rib cage, that would otherwise interfere and obscure the final image. The higher spatial resolution of THI is also used in many abdominal investigations to image small objects in e.g. the gall bladder or kidneys and because reverberation is often very pronounced when scanning fatty tissues, THI has become the default scanning technique in many abdominal investigations.

In traditional ultrasound B-mode imaging, an image is acquired by transmitting a waveform with a specific center frequency, f_0 and imaging the response at that same center frequency. In THI, a waveform is transmitted at f_0, and the response is received at an integer value of the originally transmitted center frequency ($n \cdot f_0$, $n = 1, 2, \cdots$). Since the magnitude of the harmonics in a received waveform is dependent on the magnitude of the transmitted waveform, it is important to ensure, that the energy field that is being emitted is intense enough to generate sufficiently strong harmonics for imaging. This can either be achieved by increasing the transmit voltage over a transducer element or by employing several transducer elements in transmit.

Synthetic aperture imaging (SAI) is a focusing technique that can generate highly and uniformly focused ultrasound images. In traditional synthetic aperture imaging (SAI), a single element in the transducer array is used in transmit and receive [4]–[7]. For every position of the active aperture, a low resolution image is constructed and in the end all low resolution images are combined to create one high resolution image. Naturally, because only one element is used, the signal-to-noise ratio (SNR) is very poor using this technique. As a consequence of this, it would seem disadvantageous to combine SAI with THI. However, Li et al. [8] suggested nonetheless a THI-SAI technique for a single element transducer.
By employing several elements in transmit and by focusing the elements into a single point in transmit, the SNR in SAI is increased and a virtual source is created. This was first described by Passmann and Ermert [9] and further investigated by Frazier and O'Brien [10], Nikolov and Jensen [11], [12], Gammelmark and Jensen [13], and Bae and Jeong [14]. Bae et al. were the first to suggest an implementation for THI-SAI for a multi element array transducer using a single position for the virtual source [15]. Recently, Bae et al. suggested using several virtual sources distributed throughout the image to level out the harmonic energy in the image [16]. While the studies showed good results in terms of focusing and resolution, the computational load required to produce THI-SAI is still a major drawback. And in the case where several virtual sources were applied, the obtained frame rate was to low to be useful in any clinical setup.

Synthetic aperture sequential beamforming (SASB) is a SAI technique that utilizes a two step beamformer to

significantly reduce computational processing load compared to traditional SAI [17], [18]. In SASB, a set of image lines are first obtained and beamformed using a fixed focus in both transmit and receive. Secondly, the image data are beamformed using the fixed focus points as virtual sources to obtain the final synthetic aperture image. The advantage of SASB, besides the reduction in computational load, is that the lateral resolution remains higher and more uniform over depth compared to regular dynamic receive focusing (DRF) [19]. The use of virtual sources in SASB has been shown to create an acoustic field intense enough to generate harmonics for THI [20]. By combining THI with SASB, the final image is improved by both techniques. The improvements are increased spatial resolution, reduced reverberation artifacts, reduced side lobe levels, and a narrower beam profile from THI along with a range independent fully focused image in both transmit and receive from SASB [21].

This paper presents an implementation of tissue harmonic synthetic aperture imaging on a commercial ultrasound system. The paper presents first an optimization study of tissue harmonic synthetic aperture imaging for *in-vivo* imaging. The optimal virtual source position and image line density are studied by investigations of spatial resolution, side lobe levels, and frame rate. A method for scaling areas with low energy in the images is presented. Next, a comparison of the performance of tissue harmonic synthetic aperture imaging and dynamic receive focus tissue harmonic imaging in terms of lateral resolution and cystic resolution is presented. Finally, a duplex *in-vivo* scan is acquired using the two techniques and images are compared.

II. THEORY

Synthetic aperture imaging and tissue harmonic imaging are both two well studied concepts in ultrasonics imaging. The first concept deals with focusing of the responses, while the second concept deals with signal processing of the received responses. Both are explained in the following.

A. Synthetic Aperture Sequential Beamforming

Traditionally, SAI utilizes only one active transducer element in transmit (see Fig. 1a). Because the transmitted acoustic energy in this case is very low, SAI is not capable of producing harmonic components for THI. Synthetic aperture sequential beamforming (SASB) is a SAI technique, which uses virtual sources and a dual stage beamforming approach to significantly reduce the computational load compared to SAI [22], [23]. A fixed transmit and receive focal point is used in the first stage beamformer to create a set of focused scan lines with reference r_θ and a virtual source at r_{vs} in each emission. The dotted lines in Fig. 2 show the image information at spatial positions that are found in each focused scan line. A single image point, r_{ip} may be represented in several focused scan lines as shown by the black dot. The overlapping contributions from the first stage image lines can be used to improve resolution. The first stage image data is therefore beamformed again (second stage beamforming) using a focus at each pixel in the image. This produces a set of low resolution images, which are then summed coherently to form a single depth invariant high resolution image (see Fig. 1b). The advantage of SASB, besides the improvements in

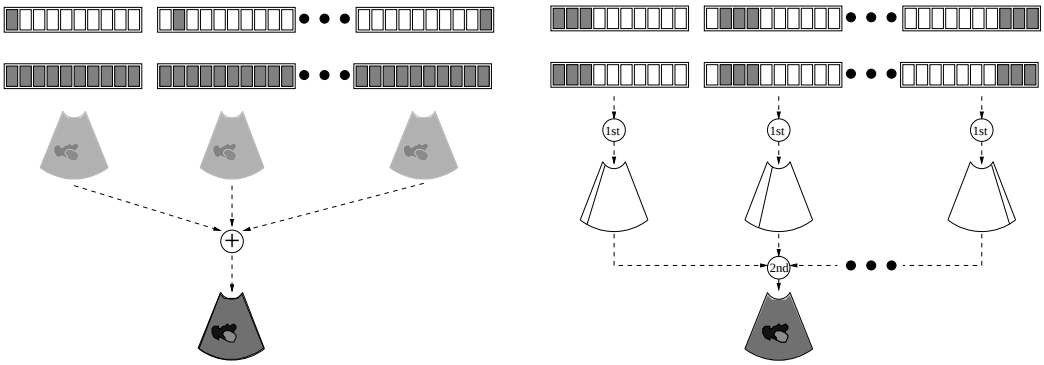

(a) Schematic illustration of SAI. (b) Schematic illustration of SASB.

Fig. 1: Concept illustrations of SAI and SASB. In SAI, a single element is used in transmit, while all elements are used in receive. Low resolution images are generated and summed. In SASB, a fixed group of elements are used in transmit and receive. A fixed focus image is generated using the first stage beamformer. The first stage image lines are used as input for the second stage beamformer using the focus point as a virtual source.

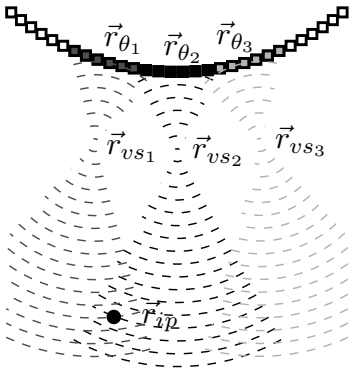

Fig. 2: Three emissions for first stage SASB. A single image point, r_{ip} is represented in several focused scan lines. Figure taken from [23].

lateral resolution, is that the transmitted acoustic energy is sufficient to produce harmonic components for THI [20]. A combination of SASB and THI can therefore be implemented.

B. Tissue Harmonic Imaging

In THI, the purpose is to image the harmonic frequency band of a pulse response, instead of the transmitted fundamental frequency. As a transmitted ultrasound waveform propagates through a medium, the waveform gets distorted due to the nonlinear properties of the medium [24]–[26]. The speed at which the waveform travels (the sound of speed) depends on the instantaneous acoustic pressure within the waveform. Because there is a pressure difference between the high pressure peaks and the relatively low pressure troughs of the waveform, different parts

of the waveform travels at different speed [27], [28]. This causes the high pressure peaks to travel a a higher speed of sound than the relatively low pressure troughs. As the waveform gets continuously distorted, higher harmonics are generated in the waveform. The strength of these harmonics is dependent on the acoustic pressure of the emitted ultrasound field. It is therefore important to emit a field intense enough to ensure good development of harmonic waveforms.

In THI it is also important to ensure good separation of the desired harmonic frequency from unwanted neighboring frequencies, since these will influence the spatial resolution. Several techniques exist to separate and enhance harmonic frequencies such as matched filtering, power modulation, and pulse inversion (PI) [29]–[31]. In PI, two identical but phase shifted pulses (0° phase shifted and 180° phase shifted pulse) are transmitted in turn for the same transducer geometry. Under the assumption that there has been no motion in the medium in the time between the two waveforms were transmitted, differences in the responses are purely a result from how the waveforms were distorted by the medium. For the received pair of responses, a 180° phase shift between the two waveforms can be detected at the fundamental frequency. However, for the 2nd and 3rd harmonic frequencies, a corresponding 360° and 540° phase shift can be detected in the pair of waveforms respectively [32], [33]. If the two responses are summed, all signals that are perfectly in phase will double in signal strength, while all signals that have opposite phases will cancel out. To suppress the odd order harmonics then, each pair (regular and phase shifted) of the received responses are summed (see Fig. 3). The harmonic frequencies that are in phase (all even harmonics) will double in amplitude, while out of phase harmonic frequencies (all odd harmonics) will cancel out (see Fig. 4). This separates and enhances the 2nd harmonic frequency, which in turn then can be extracted using a matched filter and used for imaging.

III. Equipment

The implementation of the suggested scan technique is performed on commercially available ultrasound equipment. The application of a research interface to the ultrasound scanner allows user defined scan sequences to be used. By using equipment that have already been approved by regulatory mandates, the scan sequences that are suggested in the following can be implemented on the system and used in clinical investigations without any further regulatory approval.

A. The Research Interface

A commercially available BK 2202 UltraView scanner from BK Medical is fitted with a research interface. The research interface allows the user to control many of the manufacturer defined scan settings such as focal points, F#'s, line density , number of emissions, etc. in a predefined usecase. The research interface also allows the user to access and extract image data at different points in the beamforming process. In this case, image data is extracted via a grabber card X64-CL Express grabber card produced by Teledyne DALSA, Canada and camera link to a

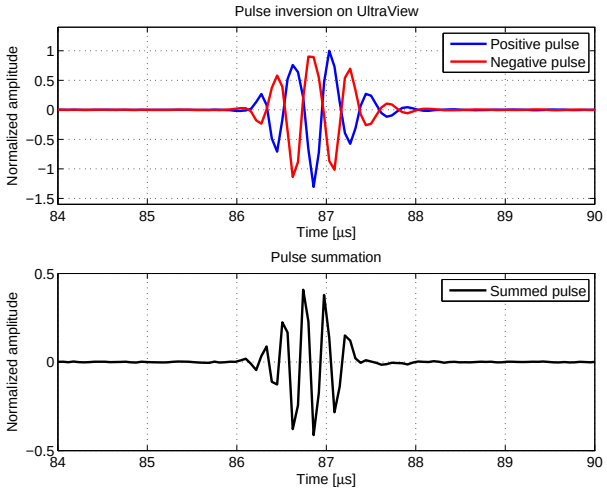

Fig. 3: Pulse responses acquired using pulse inversion. The positive and the negative pulse responses are shown in the top. Response length and zero-intersections are almost identical. Shown below is the summed pulse, which is the result of harmonic distortion of the two original positive and negative responses.

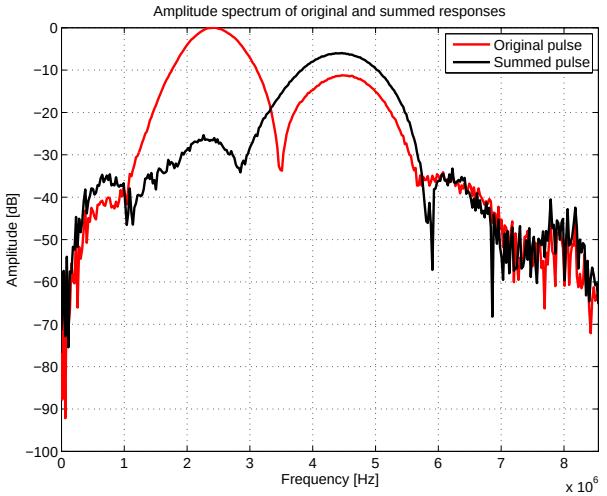

Fig. 4: Spectrum of the the pulse response prior to and after pulse summation. The fundamental frequency is located at 2.14 MHz and is normalized to 0 dB. The 2nd harmonic frequency is visible in the original response at 4.28 dB at a magnitude of approximately -12 dB. The magnitude of the 2nd harmonic frequency is enhanced by approximately 6 dB after pulse summation, while the fundamental frequency is attenuated by approximately 25 dB.

desktop PC running MATLAB.

The scanner is fitted with a 192 element convex array transducer typically used in THI investigations in e.g. abdominal scans (see Table I). The default scanning technique using this transducer on the UltraView scanner is tissue harmonic dynamic receive focusing (DRFTHI) B-mode. For this technique the scanner uses a one-and-a-half cycle sinusoid transmit waveform with center frequency of 2.14 MHz and 14 MHz sampling frequency. The 2nd

TABLE I: Convex array transducer parameters.

Transducer Parameters	Value
Pitch	0.33 mm
Elevation focus	65 mm
Number of elements	192
Radius of curvature	60 mm
Field of view	60.5 deg
Center frequency	3.5 MHz
Operating frequency	2-6 MHz

harmonic component of the received signal used for DRFTHI should therefore have an expected center frequency of 4.28 MHz. This is confirmed by the spectrum of a received pulse response in Fig. 4 acquired using the UltraView scanner and research interface. A transmit focus of 85 mm and F# of 5.67 is applied with an active aperture of 64 elements using boxcar transmit apodization. In receive, a dynamically expanding aperture is used with gauss apodization and an F# of 0.8.

B. The Scan Sequence

In this study, the UltraView scanner is set up to perform both SASBTHI and DRFTHI simultaneously in a duplex scan. The usecase specifies the general scanner settings such as speed of sound, maximum scan depth, and transducer parameters as well as the specific scan sequence settings for SASBTHI and DRFTHI. For DRFTHI, the settings are kept at the default settings defined by the scanner. For SASBTHI, the settings are the same as for DRFTHI except for the position of the transmit/receive focal point, the transmit/receive F#, and the focusing technique. A schematically illustration representation of the usecase and the scan sequence is shown in Fig. 5.

For both scans, THI is performed using pulse inversion and matched filtering to achieve 2nd harmonic IQ-data. The first two emissions in the full emission sequence are the PI emissions for scan line number one for SASBTHI. The next two emissions are for scan line number two for SASBTHI and so on, until the first full set of emissions for one frame has been performed for SASBTHI. Next, the emissions belonging to DRFTHI are conducted in the same manner. The emission sequence is set this way to minimize tissue movement between the individual image lines, which could otherwise introduce errors in the beamforming stage. Summing and matched filtering of the received paired PI responses is then conducted by the scanner, giving the 2nd harmonic responses. Next, beamforming using either dynamic receive focusing for DRFTHI or fixed focusing for first stage SASBTHI is performed using the beamformer implemented on the scanner. Beamformed 2nd harmonic IQ image data is then exported via the data acquisition card on to the external PC for IQ-to-RF data conversion and second stage beamforming.

IV. SASB Optimization

In order to optimize the settings for SASBTHI for *in-vivo* imaging, a series of measurements on wire and speckle phantoms are conducted. The scope of these measurements is to find the optimal depth for the virtual source and

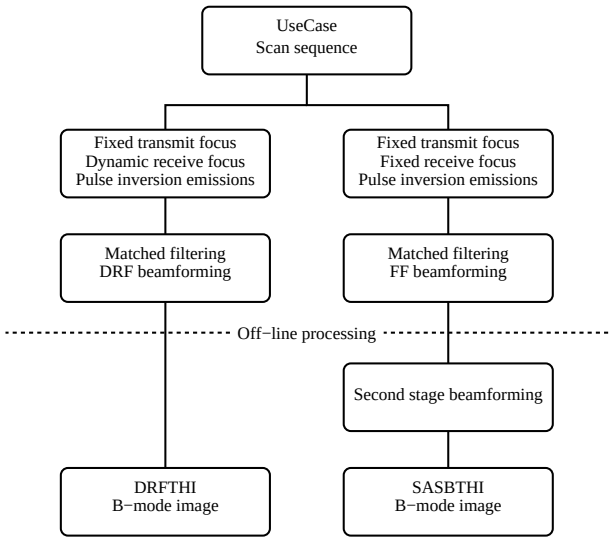

Fig. 5: Scan sequence on the BK 2200 Pro Focus UltraView scanner. The usecase defines a scan sequence that performs two scans simultaneously in parallel. The scan for SASBTHI utilizes a fixed focus (FF) in transmit and receive, while the scan for DRFTHI utilizes dynamic receive focusing (DRF).

the imaging line density for SASBTHI that will result in high and depth independent resolution, while maintaining low levels of side lobe energy and highest possible frame rate.

A. Virtual Source Position

The scope of these measurements is to find the optimal depth for the virtual source and the imaging line density for SASBTHI that will result in high and depth independent resolution, while maintaining both low levels of side lobe energy and the highest possible frame rate. A wire phantom is scanned using different virtual source positions and line densities. By measuring the full width at half max (-6 dB lateral resolution), the lateral resolution is quantified. For each measurement a different virtual source position and line density is set. The virtual source position varies between 5 cm and 7 cm, while the line density varies between 192, 269, and 384 image lines per B-mode image as seen in Table II. In total, 9 measurements are made with the different settings. The transducer is fixed in a scaffold in position over the wires so the scan geometry is the same for all measurements. All first stage image data are stored on the desktop PC and second stage beamforming is completed for each measurement.

Fig. 6 shows three examples of SASBTHI B-mode images of the wire phantom using different line densities and positions of the virtual source. An increase in the number of image lines from 192 to 384, causes the level of side lobes to decrease as seen from Fig. 6a and Fig. 6b. This indicates, that the number of image lines should be maximized within reasonable limits as to not compromise the imaging frame rate. Furthermore, the level of side lobes increases with distance from the virtual source. Point scatterers near the virtual source have lower levels of side lobes compared to scatterers further away from the virtual source. By moving the location of the virtual source

TABLE II: Scan parameters for SASBTHI optimization.

Scanner Parameters	SASBTHI
Transmit center frequency	2.14 MHz
Waveform cycles	1.5
Sampling frequency	17 MHz
Number of scanlines	[192, 269, 384]
Number of active elements	64
Focus Tx/Rx (mm)	[50, 60, 70]
Imaging depth (mm)	160
F# Tx/Rx	2
Apodization Tx/Rx	Gauss

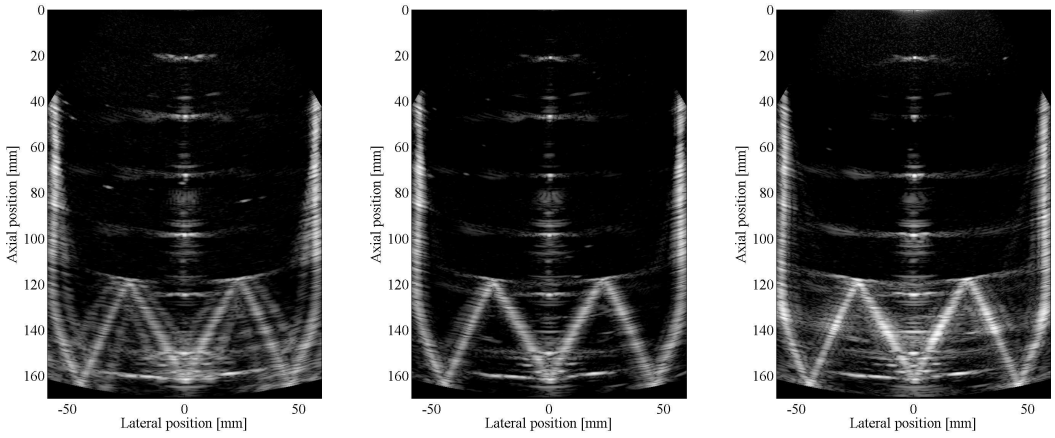

(a) 192 image lines, 70mm focus (b) 384 image lines, 70mm focus. (c) 384 image lines, 50mm focus.

Fig. 6: SASBTHI B-mode scans of wire phantom using varying number of image lines and transmit/receive focus depths.

from 70 mm to 50 mm in Fig. 6b and Fig. 6c, the level of side lobes at the top and bottom of the image shifts. It is seen, that the side lobes fan out from the position of the virtual source. This indicates, that the virtual source should be positioned near the half of the maximum imaging depth as to decrease the level of side lobes throughout the entire image.

In Fig. 7, the lateral -6 dB resolution is shown for different positions of the virtual source and for varying line density. By increasing the number of lines in the image, in Fig. 7a to Fig. 7c, the lateral resolution for all positions of the virtual source becomes more uniform and more depth invariant. It is also seen from in the figures, that as the the number of image lines increases, the lateral resolution graphs for all three positions of the virtual become more identical. This indicates, that the lateral resolution in the image is less affected by the change of focus point as the

line density increases. In all cases in Fig. 7, it is seen, that having the virtual source near 70 mm depth produces both the lowest values of -6 dB resolution and the most depth invariant values. Therefore, in order to keep the most depth invariant and best lateral resolution, the line density should be maximized, while the focus point and thereby the position of the virtual source should be at 70 mm depth.

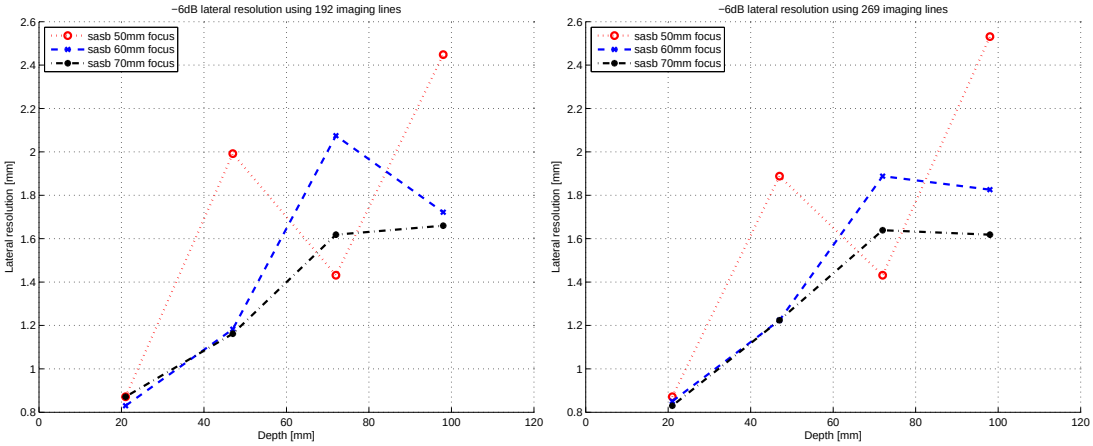

(a) 192 image lines.

(b) 269 image lines.

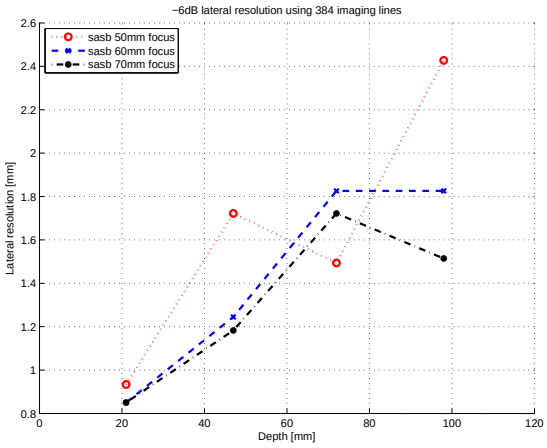

(c) 384 image lines.

Fig. 7: Measured -6 dB lateral resolution for SASBTHI using 192 (7a), 269 (7b), and 384 (7c) image lines and transmit/receive focus depths. By increasing the line density, the lateral resolution improves. Furthermore, by increasing the depth of the focus point and thereby the position of the virtual source, the lateral resolution is additionally improved. This suggest that in order to achieve the best and most depth invariant lateral resolution, the line density should be maximized, while the virtual source should be positioned at half the maximum imaging depth.

B. Line Density

As described in section IV-A, increasing the line density in SASBTHI drastically reduces the energy levels of the side lobes. However, it also affects the time it takes to complete a B-mode frame. Table III shows the frame rates that can be accomplished for different line densities when the scan sequence is performing a duplex scan with both SASBTHI and DRFTHI with equal line density. While having 384 scan lines available improves the spatial resolution and the levels of side lobes, the frame rate of the scan drops to just 3 frames per second. The display of continuously moving tissues in an *in-vivo* scan is disrupted by the low frame rate to a degree where finding and scanning the desired area is near impossible for the user. By decreasing the number of available imaging lines to 269, the frame rate is increased to 5 frames per second which shows a remarkably improvement to the eye of the user. For scans where only either SASBTHI or DRFTHI is required, the available frame rate can be doubled because no duplex scan is needed. This will allow the use of maximum line density (384 scan lines per frame) without disrupting the display of moving tissues.

TABLE III: Available frame rates for B-mode SASBTHI-DRFTHI duplex scan for various line densities.

Scan lines	Frame rate
192	6 frames/s
269	5 frames/s
384	3 frames/s

C. Virtual Source Scaling

In Fig. 9a is shown a SASBTHI scan of a cyst phantom. A section of the phantom containing almost no cysts is scanned thereby producing a scan that shows the speckle pattern of SASBTHI. The image shows, apart from the cysts in the right hand side of the image, a darkened region across the image at the focal depth at 70 mm depth as well as a darkened region in the top 10 mm of the image due to low energy in the image. The dark region at the top of the image is caused by the lack of 2nd harmonic energy in the transmitted waveform. Since the harmonics in a waveform are progressively generated by distortion of the transmitted waveform, the 2nd harmonic will build up in signal strength as the distance the waveform has propagated increases. At the top of the image, the distance the waveform has propagated is small, causing the distortion of the waveform and the level of 2nd harmonic energy to be very low as well. This results in a dark region in the image where the 2nd harmonic energy is low compared to the rest of the image as seen in Fig. 9a.

The dark region near the focal point is caused by the low number of first stage image lines that contribute to an imaging point near the virtual source and because of the geometrical shape of the transducer. As seen from Fig. 2, an imaging point may be represented by several image lines. For an imaging point close to the virtual source, however, the point may only be represented in just one line. This will cause the energy in the second stage image

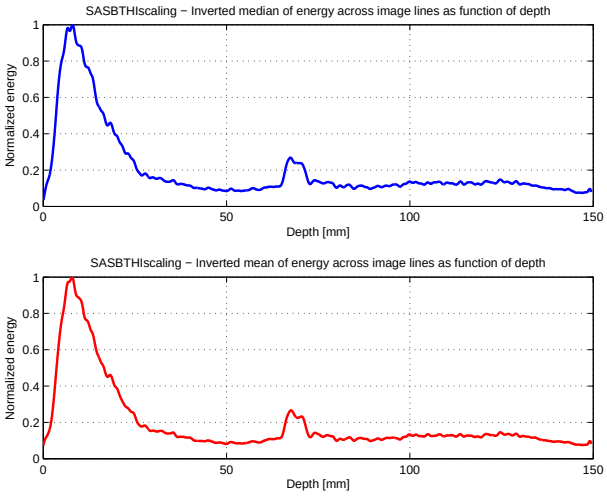

Fig. 8: VS-scaling curves for SASBTHI. Median VS-scaling and mean VS-scaling.

to drop in the vicinity of the virtual source. Furthermore, because a convex array transducer is used, the first stage scan lines are not parallel to each other, but spread out like a fan with imaging depth. This further contributes to less first stage lines representing imaging points near the virtual source.

In order to equalize the dark regions in the SASBTHI image, some sort of scaling must be done to the image. By calculating the median and mean of the energy across image lines in Fig. 9a for every sample depth, a map of the energy in the image can be drawn. The measured energy is inverted and low pass filtered to exclude rapid fluctuations in order to generate a set of virtual source scaling (VS-scaling) curves that can be used to equalize gain in the SASBTHI images where the energy is low. As can be seen from the VS-scaling curves in Fig. 8, the energy is enhanced primarily at the top of the image and to a lesser degree at the position of the virtual source at 70 mm. Figure 9b shows the same scan of the cyst phantom with the median VS-scaling applied to every image line. As can be seen from the image, the dark regions near the virtual source and at the top of the image have now been neutralized and a uniform gray level has been attained. In Fig. 10, an *in-vivo* scan of the liver of a healthy 31 year old male is shown with and without VS-scaling applied. The images were acquired using the UltraView and the research interface. The dark region of the virtual source is neutralized by VS-scaling and does not introduce any visual artifacts in the *in-vivo* image. The energy is also increased at the top of the image after VS-scaling to obtain a more uniform gray scale throughout the entire image.

A similar scaling curve based on a DRFTHI speckle scan is made for DRFTHI, only this curve only adjusts for low 2nd harmonic energy at the top of the image, since no virtual sources are used in this imaging technique. An example of a DRFTHI scan where the median scaling curve has been applied is shown in Fig. 12a.

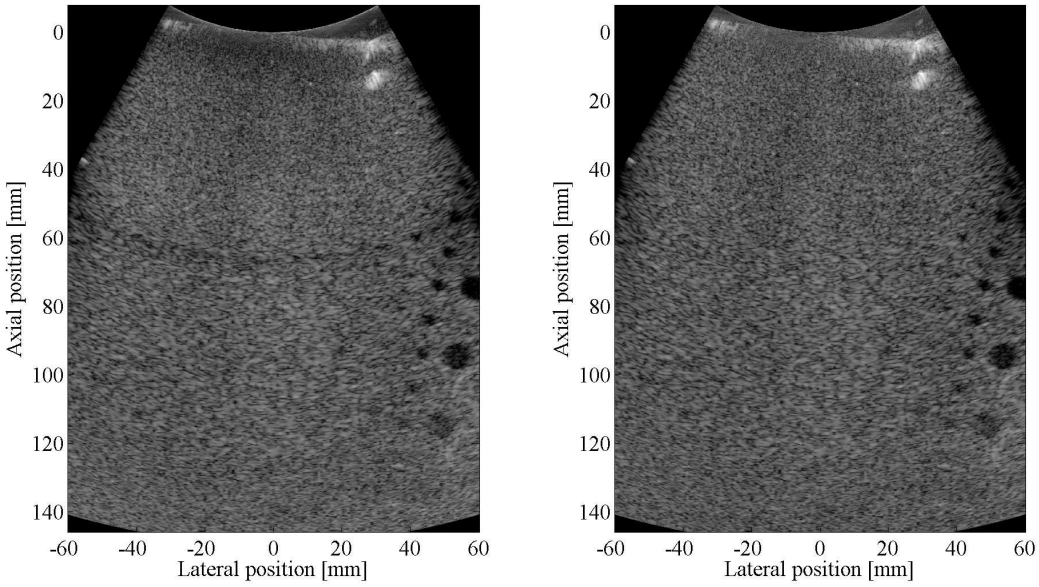

(a) No VS-scaling applied.

(b) Median VS-scaling applied.

Fig. 9: B-mode speckle scan of tissue mimicking cyst phantom using SASBTHI. No VS-scaling is applied in 9a. Here, a dark region is visible at the position of the virtual source at 70 mm depth. A dark area is also seen in the top part of the image, where the 2nd harmonic signal strength is low. In the image in 9b, median VS-scaling is applied to correct for the regions with low signal strength. The top region and the virtual source region are now equal in gray scale compared to the rest of the image.

V. Results

Based on the results from section IV-A and section IV-B, a usecase with the scan parameters in Table IV was suggested as being the optimal for a SASBTHI-DRFTHI *in-vivo* duplex scan. A transmit/receive focus at 70 mm depth, a maximum scan depth at 145 mm, and 269 scan lines were all used for SASBTHI. Default parameters that were optimized by the manufacturer of the UltraView scanner were used for DRFTHI.

In Fig. 11, the -6 dB lateral resolution and 20 dB cystic resolution for SASBTHI and DRFTHI is compared for a line density of 269 lines per image. From Fig. 11a it is seen, that SASBTHI generally produces better lateral resolution compared to DRFTHI. Only near the position of the virtual source at 70 mm does DRFTHI produce better lateral resolution than SASBTHI. This is due to the fact that only few first stage image lines contribute final second

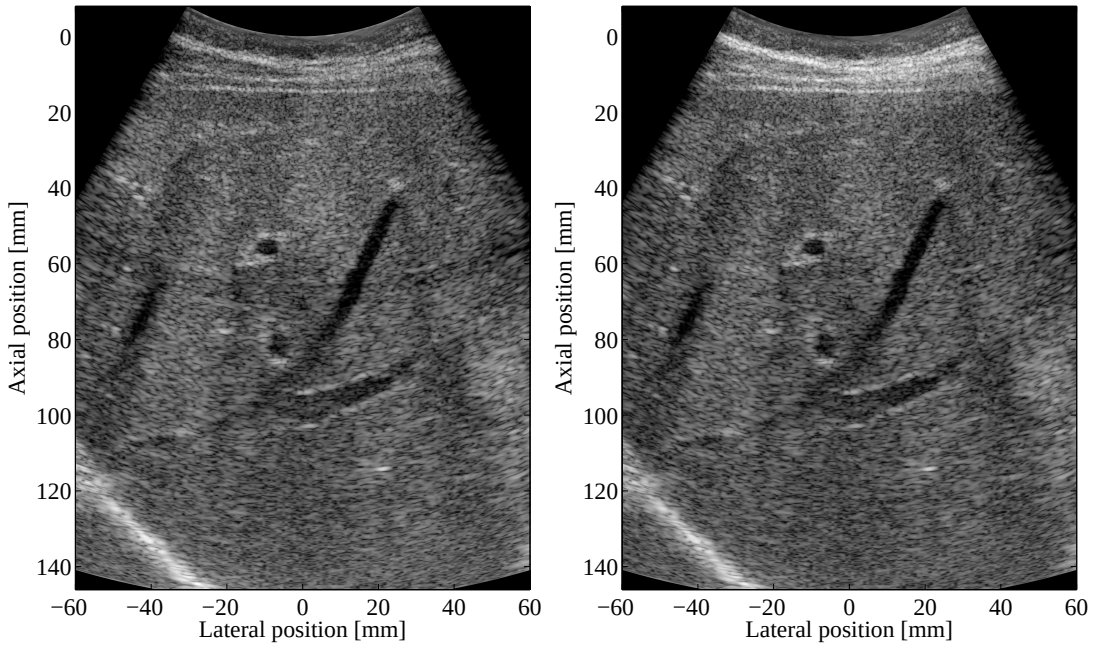

(a) No VS-scaling applied.

(b) Median VS-scaling applied.

Fig. 10: B-mode *in-vivo* scan of liver tissue using SASBTHI without VS-scaling in 10a and with median Vs-scaling in 10b. The dynamic range in the images is 60 dB. It is seen from the images, that VS-scaling successfully equalizes the gray scale in the region near the virtual source to match the gray scale in the rest of the image. The region at the top of the image is amplified by VS-scaling to compensate for low 2nd harmonic signal strength.

TABLE IV: Scan parameters for clinical comparisons of SASBTHI and DRFTHI.

Scanner Parameters	SASBTHI	DRFTHI
Transmit center frequency	2.14 MHz	2.14 MHz
Waveform cycles	1.5	1.5
Sampling frequency	17 MHz	17 MHz
Number of scan lines	269	269
Number of active elements	64	64
Focus Tx (mm)	70	85
Focus Rx (mm)	70	Dynamic
Imaging depth (mm)	145	145
F# Tx	2	5.67
F# Rx	2	0.8
Apodization Tx	Boxcar	Boxcar
Apodization Rx	Gauss	Gauss

stage image near the virtual source. The measured values for the lateral resolution are also shown in Table V. Here it is clearly seen that SASBTHI generally produces the best lateral resolution except for regions near the virtual source.

The level of side lobe is determined by measuring the amount of energy inside an expanding region relative to the total energy of a wire. By measuring the width of the expanded region where the relative energy difference is 20 dB, the level of side lobes is quantified (20 dB cystic resolution). In Fig. 11b, the cystic resolution of the two

TABLE V: Measured values for -6 dB lateral resolution for SASBTHI and DRFTHI and the difference in percentage between SASBTHI and DRFTHI.

Image depth	SASBTHI	DRFTHI	Difference
21	0.8	1.0	20%
47	1.2	1.3	8%
72	1.6	1.5	-8%
98	1.6	2.0	20%

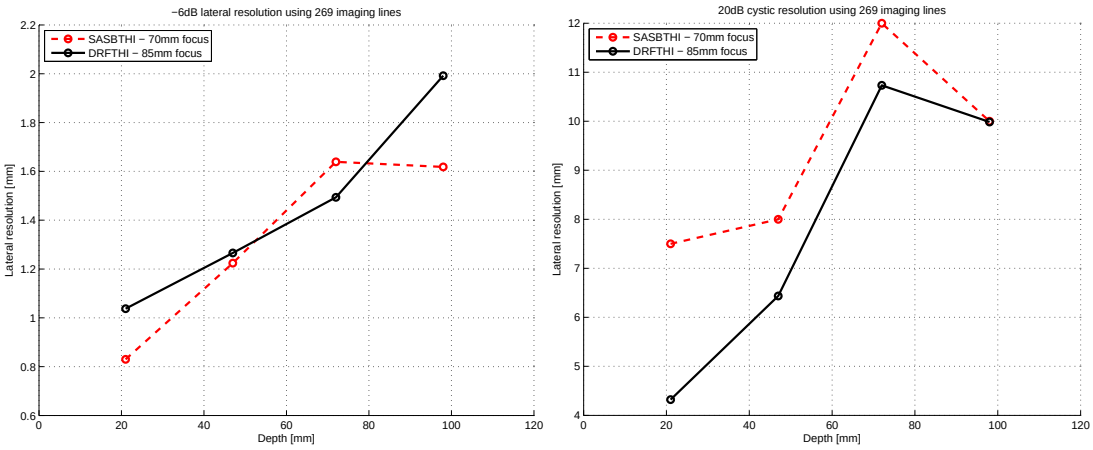

(a) -6 dB lateral resolution.

(b) 20 dB cystic resolution.

Fig. 11: Measured -6 dB lateral resolution (11a) and 20 dB cystic resolution (11b) for SASBTHI and DRFTHI. The line density is 269 lines per image in both cases. The transmit focus is at 85 mm for DRFTHI and the virtual source is at 70 mm for SASBTHI.

techniques is compared again using 269 image lines and focus point of 85 mm for DRFTHI and virtual source position of 70 mm for SASBTHI. It is seen from the figure, that DRFTHI produces better cystic resolution for all depth compared to SASBTHI.

An *in-vivo* SASBTHI-DRFTHI duplex scan of the liver of a healthy 31 year old male is done using the scan parameters described in Table IV. The B-mode images are shown in Fig. 12. In the SASBTHI case, median VS-scaling is applied and for DRFTHI, a similar median scaling is applied to equalize the gray scale between the two images. The images show the same view of the liver proving that the simultaneous acquisition of images using the research interface works. In both images, structures such as blood vessels and liver boundaries are clearly visible. The scaling applied to both images corrects for low 2nd harmonic signal strength at the top region of the image, and for low signal strength due to the virtual source position in the SASBTHI image. There are no visible differences in terms of gray scale levels between the two images. Overall, no visible differences are found in the two images, making it very difficult to distinct the two techniques from each other.

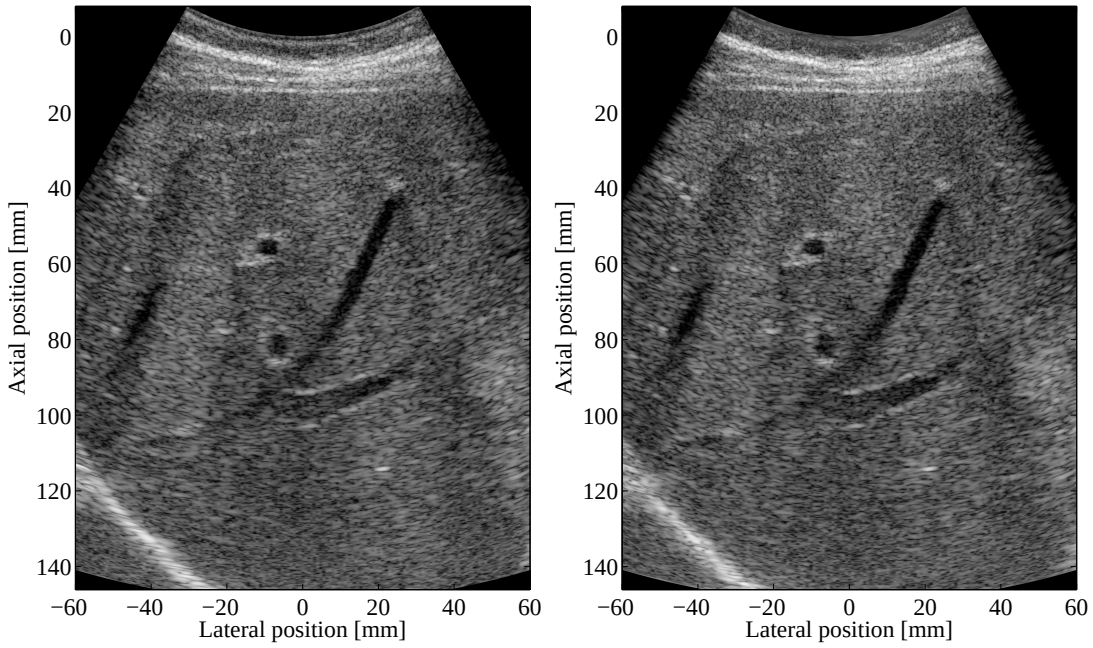

(a) DRFTHI. (b) SASBTHI.

Fig. 12: B-mode *in-vivo* scan of liver tissue using DRFTHI in 12a and SASBTHI in 12b. Median scaling has been applied to both images to neutralize low signal regions from virtual sources and due to low 2nd harmonic energy. The dynamic range in both images is 60 dB.

VI. Discussion

The comparisons of the lateral resolution in Fig. 11a show that SASBTHI produce a higher -6 dB resolution value than DRFTHI for the wire close to the virtual source. This indicates, that the lateral resolution of SASBTHI is worse than DRFTHI at his image depth. The reason why the lateral resolution for SASBTHI is worse near the virtual source is due to the amount of first stage image lines that contribute to the second stage image near the virtual source as was also described in Section IV-C. This effect is similar to using a lower line density in the usecase, which would also cause the lateral resolution to decrease (see Fig. 7). However, excluding the measurement near the virtual source, SASBTHI generally produces higher lateral resolution compared to DRFTHI. In some cases, SASBTHI produces up to 20% better lateral resolution compared to DRFTHI and in the worst case near the virtual source, the difference between SASBTHI and DRFTHI is no more than 0.1 mm or 8%.

It is also seen from Fig. 11a, that the slope of lateral resolution as function of image depth is less for DRFTHI than it is for SASBTHI. This indicates, that in this case, depth invariance is more pronounced for DRFTHI. However, as seen from Fig. 7, by increasing the line density from 269 lines per image to 384 lines per image for SASBTHI, the slope of the lateral resolution as function of depth becomes smaller, if the values near the position of the virtual source are neglected. This would suggest, that SASBTHI could be further improved compared to DRFTHI if the

line density is increased.

The measured 20 dB cystic resolution of the two techniques was compared in Fig. 11b. The results show that DRFTHI scores 6.4 mm and 10.7 mm in 20 dB cystic resolution for 47 mm and 72 mm depths, while SASBTHI scores 8 mm and 12 mm for the same depths. This means that DRFTHI is capable of displaying cysts that are approximately 1.5 mm smaller in diameter with 20 dB difference in dynamic range.

The scan settings for SASBTHI were optimized for this study based on the decision that the technique should work in a simultaneous duplex scan setup with DRFTHI to allow for future clinical evaluation. Restrictions were therefore made to the line density in order to keep the frame rate high enough to allow for use in clinical investigations. If SASBTHI was to be implemented not in a duplex sequence, but by itself, the line density could be doubled without loss in the frame rate compared to the duplex scan. The increased line density would further improve the lateral resolution for all imaging depths (see Fig 7) and the cystic resolution.

VII. Conclusion

An implementation of a tissue harmonic synthetic aperture imaging technique was performed on a commercial ultrasound system. A scan sequence that can perform a simultaneous SASBTHI and DRFTHI duplex scan was developed and optimized for *in-vivo* imaging. Line density and position of the virtual source for SASBTHI were optimized for the duplex scan sequence based on lateral resolution, side lobe levels, and frame rates. A scaling curve was developed to compensate for low distribution of contributing image lines near the virtual source and for low 2nd harmonic signal strength at the top of the image. The scaling curve equalized the gray scale throughout the image and also in between the SASBTHI and DRFTHI images. Measurements of the -6 dB lateral resolution on a wire phantom showed that SASBTHI produced up to 20% higher resolution than DRFTHI except near the position of the virtual source where DRFTHI produced 0.1 mm higher resolution. In general, DRFTHI produced the most depth invariant lateral resolution of the two techniques, however it is expected that the resolution in SASBTHI can be made more depth invariant by increasing the line density. For 47 mm and 72 mm image depths DRFTHI produced approximately 1.5 mm better 20 dB cystic resolution than SASBTHI. An *in-vivo* scan of the liver of a healthy 31 year-old male was acquired using the duplex scan sequence. No visible differences were seen in the two images indicating, that SASBTHI performs as good as DRFTHI in the suggested setup.

Acknowledgment

This work is supported by grant 024-2003-3 from the Danish Advanced Technology Foundation and by BK Medical Aps, Herlev, Denmark.

REFERENCES

[1] B. Ward, A. C. Baker, and V. F. Humphrey, "Nonlinear propagation applied to the improvement of resolution in diagnostoc medical ultrasound," *J. Acoust. Soc. Am.*, vol. 101, no. 1, pp. 143–154, 1997.

[2] T. Christopher, "Finite amplitude distortion-based inhomogeneous pulse echo ultrasonic imaging," *IEEE Trans. Ultrason., Ferroelec., Freq. Contr.*, vol. 44, no. 1, pp. 125–139, 1997.

[3] M. A. Averkiou and M. F. Hamilton, "Measurements of harmonic generations in a focused finite-amplitude sound beam," *J. Acoust. Soc. Am.*, vol. 98, no. 6, pp. 3439–3442, 1995.

[4] L. J. Cutrona, W. E. Vivian, E. N. Leith, and G. O. Hall, "A high resolution radar combat-surveillance system," *IRE Trans. Mil. Elect.*, vol. MIL-5, no. 2, pp. 127–131, 1961.

[5] C. W. Sherwin, J. P. Ruina, and D. Rawcliffe, "Some early developements in synthetic aperture radar systems," *IRE Trans. Mil. Elect.*, vol. MIL-6, no. 2, pp. 111–115, 1962.

[6] J. C. Curlander and R. N. McDonough, *Synthetic Aperture Radar: Systems and Signal Processing*. John Wiley & Sons, Inc., 1991.

[7] R. Thomson, "Transverse and longitudinal resolution of the synthetic aperture focusing technique," *Ultrasonics*, vol. 22, pp. 9–15, 1984.

[8] M. L. Li, W. J. Guan, and P. C. Li, "Improved synthetic aperture focusing technique with application in high-frequency ultrasound imaging," *IEEE Trans. Ultrason., Ferroelec., Freq. Contr.*, vol. 51, no. 1, pp. 63–70, January 2004.

[9] C. Passmann and H. Ermert, "A 100-MHz ultrasound imaging system for dermatologic and ophthalmologic diagnostics," *IEEE Trans. Ultrason., Ferroelec., Freq. Contr.*, vol. 43, pp. 545–552, 1996.

[10] C. H. Frazier and W. D. O'Brien, "Synthetic aperture techniques with a virtual source element," *IEEE Trans. Ultrason., Ferroelec., Freq. Contr.*, vol. 45, pp. 196–207, 1998.

[11] S. I. Nikolov and J. A. Jensen, "Virtual ultrasound sources in high-resolution ultrasound imaging," in *Proc. SPIE - Progress in biomedical optics and imaging*, vol. 3, 2002, pp. 395–405.

[12] ——, "3D synthetic aperture imaging using a virtual source element in the elevation plane," in *Proc. IEEE Ultrason. Symp.*, vol. 2, 2000, pp. 1743–1747.

[13] K. L. Gammelmark and J. A. Jensen, "Multielement synthetic transmit aperture imaging using temporal encoding," *IEEE Trans. Med. Imag.*, vol. 22, no. 4, pp. 552–563, 2003.

[14] M. H. Bae and M. K. Jeong, "A study of synthetic-aperture imaging with virtual source elements in B-mode ultrasound imaging systems," in *IEEE Trans. Ultrason., Ferroelec., Freq. Contr.*, vol. 47, 2000, pp. 1510–1519.

[15] M. Bae, H. Lee, S. B. Park, R. Yoon, M. H. Jeong, D. G. Kim, M. Jeong, and Y. Kim, "A new ultrasonic synthetic aperture tissue harmonic imaging system," in *Proc. IEEE Ultrason. Symp.*, 2008, pp. 1258–1261.

[16] M. H. Bae, S. B. Park, H. W. Lee, S. G. Nam, and M. K. Jeong, "A new extended range ultrasonic synthetic aperture tissue harmonic imaging system," in *Proc. IEEE Ultrason. Symp.*, vol. 2011 IEEE INTERNATIONAL ULTRASONICS SYMPOSIUM (IUS), 2012, pp. 401–404.

[17] J. Kortbek, J. A. Jensen, and K. L. Gammelmark, "Sequential beamforming for synthetic aperture imaging," *Ultrasonics*, vol. 53, no. 1, pp. 1–16, 2013.

[18] J. A. Jensen, J. Kortbek, S. I. Nikolov, M. C. Hemmsen, and B. Tomov, "Implementation of synthetic aperture imaging in medical ultrasound: The dual stage beamformer approach," in *EUSAR*, 2010, pp. 434–437.

[19] M. C. Hemmsen, J. M. Hansen, and J. A. Jensen, "Synthetic Aperture Sequential Beamformation applied to medical imaging using a multi element convex array transducer," in *EUSAR*, Apr. 2012, p. Accepted for publication.

[20] Y. Du, J. Rasmussen, H. Jensen, and J. A. Jensen, "Second harmonic imaging using synthetic aperture sequential beamforming," in *Proc. IEEE Ultrason. Symp.*, 2011, pp. 2261–2264.

[21] J. H. Rasmussen, M. C. Hemmsen, S. S. Madsen, P. M. Hansen, M. B. Nielsen, and J. A. Jensen, "Implementation of tissue harmonic synthetic aperture imaging on a commercial ultrasound system," in *Proc. IEEE Ultrason. Symp.*, 2012.

[22] J. Kortbek, J. A. Jensen, and K. L. Gammelmark, "Synthetic aperture sequential beamforming," in *Proc. IEEE Ultrason. Symp.*, 2008, pp. 966–969.

[23] M. Hemmsen, P. M. Hansen, T. Lange, J. M. Hansen, K. L. Hansen, M. B. Nielsen, and J. A. Jensen, "In vivo evaluation of synthetic aperture sequential beamforming," *Ultrasound Med. Biol.*, vol. 38, no. 4, pp. 708–716, 2012.

[24] R. T. Beyer, *Nonlinear Acoustics*. Department of the Navy, 1974.

[25] J. A. Shooter, T. G. Muir, and D. T. Blackstock, "Acoustic saturation of spherical waves in water," *J. Acoust. Soc. Am.*, vol. 55, no. 1, pp. 54–62, 1974.

[26] H. C. Starritt, M. A. Perkins, F. A. Duck, and V. F. Humphrey, "Evidence for ultrasonic finite-amplitude distortion in muscle using medical equipment," *J. Acoust. Soc. Am.*, vol. 77, pp. 302–306, 1985.

[27] F. A. Duck, "Nonlinear acoustics in diagnostic ultrasound," *Ultrasound Med. Biol.*, vol. 28, pp. 1–18, 2002.

[28] T. L. Szabo, *Diagnostic ultrasound imaging inside out*. Elsevier, 2004.

[29] C. S. Chapman and J. C. Lazenby, "Ultrasound imaging system employing phase inversion subtraction to enhance the image," US Patent 5632277, 1997.

[30] D. H. Simpson, C. T. Chin, and P. N. Burns, "Pulse inversion Doppler: a new method for detecting nonlinear echoes from microbubble contrast agents," *IEEE Trans. Ultrason., Ferroelec., Freq. Contr.*, vol. 46, no. 2, pp. 372–382, 1999.

[31] X. A. A. M. Verbeek, L. A. F. Ledoux, J. M. Willigers, P. J. Brands, and A. P. G. Hoeks, "Experimental investigation of the pulse inversion technique for imaging ultrasound contrast agents," *J. Acoust. Soc. Am.*, vol. 107, no. 4, pp. 2281–2290, 2000.

[32] J. A. Jensen, "Medical ultrasound imaging," *Prog. Biophys. Mol. Biol.*, vol. 93, pp. 153–165, 2007.

[33] M. A. Averkiou, "Tissue harmonic imaging," in *Proc. IEEE Ultrason. Symp.*, vol. 2, 2000, pp. 1563–1572.